5-2015

Energy selective neutron imaging for the characterization of polycrystalline materials

Robin Woracek
University of Tennessee - Knoxville, rworacek@vols.utk.edu

To the Graduate Council:

I am submitting herewith a dissertation written by Robin Woracek entitled "Energy selective neutron imaging for the characterization of polycrystalline materials." I have examined the final electronic copy of this dissertation for form and content and recommend that it be accepted in partial fulfillment of the requirements for the degree of Doctor of Philosophy, with a major in Engineering Science.

Dayakar Penumadu, Major Professor

We have read this dissertation and recommend its acceptance:

Hahn Choo, Claudia Rawn, John Landes

Accepted for the Council:
Dixie L. Thompson

Vice Provost and Dean of the Graduate School

(Original signatures are on file with official student records.)

Energy selective neutron imaging for the characterization of polycrystalline materials

A Dissertation Presented for the

Doctor of Philosophy

Degree

The University of Tennessee, Knoxville

Robin Woracek

May 2015

Acknowledgements

The work that is presented herein has been undertaken over the course of the last five years and it would have not been possible without the help of many people who I would like to thank. First of all, I would like to express my deepest gratitude to my advisor Prof. Dayakar Penumadu for his guidance and constant support on my research during my M.S. and my PhD project at the University of Tennessee, Knoxville (UTK). He encouraged me to pursue a variety of research topics, much beyond the scope of this dissertation, and to attend several international workshops and conferences, through which I gained profound knowledge in many fields. His support and encouragement was the backbone to complete this work. I would also like to thank my committee members, Prof. Claudia Rawn, Prof. Hahn Choo and Prof. John D. Landes, as well as my external advisory board members Dr. Nikolay Kardjilov (Helmholtz Zentrum Berlin, Germany) and Dr. Axel Steuwer (Invest in Skåne, Resilient Consulting, Sweden and Nelson Mandela Metropolitan University, South Africa) for their precious time and effort devoted to the completion of my PhD degree.

I am extremely grateful that I was part of a wonderful and diverse environment and research group at UTK. In particular, I would like to express my gratitude to my friends in colleagues from the research group: Dr. Akawut Dr. “O” Siriruk, Dr. Jeff Bunn, Dr. Matthew Kant, Mr. Stephen Puplampu, Mr. Aashish Sharma, Dr. Stephen Young, Dr. Felix Kim and Mr. Nathan Meek. I appreciate the help of Mr. Larry Roberts and would like to accentuate the help, support and friendship offered by Mr. Ken Thomas.

A big part of my research was performed at the BERII research reactor at the Helmholtz Zentrum Berlin (HZB) in Germany and I would like to deeply thank Dr. Nikolay Kardjilov who served as my host and advisor during my times there. His expertise and ideas were fundamental to this work. I also would like to thank all my colleagues at HZB, especially Dr. Andre Hilger, Dr. Ingo Manke, Dr. Mirko Boin, Dr. Robert Wimpory, Dr. Markus Strobl (now at ESS), Mr. Frank Wieder, Dr. Christian Toetzke, and Prof. John Bahnhart. I would

especially like to thank my friends in the U.S. for the support throughout the long periods I spent away from them during this time.

I also greatly acknowledge the instrument scientists and user support at HZB, Oak Ridge National Laboratory, ISIS at Rutherford Appleton Laboratory (RAL), the Center for Neutron Research at the National Institute of Standards and Technology (NIST), and the Los Alamos Neutron Science Center (LANSCE), for helpful discussions and support during the experiments, and for often burning the midnight oil at the beamlines. The collaboration with Dr. Anton Tremsin (UC Berkeley) is greatly acknowledged, as Anton is one of the hardest working and kindest persons I have encountered.

I am especially thankful for my great friends – the old ones who have supported me for a long time and to whom I could always return, and then all the new friends I made from all over the world throughout this incredible journey, starting with the Fulbright scholarship in 2006. Finally, I am especially thankful to my wonderful family for all the assistance, moral support and kindness that I received throughout this time. I would like to thank them in German – Ganz lieben Dank an euch alle zu Hause für die Unterstützung in den letzten Jahren! Last, but certainly not least, I would like to deeply thank Anja, who was a strong and outstanding support to complete this journey!

Abstract

This multipart dissertation focuses on the development and evaluation of advanced methods for material testing and characterization using neutron diffraction and imaging techniques. A major focus is on exploiting diffraction contrast in energy selective neutron imaging (often referred to as Bragg edge imaging) for strain and phase mapping of crystalline materials. The dissertation also evaluates the use of neutron diffraction to study the effect of multi-axial loading, in particular the role of applying directly shear strains from the application of torsion. A portable tension-torsion-tomography loading system has been developed for in-situ measurements and integrated at major user facilities around the world.

Promising applications for the Bragg edge technique are implemented at the neutron imaging facility CONRAD at the reactor source BER-II as well as at neutron time of flight instruments. Strain mapping is successfully demonstrated for all cases to yield quantifiable results, but is limited in practicality due to limitations in choice of the scattering vector (direction of probed strain tensor component) and the gauge volume selection. The use of Bragg edge imaging for crystalline phase mapping was explored and appears to be a very promising technique. The extension to three-dimensionally resolved tomography is presented for samples exhibiting the TRansfomation Induced Plasticity (TRIP) effect, while challenges with characterizing textured samples are discussed.

Individual crystallites within a polycrystalline material exhibit elastic anisotropy which is significant as that can lead to stress concentrations and inhomogeneities during plastic deformation. Characterization of elastic anisotropy is important to understand the effects of texture on the macroscopic mechanical properties. Diffraction methods can do this, by probing the response of individual lattice planes to externally applied mechanical stress. Past experimental data using diffraction based methods have largely been limited to uni-axial tensile and/or compressive loading conditions, even though shear dominates

most common failure mechanisms for structural materials. Within this dissertation, experimental techniques have been established for the measurement of lattice strains under applied torsion (pure shear) and lattice specific shear moduli are reported. This is accomplished using a (traditional) neutron diffractometer instrument, in conjunction with special alignment procedures and the specifically designed axial-torsional loading system.

Table of Contents

1 Chapter 1 Introduction and General Information 1

1.1 Motivation and Scientific Issues 3

2 Chapter 2 Background and Literature Review 8

2.1 Related Mechanics and Materials Background 9

2.1.1 Strength of Materials 9

2.1.2 Torsional Deformation 12

2.1.3 Transformation Induced Plasticity 16

2.2 Polycrystalline Materials and Available Characterization Techniques 18

2.3 Neutron Diffraction (for Strain Measurements) 20

2.3.1 Stress-Strain Basics and Available Characterization Techniques 20

2.3.2 Diffraction Basics 21

2.3.3 Application Examples of Neutron Diffraction 25

2.4 Neutron Imaging 27

2.4.1 Basics and Instrumentation 27

2.4.2 Neutron Imaging Methods 33

2.4.3 Bragg Edge Spectroscopy (1D) and Imaging (2D) 42

2.5 Recent Developments for Crystallographic Imaging 58

3 Chapter 3 Neutron Bragg Edge Imaging at a Reactor Source: Strain Mapping using a Monochromator 63

3.1 Introduction 65

3.2 Experimental Approach 66

3.3 Results 69

4 Chapter 4 Neutron Bragg Edge Imaging at a Reactor Source: Strain Mapping using the Time-Of-Flight Method 74

4.1 Introduction 76

4.2 Instrument and Experimental Setup 78

4.2.1 TOF Instrumental Setup 78
4.2.2 Detector System 81
4.2.3 Instrumental Setup for Imaging 82
4.2.4 Sample Environment and Sample 83
4.3 Measurements 87
4.3.1 Measured Stress States 87
4.3.2 Data Acquisition and Raw Data 88
4.4 Results 90
4.4.1 Data Processing 90
4.4.2 Data Interpretation 91
4.5 Discussion and Outlook 96

5 Chapter 5 Neutron Bragg Edge Imaging at a Spallation Source: Strain Mapping Case Study 99

5.1 Introduction 101
5.2 Sample and Finite Element Modelling 105
5.2.1 Basic Sample Considerations 105
5.2.2 Finite Element Modelling and Thickness Selection 110
5.3 Mechanical Deformation and Surface Strains 114
5.3.1 Strain Gauge Results 114
5.3.2 Digital Image Correlation 119
5.4 Neutron Transmission Experiment 121
5.4.1 ENGIN-X Beamline 121
5.4.2 MCP Detector 122
5.5 Neutron Bragg Edge Imaging Results 126
5.5.1 Collected Data and Analysis 126
5.5.2 Strain Maps and Comparison 132
5.6 Neutron Diffraction Results from E3 140
5.7 Conclusion 143

6 Chapter 6 Method to Determine hkl Strains and Shear Moduli under Torsion Using Neutron Diffraction 146
6.1 Introduction 148
6.2 Experimental Procedure 150
6.2.1 Neutron Diffraction Considerations 150
6.2.2 Mechanical Loading and Sample 152
6.3 Experimental Results 157
6.4 Conclusion 159

7 Chapter 7 Neutron Bragg Edge Imaging for Crystallographic Phase Mapping . 163
7.1 Motivation and Related Work 165
7.2 Introduction 168
7.3 Experimental 170
7.3.1 Radiography 171
7.3.2 Tomography 171
7.4 Conclusion 172
7.5 Technical Experimental Details 176
7.6 Supplement to Chapter 7 177
7.6.1 Supplementary Discussion 177
7.6.2 Supplementary Experimental Section 180
7.7 Complementary Experimental Data 183
7.7.1 Surface Strains by Strain Gauges and VIC-3D 183
7.7.2 Texture and Phase Measurements using Neutron Diffraction 186
7.7.3 EBSD Mapping 190
7.7.4 Time-Of-Flight Bragg Edge Measurements 194
7.8 Outlook: Further Work on Textured Samples 198

8 Chapter 8 Summary, Conclusion & Outlook 201
8.1 Summary and Conclusion 202

8.2 Outlook and Future Work 203

9 List of References 206

10 Appendix 226

10.1 Portable Loading System 227

10.2 Properties of Radiation Relevant for Diffraction 236

10.3 Neutron Classification 237

10.4 Linear Attenuation Coefficients 239

10.5 Double Crystal Monochromator at HZB 240

10.6 HIPPO and GEM Instrument Layouts 243

10.7 Time of Flight Transmission Spectra from ENGIN-X 244

10.8 Refereed Publications 245

Vita 249

List of Tables

Table 4-1. Chemical composition (weight percent) of A36 steel 86
Table 5-1. Reflections for which Bragg edges were recorded, with correspodning lattice spacing, the position of the Bragg edge and the range of the recorded data. 126
Table 6-1. Chemical composition (weight percent) and mechanical properties of annealed (stress relieved) 12L14. 156
Table 6-2. Macroscopic values of shear moduli G [GPa] as calculated for α-Fe and experimentally determined (via strain gauge rosette) for 12L14. 157
Table 6-3. Calculated values of Young's moduli E_{hkl} and shear moduli G_{hkl} for α-Fe and experimentally determined E_{hkl} and G_{hkl} for 12L14. 162
Table 7-1. Phase fractions near the outer diameter, reported for nine samples of austenitic stainless steel that were subjected to torsion. *From* (*Cakmak et al. 2011,*[32]) 167
Table 7-2. Pole Figures for the undeformed and Torsion samples measured at HIPPO. 187
Table 7-3. Pole Figures for Tensile samples measured at HIPPO. 188
Table 7-4. Pole Figures for the undeformed and one Torsion sample measured at GEM. ..189
Table 7-5. Overview of samples for EBSD analysis. 191
Table 7-6. Overview of experimental parameters for energy scan at CONRAD and ENGIN-X for the same samples. 196
Table 7-7. Overview of experimental parameters for tomography scan at CONRAD and ENGIN-X for the same samples. 196
Table 10-1. Electronic components of the Load Frame. 231
Table 10-2. Comparison of various properties important for diffraction (and imaging) measurements, when using electrons, x-rays, photons and neutrons. *From* (*Hutchings et al. 2005,*[1]) 236
Table 10-3. Linear attenuation coefficients for thermal neutrons. *From* (*http://www.psi.ch/niag/neutron-interaction-with-matter 2014,*[99]) 239
Table 10-4. Linear attenuation coeffitients for 150 keV X-ray. *From* (*http://www.psi.ch/niag/neutron-interaction-with-matter 2014,*[99]) 239

List of Figures

Figure 2-1. Element under (a) Multi-axial state of stress (b) Uni-axial tensile stress ($\sigma = F/A$) and (c) State of pure shear ($\tau = FS/A$). 9

Figure 2-2. Von-Mises and Tresca yield criterion graphically shown as yield surfaces. *From http://commons.wikimedia.org/wiki/File%3AYield_surfaces.svg* 11

Figure 2-3. Solid cylindrical bar subjected to torsional moment, MT. L=length; 2a=diameter, 2a, also shown are the counteracting shear stresses (τ) at a radius r. *From* (*Dieter 1986,*[6]) 13

Figure 2-4. A three-dimensional infinitesimal element, as part of cylindrical bar, in a state of pure shear. *From* (*Byars et al. 1975,*[34]) 14

Figure 2-5. A three-dimensional infinitesimal element, as part of cylindrical bar, in a state of pure shear. *From* (*Byars et al. 1975,*[34]) 14

Figure 2-6. Modes of failure in torsion. *From* (*Dieter 1986,*[6]) 15

Figure 2-7. Applied Stress-Lattice Strain relation showing the load partitioning between the constituent phases: parent fcc austenite and product hcp and bcc martensites. *From* (*Tao et al. 2007,*[40]) 17

Figure 2-8. Interaction of matter with (a) x-rays and (b) neutrons. *From* (*Strobl et al. 2009,*[53]) 19

Figure 2-9. Mass attenuation coefficients for thermal neutrons and 100 keV x-rays for the elements (natural isotopical mixture). *From* (*Banhart 2008,*[54]) 19

Figure 2-10. Different types of stresses. *From* (*Fitzpatrick et al. 2003,*[65]) 22

Figure 2-11. Elastic neutron scattering and Bragg's law. *From* (*Bunn et al. 2014,*[66]) 22

Figure 2-12. Schematic of an incident and diffracted high energy X-ray beam with corresponding diamond shaped gauge volume. *From* (*www.veqter.co.uk 2014,*[67]) 24

Figure 2-13. Schematic of a neutron diffraction setup. *From* (*Aydıner et al. 2005,*[68]) 24

Figure 2-14. Neutron diffraction measured (symbols) and EPSC modeled (lines) lattice plane strains in an austnitic steel parallel to the loading direction plotted versus the applied stress. *From* (*Bourke et al. 1999,*[70]) 27

Figure 2-15. Neutron scattering and capture interaction probabilities (left) and exponential attenuation of neutrons in matter according to Beer-Lambert law (right). *From (http://www.psi.ch/niag/neutron-interaction-with-matter 2014,[99])* 29
Figure 2-16. Typical neutron imaging setup, depicting the effect of L/D on the image resolution. *From* (*Strobl et al. 2009,[53]*) 31
Figure 2-17. Neutron imaging instrument CONRAD (COld Neutron RADiography) at HZB. 31
Figure 2-18. Photograph of the measurement position at CONRAD (COld Neutron RADiography) at HZB..... 32
Figure 2-19. Neutron spectrum for the upgraded neutron imaging instrument CONRAD at HZB..... 32
Figure 2-20. Double Crystal Monochcromator for CONRAD at HZB. 35
Figure 2-21. Phase Grating Interferometer setup with three gratings, sample, and detector system. *From* (*Strobl et al. 2008,[94]*)..... 38
Figure 2-22. The principles of the image contrast forming due to (a) Phase shift: "The phase grating (G1) forms a periodic interference pattern in the plane of the analyzer grating. A phase object in the incident beam will cause a slight refraction which results in changes of the locally transmitted intensity through the analyzer." *From (Pfeiffer et al. 2006,[93])* and (b) Small angle scattering: The interference pattern induced by grating G1 smeared due to scattering in the sample, resulting in a loss in the amplitude of the oscillation. *From (Pfeiffer et al. 2008,[144])* 39
Figure 2-23. Radiographic images of an AL reference sample : (a) attenuation, (b) differential phase (refraction), and (c) ultrasmall-angle scattering (dark-field image). (d) Attenuation parameter a0 (offset), differential phase parameter b1 (interferometer phase shift), and dark-field parameter basis a1 (amplitude). (e) Line profiles corresponding to lines in (a–c). *From (Strobl et al. 2008,[94])* 40
Figure 2-24. Setup used for polarized-neutron imaging. *From* (*Kardjilov et al. 2011,[98]*)..... 42
Figure 2-25. (a-c) Principle of Bragg edge radiography: Neutrons of different wavelengths vary in transmitted intensity through polycrystalline samples due to diffraction. This leads to characteristic transmission Bragg edge spectra for crystalline samples. The

position of these so called Bragg edges is directly related to the d-spacing of the lattice planes. (d) Example Bragg edge spectrum for Fe-powder, with arrows at wavelenghts that correspond to diffraction conditions in cases a-c. 44
Figure 2-26. In-situ phase transformation through transmission at ISIS: Total neutron cross section of EN24 steel after austenization at 830 °C and kept in a furnace at 380 °C for the time specified. (inset: evolution of the volume fraction of the α and γ phases) *From (Santisteban et al. 2002,[167])* 48
Figure 2-27. Transmisison measurements of a welded AL plate at ISIS: (a) Total cross-section along different directions compared to prediction for an untextured sample (b) Schematic view of welded specimen (c) Total cross-section along LD measured at the points indicated in (b). The pixellated detector used in this work consists of a 10×10 array of 2×2 mm^2. The graphs reveal large variations in edge height between different directions, e.g. the absence of the (111) edge along the normal direction (ND) means that no crystallite has directions from this family aligned to ND, while a texture of at least 6× random is revealed along the transverse direction (TD). *From (Santisteban et al. 2006,[176])* 48
Figure 2-28. Transmission measurement at ISIS showing the residual elastic strain around a cold-expanded hole in a 12 mm thick steel plate. The measured strains correspond to the through thickness average of the out-of-plane strains. The pixellated detector used in this work consists of a 10×10 array of 2×2 mm^2. *From (Santisteban et al. 2002,[167])* 49
Figure 2-29. Energy selective neutron images of weld joint between two austenitic steel plates. (a) Photographic image. (b) Radiographic images at two wavelengths around the Bragg edge for iron corresponding to (110) lattice space. Bragg scattering from individual crystallites causes contrast in the radiographs due to preferred crystallographic orientations inside the weld, while no more scattering takes place after the Bragg-cut-off. *From* (*Kardjilov et al. 2012,[188]*) 51
Figure 2-30. First demonstration at HZB of a monochromatic neutron tomography for discremination of two different crystalline phases. The measurement was taken at 4.06 Å 51

Figure 2-31. Bragg edge spectra measured by Boin at ENGIN-X in TOF mode for a textured sample at five different orientations. Texture influence can clearly be seen as the shape of the Bragg edges changes enormously. The dashed line shows the texture-free Al curve calculated with nxsPlotter. *From* (*Boin 2010,*[5]) 53
Figure 2-32. Photograph of the (VAMAS) ring and plug sample (left). Theoretical ring and plug strain values for the hoop, radial and axial directions after plotted against the sample radius (right). *From* (*Boin 2010,*[5]) 53
Figure 2-33. (a) Neutron transmission probes the projected strain which for the ring and plug sample consists of a combination of hoop and radial strain components. (b) Projected strain as a function of sample radius and corresponding data collected at ENGIN-X. *From* (*Boin 2010,*[5]) 54
Figure 2-34. Abbey et al. showing the transmission strain components as a function of radial and hoop strains in an axisymmetric sample. *From* (*Abbey et al. 2012,*[193]) 57
Figure 2-35. (left) Experimental setup, showing acquisition geometry, the sample and both diffracted and transmitted signal on one detector. *From* (*Johnson et al. 2008,*[205]) (right) Example result obtained by Ludwig et al. at the ESRF showing rendition of the 3D grain structure in a cylindrical beta-Ti specimen containing 1008 grains, as obtained by the DCT processing routine. The colors represent the grain orientation. *From* (*Ludwig et al. 2009,*[57]) 60
Figure 3-1. Portable loading system b) Specimen dimensions in mm. 68
Figure 3-2. a) Recorded stress-strain curve of tensile test b) Schematic sketch of CONRAD (inset). 68
Figure 3-3. Bragg edge Transmission profile, Derivative and Gauss-Fit (one pixel). 72
Figure 3-4. Map of Transversal Strains obtained by radiography. 72
Figure 3-5. Transversal strains along the specimen height for investigated stress states. .. 73
Figure 3-6. Comparison with Diffractometer results. 73
Figure 4-1. BioRef, a versatile TOF reflectometer used for TOF imaging in the presented work, to record Bragg edge transmission spectra. The instrument consists of an optically blind double chopper system (left) by which the resolution can be tuned

through changing the distance between these choppers. Another chopper (middle) allows the system to define the utilized wavelength range. The first of the two slits (right) has been used as a "pinhole" to achieve spatial resolution for the herein presented measurements (while the second slit was fully opened). The sample has been placed in front of the detector (right, blue) which was placed at the very end of the support arm. 80

Figure 4-2. (a): Configuration of the sample and sample environment – a portable mechanical loading system – in a CAD model. (b): Photograph of the actual setup on the BioRef instrument..... 84

Figure 4-3. Sample; (a): Drawing of the sample with dimensions. (b): Strain distribution predicted by finite element calculations for the sample corresponding to an axial stress of 225 MPa. 86

Figure 4-4. (a): Bragg edge as measured by the relation of the empty beam image and sample (inset: full spectrum of empty beam and with sample; area corresponding to 3.5 x 7 mm and 1 h counting time). Note that the additional dips in the empty spectrum (inset) are due to an upstream monochromator of another instrument at 4.76Å (V12a (*Strobl et al. 2007,*[228])) and to Al windows in the beam (around 4Å). (b): Illustration of the spatial variation of the Bragg edge position with respect to the time-of-flight (TOF) due to chopper and pinhole geometry..... 90

Figure 4-5**.** (a): Tensile Stress versus axial strain (ε_y) and Poisson strain(ε_z), highlighting the stress states at which Bragg edge transmission measurements were performed, (b): spatial distribution of measured ε_z strain based on (110) peak shifts from Bragg edge transmission imaging data. Note a slight variation in horizontal(x) direction. 93

Figure 4-6. (a): Measured ε_z strain along specimen height with values averaged horizontally, one pixel corresponding to 3.5 mm height. (b): comparison of measured strain values for a point in the center of the sample including diffraction data (blue diamonds), imaging with monochromators at CONRAD (red circles) and the herein reported TOF measurements (green squares). 95

Figure 5-1. The sample geometry to be used for the tensile test (using two different thicknesses). 108
Figure 5-2. Stress concentration due to a center hole. *From* (*McGinty 2014,*[242]) 109
Figure 5-3. Finite Element Model (FEM) and strain state for of the a proposed (thick (9.5 mm)) steel sample geometry. The strain component ε33 will be probed during the transmission measurement and varies in the z-direction (along thickness direction) as can be seen. 111
Figure 5-4. Finite Element Model (FEM) and strain state of a thin (3 mm) steel sample. The strain component ε33 is relatively uniform in the z-direction. 111
Figure 5-5. Variation of strain component ε_{33} from FEM: The strain variation at three different locations through the thickness relative to the integral (sum averaged) strain in that direction. 112
Figure 5-6. Microstructure of the machined samples, before (top) and after the annealing process (below). Magnification corresponds to ruler size of 50 μm. 113
Figure 5-7. (a) Strain gauges mounted around the hole on both sides (b) Notation of strain gauges (c) The same sample painted for Digital Image Correlation (d) Stress-Deformation and Stress-Strain results as recorded during the transmission measurements (for sample R#124) at ENGIN-X, where eight strain gauges were positioned as indicated above. 117
Figure 5-8. (a) Two strain gauges mounted around the hole of the thick sample during the imaging experiment (I20-2) (b-d) Notation and layout of strain gauges mounted around the hole of the thick sample during the diffraction experiment. The notation is same as in Figure 5-7 (e) Stress-Deformation and Stress-Strain results as recorded during the imaging and diffraction measurements (including strain gauge data from samples I20-2 and R#105). 118
Figure 5-9. Principle of digital image correlation (here VIC-3D). The example shows the dual camera setup and the speckle pattern that is used to calculate the strains on the surface of the sample. 120

Figure 5-10. Surface strain (2 strain components in x- (ε_{11}) and y- (ε_{22}) direction) measured by digital image correlation on the thick sample. (Note: The neutron transmission measurement will probe the strain component in the z-(ε_{33}) direction.)....121
Figure 5-11. Schematic of the ENGIN-X beamline. *From* (*ISIS 2015,*[246])....122
Figure 5-12. Microchannel Plate (MCP) detector that was used for the transmission measurements. It features a Medipix-Timepix readout and an of 512 x 512 pixels, with a pixel size of 55 μm. 123
Figure 5-13. Experimental setup at ENGIN-X for measurement of the thin sample gemeotry. The Microchannel Plate (MCP) detector is positioned behind the sample for the transmission measurement. An improved gripping system was used, compared to measurement of the thick sample (done several months before). VIC-2D was attemped to be carried out simultaniously....124
Figure 5-14. Experimental setup at ENGIN-X for measurement of the thick sample geometry. 125
Figure 5-15. Lattice planes for the first three reflections of a bcc unit cell. 127
Figure 5-16. One slice of the image stack (containing 2452 images), where every slice corresponds to a certain time of flight (wavelength) for (a) the thin sample and (b) the thick sample. (c) Example neutron spectra for the thin sample image stack, where the spectrum is built from an area of 100 x 100 pixels, corresponding to 5.5 x 5.5 mm^2. 128
Figure 5-17. Transmission spectrum recorded around the Bragg edges for the thin sample. 128
Figure 5-18. Transmission spectrum recorded around the Bragg edges for the thick sample. 129
Figure 5-19. Examples of the analytical fitting functions for two measured Bragg edges for the thin sample. 131
Figure 5-20. Example transmission image and picture for the sample rotated 90 degrees with respect to the neutron beam, resulting in strain component along the width direction. 131

Figure 5-21. Example of the influence of integration times in the present experiment for the thin sample geometry. (a) Derived maps of the Bragg edge position corresponding to the (110) lattice planes (in this case for stress state S3). (b) The strain maps that are obtained after these acquisition times, using the average lattice paramter that was determined for stress state S1.....132
Figure 5-22. (a) Strain maps for the thin sample, derived from the Bragg edges corresponding to (a) the (110) lattice planes and (b) the (211) lattice planes. (c) FEM results for three locations (indicated above) at stress state S3 (effective stress of 150 MPa) showing the strain variation through the sample thickness (9.5 mm). It must be noted that the FE model does not consider plasticity (see discussion in text). 137
Figure 5-23. Strain maps for the thick sample, derived from the Bragg edges corresponding to (a) the (110) lattice planes and (b) the (211) lattice planes. (c) FEM results for three locations (indicated above) at stress state S3 (effective stress of 140 MPa) showing the strain variation through the sample thickness (9.5 mm). It must be noted that the FE model does not consider plasticity (see discussion in text). 138
Figure 5-24. Thin sample (i): The edge width parameter for the (110) lattice obtained using the fitting routine. Spatial maps are shown on top. The graphs show a line profile across (the hole center is at 10 mm in this case) and along (the hole center is at 0 mm in this case) the sample for all three stress states, as indicated in the above map. An increase of the width can be noticed at the side of the hole for stress state S3. A strong increase of the width is noticed for stress state S4. 139
Figure 5-25. Thick sample (ii): The edge width parameter for the (110) lattice plane. Spatial maps are shown on top. The graphs show a line profile across (the hole center is at 10 mm in this case) and along (the hole center is at 0 mm in this case) the sample for all three stress states, as indicated in the above map. A significant increase of the width can be detected at the sides of the hole for stress state S4. It appears that an effect is also visible for the side of the hole at S3 (however some effect is also visible under S1, so it might also just be due to poorer counting statistics close to the hole). 140

Figure 5-26. Experimental setup at E3, with the loading system positioned sideways on top of the sample positioning table. 141
Figure 5-27. Strain results from neutron diffraction for strain component in through-thickness Poisson direction (ε_{33}) measured at three locations (A, B, C) for stress states S3 and S4 (where S1 was used as the d0 reference). 142
Figure 6-1. (a) Experimental setup at NRSF2 with loading system shown at 41.3° inclination (b) Sample dimensions (mm) and directions of measured strains at a gauge location 2 mm from the cylinder axis (B = bottom and T = top of sample) (c) Linear variation of shear stress along each radial line of the cylinder cross section with gauge location shown as yellow square. 153
Figure 6-2. Sample positioning to obtain the three strain components. The yellow arrow represents the incident neutron beam; the cyan arrow represents the diffracted beam (the direction of measured strains bisects these two). The sample coordinate system is denoted by the dashed red lines and the instrumental coordinate system is shown in blue. The angle φ denotes the sample rotation inside the loading system. The gauge volumes are shown by yellow, red, green squares, respectively. **(a)** For ψ=0° the loading system is lying on its side, while **(b, c)** in the other two cases it is inclined at 41.3°. For measurement of the strain component corresponding to ψ=-41.3°, **(c)** the sample is rotated inside the loading system by 180° and the loading system is translated in x-direction, so the same spatial location within the sample is measured. 154
Figure 6-3. Pole Figures for the sample indicate mild to no bulk texture. 155
Figure 6-4. Measured strain components for ferritic bcc (211) lattice plane during elastic loading in torsion for three separate spatial locations along the same radial line (r = 2 mm, r = 1 mm, r = 0 mm). Shear stress corresponds to the maximum shear stress at the surface of the sample. 158
Figure 6-5. Shear Stress (at r = 2 mm for three *hkl's* and the surface for the strain rosette) *vs*. obtained Shear Strain (for the investigated lattice planes and strain rosette) with shear modulus ($G_{hkl} = \tau/\gamma_{xy}$) determined using a linear fit to the initial slope. 160

Figure 7-1. (a) Neutron diffraction spectrum of reversed phase transformation (by heating) in austenitic stainless steel. (b) Corresponding transmission spectrum. *From* (*Bourke et al. 1996,*[172])**.**.....165
Figure 7-2. Phase fractions for the nine samples as a function of radius, measured at 7 different locations. *From (Cakmak et al. 2011,*[32]*)*.....167
Figure 7-3. Transmission image and transmission spectra: (a) Radiograph of samples with region of interest (ROI) depicted, which was used for the plot in Figure 1b. (b**)** Bragg edge transmission spectra (131 mono-energetic radiographic projections between 1.7 Å and 4.5 Å with an exposure time of 240 seconds/projection) for the center gauge area of the five samples. The non-deformed sample "VIR" is purely austenitic, and only Bragg edges corresponding to austenite are visible. The center of tensile sample "TEN-max" is fully transformed to martensite (compare to theoretical attenuation coefficients depicted in inset and Figure S1) while "TEN-med" is only partially transformed over the selected ROI. The two torsion samples show Bragg edges of both crystallographic phases in the gauge area, which is anticipated, as the center of the sample is not expected to transform to martensite since the applied shear stress there is zero; hence tomographic reconstruction is needed for further quantification. Investigating regions outside the gauge area, the Bragg edge spectra are identical to those of the virgin sample, proving that no (significant) deformation occurred. The dotted vertical lines indicate the wavelengths where tomographic scans were performed.....173
Figure 7-4. Tomographic reconstructions: 174
Figure 7-5. Line profiles along and across the reconstructed tomographic data showing the austenitic and martensitic phase fractions. Neutron-diffraction-based results (labeled "ND") are also included to refer to a standardized characterization method. The diffraction results were obtained using a 2×2×2 mm^3 gauge volume and by scanning along/across the samples. (a) Phase fractions along the height of the tensile samples and the virgin sample. Both samples subjected to tensile loading were fully transformed to martensite in the necking region. (b) Phase fractions across the center

of the torsion samples and the virgin sample. For the torsion samples, the maximum phase changes occurred in the region near the outer diameter as expected, and no transformation occurred in the sample center. For "TOR-max", the theoretical α-martensite phase evolution is predicted using the Olson–Cohen model (*Olson et al. 1975,[264;]Cakmak et al. 2011,[32]*).....175
Figure 7-6. Supplementary Figure S1. (a) Theoretical attenuation coefficients for austenite (fcc structure) and α-martensite (bcc structure) in comparison. (b) Schematic drawings on the principle of Bragg edge tomography: Choosing a wavelength before the Bragg cut-off for austenite and after the Bragg cut-off for martensite results in differences of transmitted intensities. 178
Figure 7-7 Supplementary Figure S2. (a) Sample dimensions in mm. (b) Photograph of the five samples after deformation. 181
Figure 7-8. Supplementary Figure S3. Stress-strain and stress-deformation relationships for the (a) tensile and (b) torsion test. 182
Figure 7-9. Supplementary Figure S4. Elastic loading (up to yielding only): (a) The stress (and strain) during tensile loading is uniform in magnitude and direction while (b) the shear stress changes with radial distance r under torsion. (c) Variation with radius r of axial stress (σ) during tension and shear stress (τ) during torsion. 183
Figure 7-10. Compliance Correction of the loading system for torsion testing of sample TOR-max (d=8 mm). 184
Figure 7-11. Shear Stress vs. Shear Strain and Angle of Twist for torsion sample "TOR-max). The angle of twist (and the engineering shear strain based on this value) needs to be corrected especially in the elastic sample regime due to compliance of the loading system. The corresponding uncorrected and corrected curves are shown. Surface based strain measurements by rosette strain gauges and VIC-3D are in excellent agreement (up to the onset of plasticity). 185
Figure 7-12. Shear Strain on the surface from VIC-3D: It can be seen that the gauge section undergoes a uniform strain on the surface. The numbers refer to shear stress in MPa (the last 2 images are recorded beyond 669MPa).....185

Figure 7-13. EBSD phase maps and grain orientation maps PART I. Magnification bar = 30 µm. 192
Figure 7-14. EBSD phase maps and grain orientation maps PART II. Magnification bar = 30 µm. 193
Figure 7-15. Bragg edge transmission spectra recorded by TOF for sample TEN-max . The region in the center of the gauge center shows a full transformation to Martensite, in analogy to the data taken at CONRAD. The region outside of the gauge area has not experienced plastic deformation and hence is still fully austenitic. Two sample orientations are presented and it can be observed that the Bragg edge spectra are very similar, indicating that no strong texture is present. 197
Figure 7-16. Bragg edge transmission spectra for sample TOR-max. It can be seen that the transition from Austenite to Martensite for the last Bragg edge is resolved much more detailed than at CONRAD. 197
Figure 7-17. (a) Photograph of three samples (A: undeformed, B: Torsion sample subjected to 100% shear strain, C: : Torsion sample subjected to 250% shear strain) that were investigated at CONRAD and ENGIN-X. Radiographs taken at CONRAD: (b) at 3.9 Å (c) at 4.2 Å and (d) Diffraction contrast by normalizing images taken at 3.9 Å by 4.2 Å. 199
Figure 7-18. Screenshots from radiographs during 360 degree sample rotation: (a) at 3.9 Å (b) at 4.2 Å and (c) Diffraction contrast by normalizing images taken at 3.9 Å by 4.2 Å. 200
Figure 7-19. Bragg edge transmission profiles recorded in TOF mode at ENGIN-X reveal local differences in texture along the gauge section of the torsion sample. 200
Figure 10-1. (a) Axial loading system (with 88 kN load cell) from the University of Missouri that was used as a basis for the new design. (b) 3D-CAD drawing based on the loading system. (c) The same loading system with a hermetically sealed casing so that it can be used inside of the evacuated Large Chamber SEM. 229

Figure 10-2. CAD model and photograph of the developed loading system, capable of tension, torsion, combination of both and sample rotation under load for tomography. 229
Figure 10-3. CAD drawing of the loading system, after upgrading the loading train for improved alignment using U-Joints. 230
Figure 10-4. Schematic Setup of the Load Frame components. 230
Figure 10-5. Picture of the electronic components of the loading system. 232
Figure 10-6. Graphical User Interface (GUI) for controlling the loading system. 232
Figure 10-7. GUI of sample alignment software that was developed, based on ASTM specifications. 233
Figure 10-8. The loading system has been integrated and used at several user facilities for X-Ray and Neutron diffraction and imaging experiments, as shown in the individual photographs. 234
Figure 10-9. Components of the loading system: (a) Bottom unit that creates the axial force. (b) Top unit with ball bearing for sample rotation. (c) U-Joints. (d) Several types of grips that have been manufactured for different samples. 235
Figure 10-10. Energy dependence of neutron cross sections shown for aluminum, iron and the water molecule. Bragg edges can be seen for iron and aluminum in the thermal and cold energy spectrum, wheras resonances are visible in the high energy range. *From* (*http://www.psi.ch/niag/neutron-interaction-with-matter 2014,*[99]) 238
Figure 10-11. Diagram of time-of-flight diffractomters at LANSCE and ISI. left: HIPPO. *FROM* (*Vogel et al. 2004,*[258]). right: GEM. *FROM* (*Kockelmann et al. 2006,*[267]) 243
Figure 10-12. Transmission spectra recorded at ENGIN-X with increasing count times for different regions. The tensile sample is transformed from Austenite to Martensite in the center of the gauge section. 244

Chapter 1

Introduction and General Information

The focus of this PhD manuscript will largely be the development and further advancement of neutron diffraction and transmission (imaging) methods for the characterization of polycrystalline materials. This dissertation is largely written based on peer-reviewed and published manuscripts, also commonly referred to as a multipart, compilation or cumulative dissertation.

Chapter 1 will outline the structure and organization of the dissertation, as well as explain the motivation behind this work. Chapter 2 is intended to provide general background information for the non-expert, as well as review related work by others in fields that are relevant to the following chapters. Chapter 3, 4 and 5 describe methodological developments – with a focus on strain measurements – in the field of energy selective neutron imaging at steady state and time-of-flight (TOF) sources. The research presented in Chapter 6 utilizes a traditional neutron diffractometer, and as such may appear as the least "fitting" topic within the framework of this dissertation. However it showcases the strengths of using a traditional diffractometer versus the transmission based method from the previous chapters. It describes the experimental procedure to measure lattice strain changes in a cylindrical sample under torsional loading, in which the strain changes radially. Moreover it introduces the challenges and significances associated with the application and measurement of deformation in pure torsion. Chapter 7 explains the development of using the neutron transmission based method for spatial investigation of crystallographic phases, even extending it to three-dimensions by tomographic reconstruction. This method is demonstrated for samples that have undergone phase transformations due to plastic deformation in tension and torsion. Finally, Chapter 8 provides a summary and an outlook for future work. The appendix contains additional information that is relevant to this dissertation.

Chapter 3, Chapter 4, Chapter 6 and Chapter 7 are largely based on already published journal papers, while Chapter 5 is still planned to be published. More information will be given at the beginning of each chapter.

1.1 Motivation and Scientific Issues

The understanding of existing and new materials, as well as the development of advanced materials depends heavily on the availability of characterization methods. The majority of material scientists and engineers rely on the availability and reliability of such methods. When new and advanced methods are being developed, it is obviously beneficial if relevant and suitable applications are being used in order to demonstrate its relevance and reliability.

Polycrystalline metallic alloys are and will continue to be the most widely used structural material for engineering applications. The properties of these alloys are determined by their crystallographic structure, and hence a better understanding of these properties will aid to develop improved materials and processing techniques. Universal and specialized characterization techniques are available (reviewed in chapter 2.2), while novel methods are under development – especially for three-dimensional and bulk investigations of materials. Non-destructive radiography and tomography have become standard tools for the investigation of the internal structure of materials, while diffraction methods can provide more detailed information about the crystallographic properties. The benefits of combining both techniques have been realized and are routinely used in today's electron microscopes for example. The type of radiation to be used for imaging and diffraction depends on the applications (and availability), as they can provide different contrast mechanisms and penetration depths.

Neutron based methods have the advantage that they can probe deep into most structural materials and are hence ideal for bulk investigations (see Figure 2-9). Contrary to a neutron diffraction instrument, a radiography/tomography setup is rather simple. The neutron beam path is defined by the incident beam direction and maintained after passing through the sample. The attenuated neutron signal is recorded by a detector. Until recently, absorption was the only utilized contrast mechanism in neutron imaging. Several new methods have emerged within the last decade using other contrast mechanisms (reviewed in chapter 2.4.2). For the investigation of crystalline materials, diffraction contrast is very useful. In this case, the neutron wavelength dependent transmission intensity spectrum

contains sudden intensity changes due to Bragg diffraction from crystallographic lattice planes. Due to its potential to enable the analysis of crystallographic sample properties with shorter integration times, high spatial resolution and simple experimental setup, Bragg edge transmission was the main focus of several dissertations, for example (*Meggers 1995,[2]; Vogel 2000,[3]; Steuwer 2002,[4]; Boin 2010,[5]*), and several publications (reviewed in chapter 2.4.3). However, all of this work was undertaken at neutron spallation sources, where no dedicated imaging instruments were available, besides part of the dissertation by Boin (*Boin 2010,[5]*), who also used the same imaging beamline (CONRAD) as used in this thesis. The earlier work largely focused on developing the basic experimental routines (plus mathematical models for fitting and predicting the experimental data). The effort that was undertaken within the framework of this dissertation could be seen as a bridge between the basic development of Bragg edge transmission (that largely took place at spallation sources) and applying it to relevant and potential applications, while integrating it at a dedicated imaging beamline at a steady state source. The experiences gained through these efforts are expected to be of significant interest and importance for planned imaging beamlines at neutron spallation sources in USA (SNS), Europe (ISIS and ESS) and Japan (J-PARC), but also for existing neutron imaging beamlines at steady state sources. Furthermore, especially the use of Bragg edge imaging for phase mapping and the potential to spatially resolve texture differences – as demonstrated in this dissertation – are expected to be beneficial for a broad range of materials science and engineering applications.

Individual crystallites within a polycrystalline material exhibit elastic anisotropy which is significant as it can lead to stress concentrations and inhomogeneities during plastic deformation.(*Dieter 1986,[6]*) Characterization of elastic anisotropy is important to understand effects of texture on the macroscopic mechanical properties. Diffraction methods can probe the response of individual lattice planes to mechanical stress, and lattice specific elastic constants (E_{hkl}, ν_{hkl}) can be determined.(*Eigenmann et al. 1996,[7]; Clausen et al. 1999,[8]; Hutchings et al. 2005,[1]*) To the author's knowledge, all reported

experimental values have been determined from uni-axial tensile and compressive loading. Models and theoretical considerations can be found in past and recent literature, relating Young's modulus E and Shear modulus G to single crystal elastic constants of polycrystalline materials.(*Hill 1952,[9]; Kröner 1958,[10]; Nye 1985,[11]; Hutchings et al. 2005,[1]; Singh 2009,[12]*)

Structural components and materials in the production route of industrial components are usually experiencing a state of complex multi-axial stress (*Hertzberg 1976,[13]; Dieter 1986,[6]; Bickford 1998,[14]*), and multi-axial testing – for example through multi-axial and/or torsional loading – allows simulating even complex strain paths.

Plastic anisotropy results from the fact that crystals do not deform homogenously, but rather only on specific crystal planes (slip planes) in specific directions (slip directions). It will be an important contribution if this behavior can be probed under various stress paths, where the applied principal stress directions are rotated. Existing and new strength theories could be evaluated, checked and developed based on the experimental results of in-situ diffraction measurements for samples under loading, including effects of texture.

Torsional deformation studies for instance are very scarce compared to vast amount of knowledge under uni-axial tension or compression, and out of them, most focus on macroscopic properties or phase transformations (*Miller et al. 1996,[15]; Cakmak 2014,[16]*). Some more review is given in chapter 2.1.2 and 2.3.3. As a first step to aid the development for experimental determination of lattice strain changes under torsional loading, the experiments presented in chapter 6 were designed, and lattice specific shear moduli G_{hkl} for a ferritic steel alloy are reported.

Both research topics, the further development of the Bragg edge method, as well as torsional deformation studies, required the application of precise mechanical stress to samples. Hence, a portable tension-torsion loading system has been developed for in-situ measurements as part of the dissertation frame work. The system was successfully integrated at several neutron (and x-ray) user facilities around the world as a part of this

research and is used by other colleagues now as well. Some details about the system are summarized in the appendix.

The main objectives of this dissertation project can be summarized as follows:

(1) Development of a portable loading system, with high capacity and the capability of tensile and torsional loading, including specimen rotation for tomography investigations. This objective includes the development of hardware and control software, as well as the integration at neutron and x-ray user facilities for in-situ imaging and diffraction experiments.

Bragg edge transmission

(2) Evaluation of Bragg edge transmission imaging for quantitative strain investigations at a neutron reactor source. This is discussed for a monochromator at the imaging beamline CONRAD in chapter 3 and for a chopper system in chapter 4. Quantification assessment and repeatability are achieved by using the same mechanical loading system at the different instruments, while a simple plate sample is loaded in tension.

(3) Evaluate a potential application of strain mapping at a spallation neutron source using the novel Micro-Channel-Plate (MCP) detector technology, providing the highest possible spatial resolution to-date for such measurements. In order to address specific challenges for the investigation of more relevant and complicated cases (than those considered previously), samples of varying thickness with a stress concentration are used.

(4) Investigate the possibility of conducting quantitative and spatially resolved crystalline phase discrimination using Bragg edge transmission at the neutron imaging instrument CONRAD and at a time of flight instrument.

(5) Extending the Bragg edge method from radiographic investigations to three-dimensional tomography for quantitative phase investigations.

Torsion studies using diffraction

(6) Development of a neutron diffraction based measuring technique that allows the study of lattice strain changes under applied torsional loading.

(7) Integrate the portable loading system in neutron diffraction instruments (including specialized control software communication) and the possibility for inclined positioning of the loading system, including precise sample alignment protocols.

Chapter 2

Background and Literature Review

2.1 Related Mechanics and Materials Background

2.1.1 Strength of Materials

The major purpose of structural materials is being able to withstand loads in a very broad variety of applications. For the design of structural components it is crucial to know how much stress the material to be used can withstand. For this type of characterization, several dedicated (standardized) mechanical tests have been developed and are routinely performed in mechanical testing laboratories around the world. The by far most common tests are the uni-axial tensile test and hardness test, but also commonly performed for example are the compression test, beam impact test, shear test, torsion test, bending test, and cupping test.(*Ross 1988,*[17])

Structural components are generally subjected to complex multi-axial stress states (Figure 2-1a) and the magnitude may vary from point to point within this component. Simplifications for example exist for cases when the component is loaded uni-axially in tension (Figure 2-1b) or pure shear (Figure 2-1c). In most practical applications, shear is often the predominant loading case in structural materials during its life time and during production processes. Moreover, shear stress commonly leads to dominant failure mechanism.

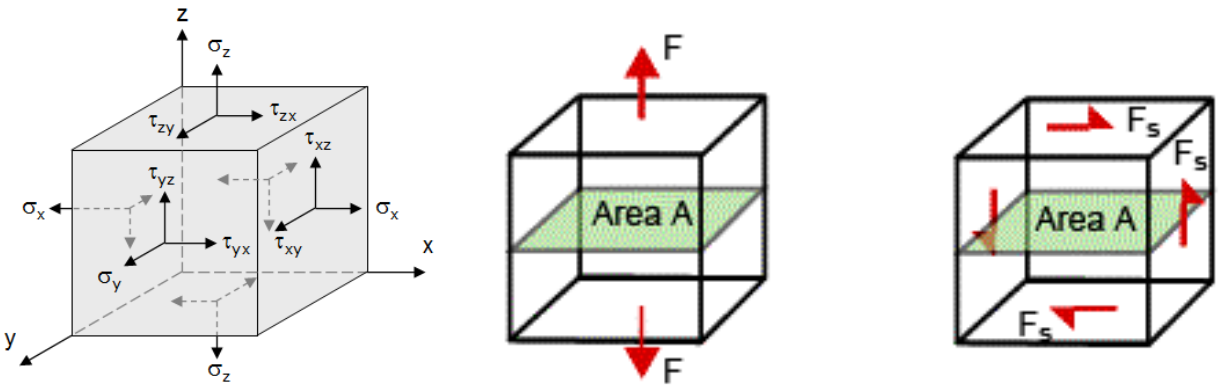

Figure 2-1. Element under (a) Multi-axial state of stress (b) Uni-axial tensile stress ($\sigma = F/A$) and (c) State of pure shear ($\tau = F_S/A$).

The tensile test is well suited to predict under which applied stress a material will yield under uni-axial loading, and allows universal comparison of materials. But as discussed, most loading occurs under multi-axial conditions. Since an experimental investigation of all possible stress conditions is usually not feasible, various strength theories (*Yu 2002,*[18]) are being used to calculate an "equivalent" stress from the stress components of the multi-axial loading case, which can then be compared to the value determined for uni-axial loading. The most commonly used strength theories are the maximum shear stress theory (also known as Tresca yield criterion) and the Von-Mises yield criterion.

$$\boldsymbol{\sigma_{Tresca}} = max(|\sigma_1 - \sigma_2|, |\sigma_1 - \sigma_3|, |\sigma_2 - \sigma_3|) \tag{2-1}$$

$$\boldsymbol{\sigma_{Von-Mises}} = \frac{1}{\sqrt{2}}\sqrt{\left(\sigma_x - \sigma_y\right)^2 + \left(\sigma_y - \sigma_z\right)^2 + \left(\sigma_z - \sigma_y\right)^2 + 6(\tau_{xy}{}^2 + \tau_{yz}{}^2 + \tau_{xz}{}^2)} \tag{2-2}$$

The choice of the appropriate method depends on the fracture characteristics and the material properties, but the determined values are always only approximations. Figure 2-2 shows the two criteria in a graphical comparison. The material is expected to yield if the stress reaches beyond the "yield surface". Detailed discussion on strength theories can of course be found in many textbooks, for example (*Cook et al. 1999,*[19]), and in review articles (*Yu 2002,*[18]).

As will be discussed detailed in section 2.3.3, so far mostly uni-axial tension/compression testing has been performed during in-situ investigations at (synchrotron) x-ray (*Hirano et al. 1995,*[20]; *Kruijver et al. 2002,*[21]) and neutron instruments (*Pang et al. 1998,*[22]; *Clausen et al. 1999,*[8]; *Steuwer et al. 2003,*[23]; *Choo et al. 2004,*[24]; *Rajagopalan et al. 2005,*[25]; *Qiu et al. 2009,*[26]; *An et al. 2011,*[27]). From these types of in-situ measurements, one can deduce a variety of information, including determination of lattice specific elastic moduli and infer how the material responds on a crystalline level to the application of uni-axial stress (e.g. gliding

mechanisms, phase transformations). Only a few detailed diffraction studies under the direct application of shear stress or the application of complex combined proportional stress have been carried out.(*Wittridge et al. 2000,[28]; Martins et al. 2001,[29]; Martins et al. 2002,[30]; Martins et al. 2005,[31]; Cakmak et al. 2011,[32]; Cakmak et al. 2012,[33]*).

A more detailed understanding how materials behave under the application of pure shear and/or multi-axial stress states could help to improve the current strength theories. Therefore it is desirable to introduce the investigation of more complex loading paths to in-situ studies. Within this dissertation, the foundation for such testing will be developed. Having access to a multi-axial loading device, one could for example study texture effects – which are not represented in the strength theories – by decoupling the effect of principle strain rotation and texture.

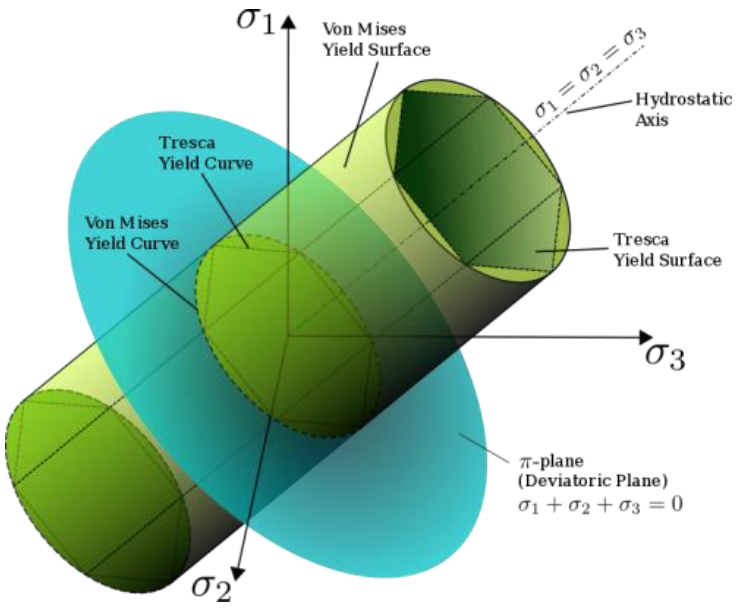

Figure 2-2. Von-Mises and Tresca yield criterion graphically shown as yield surfaces. *From http://commons.wikimedia.org/wiki/File%3AYield_surfaces.svg*

2.1.2 Torsional Deformation

Many engineering components are subjected to shear stress through direct torsional loading, such as drive shafts, axles, drills, etc. The torsion test allows probing materials directly under controlled applied shear stress. Moreover, torsion provides a unique opportunity to study the mechanical behavior of materials subjected to pure state of shear stress (vs. axial stress in a tensile test). As discussed earlier, this is of significance as most engineering components fail under the influence of shear stress, or combination of shear and axial stress, rather than solely under axial stress. Most manufacturing processes also apply shear stresses to the material, such as rolling, extrusion, forging, cutting, drilling, milling, and so on. Furthermore, torsion testing is uniquely suited to apply high strains to samples, without inconsistencies such as necking or barreling which are commonly observed in tension and compression tests. However, probably because of its more complex nature, torsional deformation has not been given the same amount of attention as uni-axial tension and compression.

When a cylindrical bar is subjected to a torsional moment at one end, the twisting moment (M_T) is resisted by shear stresses (τ) occurring in the cross section of the bar, as depicted in Figure 2-3.

$$M_T = \int_{r=0}^{r=a} \tau r \, dA = \frac{\tau}{r}\int_0^a r^2 \, dA = 2\pi \int_0^a \tau r^2 \, dr \qquad (2\text{-}3)$$

where r is the radius and r=a corresponds to the surface of the cylindrical bar. The integral part of the formula is called the polar moment of inertia (J), and for a solid cylinder can be expressed as:

$$J = \int r^2 dA = \frac{\pi D^4}{32} \qquad (2\text{-}4)$$

with D=2a. Consequently, at the outer radius of the cylinder (on the surface), the shear stress is at a maximum:

$$\tau_{max} = \frac{M_T r}{J} = \frac{16 M_T}{\pi D^3} \qquad (2\text{-}5)$$

The shear strain in a torsion member, γ, is an angular distortion and according to Figure 2-3 it can be defined, with the angle of rotation,∅, as:

$$\gamma = tan\emptyset = \frac{r\emptyset}{L} \tag{2-6}$$

If considering a rectangular element on the surface of the cylinder, where the sides are parallel and perpendicular to the longitudinal axis of the cylinder, this element is in state of pure shear and only subjected to shear forces (see Figure 2-4). This implicates that the principal normal stresses and principal axial strains occur at angle of 45° with respect to the longitudinal cylinder axis. When visualizing the case of pure shear in Mohr's circle, one can see that the maximum shear stress, maximum tensile and maximum compressive stress all have the same magnitude (see Figure 2-5). Mohr's circle of plane strain for the case of pure shear shows that the diameter of the circle represents the magnitude of the maximum shear strain. This implies that by measuring principal axial strains on the surface of cylinder under torque, one effectively measures the maximum shear strain.(*Byars et al. 1975,*[34]) In analogy to the tension test and the modulus of elasticity E, the torsion test can be used to determine the shear modulus of elasticity G (ASTM E-143), which is defined as:

$$G = \frac{\tau}{\gamma} = \frac{M_T L}{J\theta} \tag{2-7}$$

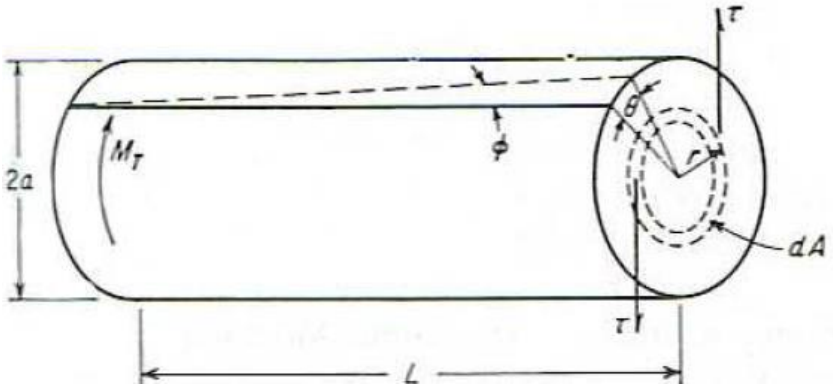

Figure 2-3. Solid cylindrical bar subjected to torsional moment, MT. L=length; 2a=diameter, 2a, also shown are the counteracting shear stresses (τ) at a radius r. *From* (*Dieter 1986,*[6])

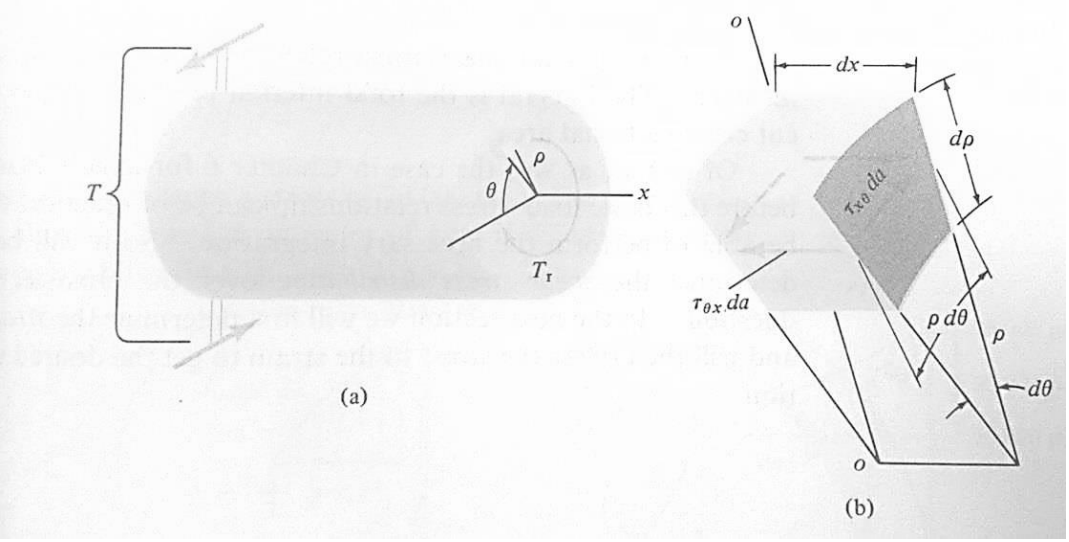

Figure 2-4. A three-dimensional infinitesimal element, as part of cylindrical bar, in a state of pure shear. *From* (*Byars et al. 1975,*[34])

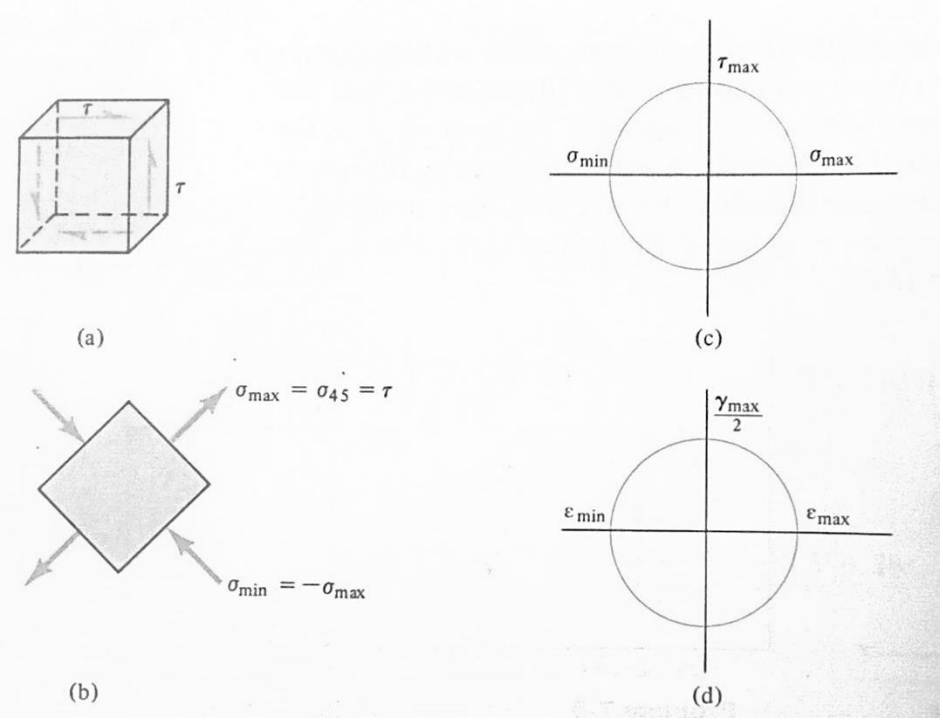

Figure 2-5. A three-dimensional infinitesimal element, as part of cylindrical bar, in a state of pure shear. *From* (*Byars et al. 1975,*[34])

Beyond the torsional yield strength, the torque-twist angle relationship is no longer linear and in the plastic range the shear stress in the bar at the outer fiber can be calculated from:

$$\tau_a = \frac{1}{2\pi a^3}\left(\theta' \frac{dM_T}{d\theta'} + 3M_T\right) \tag{2-8}$$

with θ'=θ/L. At the maximum point, the ultimate torsional shear strength becomes:

$$\tau_u = \frac{3M_{max}}{2\pi a^3} \tag{2-9}$$

Because the state of stress in torsion on the surface of a bar occurs on two mutually perpendicular planes, and the principal stresses occur at 45°, failure can occur in two major ways:

a) Shear (ductile) failure is along the maximum shear plane.
b) Tensile (brittle) failure is perpendicular to the maximum tensile stress (at 45°), resulting in a helical fracture.

For a more detailed description and discussion of non-circular cross sections, the reader is referred to textbooks by Dieter (*Dieter 1986,*[6]) and Byars & Snyder (*Byars et al. 1975,*[34]), for a more complete overview of the subject.

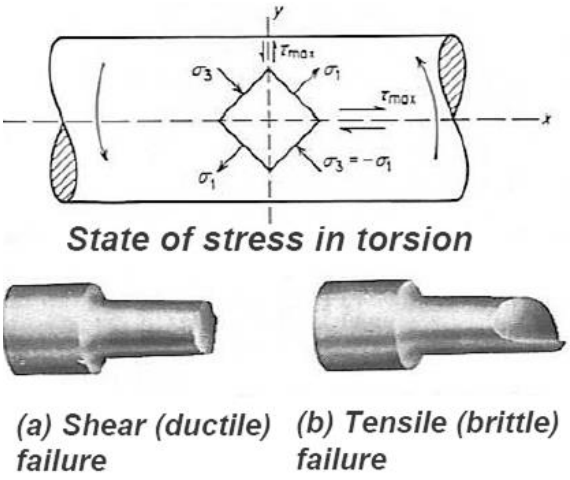

Figure 2-6. Modes of failure in torsion. *From* (*Dieter 1986,*[6])

2.1.3 Transformation Induced Plasticity

Transformation induced plasticity (TRIP) refers to the transformation of retained face-centered cubic (fcc) austenite (γ) to body-centered cubic bcc (α') and hcp (ε) martensite during plastic deformation. Steels that exhibit the TRIP effect have a high ductility, while retaining excellent strength and are hence used in many applications. Due to the excellent formability (through rolling, stamping, drawing etc.), structural components made from TRIP steel can be made thinner while their large amount of work hardening provides high strength.(*Angel 1954,*[35]) Patel & Cohen provide an early overview of the martensitic phase transformation due to applied stress (*Patel et al. 1953,*[36]), while Lo et al. give a comprehensive review of recent developments in stainless steel, including the TRIP effect (*Lo et al. 2009,*[37]).

Cakmak reports on "Phase Transformation Kinetics and Texture Evolution in a TRIP Steel under Complex Loads" in his dissertation (*Cakmak 2014,*[16]), and also provides an excellent review on details about the martensitic phase transformation in general and transformation mechanisms in detail (Chapter 2). Based on his chapter 1.1 and 2.2, the TRIP effect is summarized in the following: "In particular, the effective increase in the strain hardening rate due to the in-situ formation of the bcc martensite phase during the deformation helps to prevent premature failure and increase the ductility while maintaining the high strength of the material. In general, the harder bcc martensite phases act as barriers to dislocation motion during straining and enhance the strain hardening rate in this type of alloys (*Zackay et al. 1967,*[38]). The TRIP effect, therefore, helps increase the formability of these alloys, e.g., achieving higher rolling reductions without premature failure since the transformation occurs more readily at locations with the highest strain concentration, and allowing the manufacturing of more complex shapes. However, for enhanced ductility, gradual introduction of the martensite is essential because otherwise only the yield strength will increase if the transformation is rapid (*Zackay et al. 1967,*[38;] *Jacques et al. 2001,*[39]). Therefore, the strain-induced martensitic transformation kinetics is an important fundamental and practical issue."

Tao et al. (*Tao et al. 2007,*[40]) show for an ultrafine-grained steel under tensile loading, how the bcc martensite starts to bear more load (lattice strain) with increased applied stress (see Figure 2-7). Cakmak points out that the TRIP behavior in general, is fairly well understood under the uni-axial deformation conditions such as tension or compression, also under a variety of temperatures. He elaborates that texture evolution during plastic deformation in general can affect critical material properties such as modulus, hardening rate, ductility, and toughness during and after the manufacturing processes. He further states "One of the most important aspects of the texture evolution in TRIP steels is that it can also influence the martensitic phase transformation such that grains with certain crystallographic orientations can transform more readily than others (*Cakmak et al. 2012,*[33]). Furthermore, if the parent austenite is being textured, the resultant martensite is also expected to be textured and, subsequently, contributes to the plastic anisotropy (*Ray et al. 1990,*[41]; *Ray et al. 1994,*[42]; *Tao et al. 2006,*[43])."

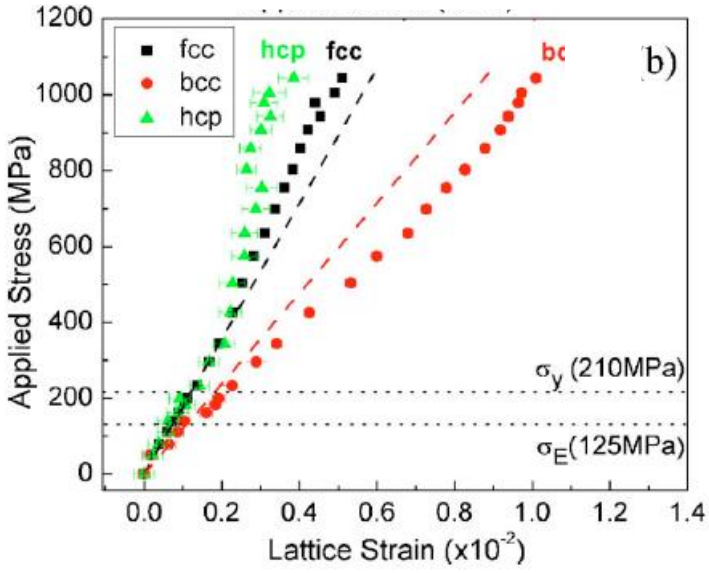

Figure 2-7. Applied Stress-Lattice Strain relation showing the load partitioning between the constituent phases: parent fcc austenite and product hcp and bcc martensites. *From* (*Tao et al. 2007,*[40])

2.2 Polycrystalline Materials and Available Characterization Techniques

The vast majority of materials which are used for structural purposes and in engineering applications are polycrystalline metallic alloys. The global mechanical properties of these materials largely depend on their microstructure. Individual crystallites within polycrystalline samples often exhibit anisotropic elastic and plastic properties, e.g. the elastic moduli vary largely depending on the crystallographic orientation. When polycrystalline materials are subjected beyond a certain mechanical stress, due to elastic anisotropy, they develop local incompatibility stresses which ultimately cause failure (plasticity) in these regions. This in return causes physical mechanisms in these regions, like dislocation glide, grain boundary sliding, grain rotation, phase transformations or twinning.(*Dieter 1986,[6]; Ludwig 2011,[44]*)

Obviously, the characterization of polycrystalline materials, in particular their microstructural properties and their state of stress, is of tremendous significance and interest. Established characterization techniques for example include light microscopy (metallography), electron microscopy (transmission electron microscopy and scanning electron microscopy), electron backscatter diffraction (EBSD) and (laboratory) X-ray diffraction. However, all of these techniques are mostly limited to the surface and/or require the sample to be destructed. Hard X-rays (for example at a synchrotron source) can penetrate deep into most metals, with limitations to be discussed in Chapter 2.3.2. While X-rays and electrons interact with the electrons of an atom, neutrons interact with the nucleus (see Figure 2-8) and hence neutron radiation provides the ability to penetrate deep into most structural materials (see Figure 2-9). As such, neutron diffraction for instance is considered the only true bulk investigation technique for stress and strain measurements. (*Allen et al. 1985,[45]; Clausen et al. 2003,[46]; Hutchings et al. 2005,[1]*)

It should be noted that especially in the field of diffraction-based imaging using synchrotron X-rays and transmitted electrons, tremendous advances have been made within the last decade for non-destructive three-dimensional (3D) microstructural characterization of crystalline materials.(*Larson et al. 2002,[47]; Poulsen 2004,[48]; Pfeifer et al. 2006,[49]; Bleuet et al. 2008,[50]; King et al. 2008,[51]; Liu et al. 2011,[52]*)

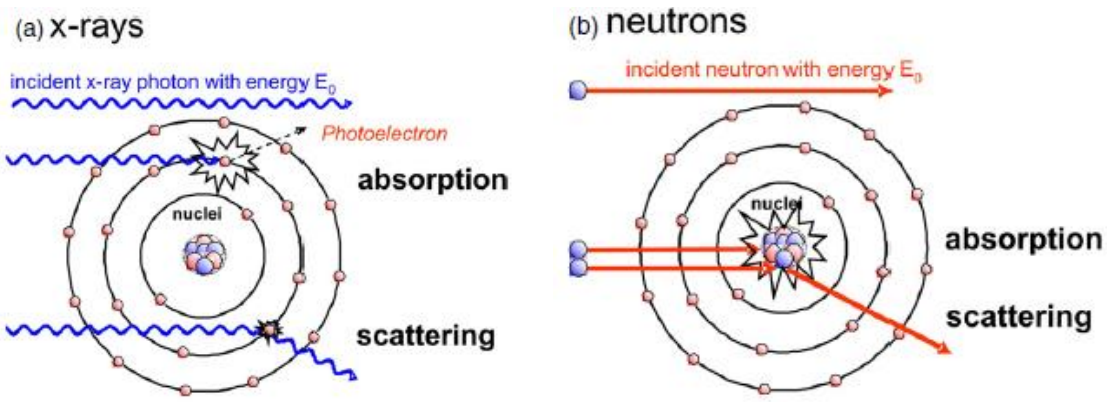

Figure 2-8. Interaction of matter with (a) x-rays and (b) neutrons. *From* (*Strobl et al. 2009,*[53])

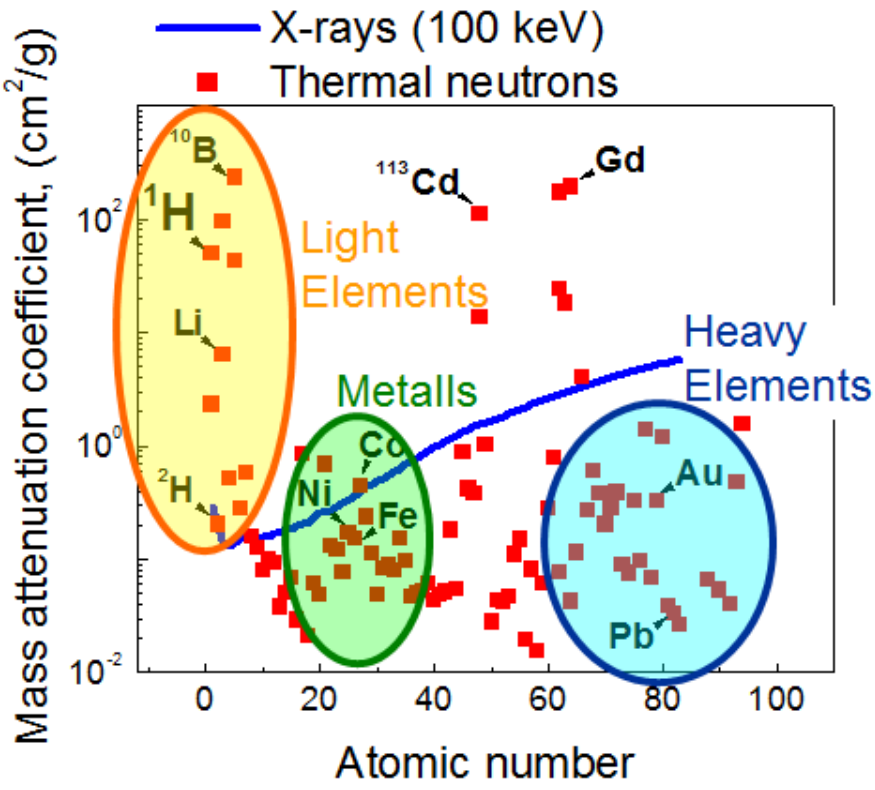

Figure 2-9. Mass attenuation coefficients for thermal neutrons and 100 keV x-rays for the elements (natural isotopical mixture). *From* (*Banhart 2008,*[54])

However, even these techniques are still limited to small sized sample sizes and neutrons are required for bulk investigations.(*Banhart 2008,*[54]) Characterizing the bulk properties is crucial to understand the meso-scale effects for polycrystalline materials.(*Doherty et al. 1997,*[55])

Electron and X-Ray based imaging techniques are very popular amongst scientists and engineers as they provide spatial information, and through the combination with scattering and diffraction modes have evolved to very powerful and versatile characterization and analysis tools. This makes it possible to perform chemical analysis (Energy-dispersive X-ray spectroscopy, EDS (*Goldstein et al. 2003,*[56])) and enables crystallographic investigations like grain, strain and phase mapping (EBSD (*Goldstein et al. 2003,*[56])), even in three dimensions at synchrotron sources (3D-X-ray diffraction, 3D-XRD (*Poulsen 2004,*[48]), Diffraction Contrast Tomography, DCT (*Ludwig et al. 2009,*[57])). Some more details on synchrotron based 3D-XRD and DCT will be given in section 2.5

2.3 Neutron Diffraction (for Strain Measurements)

2.3.1 Stress-Strain Basics and Available Characterization Techniques

Evaluation of applied and residual stress is of fundamental interest for the characterization of engineering components and materials. Stress is a complex tensor field that cannot be evaluated at only one point, but over a finite volume. As there are three different types of stresses that can arise in a polycrystalline material, we shall clarify those at this point (see Figure 2-10). “Residual stresses arise from misfits and these misfits can have many origins and length scales. As regards structural integrity considerations, continuum long-range (often termed Type I) stresses are generally of most concern. Grain-scale stresses (Type II), as might arise from grain to grain anisotropy or variation in properties, or sub-grain-scale stresses (Type III) as might arise from defects, dislocations and precipitates, are usually neglected.”(*Withers et al. 2008,*[58])

There are various destructive measurement techniques for the assessment of residual stress, e.g. block sectioning, slitting, layer removal, hole drilling and the deep hole method

(*Leggatt et al. 1996,[59]; Withers et al. 2008,[58]; Schajer 2013,[60]*). When a sample cannot be destroyed (and/or when applied stresses should be measured), a non-destructive measurement technique is needed. Most commonly used are diffraction methods, using either X-ray or neutrons. These techniques measure the elastic strain component of specific atomic lattice plane (*hkl*) and hence indirectly describe the state of stress. In a diffraction experiment, the probed gauge volume is defined by the size of the incident beam and usually by slits (or collimators) defining the diffracted beam.

2.3.2 Diffraction Basics

The basic concepts of diffraction were formulated by W.L. Bragg and his father W.H. Bragg in 1913 (*Bragg et al. 1913,[61]; Bragg 1913,[62]*), describing the relationship between the wavelength of radiation, λ, the distance between the atomic lattice planes in a crystal, d_{hkl}, and the scattering angle, $2\theta^{B}_{hkl}$, at which the radiation is elastic coherently scattered by the correctly orientated lattice planes hkl:

$$\lambda = 2d_{hkl}\sin\theta^{B} \tag{2-10}$$

X-Ray and neutron diffraction have become standard methods to be used for crystallographic investigations. Diffractometers probe the atomic d-spacing in crystalline materials, where a selected volume is illuminated and the diffracted neutrons (or x-rays) are recorded in scattering geometry. While laboratory x-rays are widely available, the main shortcoming is the small penetration depth into most engineering materials (typically a few tens of microns), which limits all studies to the (near) surface. Hence, neutron diffraction is traditionally the method of choice for bulk investigations (*Hutchings et al. 2005,[1]*) and is capable of probing up to 50 mm deep into steel (*Daymond et al. 2004,[63]; Pirling et al. 2006,[64]*).

With the advent of third-generation synchrotron sources and using very high energies (80–300 keV), X-ray beams can now penetrate about as deep into steel as neutrons. But like neutron sources, hard x-ray sources also require large scale user facilities.

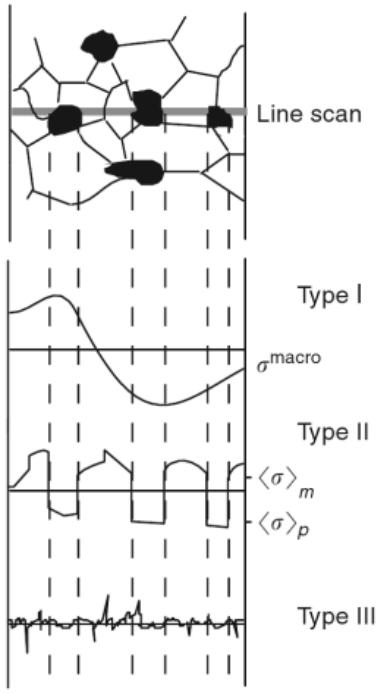

Figure 2-10. Different types of stresses. *From* (*Fitzpatrick et al. 2003,*[65])

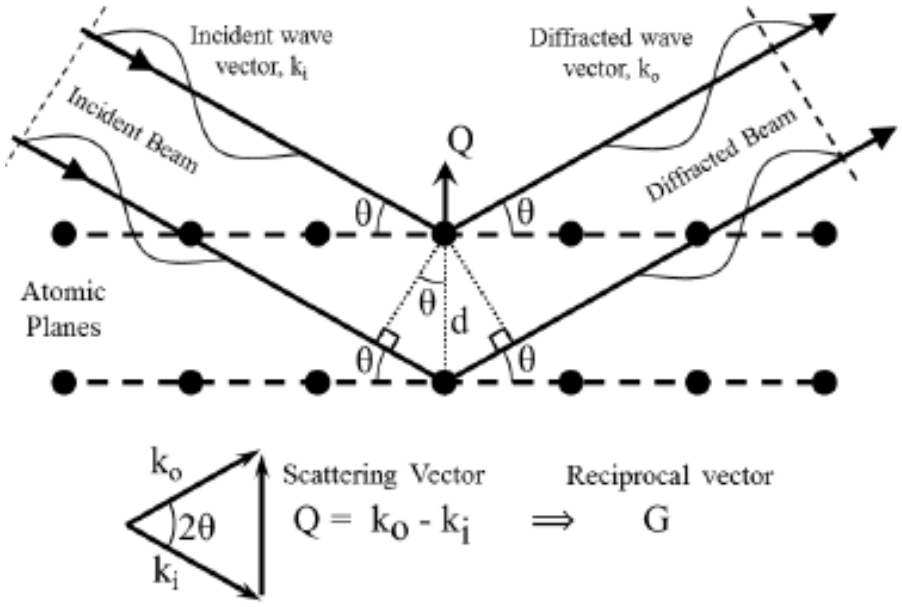

Figure 2-11. Elastic neutron scattering and Bragg's law. *From* (*Bunn et al. 2014,*[66])

However, the significant difference is that the wavelengths at these energies (at synchrotron sources) are very short (~0.1 Å), leading to very small scattering angles (typically 2–20°). This in return causes the sampled (gauge) volume to be strongly elongated (see Figure 2-12) and probed volumes cannot be defined very well. The method however is well suited for strain mapping of plate samples, where simplifying approximations (e.g. plane stress) can be made. In more complicated stress fields, where several components of the strain tensor need to be measured for the gauge volume, neutron diffraction remains superior. For a comprehensive review of available measurement techniques for residual stress, I refer to an article by Withers (*Withers et al. 2008,*[58]).

In a diffractometer that utilizes a constant wavelength of radiation, one measures the position of the scattering angle $2\theta^{B}_{hkl}$, from which the lattice spacing d_{hkl} can be derived using Bragg's law. At neutron Time-Of-Flight (TOF) instruments (as installed at most neutron spallation sources), pulses of neutrons are produced in time intervals and the neutrons velocity is measured by timing its passage over a known distance. The detector(s) are usually positioned at $2\theta^{B}=90°$ and since a single pulse contains a continuous spectrum of wavelength, one can determine the wavelength of each detected neutron by its Time-Of-Flight t_{TOF}.

Using diffractometers, the derived information about the lattice spacing d_{hkl} is averaged over the illuminated volume. It is usually very time consuming to produce spatially resolved strain maps of large samples, as it requires scanning the entire part. For selected samples, neutron imaging at selected wavelengths, has recently gained attention due to its possibility to produce 2D strain maps of entire samples, and details will be discussed in section 2.4.

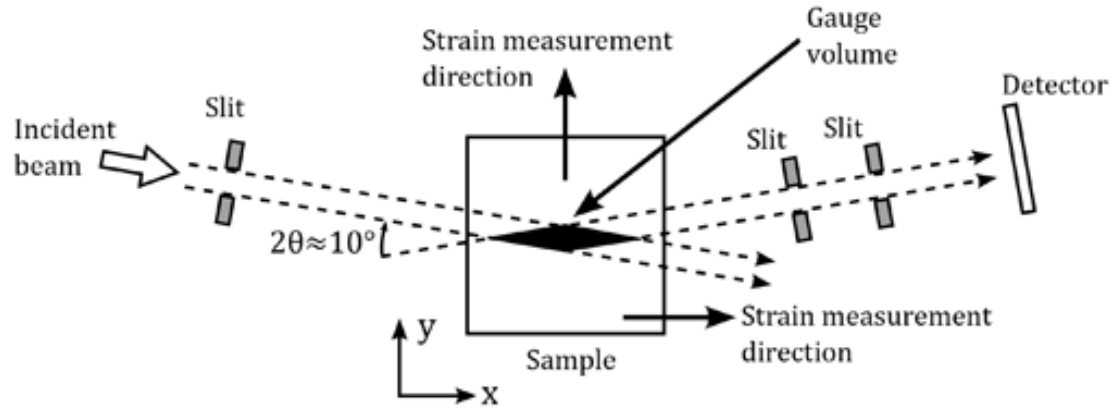

Figure 2-12. Schematic of an incident and diffracted high energy X-ray beam with corresponding diamond shaped gauge volume. *From* (*www.veqter.co.uk 2014,*[67])

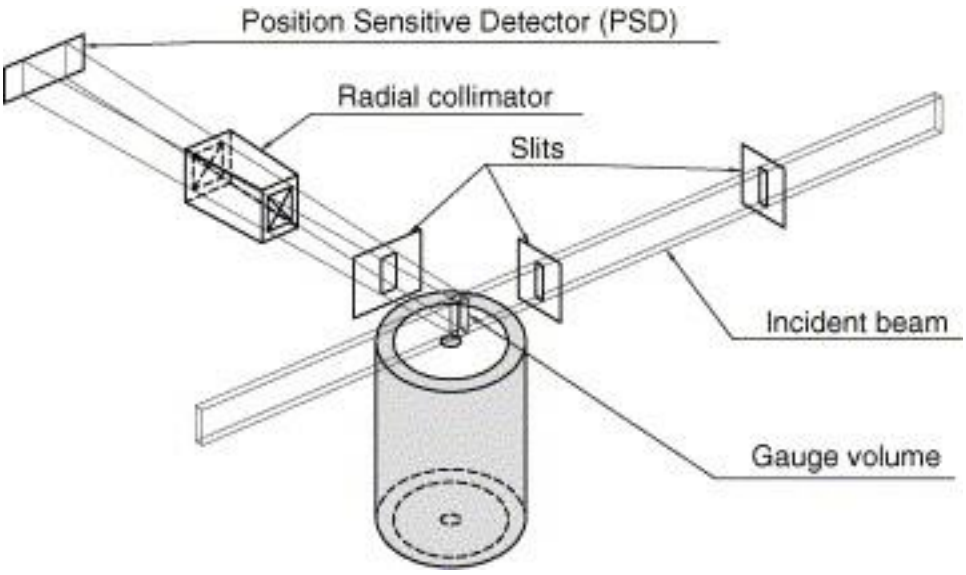

Figure 2-13. Schematic of a neutron diffraction setup. *From* (*Aydıner et al. 2005,*[68])

2.3.3 Application Examples of Neutron Diffraction

Neutron diffraction is an essential research tool for the study of mechanical behavior in engineering materials, as described in several textbooks and review articles. (*Fitzpatrick et al. 2003,[65]; Hutchings et al. 2005,[1]; Wang 2006,[69]*) While the method is vital for the evaluation of residual stress and strain, it is also commonly used to study the strain evolution in samples under applied mechanical and thermal loading conditions. Bourke summarizes the motivations to perform in-situ loading (*Bourke et al. 1999,[70]*) and points out that at LANSCE in 1999 the three main research areas in this field were "validating polycrystalline deformation models, understanding composite behavior, and studying stress induced phase transformations." Most engineering diffractometer instruments are equipped with tensile/compression devices, for example ENGIN-X at ISIS (*Daymond et al. 2004,[63]; Santisteban et al. 2006,[71]*), SMARTS at LANSCE (*Bourke et al. 2002,[72]*), STRESS-SPEC at FRM-2 (*Hofmann et al. 2006,[73]*), VULCAN at SNS (*Wang et al. 2006,[74]; An et al. 2011,[27]*), E3 at HZB (*Boin et al. 2014,[75]*), NRSF2 at HFIR (*An et al. 2007,[76]*), KOWARI at ANSTO (*Kirstein et al. 2008,[77]*) and TAKUMI at J-PARC (*Harjo et al. 2011,[78]*).

Neutron diffraction can be used to study the response of individual *hkl* lattice plane families in polycrystalline samples to applied stress (this information is for example being used in deformation models). The example in Figure 2-14 shows data for austenitic steel loaded in tension. The strains vary linearly up to yielding, but the slope is different for the individual *hkl* families. This is due to elastic anisotropy; and the elastic constants (E_{hkl} , ν_{hkl}) for different crystallographic planes can be used to describe this effect. In polycrystalline materials, elastic anisotropy can lead to stress concentrations and inhomogeneities during plastic deformation.(*Dieter 1986,[6]*) X-ray and neutron diffraction have been used extensively to determine the elastic constants for different crystallographic planes, in single crystals and polycrystalline materials.(*Clausen et al. 1998,[79]; Bourke et al. 1999,[70]; Clausen et al. 1999,[8]; Choo et al. 2004,[24]; Rajagopalan et al. 2005,[25]*) Such measurements are important for understanding the effects of anisotropy and texture on the macroscopic mechanical properties of polycrystalline materials. Beyond yield, the differences are even more significant, which can be explained by intergranular or, more precisely, grain-

orientation dependent strains. Elastic-plastic self-consistent (EPSC) modeling is used for a better understanding of this effect, and the model values are included in Figure 2-14. (*Clausen et al. 1998,[79]; Daymond et al. 2000,[80]; Daymond et al. 2002,[81]*) Wang elaborates (*Wang 2006,[69]*), "the essential physics can be explained within the framework of the Taylor model. By considering an ensemble of grains, Holden et al. (*Holden et al. 1997,[82]*) demonstrated that the <111>//LD grains (i.e., all grains with (111) plane parallel to Loading Direction) yielded first, although the <111> direction has the highest yield strength. This unusual behavior is a result of a combination of elastic and plastic anisotropy. For stainless steel, the <111> direction is the stiffest elastically. As a result, in a polycrystalline environment, <111>//LD grains carry the highest load, causing <111>//LD grains to reach the yield strength faster than other grains. Similarly, <100>//LD grains yield last, despite having the lowest yield strength, because the <100> is the softest direction. Unloading from the maximum tensile load will leave a tensile residual strain for this family of grains."

Uni-axial tensile loading was the major focus of deformation based diffraction studies in polycrystalline materials, to study the lattice strain responses (see above), and in certain cases associated phase changes (*Tomota et al. 2004,[83]; Tao et al. 2006,[43]; Tao et al. 2007,[40]*). In practical applications, however, shear is often the predominant loading case and leads to dominant failure mechanism, (*Yu 2002,[18]*) but only a few detailed diffraction studies (using neutrons or x-rays) under direct application of shear stress (for example under torsion) have been carried out. Moreover, these are actually concerned about texture and phase changes (*Lebedev et al. 2000,[84]; Wittridge et al. 2000,[28]; Martins et al. 2001,[29]; Cakmak et al. 2011,[32]; Cakmak et al. 2012,[33]*). Recently, Bunn and colleagues (*Bunn et al. 2010,[85]; Bunn et al. 2014,[66]*) have shown that residual intergranular strains generated by the application of shear deformation behave differently than those generated by tensile deformation when explored on an ex-situ basis for hollow cylinders made from 12L14 steel alloy.

More studies under applied multi-axial loading conditions, using neutron diffraction, are expected in the near future and instruments have recently started to be equipped with torsion and multi-axial capabilities (VULCAN at SNS, Stress-Spec at FRM-2, POLDI at PSI).

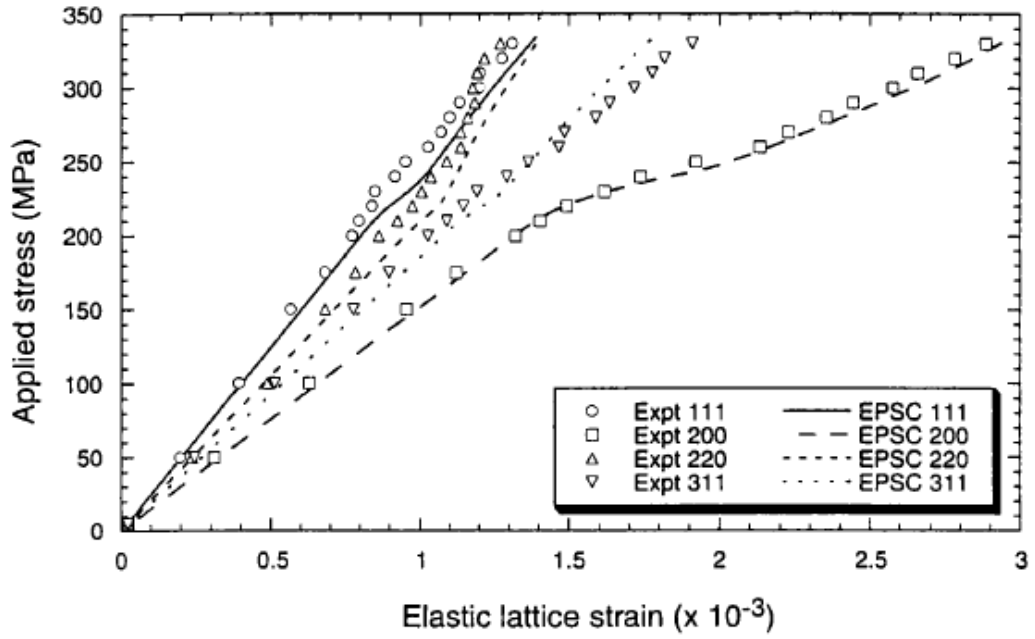

Figure 2-14. Neutron diffraction measured (symbols) and EPSC modeled (lines) lattice plane strains in an austnitic steel parallel to the loading direction plotted versus the applied stress. *From* (*Bourke et al. 1999,*[70])

2.4 Neutron Imaging

2.4.1 Basics and Instrumentation

Neutron Imaging began only shortly after the discovery of the neutron (*Chadwick 1932,*[86]). Kallmann and Kuhn filed a patent for the photographic detection of neutrons in 1938 (*Kallmann et al. 1940,*[87]), and Peter produced neutron radiographs of fair quality in a few minutes (*Peter 1946,*[88]). Thewlis et al. demonstrate radiographic inspections ranging from plant tissue to uranium disks.(*Thewlis 1956,*[89]) From the 1960's onwards, neutron radiography became a viable nondestructive inspection method. It should be noted however, that it is still a specialized method, as it usually requires a large scale facility, as was for example pointed out by Halmshaw in "Industrial radiology: theory and practice" (*Halmshaw 1995,*[90]). Portable sources (for example californium-252) are generally not

capable of producing high quality images, due to flux limitations. A comprehensive overview of the history of neutron imaging is given by Heller &. Brenizer (*Heller et al. 2009,*[91]).

Only within the last decade, neutron imaging evolved from strict absorption based contrast, to more complicated contrast mechanisms, while many of the techniques are still under development. These include for example phase contrast (*Allman et al. 2000,*[92]), differential phase contrast (*Pfeiffer et al. 2006,*[93]), dark-field imaging (*Strobl et al. 2008,*[94]), polarized neutron imaging (*Kardjilov et al. 2008,*[95]), Bragg edge imaging (*Santisteban et al. 2002,*[96]), and neutron resonance absorption imaging (*Tremsin et al. 2012,*[97]). The interested reader is referred to comprehensive review articles regarding the current state-of-art neutron imaging by Strobl (*Strobl et al. 2009,*[53]) and Kardjilov (*Kardjilov et al. 2011,*[98]), while a short summary, largely based on these two articles is given in the following.

As previously discussed, contrary to X-rays, neutrons do not interact with the electronic charge of the electrons, but they interact strongly with the atomic nucleus (Figure 2-8), enabling unique properties to be detected in transmission based imaging. The neutron radiation through a sample, with thickness d, is attenuated according to the exponential Beer–Lambert attenuation law:

$$I = I_0 \cdot e^{-\int \Sigma_T(\rho,\mathrm{Z},E_0)\cdot dx} \tag{2-11}$$

where I_0 and I are the incident and attenuated intensities, respectively, $\Sigma_T(\rho, \mathrm{Z}, E)$ is the macroscopic cross-section, which depends on material density ρ, material atomic composition Z, and neutrons with energy E_0 (monochromatic). However, most commonly polychromatic neutrons are being used for neutron imaging. Hence, when a polychromatic beam passes through a sample with a line l, which may be characterized by various total macroscopic cross sections, the intensity of the exit beam may be expressed as:

$$I = \int_{E_{min}}^{E_{max}} I_0(E) \cdot e^{-\int_l \Sigma_T(\rho,\mathrm{Z},E_0)\cdot dl}\, dE \tag{2-12}$$

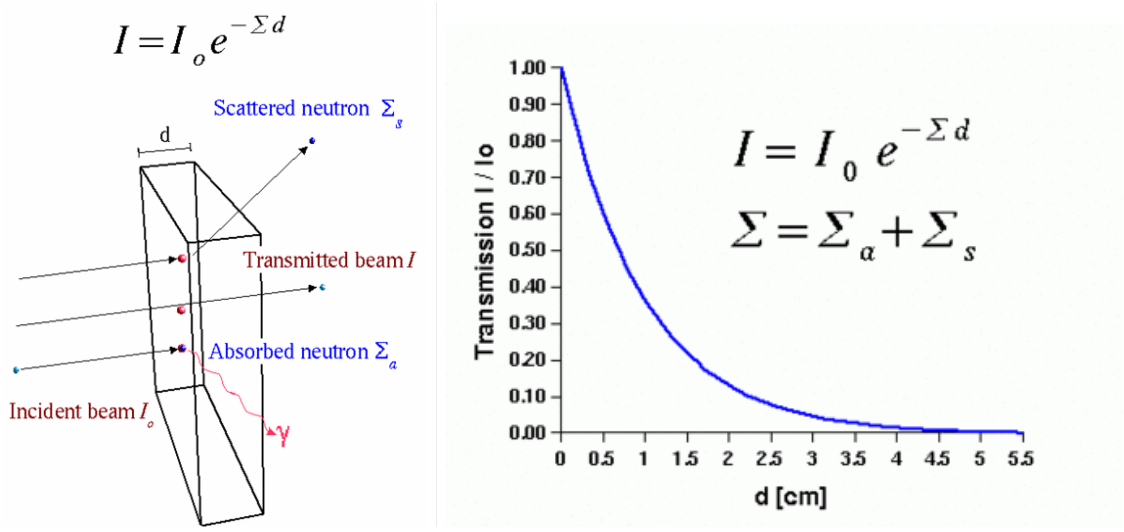

Figure 2-15. Neutron scattering and capture interaction probabilities (left) and exponential attenuation of neutrons in matter according to Beer-Lambert law (right).
From (http://www.psi.ch/niag/neutron-interaction-with-matter 2014,[99])

Obviously, by recording several projections of a sample, tomography can be performed and is used routinely. It should be noted however, that a monochromatic beam is generally assumed during tomography reconstruction. The "reconstructed" voxel value will hence present an average total macroscopic cross section or attenuation coefficient over the utilized wavelengths. The most widely used reconstruction algorithms for neutron tomography is the filtered back projection (FBP) algorithm.(*Kak et al. 2001,[100]; Buzug 2008,[101]*) Only recently, iterative reconstruction algorithms (*Kak et al. 2001,[100]; Buzug 2008,[101]*) have started to gain some popularity for certain applications in neutron imaging. A comprehensive overview of the reconstruction algorithms is also given in the dissertation by Kim.(*Kim 2013,[102]*)

In neutron based imaging, one has to take into account and correct a variety of artifacts, among them spatial and temporal variations in the incident beam intensity, inhomogeneities in the scintillator and detector and white spots caused by fast neutrons and gamma radiation. The latter issue can be eliminated or marginalized by filter operations using several images of the same projection, while the other artifacts are

corrected for by image normalization with respect to the measured background (dark field) and the beam intensity distribution (flat field) measurements.

The main components for a neutron imaging instruments are: the source, the collimation (or flight path) and the detector. A typical setup for an (tomography) imaging setup is shown in Figure 2-16. As a reference, the linear attenuation coefficients for thermal neutrons and X-rays are presented in Table 10-3 and Table 10-4. Figure 2-17 and Figure 2-18 depict the neutron imaging beamline CONRAD at HZB, which was used for a large portion of the experiments in this dissertation. CONRAD is also equipped with a curved neutron guide and devices for wavelength selection (double-crystal monochromator and velocity selector).

Neutron imaging is so far mostly being performed at continuous sources (typically research reactors), while spallation sources are expected to further exploit the advantages of energy resolved imaging. Obviously, the design of the source, the neutron moderator, and (if installed) neutron guide system has a significant impact on the imaging instrument. The interested reader is referred to (*Strobl et al. 2009,*[53]) and the dissertation by Gruenauer (*Gruenauer 2005,*[103]). The neutron spectrum shows the neutron intensity vs wavelength and is an important characteristic for an instrument. Figure 2-19 depicts the available spectrum at the CONRAD imaging instrument at HZB. Most scattering instruments use only selected wavelengths of such a spectrum, while imaging instruments often use the entire spectrum due to the higher flux, but energy selectivity became recently available as will be discussed in section 2.4.2.

The spatial resolution of a neutron imaging instrument depends on the geometry of the beamline and the detector resolution. The optimum geometry is considered to be a point source, which is usually achieved by a small pinhole with a diameter D and a long pinhole-to-sample distance L (Figure 2-16). The ratio L/D is typically used to describe the collimation of a neutron imaging instrument. The best achievable geometric resolution d is hence formulated as:

$$d = l / \left(\frac{L}{D}\right) \tag{2-13}$$

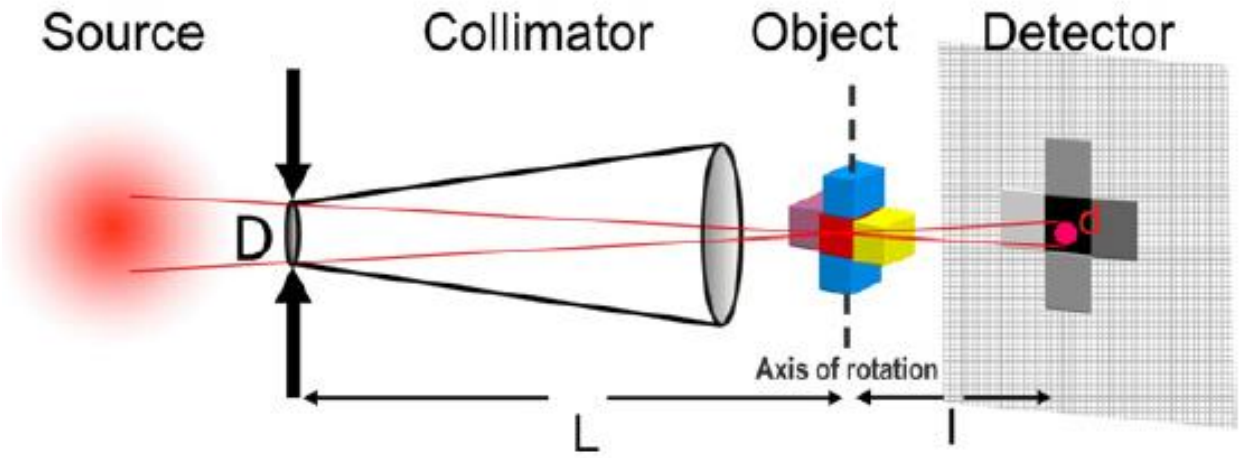

Figure 2-16. Typical neutron imaging setup, depicting the effect of L/D on the image resolution. *From* (*Strobl et al. 2009,*[53])

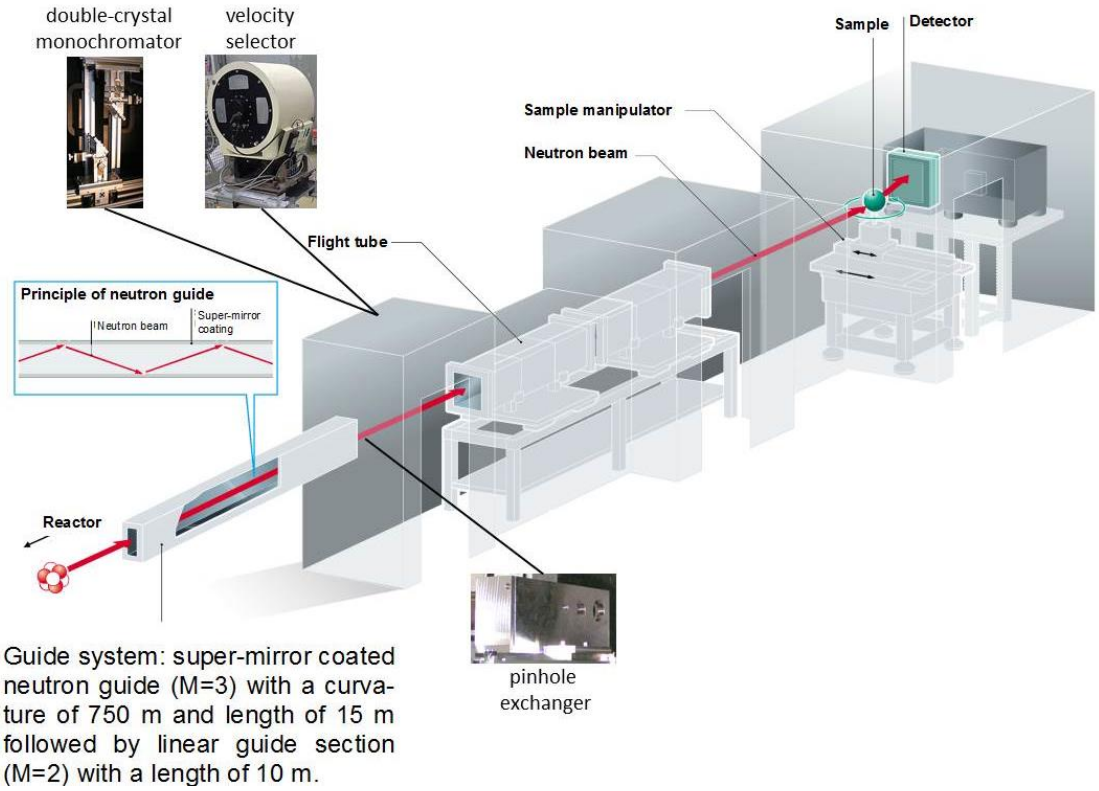

Figure 2-17. Neutron imaging instrument CONRAD (COld Neutron RADiography) at HZB.

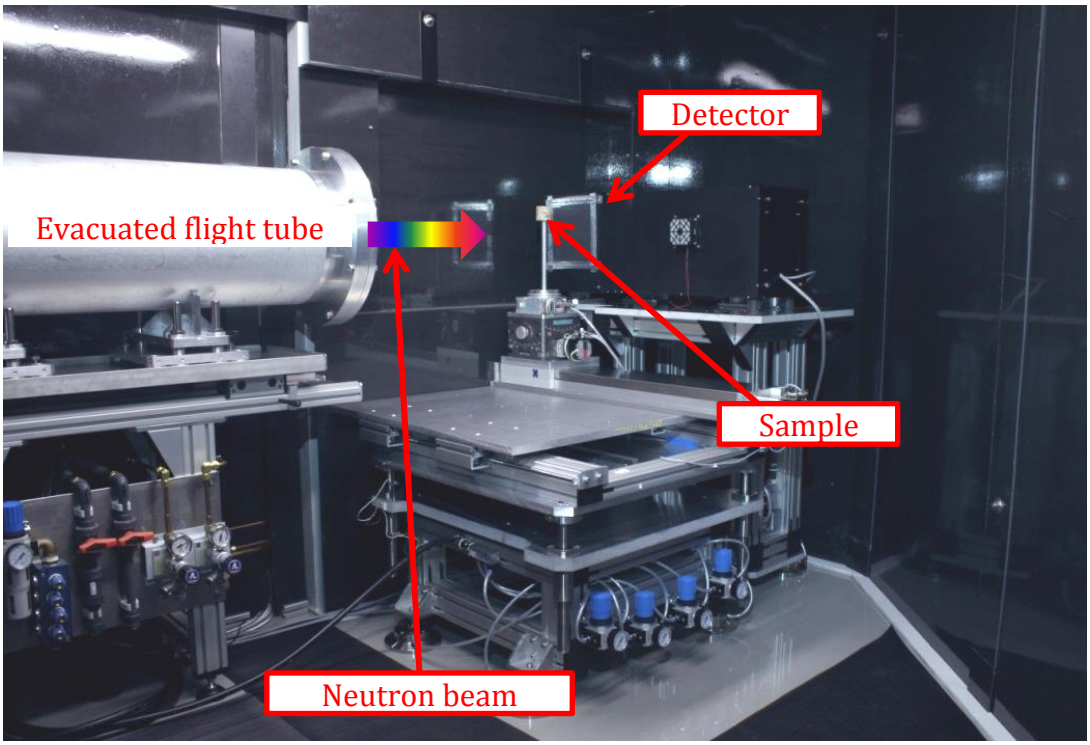

Figure 2-18. Photograph of the measurement position at CONRAD (COld Neutron RADiography) at HZB.

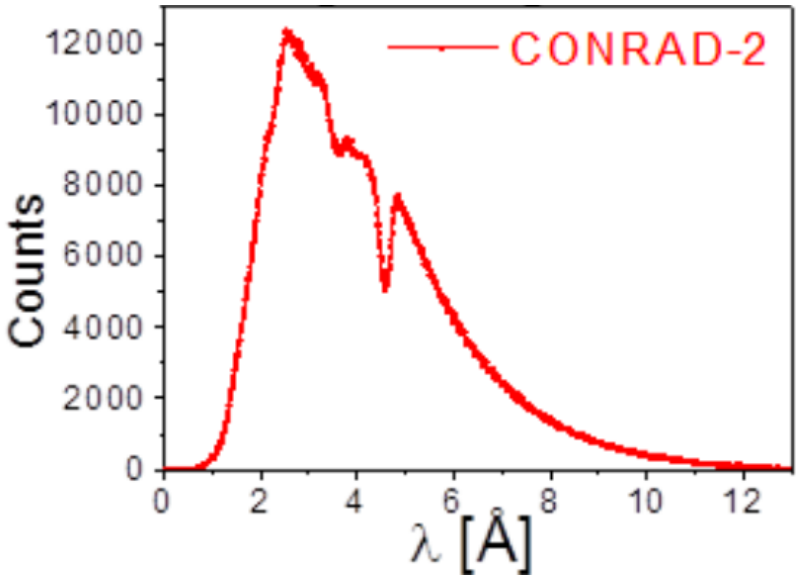

Figure 2-19. Neutron spectrum for the upgraded neutron imaging instrument CONRAD at HZB.

A longer collimator results in a better resolution, but at the same time the intensity is decreasing with distance from the moderator. The divergence due to the beam emanating from the point source can also result in a beam cross section that is not having a homogenous wavelength distribution, if neutron guides are used for example.(*Kardjilov et al. 2005,*[104])

Only the rapid evolution of digital imaging detectors has enabled the development of modern neutron imaging instruments, which in return caused developments of advanced imaging methods to flourish. The most widely used detectors at current instruments are scintillator screens in conjunction with either charge-coupled device (CCD) or complementary metal–oxide–semiconductor (CMOS) cameras, or sometimes flat amorphous-Si detectors are utilized.(*Strobl et al. 2009,*[53]) The most widely used scintillator screens, which convert neutrons into visible light, are crystalline ^{6}LiF/ZnS:Ag and GADOX (Gd_2O_2S(Tb)) screens. However, none of these detector technologies will provide the time resolutions that will be needed to record the time-of-flight spectrum for energy resolved imaging at spallation neutron sources. Coated micro channel plates (MCP), exploiting the ^{10}B(n,α)^{7}Li capture conversion of neutrons to electrons, appear to be most promising for energy resolved imaging at spallation sources.(*Tremsin et al. 2005,*[105]; *Siegmund et al. 2007,*[106]; *Tremsin et al. 2011,*[107]) In collaboration with A. Tremsin (UC Berkeley), such a device was used for neutron imaging at spallation sources as part of this PhD work.

2.4.2 Neutron Imaging Methods

Conventional (attenuation based) neutron imaging has a long history for the investigation of structural investigations of large metallic components, which cannot be performed using X-rays (*Stewart 1980,*[108]; *Banhart 2008,*[54]). It is still very popular and has many applications in diverse fields, such as biology, geology, archaeology, artworks, materials science and physics.(*Strobl et al. 2009,*[53]; *Kardjilov et al. 2011,*[98]) Due to the unique attenuation of hydrogen and lithium for example, popular applications in recent past have included fuel cell research (*Satija et al. 2004,*[109]; *Manke et al. 2007,*[110]; *Bazylak 2009,*[111]; *Mukundan et al. 2009,*[112]), hydrogen storage (*Sakaguchi et al. 2003,*[113]) water transportation

in plants (*Oswald et al. 2008,[114]; Matsushima et al. 2009,[115]; Warren et al. 2013,[116]*), battery research (*Lanz et al. 2001,[117]; Goers et al. 2004,[118]; Siegel et al. 2011,[119]*) and cultural heritage (*Lehmann et al. 2005,[120]; Festa et al. 2008,[121]; Lehmann et al. 2010,[122]; Peetermans et al. 2012,[123]*).

Within the last decade, a wide range of new imaging concepts, which utilize more of the unique properties of neutron radiation to achieve image contrast, promise to further expand potential applications to be investigated using imaging. (*Kardjilov et al. 2009,[124]*) Some of the major technique developments include energy selective (monochromatic) imaging, Bragg edge imaging, phase-contrast imaging, dark-field (USANS) imaging, polarized neutron imaging and neutron resonance absorption imaging. A short description of each imaging method will be given in the following, while more attention is given to Bragg edge imaging in the section 2.4.3, which is a major focus of this dissertation. It should be noted that Bragg edge imaging is an energy selective method, and sometimes is referred to as energy-dispersive imaging or also strain-radiography (when strains are being measured).

Energy selection: By using distinct wavelengths, the specific absorption spectrum of a material can be exploited to enhance contrast in the images. Furthermore, diffraction contrast occurs due to Bragg Scattering and can be used for crystallographic investigations. This method is commonly referred to as "Bragg edge Imaging" and details will be described in section 2.4.3. However, to make this contrast visible, only a narrow wavelength-band of neutrons (referred to as monochromatic neutrons from here on) need to be used.

At several neutron imaging beamlines, monochromator devices are available or are currently being installed, which allow choosing a certain neutron energy (wavelength). The most common monochromator devices at continuous sources are velocity selectors and double crystal monochromators, which provide an unchanged beam direction and usually can be tuned to different energies. Velocity selectors (also called turbine selectors) typically provide energy resolutions of $\Delta\lambda/\lambda$ of $\approx$ 10-15 %, while a double crystal monochromator (*Treimer et al. 2006,[125]*) provides about 3 % (can be varied between 1-

10 % depending on the type of crystal being used). For pulsed sources (e.g. a spallation source), time resolved data analysis provides the option to record neutrons of particular wavelengths. The same can also been performed at a continuous source if choppers are being used. (*Van Well 1992,*[126]*; Strobl et al. 2010,*[127]) In all cases, if a better $\Delta\lambda/\lambda$ is desired, a (dramatic) loss of neutron intensity is to be expected. Neutron imaging at time-of-flight (spallation based) sources has only recently started and cannot yet be considered an established method. However, it has the advantage that the wavelength spectrum is readily available, but sophisticated time resolving imaging detectors are necessary and only recently have become available (*Tremsin et al. 2005,*[105]*; Siegmund et al. 2007,*[106]*; Tremsin et al. 2008,*[128]*; Tremsin et al. 2009,*[129]*; Tremsin et al. 2010,*[130]*; Tremsin et al. 2010,*[131]), but it is believed that tremendous advancements will happen within the next few years. A comprehensive overview of energy selective options for neutron imaging is given by Lehmann et al (*Lehmann et al. 2009,*[132]). The double crystal monochromator at the CONRAD instrument was redesigned as part of this dissertation (see Figure 2-20; more details can be found in the appendix 10.5).

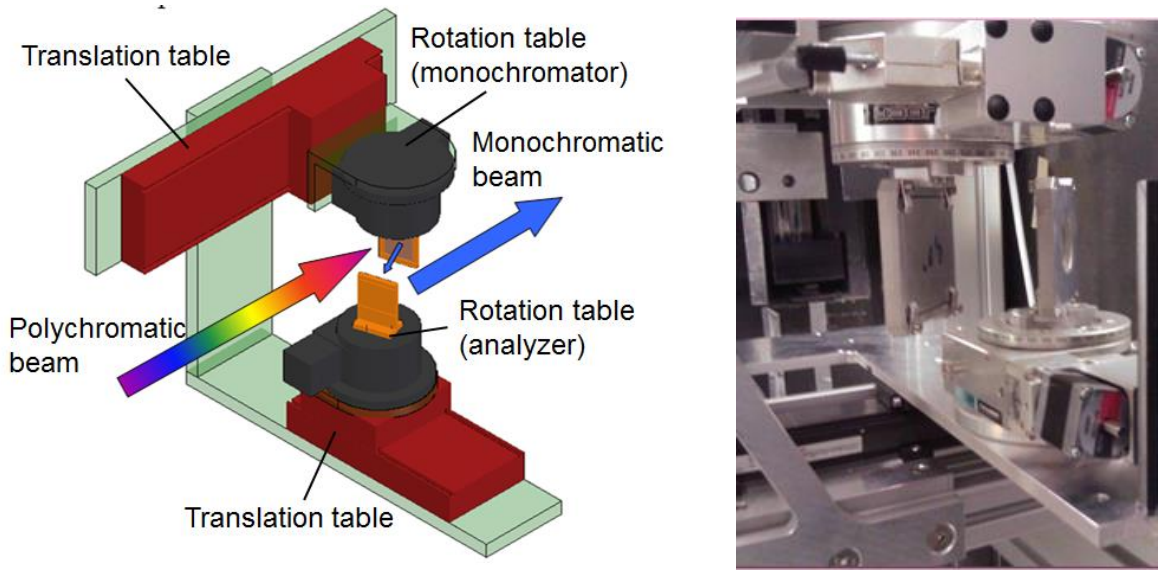

Figure 2-20. Double Crystal Monochcromator for CONRAD at HZB.

Another novel and promising application of energy resolved imaging is based on **neutron resonance absorption**, which can be performed if the "epithermal" range of energies is accessible. It should be noted that some ambiguous definitions of epithermal range were found (see appendix 10.3). The underlying principle is that individual isotopes of each element absorb neutrons of defined energies. This absorption in return causes an excitation of the nucleus, resulting in the emission of several gamma-ray photons in order to return to its ground state.(*Tremsin et al. 2012,*[97]) The conventional neutron resonance capture analysis (NRCA) detects the gamma-rays as a function of incident neutron energies, and requires a pulsed neutron beam for time of flight analysis (there is no need to measure the energy of the gammas).(*Postma et al. 2003,*[133]; *Postma et al. 2009,*[134]) Neutron resonance absorption imaging (NRAI) is performed at spallation sources by directly measuring transmitted neutron beam through the sample, and "dips" become visible in the time of flight spectrum whenever a neutron is absorbed, while the depths of neutron absorption resonances can be used to quantify amounts of specific elements in the sample, while even temperatures could be measured analyzing the Doppler broadening effect. Example measurements are presented in (*Sato et al. 2009,*[135]; *Cippo et al. 2011,*[136]; *Tremsin et al. 2012,*[97]; *Tremsin et al. 2013,*[137]). For most elements the energies of neutron resonant absorption are in the range of 1 eV (~0.28 Å) to 1000 eV (~0.009 Å).(*Tremsin et al. 2013,*[137]) According to Postma (*Postma et al. 2003,*[133]), "for some light and heavy nuclei, resonances occur at higher energies, but in many cases still below, let's say 50 keV." Existing analysis software for NRCA (for example SAMMY (*Larson 2001,*[138])) can be used for the analysis of NRAI data.(*Vogel et al. 2014,*[139])

Grating Interferometer: The use of a phase grating interferometer setup, as described by Pfeiffer (*Pfeiffer et al. 2006,*[93]; *Grünzweig et al. 2008,*[140]) and depicted in Figure 2-21, decouples angular and spatial resolution and allows detecting phase contrast (shift of phase due to refraction) and dark field contrast (due to small angle scattering), in addition to attenuation contrast. The gratings typically consist of a glass plate with deposited gadolinium lines (acting as an absorber) in equidistant distances. In such a setup, the

incoming neutron beam passes the source grating (G0) and creates an array of individually coherent, but mutually incoherent sources. Next, the neutrons hit a second (G1), finer grating and create a characteristic pattern of alternating high and low neutron intensity– so-called interference fringes–on the far side.

If a sample is placed between the first and second grating, refraction of neutrons causes a shift of the interference pattern produced after the second grating. Since neutron detectors don't have the resolution to image the interference fringes or tiny shifts in them, a third grating (G2) is placed behind the second, with a spacing chosen to match the periodicity of the fringes. The differences can then be resolved using a common imaging detector, by stepwise moving the third grating across the interference pattern.

Strobl et al describe how contrast due to small angle scattering can be detected using the same setup (*Strobl et al. 2008,*[94]): "In contrast to differential phase effects, scattering to very small angles does not cause a shift directed to one direction, but a broadening of the angular intensity distribution. This broadening is of the order of arc-seconds and can be detected and exploited for x-ray and neutron imaging with perfect crystals (*Rigon et al. 2003,*[141]; *Strobl et al. 2004,*[142]; *Ando et al. 2005,*[143]; *Pfeiffer et al. 2008,*[144]). Consequently it causes also a spatial broadening of the maxima of the fringe pattern in the grating interferometer, which has a comparable angular resolution. Indeed the broadening of the maxima at constant periodic positions reduces the visibility of the fringe pattern. Hence, the spatially resolved relative visibility, i.e., the variation of the local amplitude of the fringe pattern is – as described in (*Pfeiffer et al. 2008,*[144]) – a scattering related imaging parameter analogue to dark-field imaging or ultrasmall-angle scattering contrast. The high efficiency of this technique enables an expansion of the field of applications to three-dimensional tomographic investigations, provided that a tomographic reconstruction method is available for this parameter." The principles of the image formation process are visualized in Figure 2-22 and an example result for an image with the three contrast mechanism is given in Figure 2-23.

It should be noted for completeness, that phase contrast can also be achieved without the use of a grating interferometer by three other approaches. One method is the use of a

perfect crystal interferometer for direct measurement phase variations (*Rauch et al. 2000,*[145]), while diffraction enhanced imaging is based on a crystal diffractometer and measures refraction effects (phase gradients) with high angular sensitivity (*Treimer et al. 2003,*[146]). The third possibility is the free-space-propagation based method (or "in-line holography"), where the sample is placed samples at certain distances with respect to the detector. (*Allman et al. 2000,*[92]; *Kardjilov et al. 2004,*[147]) However, according to Strobl (*Strobl et al. 2009,*[53]) and Grünzweig (*Grünzweig et al. 2008,*[140]) all of these approaches suffer from low flux densities caused either by monochromatization, collimation, or by other beam preparation steps.

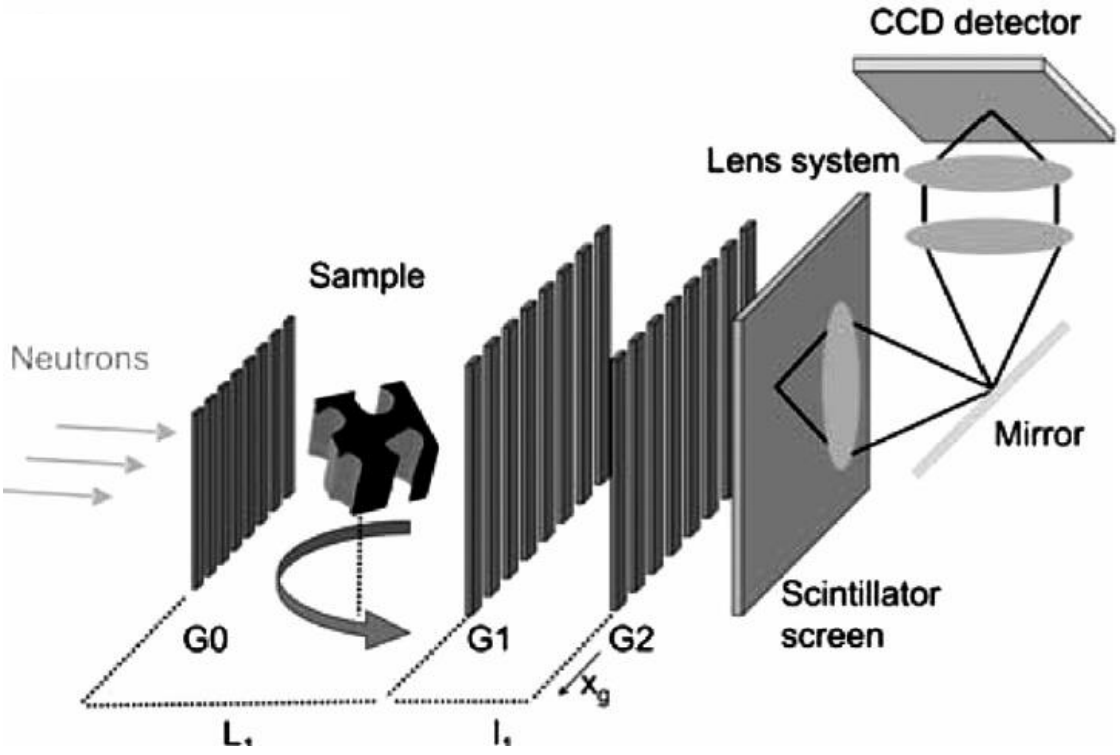

Figure 2-21. Phase Grating Interferometer setup with three gratings, sample, and detector system. *From* (*Strobl et al. 2008,*[94])

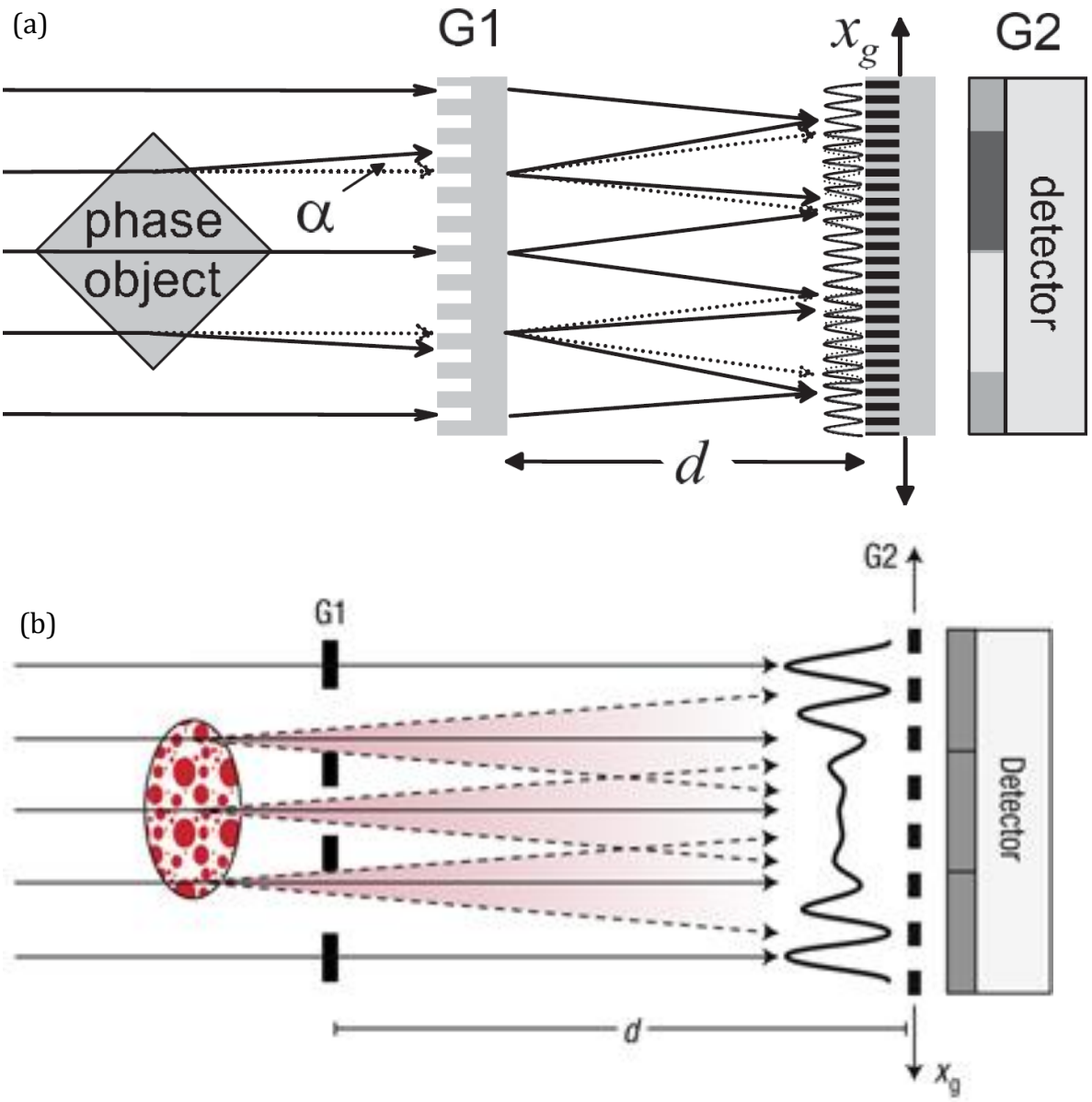

Figure 2-22. The principles of the image contrast forming due to (a) Phase shift: "The phase grating (G1) forms a periodic interference pattern in the plane of the analyzer grating. A phase object in the incident beam will cause a slight refraction which results in changes of the locally transmitted intensity through the analyzer." *From (Pfeiffer et al. 2006,[93])* and (b) Small angle scattering: The interference pattern induced by grating G1 smeared due to scattering in the sample, resulting in a loss in the amplitude of the oscillation. *From (Pfeiffer et al. 2008,[144])*

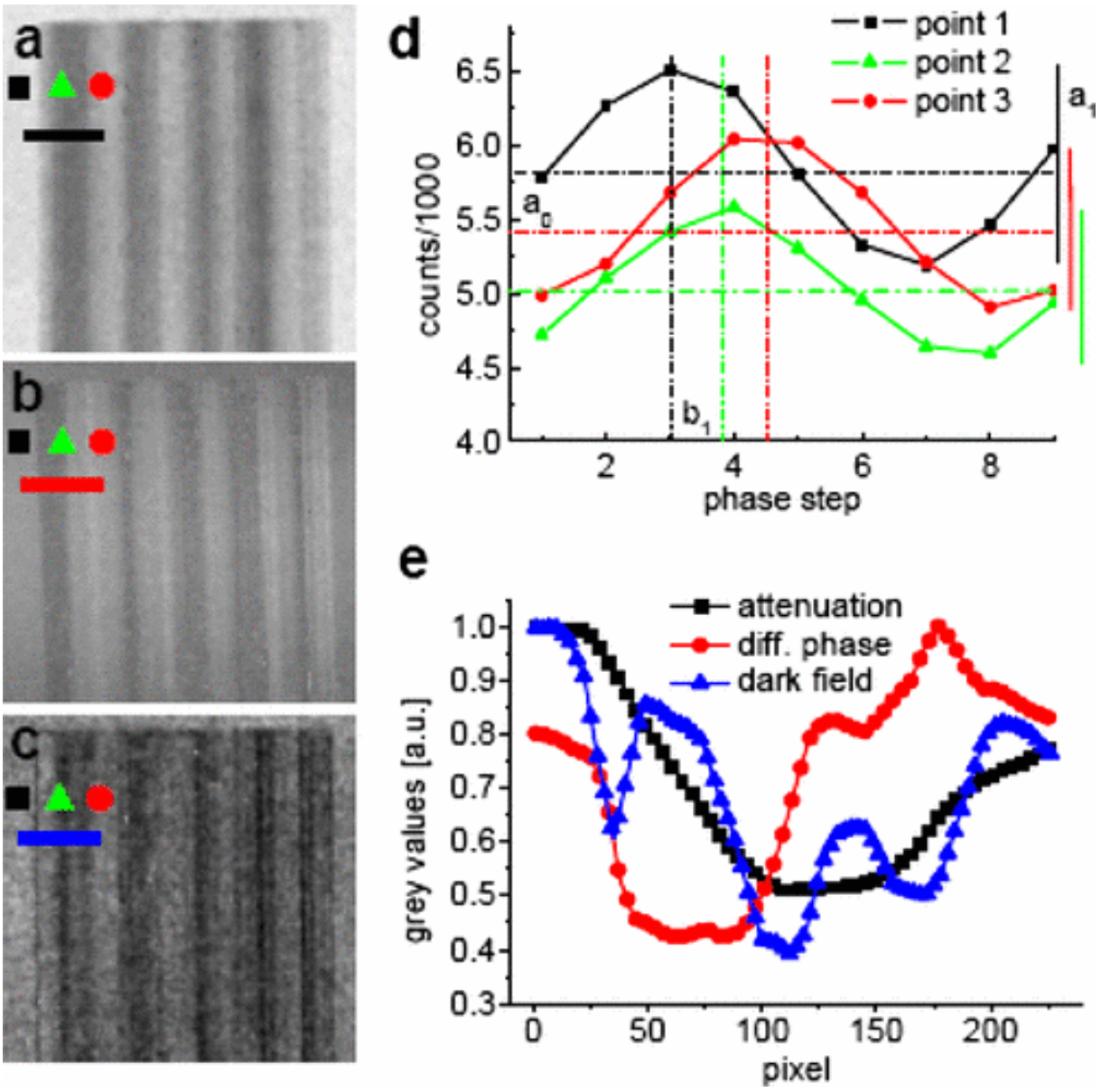

Figure 2-23. Radiographic images of an AL reference sample : (a) attenuation, (b) differential phase (refraction), and (c) ultrasmall-angle scattering (dark-field image). (d) Attenuation parameter a0 (offset), differential phase parameter b1 (interferometer phase shift), and dark-field parameter basis a1 (amplitude). (e) Line profiles corresponding to lines in (a–c). *From (Strobl et al. 2008,[94])*

It should be noted at this point, especially with respect to the next section (polarized neutron imaging), that grating interferometry is suited to study magnetic fields. Kardjilov et al. provide a comprehensive description of this technique (*Kardjilov et al. 2011,*[98]): The magnetic moment of neutrons "can interact with magnetic fields or magnetic moments in magnetic materials and can hence provide information about these (*Kardjilov et al. 2008,*[95; *Dawson et al. 2009,*[148]). The specific refractive index of a neutron depends on the orientation between the magnetic moment of the neutron and the local magnetic field it is exposed to (*Strobl et al. 2007,*[149; *Banhart 2008,*[54]). This implies that for the two possible orientations of the magnetic moment in this field, parallel or antiparallel, different refractive indices apply. This has important consequences when, for example at domain walls in magnetic materials, the magnetic field orientation changes abruptly. Under such conditions, the two spin states, represented in equal contributions in an incident unpolarized neutron beam, are separated by refraction and the beam splits. In analogy to small-angle scattering, described in the previous paragraph, this beam splitting can also be detected by grating interferometry. One observes a decrease of the amplitude of the interference pattern and can use this information to detect and visualize the domain walls in magnetic materials (*Grünzweig et al. 2008,*[150; *Lee et al. 2010,*[151]).

Polarized neutron imaging: Due to the fact that neutrons have a magnetic moment (and spin), neutron scattering techniques have a long history of being used to study magnetic fields and materials; and a comprehensive overview is given in the textbook by (*Zhu 2005,*[152]). Relatively recently, polarized neutron imaging has been developed as a spatially resolving method.(*Kardjilov et al. 2008,*[95]) As shown in Figure 2-24, neutrons are first polarized by removing neutrons with the unwanted spin orientation. They then pass the magnetic field under investigation, which changes the initial spin direction due to Larmor precession, which is a rotational change. Afterwards, the neutrons that now have altered spin states pass through another polarizer (referred to as spin analyzer). Neutrons that have a spin parallel to the original spin will pass though the analyzer, while neutrons that possess an antiparallel spin, will be absorbed. Hence, the grey values in the image

transmission based image are a function of not only the attenuation, but also the spin states. By using monochromatic neutrons (having a uniform velocity), the gray value and hence precession angle can be related to the field integral along the path of the neutrons through the field.

2.4.3 Bragg Edge Spectroscopy (1D) and Imaging (2D)

Information related to the crystal structure of crystalline materials (strain, phase, texture) is traditionally obtained using (X-ray or neutron) diffractometers. In a diffractometer where a fixed wavelength is used, the diffraction angle is determined. If a wavelength spectrum is available (typically at neutron spallation sources), a wavelength-dependent intensity spectrum is recorded under some fixed angle to the direction of the incident neutron beam. The detected intensity maxima (so-called Bragg peaks) are accordingly plotted as a function of diffraction angle or wavelength.

Due to the same (Bragg scattering) effect, the same information can (in principle) be obtained by recording the transmitted neutron beam through the sample: Some neutrons travel without interaction through the sample, some are absorbed, while those that are scattered out of the direction of the incident beam (which would be detected in a diffractometer), leave a characteristic pattern in the incident intensity spectrum, so-called Bragg edges. Hence, spatial information in two dimensions can be obtained if an imaging detector is used.

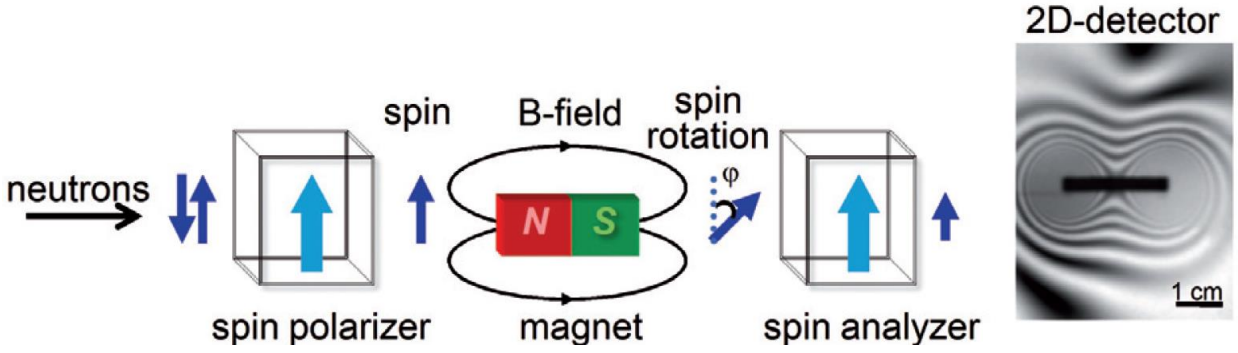

Figure 2-24. Setup used for polarized-neutron imaging. *From* (*Kardjilov et al. 2011,*[98])

Performing Bragg edge transmission imaging with a detector positioned behind the sample, requires the possibility to record the transmitted neutron intensity as a function of wavelength. For a particular *hkl* family, the scattering angle increases as the wavelength is increased until the Bragg scattering condition cannot be fulfilled any longer, which occurs for wavelengths larger than $\lambda = 2d_{hkl}\sin 90° = 2d_{hkl}$. At this particular wavelength, the transmitted intensity increases drastically (the so called Bragg edge: see Figure 2-25). Obviously, any change in d_{hkl} would shift the Bragg edge correspondingly, and consequently, strains along the beam direction ($\theta^{B}_{hk} = 90°$) can be resolved, hence the method is sometimes termed "strain radiography". Analogous to a diffraction pattern, phase and texture differences will also lead to differences in the Bragg edge spectrum, and examples are given in Figure 2-26, Figure 2-27 and Figure 2-28.

The Bragg edge transmission technique has recently gained attention again, due to the new generation of spallation sources (SNS, J-PARC, ISIS 2nd target station, ESS) and the fact that many existing neutron imaging facilities now provide the possibility of (tunable) wavelength selection.

Early experiments to study the nuclear cross-sections of elements, using transmission measurements, have already been reported by Fermi et al. in 1947 (*Fermi et al. 1947,*[153]) and Winsberg et al. in 1949 (*Winsberg et al. 1949,*[154]). The transmission technique was even applied to study the effect of cold rolling on brass, including discussion of grain size effects, by Weiss et al. back in 1952 (*Weiss et al. 1952,*[155]). In 1950, Cassels provided a summary on total neutron scattering cross sections, including Bragg edges.(*Cassels 1950,*[156]) In the mid-1990', a group of the Nuclear Physics Institute (Czech Republic) implemented the Bragg edge transmission method at a neutron diffractometer instrument at a reactor source, aiming to measure (residual) strain (*Mikula et al. 1995,*[157]; *Strunz et al. 1997,*[158]; *Wagner et al. 1997,*[159]). Those measurements were performed at reactor sources using monochromator crystals, which was time consuming and no spatially resolving detectors were available.

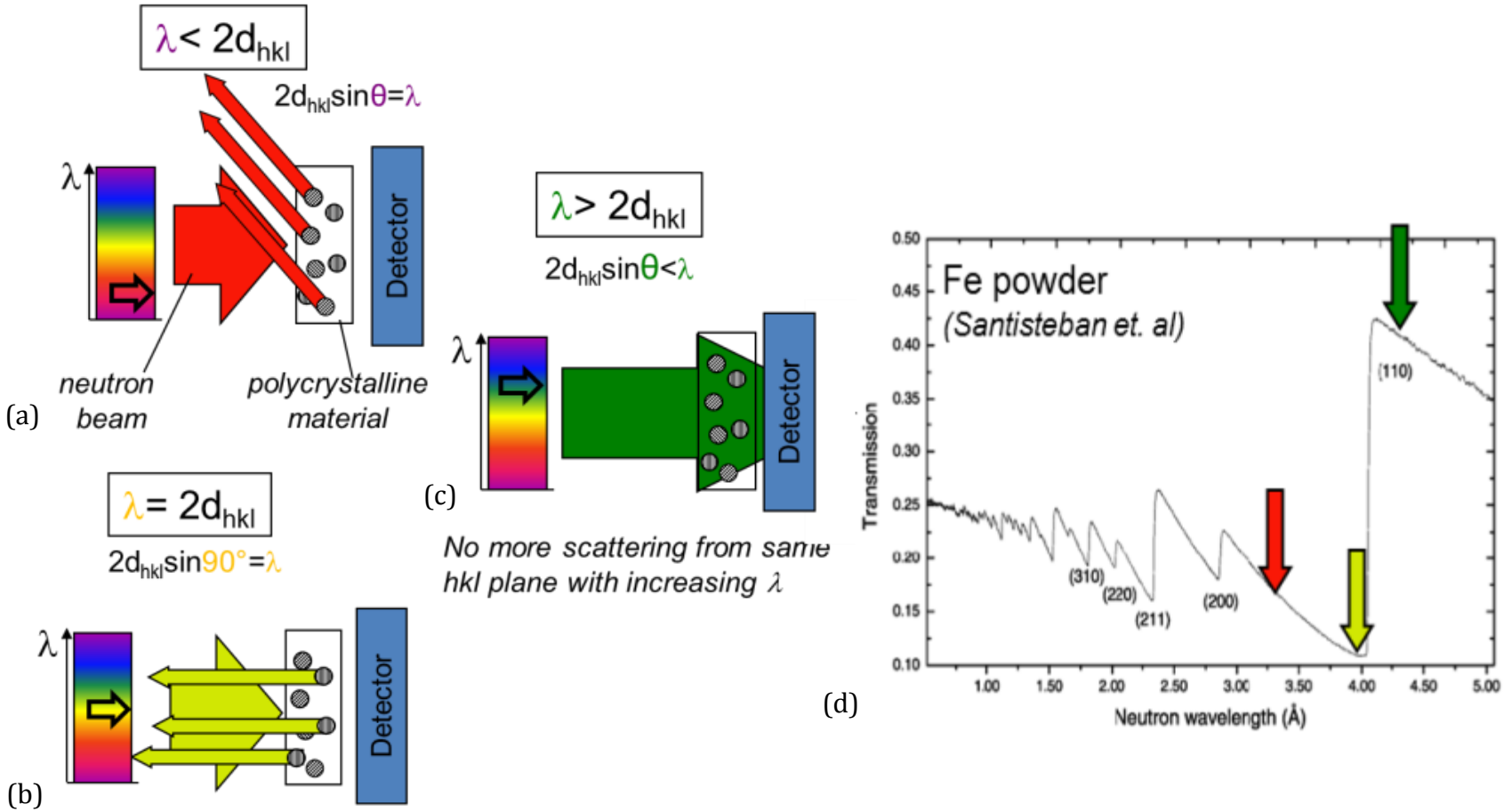

Figure 2-25. (a-c) Principle of Bragg edge radiography: Neutrons of different wavelengths vary in transmitted intensity through polycrystalline samples due to diffraction. This leads to characteristic transmission Bragg edge spectra for crystalline samples. The position of these so called Bragg edges is directly related to the d-spacing of the lattice planes. (d) Example Bragg edge spectrum for Fe-powder, with arrows at wavelenghts that correspond to diffraction conditions in cases a-c.

With the advent of ***neutron spallation sources*** in the 1970's (*Carpenter 1977,*[160]), the time of flight technique now provided the possibility to record the transmission spectrum much more efficiently. In 1982, Johnson and Bowman used the NBS (now National Institute of Standardization) 100 MeV Electron Linac to record and distinguish Bragg edges for iron.(*Johnson et al. 1982,*[161]). The next generation of spallation sources installed at Los Alamos National Laboratory (USA; LANSCE) and Rutherford Appleton Laboratory (UK; ISIS), provided unprecedented opportunities. Novel detector technology (*Bowman et al. 1990,*[162]) was used at LANSCE by Meggers and Priesmeyer et al. to study the phase transformation of austenite to bainite in gray iron in real time.(*Meggers et al. 1994,*[163; *Meggers et al. 1994,*[164]) At ISIS, D. Wang showed in his dissertation in-situ (tensile and compressive) loading of steel samples measured by neutron transmission vs. surface strain gauges.(*Wang 1996,*[165]) The Bragg edge transmission technique was further developed at LANSCE, with a focus to investigate kinetics of structural phase transitions, and at ISIS, with a focus on the measurement of d-spacings and strain. Some notable publications as part of these developments at LANSCE and ISIS include the work by Priesmeyer (*Priesmeyer et al. 1999,*[166]) and Santisteban (*Santisteban et al. 2002,*[167]), as well as the dissertation projects by Vogel at LANSCE (*Vogel 2000,*[3]) and Steuwer at ISIS (*Steuwer et al. 2001,*[168; *Steuwer et al. 2003,*[23]). A comparison of Bragg edge neutron-transmission spectroscopy at both facilities is given by both groups in (*Santisteban et al. 2002,*[169]).

Priesmeyer gives a summary, titled "The use of neutron transmission for materials analysis", in (*Fitzpatrick et al. 2003,*[65]) and points out the "single shot capability" of spallation sources (the complete Bragg edge spectrum can be recorded between <100 μs and several miliseconds), making it extremely useful for the study of in-situ processes, which is also discussed in (*Bowman et al. 1991,*[170]) He also discussed optimal specimen thicknesses for best contrast from a Bragg edge, based on the macroscopic cross section for coherent scattering, and states an optimal thickness of 1.7 cm for iron and 19 cm for aluminum.

Vogel (*Vogel 2000,*[3]) and Steuwer (*Steuwer 2002,*[4]) provide detailed discussions in their dissertations regarding the Bragg edge profiles with special emphasis on mathematical approximations that can be used for fitting. Beyond basic functions, such as the Heaviside step-function and the error function, they consider the Jorgensen et al. profile function, the Ikeda-carpenter profile function, and the Kropff profile function. Steuwer points out that at reactor sources, the profile is symmetric and the integral of a Gaussian, i.e. the error function or probability integral, describes Bragg edge reasonably well (for example demonstrated at GKSS Geesthacht (*Mikula et al. 2000,*[171])). At spallation sources, due to the brief moderation process of the burst of fast neutrons emitted in the spallation process, the Bragg edge profiles (as well as Bragg diffraction peaks) display a characteristic asymmetry. Steuwer and Vogel hence emphasize that the simple error function does not accurately describe the Bragg edge profile at spallation sources, especially when the position of the edge needs to be determined with high precision (i.e. stress/strain measurements). The Jorgensen et al. profile function was incorporated at LANSCE by Vogel into a specialized Rietveld code for transmission analysis (BETMAN), while Steuwer mostly used the Kropff profile function at ISIS for his analysis. In this context, it should also be noted that Steuwer points out that the simple error function can still be used for relative strain measurements at spallation sources, i.e. if the reference d-spacing is taken from the same sample under the same conditions. This is of significance for the experiments that will be discussed in chapter 5 of this dissertation.

However, despite the major advancements for transmission at spallation sources, one major drawback was so far a lack of suitable detectors, which provide both spatial and time resolution. Nonetheless, the term "imaging" was sometimes used in foresight of the developments that should follow. The fundamentals and potentials of crystallographic characterization were demonstrated at the spallation sources LANCSE, ISIS and J-PARC, for the determination of:

- Phases (*Bourke et al. 1996,*[172]*; Vogel 2000,*[3]*; Santisteban et al. 2002,*[167]*; Steuwer et al. 2004,*[173]*; Steuwer et al. 2005,*[174]*; Huang et al. 2007,*[175]): example see Figure 2-26

- Texture corresponding to preferential orientation (*Santisteban et al. 2006,[176]; Iwase et al. 2007,[177]; Sato et al. 2010,[178]*): example see Figure 2-27
- Strain and stress (*Santisteban et al. 2001,[179]; Steuwer et al. 2001,[168]; Santisteban et al. 2002,[96]; Steuwer et al. 2003,[23]; Iwase et al. 2012,[180]*): example see Figure 2-28

All of the above work did either use single element (no spatial resolution at all) or (relatively coarse) pixelated transmission detectors. The implementation of a conventional imaging detector (as used at steady state sources), but triggering it to the TOF signal at ISIS by a gated image-intensified CCD, was presented by Kockelmann and co-workers (*Kockelmann et al. 2007,[181]*). Using a gated time-integrating detector for TOF imaging at a continuous source was reported by Strobl et al. (*Strobl et al. 2011,[182]*).

New detectors are being developed for ***time of flight imaging*** applications. Kiyangai et al. report about the developments at J-PARC (*Kiyanagi et al. 2014,[183]*), that those detectors typically have a high counting rate with a medium to low spatial resolution (about 2–3 mm pixel size) or a medium counting rate with smaller pixel sizes (approx. 1mm), while the active area is reasonably large (4-100 cm^2). The detector technology that was developed in by Tremsin and co-workers, is based on (doped with neutron absorbing atoms) microchannel plates (MCPs) and a Medipix/Timepix readout sensor.(*Tremsin et al. 2005,[105]; Siegmund et al. 2007,[106]*) Tremsin describes the detection principle: "The process of neutron detection by the MCP consists of three stages: absorption of incoming neutron within the MCP glass; escape of the reaction products into adjacent pore; release of charged particles from the pore walls which initiate the electron avalanche in the pore producing the signal detected by the detector readout."(*Tremsin et al. 2008,[128]*)

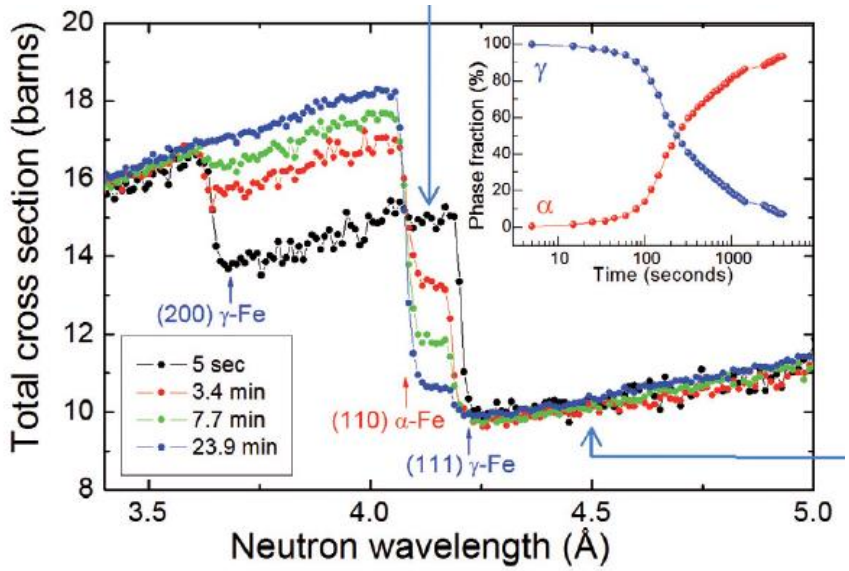

Figure 2-26. In-situ phase transformation through transmission at ISIS: Total neutron cross section of EN24 steel after austenization at 830 °C and kept in a furnace at 380 °C for the time specified. (inset: evolution of the volume fraction of the α and γ phases) *From (Santisteban et al. 2002,[167])*

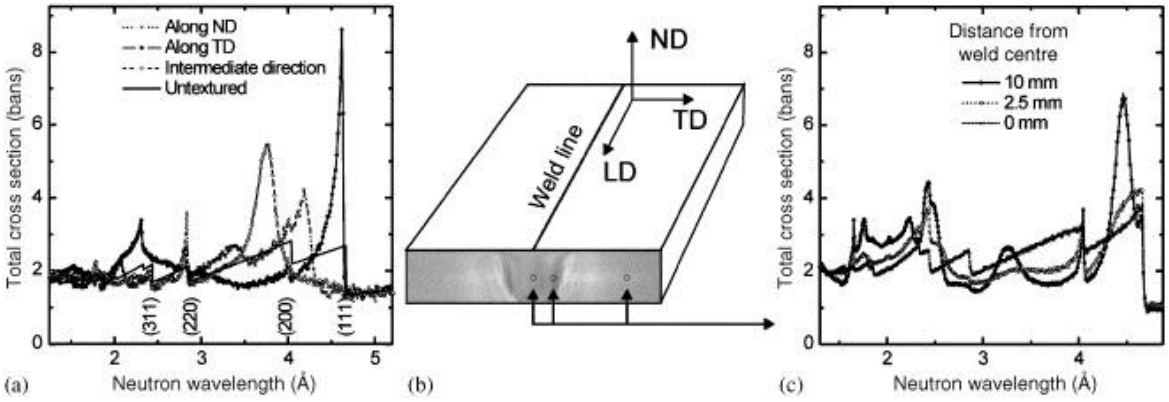

Figure 2-27. Transmisison measurements of a welded AL plate at ISIS: (a) Total cross-section along different directions compared to prediction for an untextured sample (b) Schematic view of welded specimen (c) Total cross-section along LD measured at the points indicated in (b). The pixellated detector used in this work consists of a 10×10 array of 2×2 mm^2. The graphs reveal large variations in edge height between different directions, e.g. the absence of the (111) edge along the normal direction (ND) means that no crystallite has directions from this family aligned to ND, while a texture of at least 6× random is revealed along the transverse direction (TD). *From (Santisteban et al. 2006,[176])*

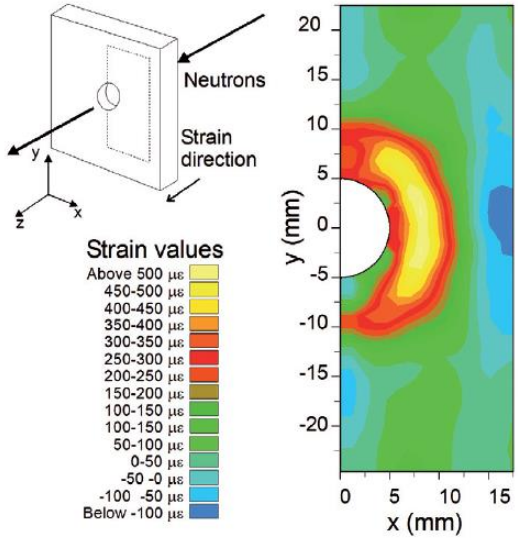

Figure 2-28. Transmission measurement at ISIS showing the residual elastic strain around a cold-expanded hole in a 12 mm thick steel plate. The measured strains correspond to the through thickness average of the out-of-plane strains. The pixellated detector used in this work consists of a 10×10 array of 2×2 mm^2. *From (Santisteban et al. 2002,[167])*

The latest version of this detector possesses a pixel size of 55 μm, a 512x512 pixel field of view, and a temporal resolution of ~1 μs. The MCP detector has been used for proof-of-concept studies at ISIS (*Tremsin et al. 2009,[129]*) and SNS (*Tremsin et al. 2010,[130]*), as well as for texture imaging of zirconium at ISIS (*Santisteban et al. 2011,[184]*). The same detector was used as part of this dissertation for strain mapping under in-situ loading, which will be described in Chapter 5. It was also used phase mapping in samples that have undergone transformation induced plasticity effect. A few examples will be given in section 7.7.4 and section 7.8, but the detailed analyses of these studies are beyond the scope of this dissertation.

On the other hand, several dedicated ***neutron radiography/tomography instruments*** at steady state sources can readily provide spatial resolutions on the order of or smaller than 50 μm (*Kardjilov et al. 2009,[124]*) and therefore implementation of energy selective Bragg edge imaging techniques could open many new applications. In principle there are two

possibilities to do such energy dependent measurements at a reactor source (*Lehmann et al. 2009,*[132]): (a) using the time-of-flight information in distance from the source using a specifically designed chopper system or (b) selection (or suppression) of neutrons from specific spectral parts. In the latter case the wavelengths can be selected by a velocity selector, the "slit method" or a wavelength tunable device, e.g. a double crystal monochromator. Using different settings or crystals allow selection of a very narrow spectral part, but one should keep in mind that the flux decreases as a narrower wavelength band is selected.

Proof of principle measurements have been reported by neutron imaging facilities, for the case of microstructural differences in welds (*Lehmann et al. 2009,*[132]; *Schulz et al. 2009,*[185]; *Josic et al. 2010,*[186]; *Josic et al. 2011,*[187]; *Kardjilov et al. 2012,*[188]), for differentiating materials and strain variations in a bend steel plate (*Treimer et al. 2006,*[125]), for texture effects in a processed aluminum foam sandwich (AFS) (*Kardjilov et al. 2009,*[124]), for microstructural differences in ancient swords (*Salvemini et al. 2012,*[189]) and historical copper (*Peetermans et al. 2012,*[123]). In 2008, the group at HZB (N. Kardjilov, I. Manke, T. Kandemir) demonstrated tomographic reconstructions of metallic samples (Figure 2-30), which consisted of varying amount of martensite and bainite, but the work has not been published. However, these experiments inspired me for the work that is reported in chapter 7.

The majority of the published results, which have been obtained at existing neutron imaging facilities using the Bragg edge method, were largely of qualitative – rather than quantitative – nature. Nonetheless, images recorded in this mode can reveal inhomogeneities and features that would remain undetected otherwise. The example radiographs for a steel weld, obtained at wavelengths before and after the Bragg cut off, shown in Figure 2-29 present such an example. A comparison of transmission measurements of different welds with electron backscatter diffraction (EBSD) have been performed by the group at PSI.(*Lehmann et al. 2014,*[190])

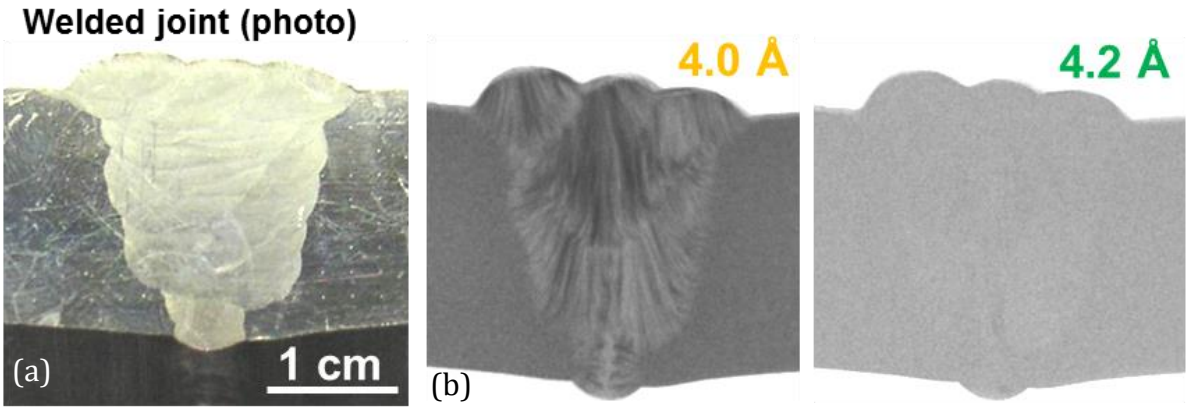

Figure 2-29. Energy selective neutron images of weld joint between two austenitic steel plates. (a) Photographic image. (b) Radiographic images at two wavelengths around the Bragg edge for iron corresponding to (110) lattice space. Bragg scattering from individual crystallites causes contrast in the radiographs due to preferred crystallographic orientations inside the weld, while no more scattering takes place after the Bragg-cut-off. *From* (*Kardjilov et al. 2012,*[188])

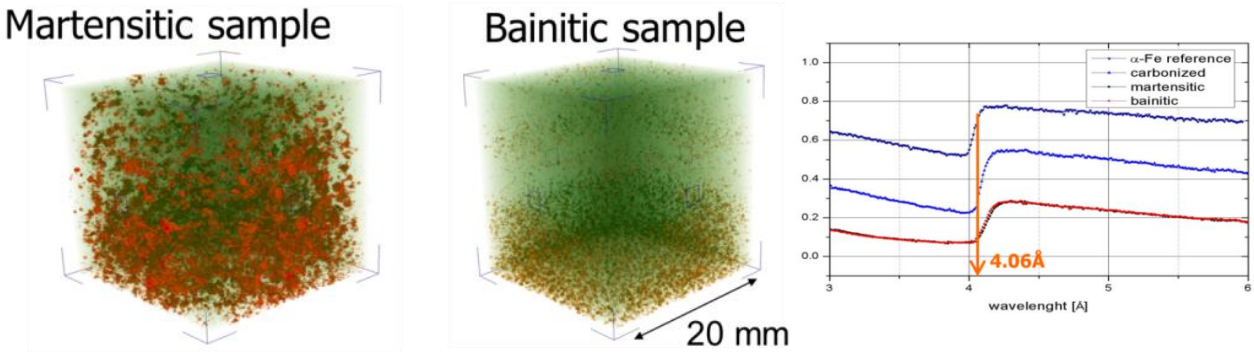

Figure 2-30. First demonstration at HZB of a monochromatic neutron tomography for discremination of two different crystalline phases. The measurement was taken at 4.06 Å.

Boin focused in his dissertation research (*Boin 2010,*[5]) on the feasibility of quantitatively measuring crystallographic properties with Bragg edge transmission, using the ENGIN-X instrument at the spallation source ISIS and the imaging beamline CONRAD at the steady state source BER-II. He integrated the calculation of the theoretical neutron cross section for crystalline samples into the McStas Monte Carlo neutron simulation (nxs), and also took instrumental parameters into account.(*Boin 2012,*[191]) In particular, Boin showed for a fiber textured aluminum sample, that transmission measurements at CONRAD and ISIS can be used to quantitatively determine the degree of texture for the given projection. An example is shown for data taken at ISIS in Figure 2-31, depicting five different sample orientations. The results were confirmed with simulations, by using the March-Dollase model for preferred orientations. Boin also attempted strain measurements in a standard residual stress (VAMAS "ring and plug") sample, where he examined the projected strain in the transmission direction. He integrated the projected strain for this particular sample into the McStas simulation and was able to predict the expected measured strain values for CONRAD and ENGIN-X. Even though, the simulation and experimental results agree well, this experiment showcases the major shortcoming of the Bragg edge method: While in traditional (neutron) diffraction, the strain components can be measured according to their principal directions, the transmission method records the projected strain, which is an average through the sample thickness. For the case of the ring and plug sample, the strain values for the hoop, radial and axial direction are depicted in Figure 2-32. The transmitted strain values will represent a combination of the radial and hoop components, at varying radii. The theoretical projected strain for the same sample is shown in Figure 2-33. The same plot also includes the data taken at ENGIN-X, which shows very good agreement. Boin observed the same trend of strain profile using CONRAD, but with a little less accuracy. Unless the strain profile is known, as is the case for the ring and plug sample, the measured projected strain for other samples with non-uniform strain profiles may not be very meaningful.

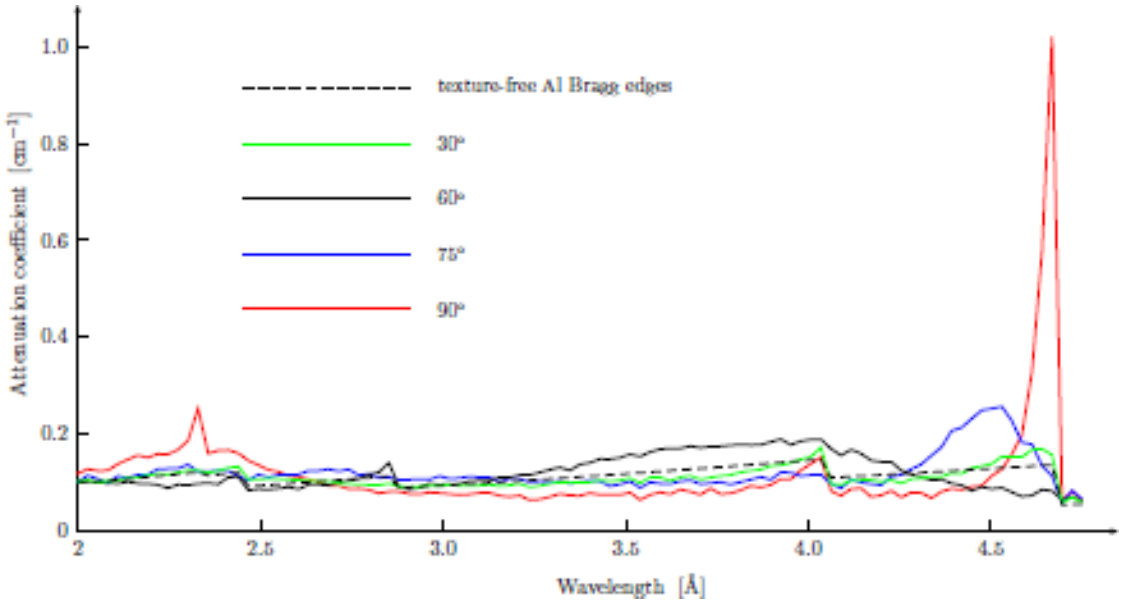

Figure 2-31. Bragg edge spectra measured by Boin at ENGIN-X in TOF mode for a textured sample at five different orientations. Texture influence can clearly be seen as the shape of the Bragg edges changes enormously. The dashed line shows the texture-free Al curve calculated with nxsPlotter. *From* (*Boin 2010,*[5])

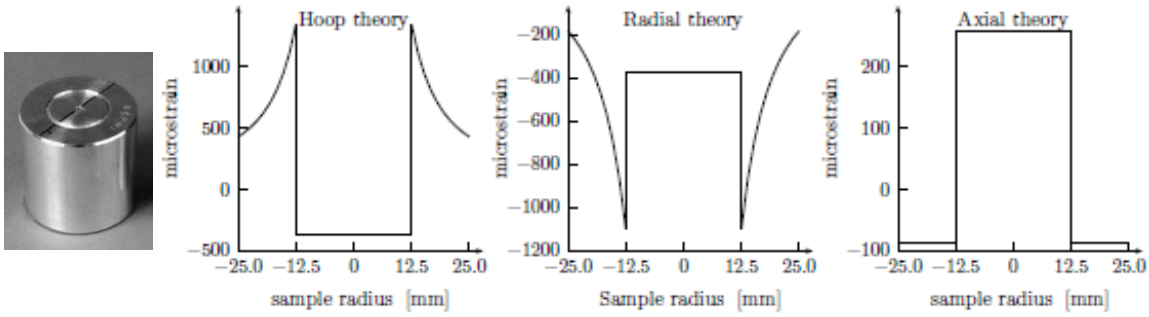

Figure 2-32. Photograph of the (VAMAS) ring and plug sample (left). Theoretical ring and plug strain values for the hoop, radial and axial directions after plotted against the sample radius (right). *From* (*Boin 2010,*[5])

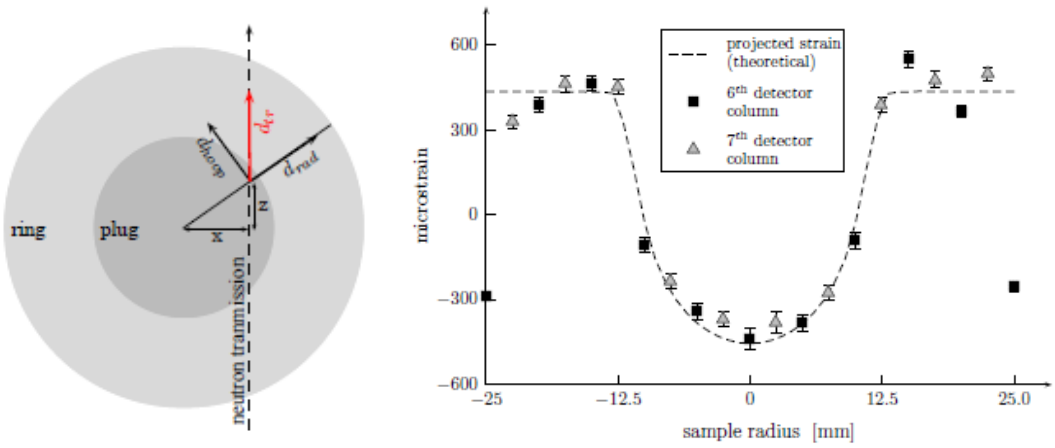

Figure 2-33. (a) Neutron transmission probes the projected strain which for the ring and plug sample consists of a combination of hoop and radial strain components. (b) Projected strain as a function of sample radius and corresponding data collected at ENGIN-X. *From* (*Boin 2010,*[5])

The idea ("or better engineers dream") however is, that principal strains can be resolved from the projected signal, i.e. to perform a strain-tomography. This is an inverse mathematical problem and in principle requires the projected signal from multiple sample orientations. This has been demonstrated for two "simple" samples, both with axisymmetric strain distribution, where the authors propose different methods to inversely determine the strain components from a Bragg edge.(*Abbey et al. 2009,*[192]; *Abbey et al. 2012,*[193]) I will give a short summary of their work in the following, but one should already note that the problem will be much more complex, when considering arbitrary strain profiles and trying to describe the state of strain at a finite volume (3x3 strain tensor).

I will attempt to briefly summarize the work by Abbey, Korsunsky et al., who are working to develop "***strain tomography***" using the projected strain from Bragg edge transmission.(*Abbey et al. 2009,*[192]; *Abbey et al. 2012,*[193]) First of all, it should be noted that only very few studies even in diffraction mode consider measuring full strain tensors, as it is very time consuming and challenging (*Winholtz et al. 1988,*[194]; *Krawitz et al. 1994,*[195]; *Winholtz et al. 1995,*[196]; *Balzar et al. 1998,*[197]; *Bunn et al. 2014,*[66]). Abbey and co-workers consider two axisymmetric cases (*Abbey et al. 2012,*[193]): a (VAMAS) ring and plug sample and a quenched circular cylinder. On the one hand, this results in the fact that all

transmission projections are the same for each sample rotation around ω. On the other hand, the strain distribution is already known (a priori knowledge) and the transmission data can be interpreted accordingly. Most importantly, it is known that the measured averaged strain in transmission direction ε(r) consists of/is related to the radial strain component and the hoop strain component if the following:

$$\varepsilon(r) = \varepsilon_{radial} \cdot \sin^2\theta + \varepsilon_{hoop} \cdot \cos^2\theta \qquad (2\text{-}14)$$

As a practical example, let's say at the location 1 depicted in Figure 2-34, ε_{radial} is 500με and ε_{hoop} is -100με. The angle θ (angle between radial direction and x-axis) at this location is 135°, hence ε(r) is 200. At location 2, the angle θ is 225°, hence ε(r) is also 200. This stays the same, even if the sample is rotated and is different for samples exhibiting more general strain fields. It should be noted that Abbey et al. do not consider the axial strain component (z-direction) at all in this case, but only the in-plane strains which are directly related.

To reconstruct the 3-D strain distribution, they present 3 approaches:

i) Linear Tent function representation

First, they use fundamental mechanics theory for axially symmetric problems, relating radial and hoop strains (strain compatibility), reducing the problem to only one unknown variable. So called "tent functions" (Triangular functions) are used to describe the radial symmetry in the ring-and-plug sample (weighting the linear variation of strain between neighboring nodes). For every node, a contribution factor can be determined (describing how much influence this particular node has onto the measured transmission value) and a coefficient matric can be formed by stacking the results for all nodes. Iterative reconstruction can be carried out in the form to find a solution which minimizes the difference of the measured strains and the forward calculation (which is the product of the coefficient matrix and the vector representing the hoop strain components).

ii) Constrained model approach

The other proposed method (described by Abbey et al. in "Feasibility study of neutron strain tomography" (*Abbey et al. 2009,*[192]) uses a model framework for determining the

strain components using a priori knowledge of the form of the strain distribution. In this case, they found a power-exponential series by FEA modeling, describing the strain distribution. The parameters which define this function are then determined using the measured values by "strain tomography". They term the average predicted strain on the detector pixel j as $\bar{\varepsilon}_{ij}(r)$ and solve a matrix equation (using least square fitting), from which the radial and hoop strain can be determined.

iii) Combined diffraction data and strain tomography

The next option uses diffraction data to deconvolute the in-plane strain components. However, because of the spatially varying admixture of the strain components, the knowledge of a particular component at the correct position within the sample is vital. In the case of the ring and plug sample, in the center of the sample, the measured strain depends only on the radial component, whilst at the edge of the sample it depends only on the hoop component. "This means that the values for the hoop strain in the center and the radial strain at the edge of the sample must either be constrained or measured directly."(*Abbey et al. 2012,*[198]) In this case, "instead of assuming a model (as in case ii) for the strains, both the radial and hoop components were independently represented via tent functions without assuming compatibility (as compared to i). To reconstruct the strains, prior knowledge (from diffraction measurements) of the radial strain at the edge of the sample and the hoop strain in the center of the sample was available" which was used to constraint the values in the iterative reconstruction.

As can be seen from the work by Abbey et al., it appears that that some knowledge of strain distribution and/or strain compatibility is needed for any strain tomography approach. The FE modeling approach seems to be the most promising approach as the measured data could be directly compared to the FE model and the parameters of the FE model parameters could be refined accordingly. However, significant knowledge and/or assumptions are usually needed in order to make this work. Additional diffraction can help to access strains which are not directly accessible with the transmission technique and could be used as constraints in iterative reconstruction. In certain cases, only strain

compatibility considerations can be sufficient and a few projections can already solve the problem.

An approach that is worth mentioning in this context is the imaging driven diffraction methodology. Tomographic reconstruction (recorded in "white" beam mode) of samples with complicated geometries can be used to precisely position the diffraction gauge volume inside the sample, and/or to detect inhomogeneities that require further investigation. Software like SScanSS (*James et al. 2004,*[199]) can then be used to precisely control the sample positioning system of the diffraction instrument, based on the 3D sample information. Examples of this can be found in the dissertation of Burca (*Burca 2012,*[200]), and in several publications (*Bleuet et al. 2008,*[50]; *Burca et al. 2011,*[201]; *van Langh et al. 2011,*[202]). The instrument IMAT, currently under construction at ISIS, is designed for combining neutron imaging and diffraction techniques, including Bragg edge imaging.(*Kockelmann et al. 2013,*[203])

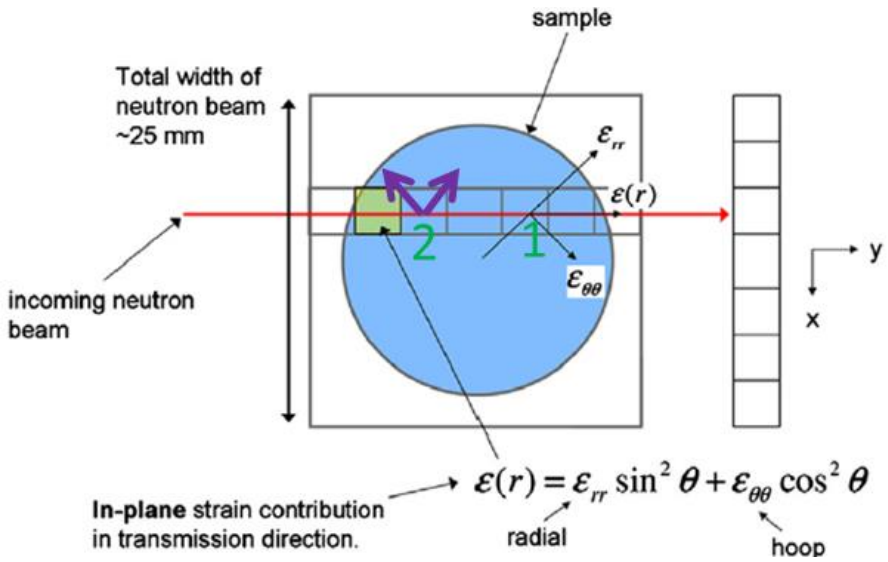

Figure 2-34. Abbey et al. showing the transmission strain components as a function of radial and hoop strains in an axisymmetric sample. *From* (*Abbey et al. 2012,*[193])

2.5 Recent Developments for Crystallographic Imaging

Even though not directly part of this dissertation, I would like to summarize some recent developments (mostly from synchrotron sources) that are relevant in in this context. On the one hand, when developing new methods, one needs to be aware of other methods that can be used to analyze similar problems. On the other hand, some of these methods could eventually be modified and integrated at neutron sources, as it has been case with grating interferometer for instance.(*Pfeiffer et al. 2006,*[93]) It should be noted that this summary is not intended to be a complete overview of existing crystallographic mapping techniques. For this I refer to the habilitation by Ludwig.(*Ludwig 2011,*[44])

Within the last few years, tremendous achievements have been made in the field of three dimensional microstructural characterizations. Especially promising techniques are currently available at synchrotron (X-ray) sources, namely three dimensional X-ray diffraction microscopy, 3DXRD (*Poulsen 2004,*[48]) , and Diffraction Contrast Tomography, DCT (*Ludwig et al. 2009,*[57]) Both methods allow mapping the 3D grain shapes and grain orientations within a polycrystalline sample and as such can be used to study complex processes, e.g. thermal treatments and mechanical deformation.(*King et al. 2008,*[51]) Using 3D-XRD and DCT, it is possible to simultaneously provide 3D information based on absorption contrast, such as cracks, porosities and other inhomogeneities. The methods are currently limited to samples exhibiting minimal orientation gradients inside the grains and a finite number of grains in the sampled volume, but ongoing developments in experimental setup and software analysis promise to further improve the capabilities. Efforts are currently being made for the implementation to laboratory x-ray sources.(*King et al. 2013,*[204])

In the following, the principle of DCT will be described (while it should be noted that 3D-XRD is very similar):

- DCT uses a conventional tomography setup and (at least until now) a monochromatic beam:

- It relies on Bragg diffraction from crystallographic lattice planes, following Bragg's law: $n\lambda = 2d_{hkl}\sin\theta^{B}$ (n = 1,2,3.. is the order of reflection, θ_l the Bragg angle, λ is the wavelength and d_{hkl} the lattice spacing).
- The (polycrystalline) sample is fully illuminated and rotated 360 degrees. During this rotation, the grains are occasionally orientated so that they fulfill the Bragg diffraction condition and hence a reduction in the intensity of the transmitted mono-energetic beam can be observed.
- The diffracted contribution (diffraction spot) of the beam is recorded by the same or a separate position-sensitive detector.
- By scanning over a range of 360 degrees, for every diffraction spot, also it's matching Friedel pair is recorded which is separated by 180 degrees. Detecting such Friedel pairs is the underlying principle of the currently used DCT technique at the ESRF. (Please note that this is a particular "trick" which leads to better stability of the analysis, but not necessarily needed.)
- The diffracted beam spots, as well as the direct ('extinction') spots, can be segmented and paired by means of digital image correlation and attributed to a single grain.
- The diffraction angles can be calculated from the intersection of several projection lines, knowing the diffraction spot position and geometry of the experimental setup, which can be used as a consistency-check and provide information about the crystallographic orientation.
- The grain volumes are reconstructed individually in a two-dimensional slice-by-slice approach (see Figure 2-35).
- A conventional absorption contrast tomography reconstruction from the direct beam part of the combined images can be performed for a single wavelength.

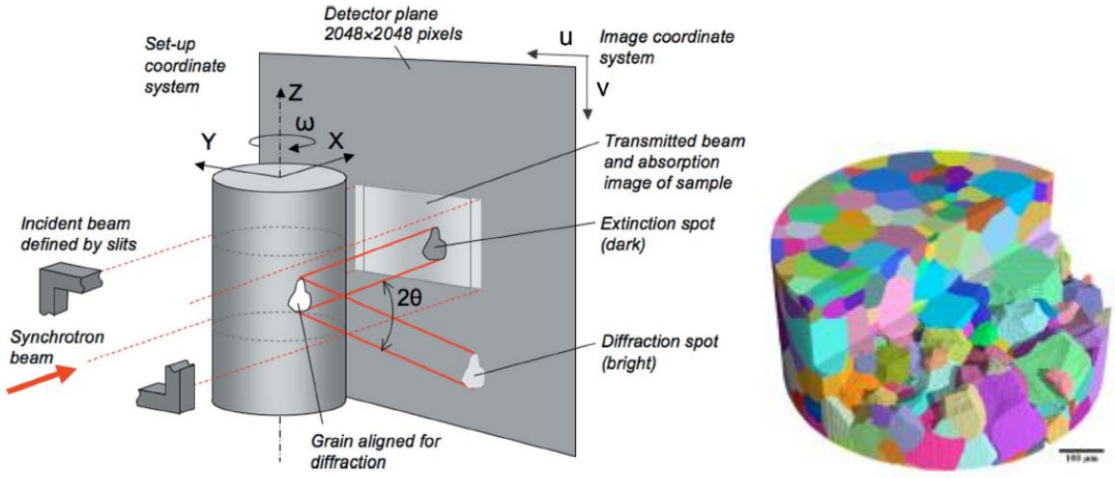

Figure 2-35. (left) Experimental setup, showing acquisition geometry, the sample and both diffracted and transmitted signal on one detector. *From* (*Johnson et al. 2008,*[205]) (right) Example result obtained by Ludwig et al. at the ESRF showing rendition of the 3D grain structure in a cylindrical beta-Ti specimen containing 1008 grains, as obtained by the DCT processing routine. The colors represent the grain orientation. *From* (*Ludwig et al. 2009,*[57])

As any other technique, DCT has certain limitations.

- For instance, the intergranular orientation spread inside a grain leads to the violation of the parallel projection approximation. It can also lead to breaking up a diffraction spots and hence pose a problem during image segmentation. According to most groups using DCT/3D-XRD, the orientation spread should be typically below 1°. The same problematic can be present for low angle grain boundaries, i.e. that 2 separate grains cannot be distinguished successfully. Defect density and/or imperfections can lead to similar problems as the diffracted signal may vary in intensity.
- The full beam illumination of the sample poses some restrictions regarding the grain size and sample size. In order to spatially reconstruct a grain, approximately >20x20 pixels are needed across a grain. The detector pixel size and # of pixels (typical CCD having 2048x2048 pixels) then dictate how large a sample (illumination area) can be and what the minimum grain size can be. By varying the energy, the diffraction angles can be varied, in order to prevent spot overlap. But obviously, a large sample

with very many grains will be similar to a powder sample and results in diffraction spots which will fill out the Debye Sherrer ring, so individual spots cannot be distinguished.

- Texture in the material can be problematic for the technique as it can also lead to spot overlap, since the diffraction signal is concentrated in certain areas. By illuminating smaller volumes and choosing an energy resulting in wider scattering angles, this situation can be improved.
- Highly attenuating materials, will of course lead to only a very weak diffraction signal leaving the sample and eventually resulting that the beam may not even reach all parts of the sample. This obviously poses significant problems for a successful reconstruction.

When considering to adopt the same methodology to a neutron source, one needs to ask the question what potential benefits could arise from that. Since neutrons interact with the nucleus (vs electrons for x-rays), they can penetrate several centimeters into most engineering materials and hence would be desirable for such a method. Neutron diffraction for instance is considered to be the only tool capable of strain measurements in the bulk of materials. Hence neutron-DCT could in principal fill this gap.

The main disadvantages with when using neutrons for this technique I see are:

- The diffraction angles are much wider and therefore more spread/separated than using high energy x-rays. There are no suitable detectors currently that provide simultaneously sufficient spatial resolution and angular coverage.
- The achievable spatial resolution is much lower than by x-rays. Even though some neutron imaging systems can reach below 10μm resolution, the Field of View will be very small and even less of the diffraction angle range can be covered.
- As mentioned, neutrons can penetrate deep into many engineering metals. But most of these materials typically have grain sizes on the order of a few to tens of micrometers, i.e. a sample of a few millimeters in size already has thousands or ten-thousands of grains. These kinds of samples can still be investigated using x-rays

and the limit in sample size is mostly determined by the number of grains, rather than the penetration depth.

- The available neutron flux is much lower than flux at a synchrotron resulting in much longer counting times.

Nonetheless, the implementation end exploration of neutron based DCT/3D-ND is desirable in my opinion, as it could be used as a complementary tool – for example for certain materials that are too attenuating using x-rays. Moreover it could boost the development of related techniques, for example spatially resolved bulk texture measurements. It should be noted that efforts have already been undertaken within the framework of this dissertation, and a set of experiments was performed at NIST in September 2012 and at CONRAD in January 2013. The group at PSI has published the reconstruction of grains in an AL sample by neutron-DCT (*Peetermans et al. 2014,*[206]), and also the current PhD project of Alberto Cereser at the Technical University of Denmark is concerned with this topic.

Chapter 3

Neutron Bragg Edge Imaging at a Reactor Source: Strain Mapping using a Monochromator

This chapter is written based on a journal paper published by Robin Woracek et al. (*Woracek et al. 2011,*[207]):

> R. Woracek, D. Penumadu, N. Kardjilov, A. Hilger, M. Strobl, R. C. Wimpory, I. Manke, J. Banhart, "Neutron Bragg-edge-imaging for strain mapping under in situ tensile loading". Journal of Applied Physics 109, 093506 (2011).

As the first author, my primary contributions include (1) proposing the study and identifying its importance, (2) design and conducting the experiments, (3) data analysis and interpretation, and (4) writing the paper.

Abstract:

Wavelength selective neutron radiography at a cold neutron reactor source was used to measure strain and determine (residual) stresses in a steel sample under plane stress conditions. We present a new technique that uses an energy-resolved neutron imaging system based on a double crystal monochromator and is equipped with a specially developed (in-situ) biaxial load frame to perform Bragg edge based transmission imaging. The neutron imaging technique provides a viewing area of 7 cm by 7 cm with a spatial resolution on the order of ~ 100 μm. The stress-induced shifts of the Bragg edge corresponding to the (110) lattice plane were resolved spatially for a ferritic steel alloy A36 (ASTM international) sample. Furthermore it is demonstrated that results agree with comparative data obtained using neutron diffraction and resistance based strain-gauge rosettes.

3.1 Introduction

Besides traditional neutron imaging (based on attenuation contrast) of materials several additional methods have recently evolved, e.g. phase contrast (*Allman et al. 2000,[92]; McMahon et al. 2003,[208]; Kardjilov et al. 2004,[147]*), differential phase contrast (*Treimer et al. 2003,[146]; Strobl et al. 2004,[209]; Pfeiffer et al. 2006,[93]; Strobl et al. 2007,[149]*), dark-field imaging (*Strobl et al. 2004,[142]; Grünzweig et al. 2008,[150]; Strobl et al. 2008,[94]*) and imaging with polarized neutrons (*Kardjilov et al. 2008,[95]; Strobl et al. 2009,[210]; Schulz et al. 2010,[211]; Strobl et al. 2011,[212]*). Energy selective neutron imaging opens possibilities to exploit the Bragg edges of crystalline materials and reveal microstructural information related to the lattice spacing, such as phase, texture and strain.(*Kardjilov et al. 2003,[213]; Treimer et al. 2006,[125]*) Neutron diffraction instruments at spallation sources have been used to investigate the transmission spectrum and the observed Bragg edge was used for strain mapping.(*Vogel 2000,[3]; Santisteban et al. 2001,[179]; Steuwer et al. 2001,[168]; Santisteban et al. 2002,[96]; Santisteban et al. 2002,[167]; Steuwer et al. 2003,[23]; Kockelmann et al. 2007,[181]*) A new technique to evaluate elastic strain components, using an established neutron imaging instrument at a reactor source in combination with a monochromator device, will be presented in this paper. The method has the potential to be a powerful tool to perform spatially resolved 2-D phase or strain mapping and opens up possibilities of phase/strain tomography and texture studies as well.(*Steuwer et al. 2005,[174]; Abbey et al. 2009,[192]*)

The transmission spectrum of neutrons in the thermal to cold energy range through a (poly-) crystalline sample shows a sharp increase at certain wavelengths. The position of these so called “Bragg Edges” is directly related to the lattice spacing d_{hkl} and therefore the method is suited for strain measurements.(*Vogel 2000,[3]; Santisteban et al. 2001,[179]; Steuwer et al. 2001,[168]*) Compared to the well-established diffraction technique, this imaging method can provide data for large areas simultaneously, while measured strains are integrated over the sample thickness. According to Bragg’s law, $n\lambda=2d_{hkl}\sin\theta$ (Equation 3.1), neutrons at a wavelength λ are coherent-elastically scattered from lattice planes with distances d_{hkl}, which are aligned at an angle θ to the incoming neutron beam, in directions with scattering angles of 2θ. For a particular *hkl*, the scattering angle increases as the wavelength is

increased until 2θ=180° (backscattering towards the source). This is reached at $\lambda=2d_{hkl}$ and for wavelengths larger than this value, no more scattering from this plane can occur, resulting in a sharp increase of transmitted intensity. Strains can be determined as $\varepsilon = (d_{hkl} - d^0_{hkl})/ d^0_{hkl}$ (Equation 3.2) with d^0_{hkl} as the unstrained or reference state lattice parameter.
Several dedicated neutron radiography/tomography instruments at steady state sources can readily provide spatial resolutions on the order of or smaller than 50 µm(*Lehmann et al. 2007,[214]; Boillat et al. 2008,[215]; Kardjilov et al. 2009,[124]; Strobl et al. 2009,[53]*) and therefore implementation of energy selective Bragg edge imaging techniques could open many new applications. Current improvements at the Helmholtz Zentrum Berlin (HZB) will lead to much higher spatial resolutions using cold neutrons and, therefore, even microstructural features such as phase differences and/or precipitates could possibly be visualized in the future.
In principle there are two possibilities to do such energy dependent measurements at a reactor source: (a) using the time-of-flight information in distance from the source using a specifically designed chopper system or (b) selection (or suppression) of neutrons from specific spectral parts.(*Lehmann et al. 2009,[132]*) In the latter case the wavelengths can be selected by a velocity selector, the "slit method" or a wavelength tunable device, e.g. a double crystal monochromator.(*Tamaki 2005,[216]; Treimer et al. 2006,[125]; Lehmann et al. 2009,[132]*) Using different settings or crystals allow selection of a very narrow spectral part, but one should keep in mind that the flux decreases as a narrower wavelength band is selected. In this case a double crystal monochromator is used and has been reported previously by Treimer et al. (*Treimer et al. 2006,[125]*).

3.2 Experimental Approach

The CONRAD instrument at HZB was used to obtain the location and stress induced shifts of the Bragg edge corresponding to the (110) lattice plane of a BCC steel sample (A36 ASTM international) under well-known 2-D stress conditions. A portable mechanical loading system (Figure 1) has been designed for the purpose of these experiments, especially suited for transmission imaging and tomography. The system offers an axial force capacity

of 0-50 kN and a torque range of 0-12 Nm. The system offers a custom developed Graphical User Interface with stress, strain and deformation controls.

Because of the selected sample dimensions (gauge length: 21.72mm, gauge width: 10mm, thickness: 1.46mm; Figure 1b), a 2-D state of stress and hence strain can be assumed. This has been verified calculating the principal strains using a rosette strain gauge and applying uni-axial loading in tension (in *z*-direction, hence $\gamma_{xy} = 0$) and torsion ($\varepsilon_x = \varepsilon_y = 0$). Strain in the measured direction using Bragg edge shifts can be therefore attributed purely to Poisson strain. The average grain size of the sample was 25 micrometer.

The energy selectivity at the CONRAD instruments was achieved by using a double-monochromator consisting of one pyrolytic graphite crystal (PCG) monochromator in the upper and lower position, each with a mosaic spread of 0.8°. The wavelength band has an approximate resolution of $\Delta\lambda/\lambda$=3% and can be tuned freely between 2.0 and 6.5 Å while the beam position remains unchanged. The approximate flux at the sample position is 2×10^4 $cm^{-1}s^{-1}$. The position of the Bragg edge at ~ 4.05 Å, corresponding to the (110) lattice plane (d_{110} = 2.02695 Å), was investigated as it is the most pronounced and the neutron flux is still reasonably high (peak flux at ~ 3 Å).

Transmission measurements were performed at four different states of stress: (i) unloaded as reference measurement to determine the unstressed lattice parameter d^0_{hkl} (S1) (ii) elastic deformation at 90% of yield strength, i.e. 200MPa (S2) (iii) plastic deformation (S3) (iv) unloaded after previous plastic deformation (S4). (Figure 3-2) The tensile test was performed in deformation (PID) control to not introduce any creep behavior over the measurement time, using a maximum deformation rate of 0.5mm/min. At each state of stress, 21 transmission measurements between 3.8 and 4.2 Å with a step size of 0.02 Å were performed. The exposure time for each transmission measurement was chosen to be 15min (+15 min for Flat-field measurement) to minimize signal to noise ratio, resulting in approximately 10.5 hours count time for one stress state.

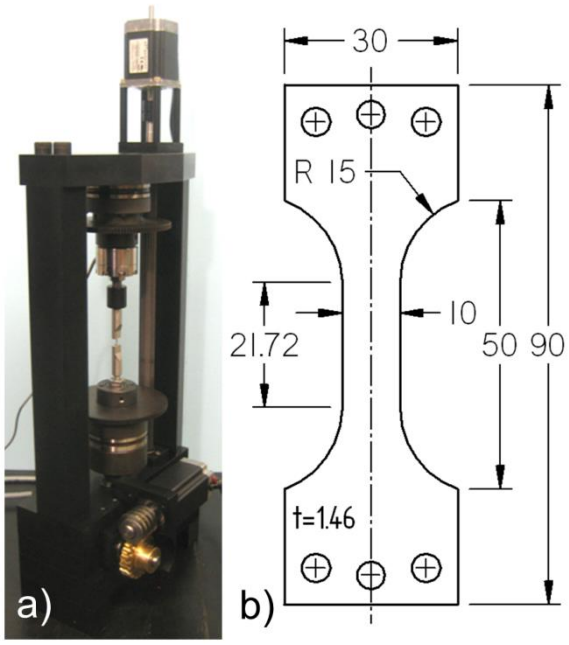

Figure 3-1. Portable loading system b) Specimen dimensions in mm.

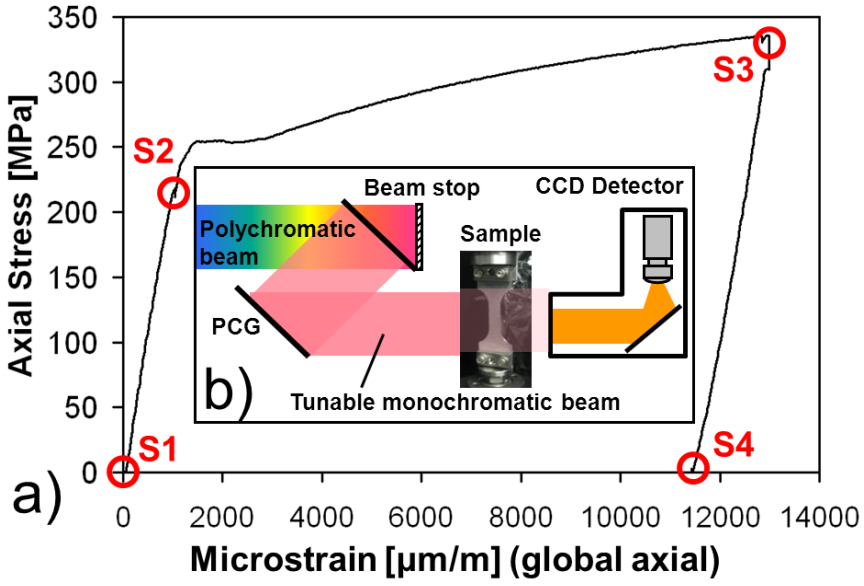

Figure 3-2. a) Recorded stress-strain curve of tensile test b) Schematic sketch of CONRAD (inset).

Figure 3-2 shows the stress-strain curve recorded during the experiment at CONRAD, and due to the long holding time some relaxation ("stress drop") is visible at stress state S3 (and also very minimal at stress state S2).

The exact same type of sample (machined from the same batch) was used for measurements undertaken at the E3 Diffractometer. The tensile test has been performed with the same equipment and same parameters as at the CONRAD instrument, only but with more stress states being measured (12 stress states total, while stress state at 90% of yield strength was measured twice). Several spatial locations along the specimen axis have been measured with a gauge volume of 2x2x2mm^3 while the count time for one point was 20 minutes. The reader should note that the data presented herein was obtained for the (220) lattice plane, which represents lattice strains for the (110) lattice plane.

3.3 Results

The (macroscopic) Poisson strain at the yield point (250MPa) for the investigated material is 325 με, which corresponds to a Bragg peak shift of 0.0013 Å, while for engineering applications it is important to quantify strain with a precision of 50 to 100 με. To obtain the position of the Bragg edge for each pixel or spatial location, a curve routine was implemented using the non-linear least-squares method. The derivative of the transmission profile was taken and a Gaussian fit applied, where the center of the Gaussian (A1) represents the location of the Bragg edge. (See Equation 3.1)

$$f(x) = A_0 e^{\frac{-\left(\frac{x-A_1}{A_2}\right)^2}{2}} + A_3 \tag{3.3}$$

In this notation, A0 corresponds to the height of the Gaussian while A2 is the width (standard deviation) of the Gaussian and A3 stands for the constant term. Based on the signal-to-noise ratio of intensity versus d-spacing data, we found it necessary to perform additional spatial binning of pixels in order to determine the edge position with the required precision. This was necessary due to (relative) short exposure times implemented

in our experiments to develop the measurement technique. By pixel binning, the edges of the sample are spatially smeared out and a widening of the edge is introduced when binning pixels in the *y*-direction due to small wavelength variations along the height of the neutron beam. This is a known artifact of the double crystal monochromator setup and special care must be taken if the reference lattice parameter is obtained from a different sample (at a different position in the neutron beam path). The resulting pixel size was 2.7 mm, but longer count times and/or higher intensities are expected to lead to significant improvements of the spatial resolution possible with our technique. Also the thin specimen geometry, and therefore resulting thin diffracting gauge volume, should be noted.

The results show general agreement with expected strain values from elasticity theory and good agreement with experimental diffraction-based results, performed at the Residual Stress Analysis and Texture Diffractometer E3 at HZB, all within a variation of less than ±60με. Figure 3.3 shows the transmission profile for one pixel in the gauge center (2.7 mm pixel size after binning) as well as its derivative and fitted function for stress state S1. It also shows the fitted Gaussian curve for stress state S2 (dotted line) corresponding to the same pixel and the reader should note the shift of peak position (see also inset Figure 3.3). The interpreted strain therefore is derived from the combination of measured experimental data and the approach identified in equation 3.3 for locating the peak position of different stress states. As is common with residual stress mapping facilities one can significantly improve the ability to measure d-spacing shifts much smaller than the available wavelength resolution $\Delta\lambda/\lambda$ with the option of using peak fitting technique. It is now routine that diffraction based instruments measure lattice strains smaller than 50με. The reader should note that detectable d-spacing resolution is not defined just by wavelength band of the monochromator, but rather by the detectable diffraction peak (or shift of diffraction peak) of the sample.

The strain for each pixel, derived from the difference of the edge position in the stressed (S2, S3) and post-stressed condition (S4) to the unstressed condition (S1), is visualized in Figure 3.4. One can note easily the differences between the stress states. The strains within the gauge area are uniform, while they are lower above and below it, corresponding to the

tapered section. This is to be expected. Figure 3.5 presents the strains at the three stress conditions along the height of the specimen, pixel 0 corresponding to location at the bottom and pixel 19 at the top of the sample. Figure 3.6 compares transmission and diffraction-based results for the same location in the specimen center (while the diffracting gauge volume was chosen as 2 x 2 x 2 mm^3). The error bars of the reported transmission data included in Figure 3.5 and 3.6 correspond to two standard deviations of all horizontal pixels in the same line, which are expected to have the same strain due to plane stress condition. The determined strain values from both techniques agree with each other within the uncertainties of the experimental errors. A similar agreement was found in other locations along the specimen's height. The dotted black straight line indicates the macroscopic elastic response (E=200GPa, ν=0.26). It is expected from literature that the elastic response specific to the (110) plane of Fe^{α} behaves slightly different from that (*Hutchings et al. 2005,*[1]) (E=210.5GPa, ν=0.25; indicated by straight blue dashed line). The experimentally determined values at E3 lie within these expected values for applied stress magnitudes smaller than 90% of the yield point. The decrease of strain magnitude for the repeatedly measured stress state at 200MPa could indicate that relaxation has occurred as more time has passed. This would also explain why the strain value of the transmission based result for stress S2 is relatively low, as the holding point has been even longer.

This work demonstrates first experiments that show the ability to do quantitative and spatially resolved strain radiography even with moderate fluxes at a reactor source. This technique could be useful for investigating typical plane stress problems using very small gauge volumes corresponding to pixel size and/or become a complementary tool for traditional diffractometers. It should be noted that the possibility of using very small gauge volumes is of course not only dependent on the technique itself, but also on the samples grain size, texture and microstructural properties. Moreover the technique can be applied to texture and phase analysis in the future. Future improvements leading to better spatial resolution and shorter count times are planned with improved monochromators and brighter sources.(*Strobl 2009,*[217])

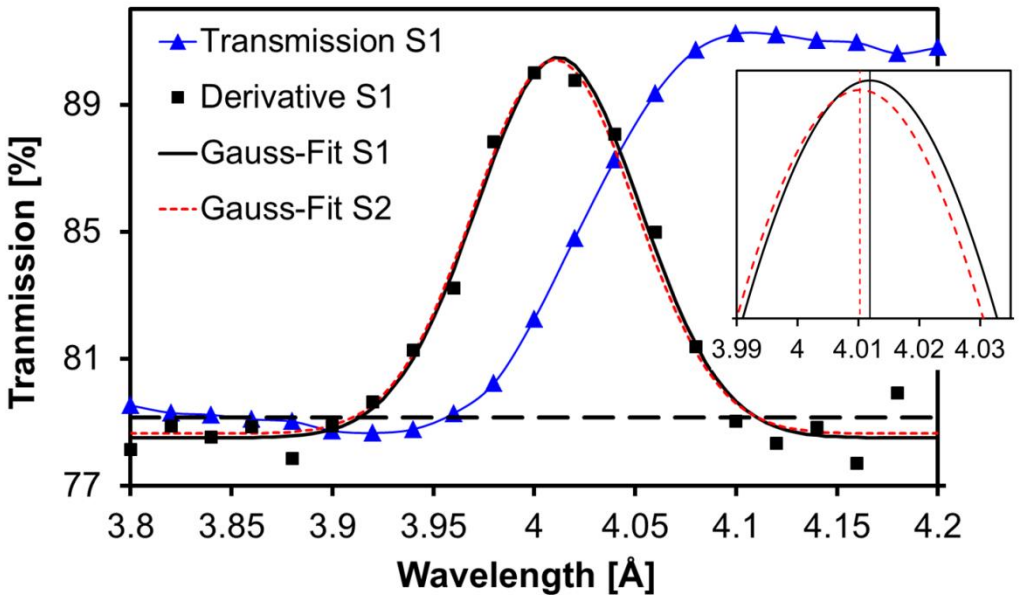

Figure 3-3. Bragg edge Transmission profile, Derivative and Gauss-Fit (one pixel).

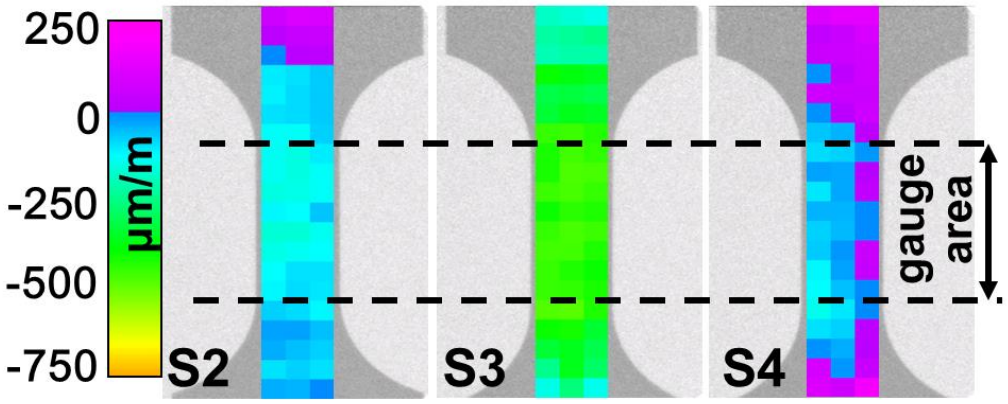

Figure 3-4. Map of Transversal Strains obtained by radiography.

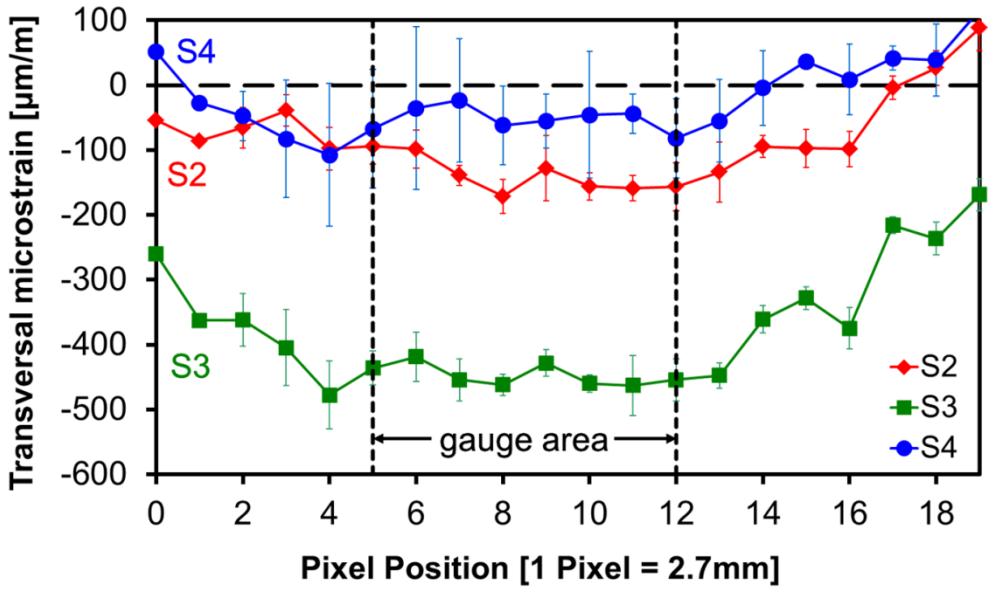

Figure 3-5. Transversal strains along the specimen height for investigated stress states.

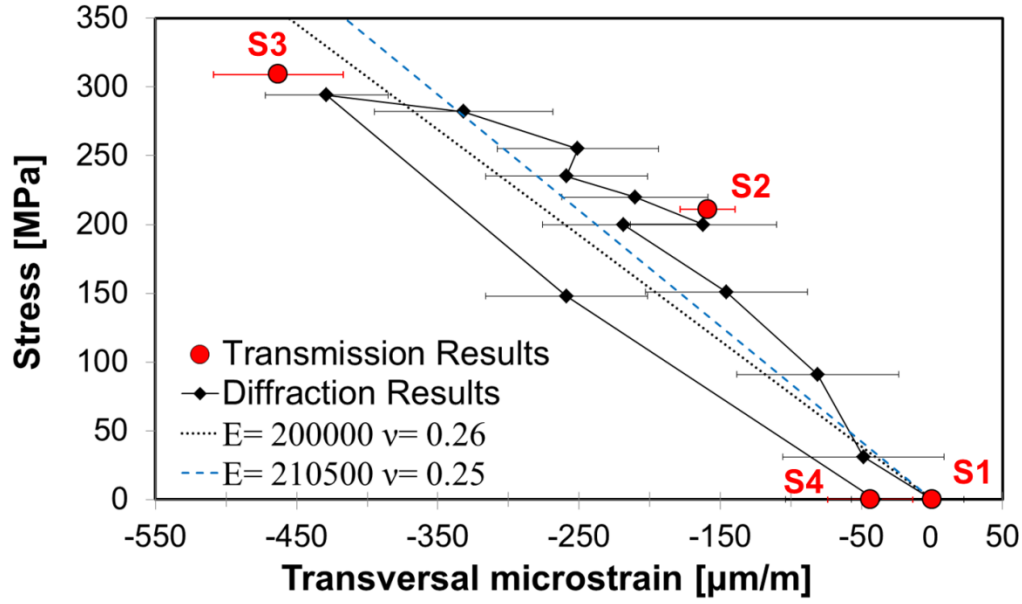

Figure 3-6. Comparison with Diffractometer results.

Chapter 4

Neutron Bragg Edge Imaging at a Reactor Source: Strain Mapping using the Time-Of-Flight Method

This chapter is written based on a paper published by Markus Strobl, Robin Woracek et al. (*Strobl et al. 2012,*[218]):

> M. Strobl, R. Woracek, N. Kardjilov, A. Hilger, R. Wimpory, A. Tremsin, T. Wilpert, C. Schulz, I. Manke, D. Penumadu, Time-of-flight neutron imaging for spatially resolved strain investigations based on Bragg edge transmission at a reactor source. Nuclear Instruments and Methods in Physics Research Section A: Accelerators, Spectrometers, Detectors and Associated Equipment 680, 27-34 (2012).

As the first author, Markus Strobl proposed the experiment and was the beamline scientist at the BioRef instrument. As the second author, my primary contributions include (1) design and conducting the experiments (in cooperation with Markus Strobl), (2) data analysis and interpretation, and (3) writing the paper (in cooperation with Markus Strobl).

Abstract:

Energy dependent neutron transmission imaging has recently gained attention for the potential to spatially resolve texture, crystallographic phase and lattice strain. Especially promising is the time-of-flight (TOF) approach that takes maximum advantage of the new generation of pulsed spallation neutron sources, such as SNS, JSNS and ESS. In this paper, the authors demonstrate the feasibility to efficiently apply the TOF approach at a continuous source in order to spatially resolve and quantify the (lattice) strain distribution in a flat steel sample under tensile loading. Although transmission-based TOF imaging for strain mapping at a pulsed source are well published, this work is the first attempt to demonstrate such measurement using choppers at a continuous neutron source. A critical component for spatially resolved TOF imaging is the availability of a high spatial resolution imaging detector, capable of the required time resolution. For the herein presented work, a conventional 2D position-sensitive ^{3}He detector with a spatial resolution of 2 x 3 mm^2 has been used for proof-of-principle measurements. The results are compared to conventional lattice strain measurements obtained at an engineering neutron diffractometer, where the same mechanical loading system was utilized. The efficiency of the time-of-flight

transmission method is discussed with respect to other methods, at continuous as well as at pulsed sources.

4.1 Introduction

The work presented here builds on the authors' previous research and is a continuation of neutron imaging experiments reported earlier (*Strobl et al. 2011,*[182]), where time-of-flight neutron imaging was performed at a reactor source using a scintillator CCD imaging detector. In this recent publication the general potential of energy dispersive (resolved) imaging to resolve microstructural features related to Bragg edges as well as the experimental methods for the realization and corresponding efficiencies have been discussed. Therefore, these points will only briefly be summarized within this paper, while the focus is on recent Bragg edge transmission-based lattice strain measurements, carried out at the continuous neutron source of Helmholtz Zentrum Berlin (HZB). Based on the results of this present study, the potential of the time-of-flight (TOF) method for strain measurements using neutron imaging methods (*Strobl et al. 2009,*[53]; *Strobl et al. 2011,*[219]), especially at continuous sources, will be discussed.

In contrast to conventional thermal or cold neutron imaging where a broad energy spectrum is used in favor of high flux densities and corresponding short exposure times, energy dispersive imaging additionally probes the energy dependence of the sample attenuation. By using such wavelength dependent Bragg edge transmission measurements, detailed information about the structure of crystalline materials, which is related to the elastic coherent scattering cross-section, can be derived and is of significant interest to the materials science and engineering community. Prominent applications and proof-of-principle measurements, both at pulsed as well as at continuous sources, are published in the literature which include the determination of phases (*Vogel 2000,*[3]; *Santisteban et al. 2002,*[167]; *Steuwer et al. 2004,*[173]; *Steuwer et al. 2005,*[174]; *Treimer et al. 2006,*[125]), texture corresponding to a preferential orientation of crystals present in a material (*Santisteban et al. 2006,*[176]; *Iwase et al. 2007,*[177]; *Kockelmann et al. 2007,*[181]; *Santisteban et al. 2011,*[184]), and strain (*Santisteban et al. 2001,*[179]; *Steuwer et al. 2001,*[168]; *Santisteban et al. 2002,*[96]; *Steuwer et*

al. 2003,[23]; Woracek et al. 2011,[207]; Iwase et al. 2012,[180]). Especially challenging is the approach of spatially resolved strain measurements in imaging geometry (*Santisteban et al. 2001,[179]; Steuwer et al. 2001,[168]; Santisteban et al. 2002,[96]; Steuwer et al. 2003,[23]; Tremsin et al. 2009,[129]; Tremsin et al. 2010,[130]; Strobl et al. 2011,[182]; Tremsin et al. 2011,[107]; Woracek et al. 2011,[207]*) with the perspective of strain tomography in selected cases (*Abbey et al. 2009,[192]*). Compared to other applications of energy dispersive imaging, strain investigations, especially when meant to compete with state-of-the-art strain scanning diffractometers, require high energy resolution (*Strobl 2009,[217]*), i.e. wavelength resolutions of the order of $\Delta\lambda/\lambda < 10^{-2}$.

Conventional strain neutron diffractometers record the diffraction peaks in scattering geometry, i.e. the diffracting crystallites lie with their *hkl* planes at the Bragg angle of θ^B_{hkl} with respect to the incident beam, and the diffracted beam is detected at an angle of $2\theta^B_{hkl}$ (ideally equal or close to 90°), described by the Bragg condition

$$n\lambda = 2d_{hkl}\sin\theta^B \qquad (4\text{-}1)$$

in which n = 1,2,3.. is the order of reflection. At continuous sources, one usually uses a monochromatic incident beam and measures the position of the scattering angle $2\theta^B_{hkl}$.(*Hutchings et al. 2005,[1]*) At spallation sources, a single time pulse contains a continuous spectrum of wavelength and one can determine the wavelength of each detected neutron by its time-of-flight (TOF) t_{TOF}.(*Hutchings et al. 2005,[1]*) Both approaches allow precise determination of the crystal lattice plane d-spacings d_{hkl}, due to wavelength and angular resolution. At continuous sources only one lattice plane d-spacing is usually probed at a time, chosen by monochromator and detector orientation, while the TOF approach allows to probe several lattice plane d-spacings simultaneously.

In energy dispersive measurements in transmission geometry, i.e. the detection angle corresponds to a "back-scattering" angle of $2\theta^B_{hkl} = 180°$, the most significant signal is given for $\theta^B_{hkl} = 90°$. At wavelengths larger than $\lambda = 2d_{hkl}\sin90° = 2d_{hkl}$, Bragg scattering for the corresponding lattice planes *hkl* cannot take place, and hence, the transmitted intensity

increases drastically. These features are referred to as Bragg edges. Obviously, any change in d_{hkl} would shift the Bragg edge correspondingly, and consequently, strains along the beam direction ($\theta^{B}_{hk} = 90°$) can be resolved if only the wavelength resolution is sufficient.

In analogy to the influence of angle and wavelength resolution onto the observed diffraction peak width when using a diffractometer device, the wavelength resolution influences the detected width of the Bragg edge in energy dispersive imaging. Using fitting algorithms, the diffraction peak and Bragg edge positions (along with all other profile parameters), respectively, can be extracted with a significantly higher accuracy than given by their actual width, the resolution defined by the corresponding full width at half maximum (FWHM) can be relaxed significantly as compared to the measured strain values. The counting statistics naturally influence the accuracy of such determination. In the case of a fixed source flux, the accuracy can be increased even if the wavelength resolution is reduced, when the counting times are increased accordingly.

The wavelength resolution is defined by the means of monochromatization for monochromator-based devices and by the ratio of the burst time τ to the time-of-flight t_{TOF} from the pulse source to the detector for TOF methods. Additionally, the time resolution of the available detector system utilized for a specific TOF measurement can have a significant impact on the achievable accuracy of peak and edge determination. Therefore, the intrinsic time resolution of the detector has to be better than the required burst time for a specific resolution requirement. Different approaches of energy resolution for such imaging-based purposes, their capabilities, limitations and efficiencies at continuous and pulsed sources are discussed extensively in the references (*Treimer et al. 2006,[125]; Lehmann et al. 2009,[132]; Strobl et al. 2011,[182]; Woracek et al. 2011,[207]*).

4.2 Instrument and Experimental Setup

4.2.1 TOF Instrumental Setup

Strain measurements in imaging geometry have been performed at the V18 BioRef instrument (*Strobl et al. 2010,[127]; Strobl et al. 2011,[220]*) of the University of Heidelberg at the

BERII reactor neutron source of the Helmholtz-Zentrum Berlin für Materialien und Energie in Berlin (Fig. 1). BioRef is a TOF reflectometer with a versatile chopper system consisting of three disk choppers. The first two choppers are operated in an optical blind mode (*Van Well 1992,*[126]), which allows for choosing a constant wavelength resolution for the utilized wavelength band by setting corresponding distances z_0 between the choppers. For that purpose the second chopper is placed on a remotely controlled linear translation stage that enables selection of distances z_0 between 80 mm and 400 mm, which correspond to constant wavelength resolutions:

$$\Delta\lambda/\lambda = \tau(\lambda)/t_{TOF}(\lambda) = \text{const.} = z_0/L \qquad (4\text{-}2)$$

of 1% to 5% for the instrument length of L = 8m from the first chopper to the detector. Here $\tau(\lambda)$ and $t_{TOF}(\lambda)$ are the wavelength dependent burst time given by the optical blind chopper configuration and the wavelength dependent flight time given by $t_{TOF}=\lambda mL/h$, where m is the mass of the neutron and h the Planck constant, respectively. However, Equ.(2) holds only up to the wavelength

$$\lambda_0 = hw/(360 \cdot m z_0 f) \qquad (4\text{-}3)$$

as a function of the window width w [deg], the chopper distance z_0 and the chopper frequency f (*Van Well 1992,*[126]). A third chopper 3.22 m downstream acts as a wavelength band chopper that limits the wavelength band at or well below λ_0. Additionally, the wavelength band chopper allows for running the chopper system at different frequencies, and thereby, to efficiently utilize a certain limited wavelength range without risking frame overlap (*Strobl et al. 2010,*[127]; *Strobl et al. 2011,*[220]).

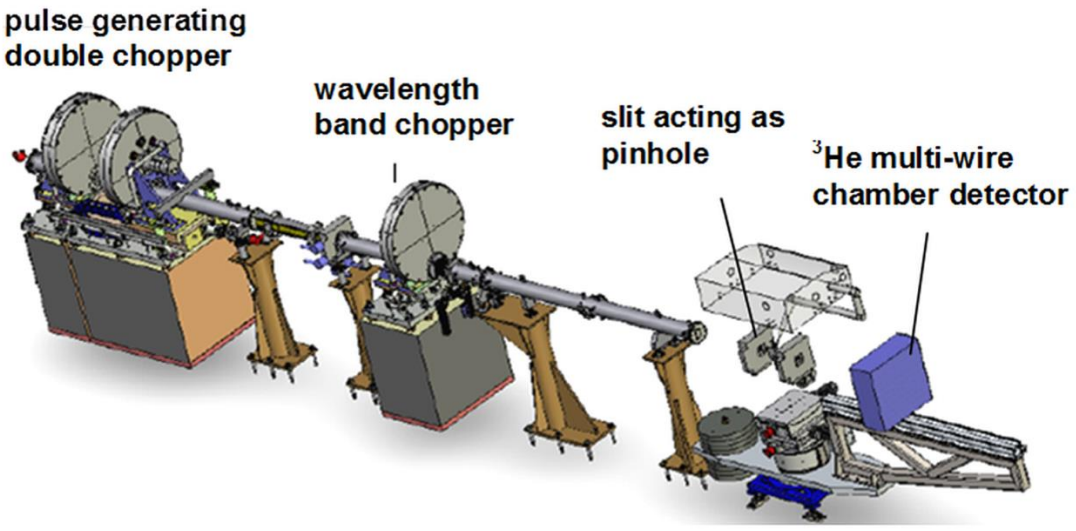

Figure 4-1. BioRef, a versatile TOF reflectometer used for TOF imaging in the presented work, to record Bragg edge transmission spectra. The instrument consists of an optically blind double chopper system (left) by which the resolution can be tuned through changing the distance between these choppers. Another chopper (middle) allows the system to define the utilized wavelength range. The first of the two slits (right) has been used as a "pinhole" to achieve spatial resolution for the herein presented measurements (while the second slit was fully opened). The sample has been placed in front of the detector (right, blue) which was placed at the very end of the support arm.

For the strain measurements of a steel alloy performed in transmission geometry in this study, our measurement focus was on the most pronounced Bragg edge of the sample material, i.e. the Bragg edge at ~4.05 Å, corresponding to the (110) lattice plane of bcc Fe, with the maximum achievable wavelength resolution. Consequently, the smallest nominal distance z_0 = 80 mm and the highest nominal frequency f = 90 Hz of the instrument have been chosen. These values correspond to a wavelength resolution of $\Delta\lambda/\lambda$ = 1% and a wavelength band width of 4.4 Å from approximately 3.1 to 7.5 Å. These values are significantly bigger than the optimum for the present purpose, i.e. a better wavelength resolution and a shorter wavelength band would have increased the accuracy and the efficiency, respectively. However, we need to keep in mind that BioRef has not been

optimized for transmission-based Bragg edge imaging and it was used to demonstrate a principle of such measurement at a reactor source for the first time. Corresponding details will be further discussed later in this paper.

4.2.2 Detector System

The availability of a detector system with combined high spatial and temporal resolution capabilities is essential for the realization of TOF imaging approaches (*Strobl 2009,[217; Tremsin et al. 2009,129; Tremsin et al. 2010,130; Strobl et al. 2011,182; Tremsin et al. 2011,107; Tremsin et al. 2012,221*). The standard detector of the BioRef instrument, which is a 2D position sensitive ^{3}He multi-wire chamber (DENEX GmbH) with delay line electronics and an active area of 30 x 30 cm^2 (*Strobl et al. 2011,[220]*), has been used for the imaging experiments. The spatial resolution of such detectors is about 2 x 3 mm^2, which is far worse than that of standard lens coupled CCD imaging detectors (reaching spatial resolutions better than 25 µm) (*Van Well 1992,[126; Lehmann et al. 2007,214; Kardjilov et al. 2009,124; Strobl et al. 2011,220]*). However, in contrast to standard imaging detectors, the ^{3}He detector provides high time resolution on the order of a few µs with far superior detection efficiency, which is essential for corresponding TOF measurements. Few detector systems are able to provide such time resolution while simultaneously offering spatial resolutions on the order of what conventional imaging detectors can provide (*Lehmann et al. 2007,[214; Kardjilov et al. 2009,124; Tremsin et al. 2011,107]*). However, a spatial resolution of 2 x 3 mm^2 is readily achievable using slits or radial collimators to obtain target gauge volumes at engineering neutron diffractometers used for strain investigations.(*Fitzpatrick et al. 2003,[65; Hutchings et al. 2005,1]*) Due to flux limitations in earlier proof-of-principle measurements, significantly better spatial resolution could not be achieved even when higher spatial resolution detectors were available (*Kockelmann et al. 2007,[181; Tremsin et al. 2009,129; Woracek et al. 2011,207]*). The work presented herein also focuses on establishing a proof-of-principle, in order to evaluate the effectiveness of corresponding measurements at continuous sources using multiple chopper systems. Additionally, the ^{3}He detector provides high efficiency for cold neutron detection. In the present research, the neutron

image data was read out for a view area corresponding to 90000 mm^2 using 512 x 512 spatial and 1024 time channels. These correspond to spatial pixel size of approximately 0.6 x 0.6 mm^2 and time bins of 10.8 μs, which was more than sufficient for the given task. The time resolution of the detector is limited by the number of time channels used and the width of the time histograms for a repetition time of 11.1 ms corresponding to 90 Hz chopper frequency.

4.2.3 Instrumental Setup for Imaging

A suitable neutron beam pin-hole geometry is essential to enable neutron imaging with a target spatial resolution. For the present experiments, cross-slits with desired opening size and shape (rectangular in this study), positioned at 2.5 m upstream of the detector position, have been employed to act as a pinhole. The spatial resolution that can be achieved in an imaging experiment is defined by the image blurring *d* due to beam divergence, as defined by the L/D ratio, which can be expressed as:

$$d = l/(L/D) \tag{4-4}$$

In the above equation, *l* is the sample to detector distance, *L* is the distance between the pinhole and the sample, and *D* represents the pinhole opening size, which means that at smaller L/D, the image blur *d* will increase. In an optimum case, i.e. for maximum efficiency without excessive reduction of the spatial resolution, the blur should match the intrinsic spatial detector (or any sufficient looser) resolution. Consequently, with the imaging conditions used in the present study, L = 2500 mm, l = 150 mm and the horizontal and vertical detector resolutions of 2 mm and 3 mm, respectively, the optimum pinhole size is calculated to be 33 x 50 mm^2. This matches the cross section of the guide upstream of the slits. However, in order to protect the detector of the reflectometer from potential damage through long-term exposure to high flux of neutrons (required for transmission-based Bragg edge imaging), the slit opening was reduced to limit the flux density to desirable limits suitable for ensuring detector safety. The vertical slit was set to size of 50 mm and a horizontal slit provided an opening of only 1.4 mm, which corresponds to a horizontal L/D of 1800. Consequently, when we discuss the efficiency of the measurement in a section

later in the paper, the corresponding flux reduction of more than an order of magnitude that was readily available to make measurements has to be taken into consideration.

4.2.4 Sample Environment and Sample

Sample environment:

A special in-situ mechanical testing system, developed at the University of Tennessee (*Woracek et al. 2009,*[222]*; Woracek et al. 2011,*[207]), was used to apply pure tension to a steel alloy sample. This portable mechanical loading system (Figure 2) has been specifically designed for the purpose of in-situ imaging, tomography and diffraction experiments. The system offers an axial force capacity range of 0-50 kN and a torque range of 0-12 Nm, while it can be used for combined axial-torsional loading to simulate realistic multi-axial loading conditions. The deformation rate can be controlled accurately and the specimen can be rotated 360 degrees while under target stress state. The system offers a custom-developed Graphical User Interface using LabView with stress, strain and deformation PID-controls, which was linked to the control software of the BioRef instrument.

Sample considerations:

A (thin) plate sample geometry has been chosen which, under uni-axial tension, yields a plane state of stress, i.e. there are no stresses present in the z-direction (Fig. 3). The stress tensor for plane stress can be written as:

$$\sigma_{ij} = \begin{bmatrix} \sigma_x & \tau_{xy} & 0 \\ \tau_{xy} & \sigma_y & 0 \\ 0 & 0 & 0 \end{bmatrix} \tag{4-5}$$

In a pure tensile test, the principal stress/strain directions are along the *x*- and *y*-axis of the sample (Fig. 3), hence stress along the axial direction is σ_y and stress in the transverse in-plane direction is σ_x.

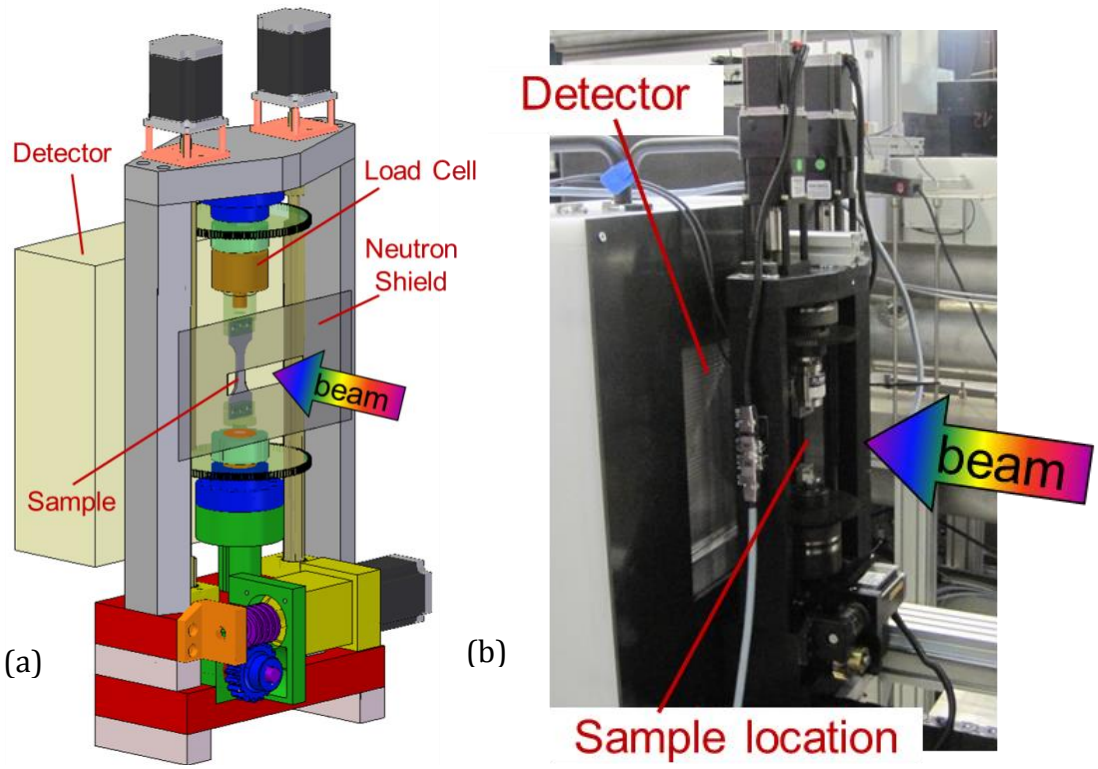

Figure 4-2. (a): Configuration of the sample and sample environment – a portable mechanical loading system – in a CAD model. (b): Photograph of the actual setup on the BioRef instrument.

Proper alignment of the sample in the testing system, premise for the previous assumptions, was verified by inferring the principal strains from measurements obtained with resistance based rosette strain gauges mounted on an elastically deforming specimen surface. While applying axial load in tension, the shear strain γ_{xy} was measured to be ≈ 0. When applying pure torsion to the specimen (while holding the axial force at zero), the principal strains were measured to be $\varepsilon_x \approx \varepsilon_y \approx 0$.(*Perry 1969,*[223])

In the transmission setup, strains in the *z*-direction (through-thickness) are probed, which can be described for the case of isotropic materials as:(*Nye 1985,*[11])

$$\varepsilon_z = (-\nu/E)*\sigma_x \qquad (4\text{-}6)$$

where ν is Poisson's ratio and E is Young's modulus. The strain in the direction of applied stress (for no lateral stress condition) is given by:(*Nye 1985,*[11])

$$\varepsilon_x = (1/E)*\sigma_x \quad (4\text{-}7)$$

Hence, the strain in the probed direction using Bragg edge shifts can therefore be attributed purely to Poisson strain, an important requirement for a straightforward interpretation of experimental results. The measured strain can be related to the strain in the direction of applied stress by $\varepsilon_z = -\nu*\varepsilon_x$. The macroscopic Poisson's ratio, measured by using the strain gauge rosette, for this sample is ν = 0.28 and Young's (tensile) modulus was determined to be E = 200GPa. Since the plate is thin and plane stress condition can be presumed, the strain through the thickness is homogenous. If a thicker plate were used, the stress state would be three-dimensional (stress tensor has 6 independent quantities) and strain would eventually not be homogenous through the thickness, which would make the interpretation of the measured lattice strain values more complicated, since they represent line integrals of d-spacing variations through the thickness for a given pixel.

The lattice strain response of polycrystalline materials under deformation is usually characteristic for each lattice plane family *hkl*, because the stiffness of a crystal is generally anisotropic.(*Chung et al. 1967,*[224]*; Dolle 1979,*[225]*; Clausen et al. 1999,*[8]*; Hutchings et al. 2005,*[1])
In polycrystalline materials, elastic anisotropy can lead to stress concentrations and inhomogeneities during plastic deformation,(*Meyers et al. 1984,*[226]) and hence, strain mapping techniques that provide a large field of view and the ability to probe individual *hkl* lattice planes could be very useful. For the (110) lattice plane of α-Fe, the lattice specific Young's modulus (E_{110}) was reported to be ~ 210 to 220 GPa, and Poisson's ratio was reported to be in the range of 0.25 to 0.28.(*Eigenmann et al. 1996,*[7]*; Hutchings et al. 2005,*[1])
The sample, which has a dog-bone shape, used in the present research has been machined from a low carbon steel plate (ASTM standard A36; Table 1 with reminder content corresponding to Fe). The geometry and dimensions are displayed in Fig. 3a (gauge length: 21.72 mm, gauge width: 10 mm). The sample had a thickness of 1.46 mm and the average

grain size for this alloy was determined to be approximately 25 μm from optical micrographs. A neutron mask (B_4C) was mounted in front of the sample to define the beam exposure area vertically (25 mm tall), corresponding to a region of (nearly) homogenous strain magnitudes. This was undertaken to also enable 1D spatially resolved data (spatial resolution only in x-direction) to be recorded in order to improve statistics. It was confirmed, using Finite Element Modeling, that strain can be assumed homogenous over the height of 20 mm and nearly homogenous over 30 mm as shown in Fig. 3b.

Table 4-1. Chemical composition (weight percent) of A36 steel

C	S	P	Si
0.25 (max)	0.05 (max)	0.04 (max)	0.4 (max)

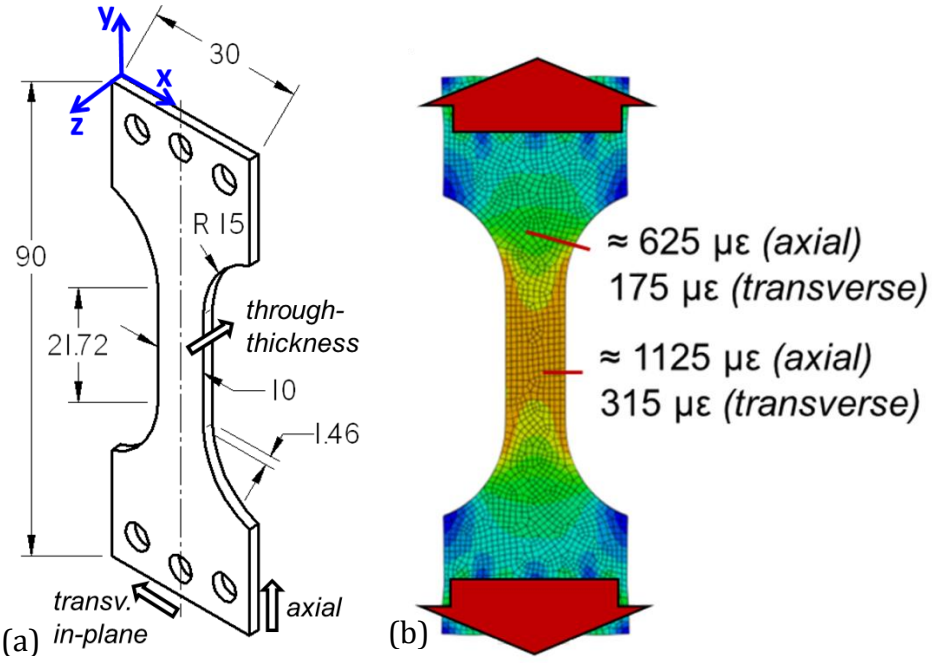

Figure 4-3. Sample; (a): Drawing of the sample with dimensions. (b): Strain distribution predicted by finite element calculations for the sample corresponding to an axial stress of 225 MPa.

4.3 Measurements

4.3.1 Measured Stress States

The location of the (110) peak was measured spatially resolved using transmission Bragg edge imaging as described above for the A36 steel alloy sample while the sample was subjected to a target state of axial stress in tensile mode. In this paper, measurements corresponding to three tensile stress states will be presented (S1, S2, S3). The sample was loaded to the target axial stress, using PID stress control, and then halted at a constant deformation during the neutron data acquisition. The loading system/sample was installed right in front of the detector, enabling a minimum sample to detector distance of l = 150 mm.

The reference measurement (S1) was used to determine the unstressed lattice parameter d^0_{110} at a small seating load, in order to prevent any unwanted movement of the sample during the subsequent measurements. Since the measured d_{110}-spacings at this condition are used as the reference lattice parameter, any residual strains prior to the application of seating loading can be ignored. The second loading condition (S2) induced elastic deformation corresponding to a state of axial stress that is approximately 90% of yield strength, and corresponding to a numerical value of tensile stress of 225 MPa. The third loading condition (S3) was chosen to be in the plastic regime, i.e. past yielding and after a significant amount of strain hardening, at ≈ 330 MPa. It must be recognized that the lattice strain response is non-linear past the yield point and is generally hard to predict, but has been chosen for our experiments for specific reasons. It is important to realize that using Bragg edge transmission imaging, we can resolve spatially three (depending on employed fitting profile also more) Bragg edge parameters corresponding to intensity, position and width (through FWHM). The changes in Bragg edge position from state of S1 and S2 correspond to internal (lattice) strains of the crystallites. Intensity provides information on texture and edge width is associated with defects such as dislocations and stacking faults within crystallites.

Bragg edge broadening is a direct result of the sample properties, such as strain gradients through the (probed) sample thickness, crystallite size and mosaic spread within which the crystallite/grain can be seen as a single diffracting entities.(*Hutchings et al. 2005,*[1]) Any defects within the crystallites, such as dislocations and stacking faults will lead to a decrease of the crystallite's entity and can therefore lead to a broadening of the Bragg edge. Plastic deformation of a sample can cause such defects to evolve and a widening of the Bragg edge might be observed during increased plastic deformation. (*Fitzpatrick et al. 2003,*[65;] *Hutchings et al. 2005,*[1]) It should be kept in mind that the overall shape of the Bragg edge is determined also by the instrumental parameters, i.e. a poorer wavelength resolution results in a wider Bragg edge.(*Vogel 2000,*[3;] *Hutchings et al. 2005,*[1])

Thus making a measurement at S3 state, well beyond yield, was intentional to probe these small length scale heterogeneities. The measurement at S3 stage also corresponds to a relatively larger change in d-spacing due to very large plastic deformation induced, and our intent was to consider a loading state where large shifts in Bragg edge location could be induced from plastic flow. For the grains inside a single or group of voxels (pixel multiplied by the sample thickness) that are being plastically deformed, elastic strain is replaced by plastic flow (after the yield limit). Thus, the rate of elastic strains decreases substantially, and its change is a function of whether the plasticity corresponds to perfect plastic flow (lattice strain saturates) or has associate hardening (lattice strain rate decreases). Hence, studies could be useful for providing additional understanding in developing reliable polycrystal plasticity models considering back stress.(*Wollmershauser et al. 2012,*[227])

4.3.2 Data Acquisition and Raw Data

Additionally, a measurement without sample was recorded in order to achieve the empty beam spectrum under the given experimental conditions of the source and the detector. The total exposure time for each stress state was 16 hours (S1, S2, S3) and 14 hours for the open beam condition. A given data set consisted of 16 measurements (corresponding to 1 h exposure time each) of 1024 images (corresponding to time channels), each having 512 x 512 pixels. The time stamps of the images have been converted to corresponding neutron

wavelengths. One image represents a time slice of 10.8 µs and hence a wavelength range of 0.005 Å. The data were reduced to the region-of-interest (ROI) in space, i.e. 8.8 mm x 24.6 mm, and time, i.e. a wavelength range between 3.7 Å and 4.5 Å. The single exposures of the measurement series at equal sample state (16 exposures of 1 h) have been averaged, and binning of 3 x 6 pixels in the spatial domain and 3 time channels (images) in the wavelength domain was implemented. The resulting spatial pixels have a size of ≈ 1.75 x 3.5 mm^2, which roughly matches the spatial resolution of the detector and the wavelength bins of 0.015 Å, i.e. still smaller than half the instrument resolution at 4 Å (i.e. 0.02 Å). The as recorded spectrum for a selected area in the sample center (6 x 12 pixels corresponding to 3.5 mm x 7 mm) and 1 h exposure time under stress state S1 is shown in Figure 4a (inset). The resulting spatially resolved wavelength spectra of the sample measurements have been normalized by the open beam measurement. The normalized spectrum (averaged exposures with sample divided by averaged exposures of empty beam), i.e. the Bragg edge, cropped to the time channel information of relevance is shown in Figure 4.4a.
Because the very narrow pinhole (slit) in the horizontal direction acts like a pinhole camera, the slight variation of opening times of the chopper with respect to the horizontal beam cross section is displayed in a corresponding spectral shift in this direction. This effect can be seen in Figure 4b, which shows the Bragg edge spatially resolved in the x-direction while the TOF information is on the y-axis. However, the variation ($\Delta t_{TOF} < 75$ µs) is lower than the wavelength resolution limit ($\Delta t_{TOF} \leq 86$ µs according to 1% resolution at 4Å), and, for these measurements, this has no further relevance as one is measuring relative d-spacing shifts with spatial resolution and relating sample data to the corresponding spectra of the empty beam measurements at the same image position (while the sample position remains unchanged throughout the experiment). In fact, it enables wavelength resolution better than the nominal theoretic value derived earlier for the overall beam.

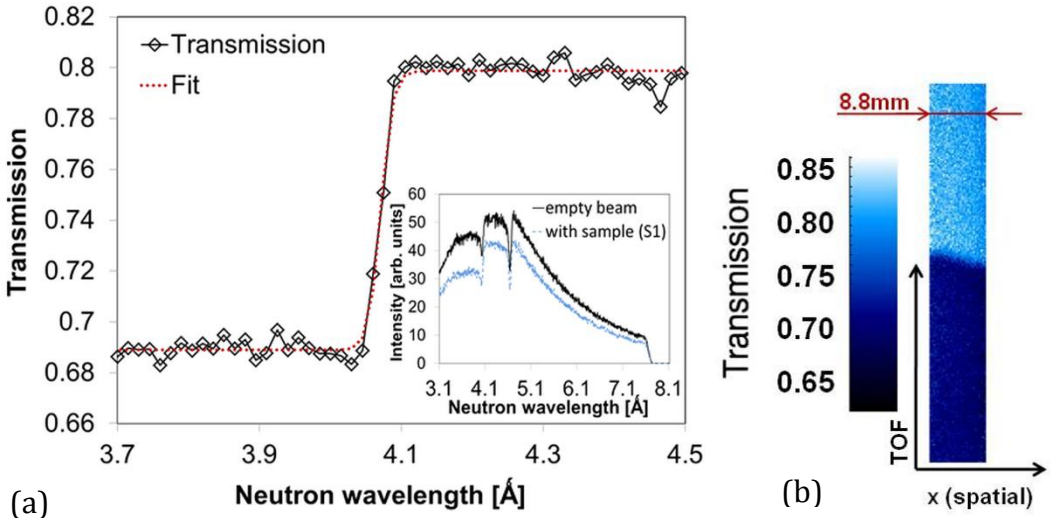

Figure 4-4. (a): Bragg edge as measured by the relation of the empty beam image and sample (inset: full spectrum of empty beam and with sample; area corresponding to 3.5 x 7 mm and 1 h counting time). Note that the additional dips in the empty spectrum (inset) are due to an upstream monochromator of another instrument at 4.76Å (V12a (*Strobl et al. 2007,*[228])) and to Al windows in the beam (around 4Å). (b): Illustration of the spatial variation of the Bragg edge position with respect to the time-of-flight (TOF) due to chopper and pinhole geometry.

4.4 Results

4.4.1 Data Processing

The resulting spatially resolved attenuation spectra have been analyzed pixel-wise, and for each pixel, the position of the Bragg edge was determined. Three different curve fitting approaches have been implemented in order to determine the position of the Bragg edge: (1) The derivative of the transmitted spectrum has been fitted using a Gaussian fit (see also (*Woracek et al. 2011,*[207])), (2) a code developed to fit TOF transmission data from pulsed sources as reported in (*Tremsin et al. 2009,*[129]; *Tremsin et al. 2010,*[130]; *Tremsin et al. 2011,*[107]) and based on theoretical considerations concerning transmission and instrumental similar to those described in (*Steuwer et al. 2003,*[23]), and (3) a non-linear least square fit that is based on the empirically derived modified gauss function described in equation 4-8.

$$f(x) = \frac{1}{A_0 e^{-\left(\frac{x-A_1}{A_2}\right)} + 1} + A_3 \tag{4-8}$$

The results reported in this paper are based on the last approach (approach 3), whereas the results of all approaches yielded very similar results. In the above notation, A_3 corresponds to a constant offset, A_0 is the height of the edge, whereas the exponential function including A_2 describes the full width at half maximum (FWHM) of the Gaussian derivative of the edge function itself and, A_1 represents the location of the edge. The function was chosen because of its good resemble of the Bragg edge and its simplicity, but it has no direct physically related meaning. However, a function based on physical considerations (as used in approach 2), should be seen as favorable. Bragg edge based strain was determined from relative shifts, numerically obtained from the A1 parameter.
After determining the position of the Bragg edge for each pixel at all three stress states, the corresponding strain of stress state S2 and S3 with respect to initial stress state S1 has been calculated (Fig 5b) based on:

$$\varepsilon^{S2,S3}=(d^{S2,S3}_{hkl}-d^{S1}_{hkl})/d^{S1}_{hkl}. \tag{4-9}$$

In order to further decrease statistical noise, the pixel values have been averaged in the x and y-directions using a 2 by 3 pixel running average filter. This of course leads to smearing of spatial resolution, but has no impact in the case of a homogenous or gradually changing strain distribution, as was the case for our imposed mechanical stress conditions in this study.

4.4.2 Data Interpretation

The induced and measured strain in the thru-thickness direction (ε_z) at stress states S2 and S3 is negative, i.e. the d-spacing becomes smaller due to the Poisson effect (Fig 5b and Fig 6a,b). The magnitude of the determined strain values generally agrees with the mechanics

of materials theory (assuming elastic modulus of E=200 GPa and ν=0.28) and reported *hkl* specific response for the (110) lattice plane of α-Fe (*Eigenmann et al. 1996,[7]; Hutchings et al. 2005,[1]*), while it is difficult to reliably predict the expected lattice strain magnitudes in the plastic flow domain. Grains that have undergone plastic deformation do not accumulate elastic load at the same rate as when deformation was still elastic.(*Clausen et al. 1999,[8]; Hutchings et al. 2005,[1]*) This leads to an expected non-linearity in the stress *vs.* lattice strain behavior. Plastic deformation is not attributed solely to d-spacing changes but rather to slipping and twinning mechanisms,(*Meyers et al. 1984,[226]*) which is not detected by Bragg edge shifts. The trend and magnitude of determined strain values is consistent along the specimen's height so that two stress states can clearly be distinguished (Fig 5b and Fig 6a,b). In the horizontal direction, the measured ε_z strain magnitude is slightly higher on the left edge of the sample, compared to the right edge (along x direction). This is likely a result from the slight misalignment in the grips with the loading train, which leads to unequal strains along the width and are pronounced in the plastic regime. This interpretation seems reasonable because a similar trend was also observed for recent lattice strain measurements by Bragg edge transmission technique while using a double crystal monochromator at CONRAD instrument at HZB (*Hilger et al. 2006,[229]*), while the authors used the same equipment and same type of sample (*Woracek et al. 2011,[207]*). This in fact underlines the importance of acquiring strain maps, rather than probing only a few fixed locations spatially in a sample, as is often the practice at residual stress diffractometers, due to the nature of the technique employed in diffraction-based d-spacing measurements.
Prior to the measurements reported in this paper, the same type of sample (machined from the same batch) was used for measurements at the engineering diffractometer E3 (*Wimpory et al. 2008,[230]*) and the cold neutron imaging instrument CONRAD (*Hilger et al. 2006,[229]*), utilizing its pioneering double crystal monochromator device for energy dispersive imaging (*Treimer et al. 2006,[125]*). This allowed for comparing corresponding results achieved by two novel approaches (TOF and double crystal monochromator based neutron transmission imaging) with results achieved using a neutron diffractometer, which is a well-established and routinely used tool by the residual stress community.

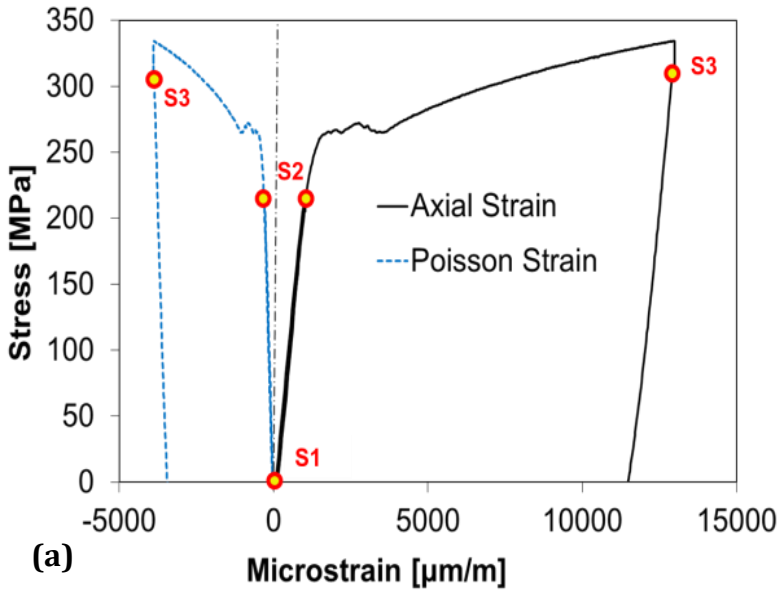

(a)

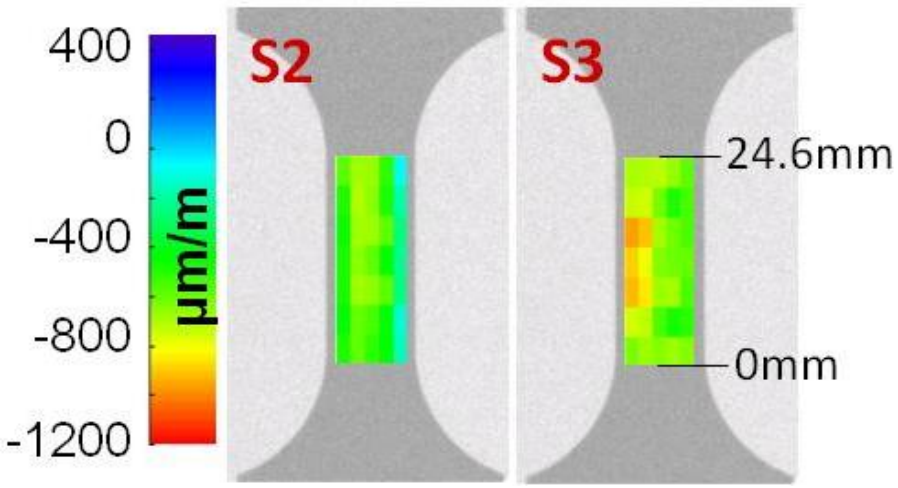

(b)

Figure 4-5. (a): Tensile Stress versus axial strain (ε_y) and Poisson strain(ε_z), highlighting the stress states at which Bragg edge transmission measurements were performed, (b): spatial distribution of measured ε_z strain based on (110) peak shifts from Bragg edge transmission imaging data. Note a slight variation in horizontal(x) direction.

The tensile tests at all three instruments have been performed with the same equipment and the same loading parameters, while only the number of investigated stress states was different each time. At CONRAD, four stress states have been measured: (i) unloaded as reference measurement to determine the unstressed lattice parameter d^0_{hkl}, corresponding to S1 in the current study (ii) elastic deformation at 90% of yield strength, i.e. 225 MPa, corresponding to S2 (iii) plastic deformation corresponding to S3 in the current TOF experiments (iv) unloaded after previous plastic deformation. The approximate count time for each stress state was 10.5 hours. At E3, we investigated 12 stress states, while stress state at 90% of yield strength was measured twice. Three spatial locations along the specimen axis have been measured with a gauge volume of 2 x 2 x 2 mm^3 while the count time for one point was 20 minutes. It should be noted that the data presented herein were obtained for the (220) lattice plane, which represent lattice strains for the (110) lattice plane. During the neutron data acquisition, the deformation was kept constant and therefore a stress-relaxation occurred in the plastic regime. This however is rather insignificant, as the amplitude of drop in the axial stress was only ~5% and the major portion of the resulting stress drop during the deformation hold segment occurred immediately after halting the deformation. Authors believe that the option of holding deformation was better than holding stress as we are measuring d-spacing changes, and hence, this option was deemed more desirable for our experimental purpose than using stress control segment, which leads to unwanted creep potentially changing d-spacing values slightly while making measurements.

Figure 4-6b compares the two transmission-based results with the diffraction-based results for approximately the same location in the specimen center. It should be noted that in the diffraction-based measurement approach, this gauge area is about 2 x 2 mm^2, at CONRAD the resulting pixel size was 2.7 x 2.7 mm^2, and we report results from TOF technique with pixel size of 1.75 x 3.5 mm^2. Thus, it is reasonable to compare the results from various experimental techniques, and as noted, very consistent results were obtained showing promise for the technique described in this paper.

(a)

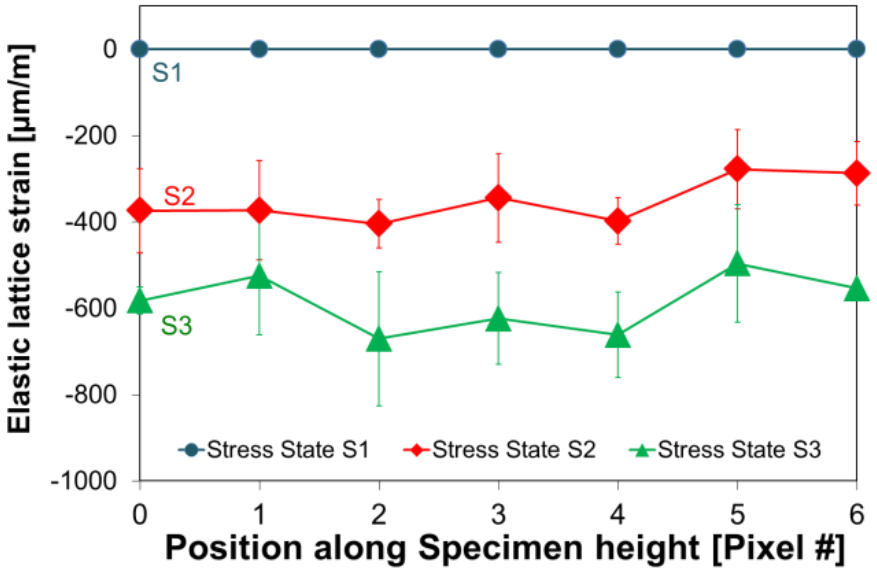

(b)

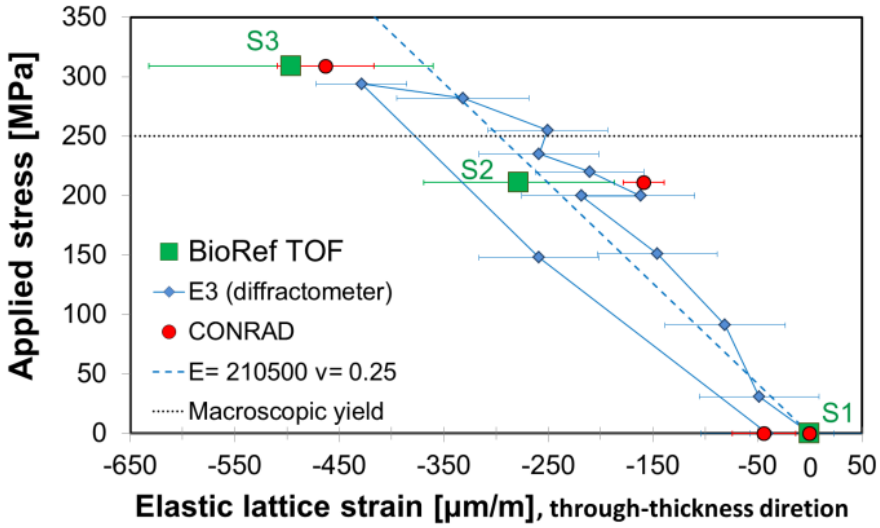

Figure 4-6. (a): Measured ε_z strain along specimen height with values averaged horizontally, one pixel corresponding to 3.5 mm height. (b): comparison of measured strain values for a point in the center of the sample including diffraction data (blue diamonds), imaging with monochromators at CONRAD (red circles) and the herein reported TOF measurements (green squares).

The error bars of the reported TOF data correspond to one standard deviation of the pixel value and all directly neighboring pixels, which are expected to have the same strain magnitude. The strain values obtained from all techniques agree with each other within the uncertainties of the experimental errors. The (blue) dashed line indicates the expected elastic response specific to the (110) plane of α-Fe. The macroscopic yield stress for this material is 250 MPa as indicated in Fig. 6b by the horizontal dashed line.

4.5 Discussion and Outlook

We conclude that the results achieved provide clear evidence that strain measurements are feasible in imaging geometry at a medium flux continuous source using a chopper setup. The concept of strain measurements based on Bragg edge analyses has been demonstrated previously by presenting TOF data from pulsed sources (*Vogel 2000,[3]; Santisteban et al. 2001,[179]; Steuwer et al. 2001,[168]; Santisteban et al. 2002,[96]; Santisteban et al. 2002,[167]; Steuwer et al. 2003,[23]; Kockelmann et al. 2007,[181]; Tremsin et al. 2009,[129]*) and also at a continuous source (*Strobl et al. 2011,[182]*) using crystal monochromators (*Woracek et al. 2011,[207]*). However, it must appear necessary to also analyze potential gains of such novel approaches as compared to more conventional methods such as neutron diffraction. It should be mentioned here that one must realize that the use of transmission-based imaging technique by investigation of Bragg edges is currently limited to two dimensional problems and the d-spacing values for a given *hkl* are averaged through the measured thickness dimension along the neutron path length, which has been addressed in detail previously. (*Santisteban et al. 2001,[179]; Steuwer et al. 2001,[168]; Santisteban et al. 2002,[96]; Steuwer et al. 2003,[23]; Santisteban et al. 2006,[176]; Iwase et al. 2007,[177]; Kockelmann et al. 2007,[181]; Woracek et al. 2011,[207]*) It has therefore to be acknowledged that the transmission technique cannot provide the flexibility of measuring components of the strain tensor as freely and conveniently as they could be on a diffraction instrument. For our discussion, we therefore consider a case where the transmission technique is applicable and suitable, such as e.g. for a sample subjected to plane stress state as described in this paper.

Comparison of lattice strain measurements using different techniques is not straightforward, although in our study, we used the same sample and investigated the results obtained from different approaches at the same neutron source. It has been discussed earlier, that the TOF approach even at a continuous source is superior to the crystal monochromator technique especially because of the unprecedented flexibility in resolution of a suited chopper set-up (*Van Well 1992,[126] Strobl 2009,[217] Strobl et al. 2010,[127] Strobl et al. 2011,[182] Strobl et al. 2011,[220]*). Hence, we limit our discussion to the presented TOF approach versus conventional diffraction measurements and to the efficiency considerations based on the introduced technique, corresponding measurements and associated results.

The spatial resolution in the diffraction measurements is defined by the incident and diffracted beam slits to be 2 x 2 mm^2 and one such point was measured in 20 min. A pixel in the TOF imaging experiment is 1.5 times larger with 1.75 x 3.5 mm^2, but 35 such "gauge areas" are measured simultaneously within 14 h. That means that, theoretically, 2 x 2 mm^2 resolution would require about 20 h as compared to about 12 h by diffraction. However, we have to keep in mind, that we closed the slit for our pinhole geometry for imaging by a factor of 20 more than necessary (1.5 mm instead of 30 mm, additionally, the reflecting coating in the guide ends already another 3 m earlier [14,15]) to achieve the given resolution in order to spare the used detector. Furthermore, due to the given chopper system we had to measure a wavelength band of 4 Å, despite the fact that we used a range of only 0.5 Å. With an adequate chopper system, we could have increased the pulse frequency and the duty factor by a factor of 8 and would all together have been able to achieve the same data in about 1/8 h. On the other hand, our resolution is with 1 % wavelength resolution about a factor 2 poorer than that available in diffraction and the filtering (spatial averaging) of our data reduces our spatial resolution by about another factor of 2 and the statistics still lead to large error bars. Hence, we find it reasonable to estimate a doubling of exposure time to improve statistics. Considering the above issues, one would end up with another factor of 8, and hence, with a total measurement time of approximately 1 h as compared to about 12 h for the diffraction measurement.

Consequently, a theoretical gain of about an order of magnitude could be achieved. Indeed, it has to be seen that such comparison and estimates are rather vague still, and the potential of the novel method needs further investigation and more direct comparison must be enabled.

Nevertheless, results are promising, and further investigations to overcome current limitations are to be expected and dedicated TOF instruments for advanced neutron imaging (*Strobl et al. 2009,*[53]; *Strobl et al. 2011,*[219]), even at continuous neutron sources, should be considered in the future. Our study can hopefully inspire the development and use of such TOF instruments in the future as the spallation neutron sources fully exploit the Bragg edge imaging capabilities, which could lead to new and novel contributions to science and engineering.

Chapter 5

Neutron Bragg Edge Imaging at a Spallation Source: Strain Mapping Case Study

Preface:

This chapter has not yet been published elsewhere. However, some of the results have been shown at various conferences and workshops. It is planned to publish parts of this chapter through an appropriate journal.

Abstract:

Wavelength dependent neutron imaging can be used to spatially resolve the effects of texture, crystallographic phase and lattice strain. Recently, proof-of-principle measurements have been demonstrated at spallation neutron sources and at continuous reactor based sources. In this chapter, a detailed case study is described, where a flat steel tensile sample with a hole in its gauge section (providing stress concentrations) is loaded in tension and neutron imaging is carried out in time-of-flight mode at the spallation source ISIS, with the aim of spatially quantifying in-situ lattice strains in the through-thickness Poisson direction. The study considers a thin (3 mm) and a thick (9.5 mm) specimen geometry for a steel alloy and imaging results and associated implications are discussed in detail. In order to interpret the neutron imaging data comprehensively, resistance based strain gauge rosettes for point based strain measurement, digital image correlation for area based surface strain measurements, and limited bulk gauge volume based neutron diffraction measurement are utilized. Finite Element Modeling technique was utilized to evaluate the experimental results and the role of thickness of the specimen in implementing planar strain measurements using Bragg edge based strain mapping.

5.1 Introduction

When neutrons interact with a polycrystalline sample, some neutrons of particular wavelengths are diffracted by atomic lattice planes (belonging to grains in certain orientation towards the incident neutron beam that satisfy Bragg condition) in defined directions. The diffraction angle can be detected at neutron diffraction instruments that use fixed wavelengths (using monochromators at reactor sources), or the corresponding wavelengths can be determined for fixed scattering angles (typically at time-of-flight instruments). Thus, the neutrons that are diffracted out of the incident beam direction will contribute to overall attenuation of the sample. Energy dispersive neutron imaging in transmission geometry makes use of this "diffraction contrast" and probes the energy dependence of the samples attenuation coefficient. The elastic coherent scattering cross-section ($\sigma_{el.coh.}$) changes suddenly at well-defined wavelengths, defined by Bragg law:

$$n\lambda = 2d_{hkl}\sin\theta^{B} \tag{5-1}$$

in which n = 1,2,3.. is the order of reflection. In transmission measurements, the detection angle corresponds to a "back-scattering" angle of $2\theta^{B}_{hkl} = 180°$, the most significant signal is given for $\theta^{B}_{hkl} = 90°$. At wavelengths larger than $\lambda = 2d_{hkl}\sin90° = 2d_{hkl}$, Bragg scattering for the corresponding lattice planes *hkl* cannot take place, and hence, the transmitted intensity increases drastically. These features are referred to as Bragg edges. Any change in d_{hkl} would shift the Bragg edge correspondingly, and consequently, strains along the beam direction ($\theta^{B}_{hkl} = 90°$) can be resolved if only the wavelength resolution is sufficient, hence the method is sometimes termed "strain radiography". By using such wavelength dependent Bragg edge transmission measurements – in analogy to diffraction measurements, information about the structure of crystalline materials, which is related to the elastic coherent scattering cross-section, can be derived.

Early experiments to study the nuclear cross-sections of elements, using transmission measurements, have been reported by Fermi et al. in 1947 (*Fermi et al. 1947,*[153]) and

Winsberg et al. in 1949 (*Winsberg et al. 1949,*[154]). The development of the Bragg edge transmission technique continued at reactor sources (*Cassels 1950,*[156;] *Weiss et al. 1952,*[155;] *Mikula et al. 1995,*[157;] *Strunz et al. 1997,*[158;] *Wagner et al. 1997,*[159]) and spallation sources (*Johnson et al. 1982,*[161]). The method was further developed with at the next generation of spallation sources installed at Los Alamos National Laboratory (USA; LANSCE) and Rutherford Appleton Laboratory (UK; ISIS).

Several publications, reporting applications and proof-of-principle measurements, both at pulsed as well as at continuous sources, were published in the literature and some are described in the following. The determination of phases for example has been demonstrated at neutron spallation sources in time-of-flight mode (*Meggers et al. 1994,*[163;] *Meggers et al. 1994,*[164;] *Bourke et al. 1996,*[172;] *Vogel 2000,*[3;] *Santisteban et al. 2002,*[167;] *Steuwer et al. 2004,*[173;] *Steuwer et al. 2005,*[174]) and at a reactor source using a tunable monochromator (*Treimer et al. 2006,*[125;] *Woracek et al. 2014,*[231]). The application of this methodology for quantitative strain measurements, with the potential of superior spatial resolution, has been presented at spallation sources (*Wang 1996,*[165;] *Santisteban et al. 2001,*[179;] *Steuwer et al. 2001,*[168;] *Santisteban et al. 2002,*[96;] *Steuwer et al. 2003,*[23;] *Tremsin et al. 2011,*[107;] *Iwase et al. 2012,*[180;] *Tremsin et al. 2012,*[221]) and reactor sources (*Strunz et al. 1997,*[158;] *Wagner et al. 1997,*[159;] *Woracek et al. 2011,*[207]). Efforts to use this method for rather qualitative, but spatially resolved, texture evaluation have been undertaken by others (*Santisteban et al. 2006,*[176;] *Iwase et al. 2007,*[177;] *Kockelmann et al. 2007,*[181;] *Boin 2010,*[5;] *Santisteban et al. 2011,*[184;] *Boin et al. 2012,*[232;] *Malamud et al. 2014,*[233]).

Because of the geometric layout of a diffractometer, the measurement location can be precisely defined in three dimensions by defining the incident and diffracted neutron beam using slits and/or radial collimators. In a transmission imaging based setup, the measurement location ('gauge volume') can only be defined in the direction of the neutron beam, as by definition all transmitted neutrons will hit the detector which is located in the direction of the incident beam. In radiographic images, all crystals which lie with lattice plane normals parallel to the incident neutron beam contribute to the diffraction contrast.

If changes in phase, texture and/or strain are present within beampath through the sample, then an unambiguous interpretation of the data is only possible with a-priori information. If the sample is not (or only mildly) textured, different crystallographic phases within a sample can be visualized and quantified in three dimensions by means of tomographic reconstruction, as was recently demonstrated (*Woracek et al. 2014,*[234]). If the sample exhibits a pronounced texture, the image contrast is not only a function of the thickness and phase of the material, but also depends on the preferred crystallographic orientation of grains in the specific sample orientation. This in principle can be corrected based on known pole figures, but a suitable methodology is not yet readily available. In the case of strain measurements, a precise determination using tomography is not straight forward, because of the tensorial properties of strain. To describe the state of strain at a point inside a sample, knowledge of nine strain components is needed, out of which six are independent. Therefore a tomographic reconstruction of the strain tensor is not possible without additional information and/or assumptions. The reconstruction of strain by tomographic techniques is reported recently by a number of publications, but has been limited to axisymmetric sample configurations (*Abbey et al. 2009,*[192]; *Abbey et al. 2012,*[193]; *Abbey et al. 2012,*[235]; *Kirkwood et al. 2013,*[236]), and in order to extend it to more arbitrary strain fields, one will need more constraints and/or additional (diffraction) data.

The case study that is presented in this work will not aim for a three dimensional reconstruction of strain, but is intended to evaluate the possibilities for high resolution strain mapping at a spallation source to-date. The herein discussed experiments were performed in time-of-flight transmission mode at the ENGIN-X beamline at the spallation source ISIS using a specialized neutron-sensitive Microchannel Plate (MCP) Detector with 55 µm pixel size. While previous pioneering studies using pixelated detectors for the Bragg edge methodology were limited to coarse pixel sizes (10 x 10 pixels, each 2 x 2 mm^2) (*Santisteban et al. 2001,*[179]; *Santisteban et al. 2002,*[167]; *Steuwer et al. 2003,*[23]), it should be noted that a similar study – to the one presented herein – also performed at ENGIN-X and using the same detector technology is published by Tremsin and co-workers (*Tremsin et al.*

2011,[107]*; Tremsin et al. 2012,*[221]). In the later study, they investigated two separate samples. A ferritic steel cantilever sample was subjected to three different bending loads by manually adjusting the displacement with a screw. The uni-axial stress field induced in such a specimen results in a linear elastic strain, tensile strains on one side and compressive strains on the other, provided that the maximum stress stays within the elastic limit.(*Mayville et al. 1982,*[237]) The strain was determined perpendicular to the applied stress, corresponding to the Poisson direction. By using the conventional diffraction mode at ENGIN-X immediately after the transmission measurement (which took ~3 h), they report that the "results could be verified with fair agreement, confirming the accuracy the transmission mode strain maps."(*Tremsin et al. 2012,*[221]) They also investigated measuring the residual strain in an austenitic steel compact-tension (CT) sample, where previously a 25 mm crack was introduced by fatigue cycling. As was pointed out in this study (*Tremsin et al. 2012,*[221]), even though the measured strain in this sample can mostly be attributed to "Poisson strain from the stresses in the crack opening direction, the stress field in around the crack in a sufficiently thick sample is triaxial". They have compared the transmission results with a finite element model, where they found that the strains in the uncracked region yield similar results. In the cracked region however, the maximum values of strains from the finite element model were reported to be significantly higher. This could indicate effects of crack tip blunting in the actual sample vs. the numerically modelled sample, demonstrating the useful potential of the Bragg edge imaging method to study such samples. However, one also carefully needs to be aware of the complex stress field in the vicinity of a CT sample and the fact that the Bragg edge method is based on a line integral, providing a mean value of strain through the thickness.

With the above described important limitations in mind, the herein presented experiment was designed, where a plate sample with a stress concentration – introduced by a center hole – was loaded in tension, while using Bragg edge imaging to map the strain magnitude around the hole. Two different sample thicknesses are considered, and the effect of through thickness variation of strain will be discussed. Since the transmitted signal is averaged over

the complete cross section, it is expected that the strain gradient will result in a widening of the Bragg edge in addition to a shift of the location. This effect has so far only been given limited attention in literature, and this chapter will present a detailed assessment of it. The advantages and limitations of the Bragg edge imaging technique are discussed in more detail, using the measured data as an example. In addition to resolving the strain component spatially by Bragg edge imaging, additional experimental considerations and measurements were carefully undertaken, including finite element analysis and several corroborative strain measurement techniques employing resistance based strain gauges, 3-D digital image correlation, and bulk neutron diffraction measurements at an engineering diffractometer (E3 at Helmholtz Zentrum Berlin).

5.2 Sample and Finite Element Modelling

5.2.1 Basic Sample Considerations

The tensile specimen was designed to represent a 'classical engineering problem' by introducing a stress concentration through a center hole. Stress concentrations are present in many engineering components, as they arise by any abrupt change of geometry (e.g. holes, notches, keyways, grooves, fillets, cracks, rough surfaces) causing the "force lines" to concentrate. Simple cases involving direct normal stresses are plates under tension or bending with holes, notches, steps, keyways. Examples for direct and bending normal stresses and torsional shear stresses are shafts in tension, bending and torsion with such geometry changes. The assessment of the peak stresses are important when designing components and are usually determined by applying a stress-concentration factor to the elementary load-stress relationship.(*Young 2002,*[238]) Stress concentration factors can been determined analytically (using Theory of Elasticity), numerically (using Finite Elements Methods) and/or experimentally (e.g. by using very small strain gauges, photoelasticity, brittle coatings or Moire Interferometry) for many geometry changes.(*Pilkey et al. 2005,*[239]; *Pilkey et al. 2008,*[240]) The *static stress concentration factor* in the elastic range, commonly denoted as K_t, quantifies how "concentrated" the stress is, by defining the highest stress in

the element to the reference (nominal) stress: $K_t = \sigma_{max}/\sigma_{ref}$. Most commonly, the nominal stress over the net-cross section at the stress concentration is used, and we will refer to corresponding factor as K_{tn}. Sometimes, the (gross) stress in the same element without the stress concentration is used for computing the nominal stress, and we will refer to the corresponding factor as K_{tg}. An example for the static stress concentration for a circular hole in plate geometry under tension is shown in Figure 5-2. The factual stress concentration factors can be affected by the microstructural properties, such as grain size and anisotropy. Moreover it should be noted that if the load on the structure exceeds the elastic limit of the material (for example local plastic deformation near the hole), the stress distribution differs from what is predicted assuming elasticity. Neuber (*Neuber 1961,*[241]) established a rule that can be used beyond the elastic limit. Defining an effective stress concentration factor ($K_\sigma = \sigma_{max}/\sigma_{ref}$) and an effective strain concentration factor ($K_\varepsilon = \varepsilon_{max}/\varepsilon_{ref}$), Neuber's rule contends that K_t is the geometric mean of K_σ and K_ε [i.e. $K_t = (K_\sigma K_\varepsilon)^{1/2}$]. This formulation can be expressed in terms of stress and strain:

$$\sigma_{max}\varepsilon_{max} = {K_t}^2\, \sigma_{ref}\varepsilon_{ref} \tag{5-2}$$

The right side of the equation is usually known, as K_t and σ_{ref} are obtained as if the max stress would be in the elastic regime, while ε_{ref} is found from the elastic stress-strain relationship for the material. The equation can then be solved by knowing the stress-strain curve for the material.(*Young 2002,*[238])

The motivation for the described experiment resulted from the fact that diffraction methods can probe the effective elastic (lattice) strain under applied stress conditions in a sample and as such are suited to probe the stress concentration experienced by the deforming material, considering all of the material properties including microstructure effects. The Bragg edge imaging method can be considered as a 'special' diffraction method that can provide superior spatial resolution (in one plane), and as such could provide valuable insight for certain problems. A sample was designed, so that it could be

investigated by using the loading system for the application of tensile stress, while simultaneously performing transmission measurements using a Micro Channel Plate (MCP) detector with a FOV of corresponding to a circle with a diameter d = 28 mm, implemented at the time-of-flight beamline ENGIN-X at ISIS. The selected sample dimensions are given in Figure 5-1. For the selected sample dimensions of w = 20 mm and d = 8 mm, the stress concentration factors can be determined as 2.24 for K_{tn} and 3.7 for K_{tg} (see Figure 5-2).

The Bragg edge method probes strain in in the direction of the incident beam, which for the loading experiment corresponds to through thickness Poisson direction. For thin samples, the stress in this direction can assumed to be zero, or in other words the sample is in under the state of plane stress. However, this must be considered a special case, since even standard tensile specimen geometries don't fulfill this condition. Thick samples could potentially, and often do, exhibit strain gradients through the thickness. For Bragg edge imaging, this means that some averaged value through this dimension will be measured.

In this case study, two sample thicknesses are investigated, with the exact thickness to be decided based on the following considerations:

(i) A thin sample geometry, for which plane stress condition can be assumed with reasonable accuracy. Plane stress state can arise in many practical structural engineering situations, but particularly for thin samples. Plane stress can however also occur in a thick component of homogenous material which is loaded uniformly in tension (x-direction), where the stress σ_x acts on the cross sectional surface while all other stress components are zero. In the case of a sample with a stress concentration however, the sample needs to be thin, in order to reach (close to) plane stress condition. In a thin sample, the stresses in the through thickness (z) direction are only truly zero at the surface, but the variance practically is so little that they can be approximated to be zero throughout the material. The sample should at the same time not be too thin, so that still a significant number of grains

will be aligned for diffraction condition during the experiment to provide good signal to noise ratio using reasonable exposure time.

(ii) A thick sample geometry is investigated as well. The sample will yield better neutron statistics for the Bragg edge measurements than the thin sample, as the number of grains is significantly higher for each line integral corresponding to a given pixel. However, in this case, plane stress cannot necessarily be assumed and strain gradients may arise in this sample due the sample (at least in some locations) being in a triaxial stress state. The maximum sample thickness should of course be within the capacity of the loading system.

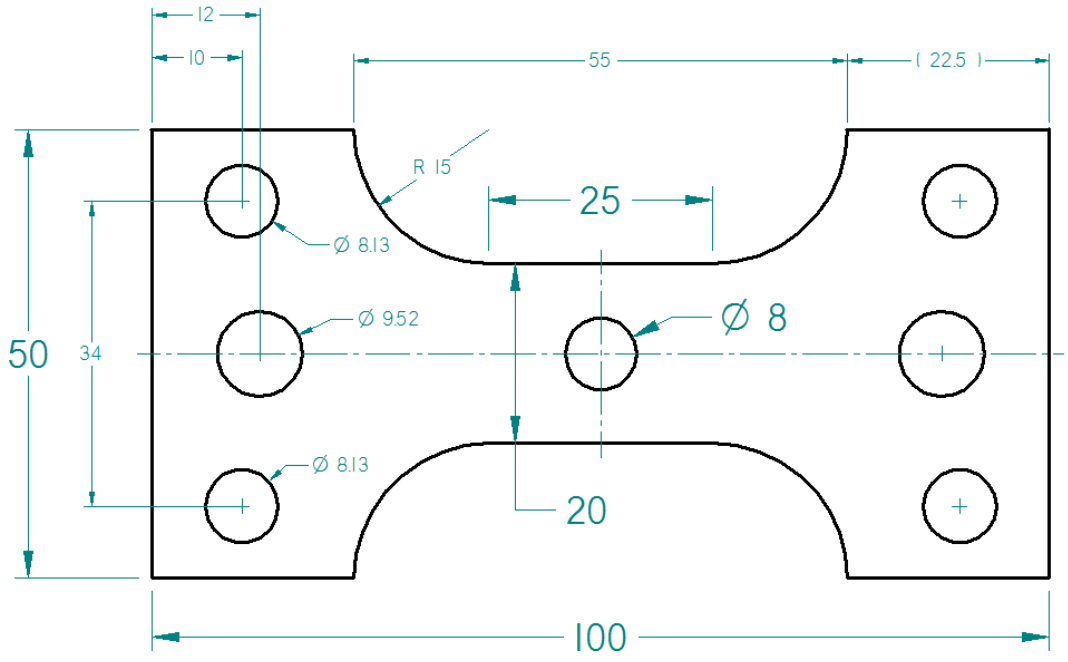

Figure 5-1. The sample geometry to be used for the tensile test (using two different thicknesses).

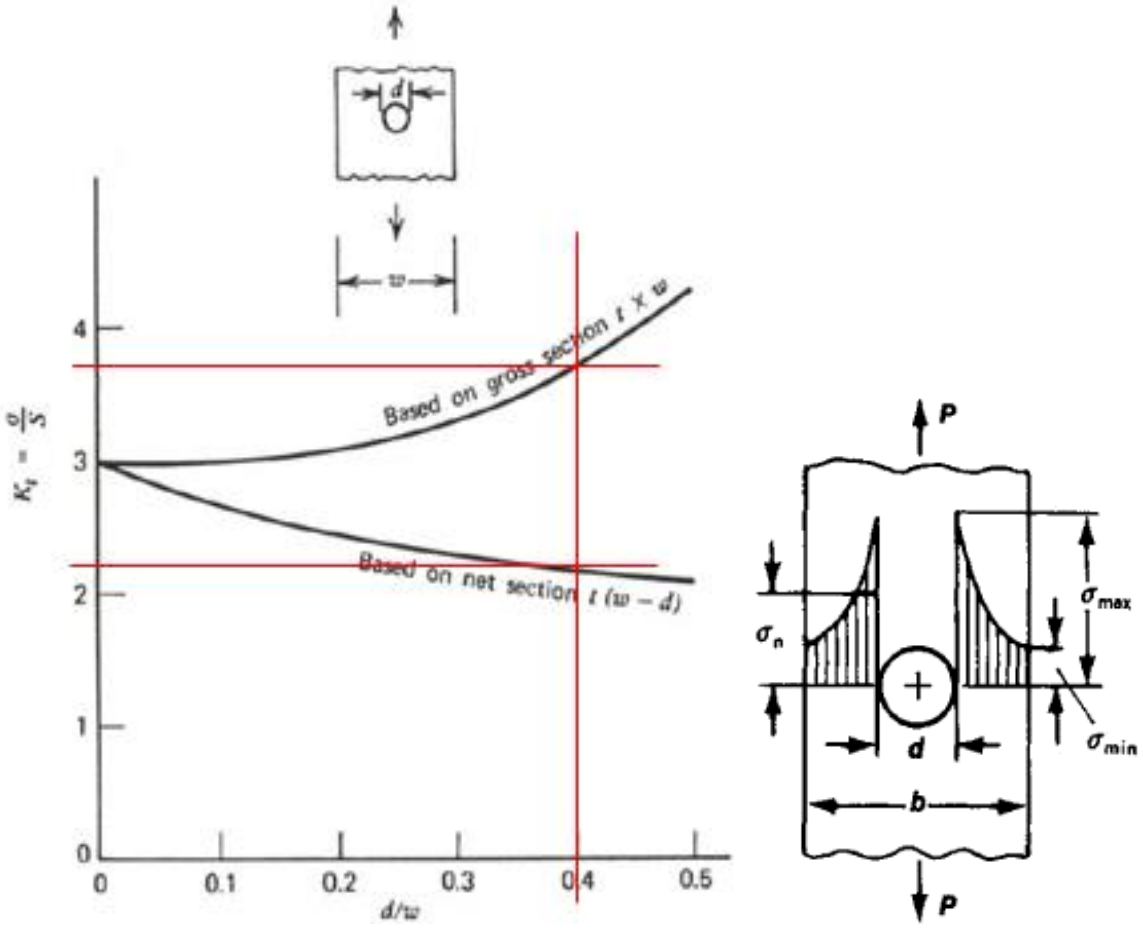

Figure 5-2. Stress concentration due to a center hole. *From* (*McGinty 2014,*[242])

5.2.2 Finite Element Modelling and Thickness Selection

Abacus finite element modeling software was used to simulate the stress and strain distribution for samples having different thicknesses under tensile loading, for linear elasticity based constitutive model. The strain distributions and relative values in the normal directions (x,y,z) are presented in Figure 5-3 for a sample of 9.5 mm thickness. While the magnitude of the strain component in the principal tensile direction (ε11) appears relatively uniform through the sample thickness around the hole, a strong variation can be observed for strain in the through-thickness direction (ε33). In comparison, Figure 5-4 shows the strain magnitude of ε33 for a sample of 3 mm thickness. Figure 5-5 depicts the strain variation of strain component ε33 (z-direction) in percentage for sample thicknesses of 3 mm, 4.6 mm and 9.5 mm, for two locations close to the hole and one away from the hole. A strong strain gradient is observed for the locations close to the hole using a thickness of 9.5 mm, while the variation is below ±4% using a thickness of 3 mm.

Accordingly the samples were chosen to have a thickness of:

(i) Thin sample: 3 mm

(ii) Thick sample: 9.5 mm

The samples were machined from a hot rolled plate of low carbon ferritic steel (ASTM A36) by laser cutting. This material was selected because it is widely used and has a stable crystallographic phase (body-centered cubic). The center hole was manufactured by mechanical drilling and reaming. The microstructure was distorted during the manufacturing process and in order to normalize the material and to remove residual stresses, the samples were annealed at 820C° for 15 minutes, followed by slow cooling. The as machined microstructure is shown in Figure 5-6a and the corresponding microstructure after annealing step in Figure 5-6b, exhibiting a nearly uniform average grain size of 25 μm. It should be noted that strain values obtained from the Finite Element Model will be compared with strain values determined using the neutron imaging method in section 5.5.2, corresponding to the same applied stress.

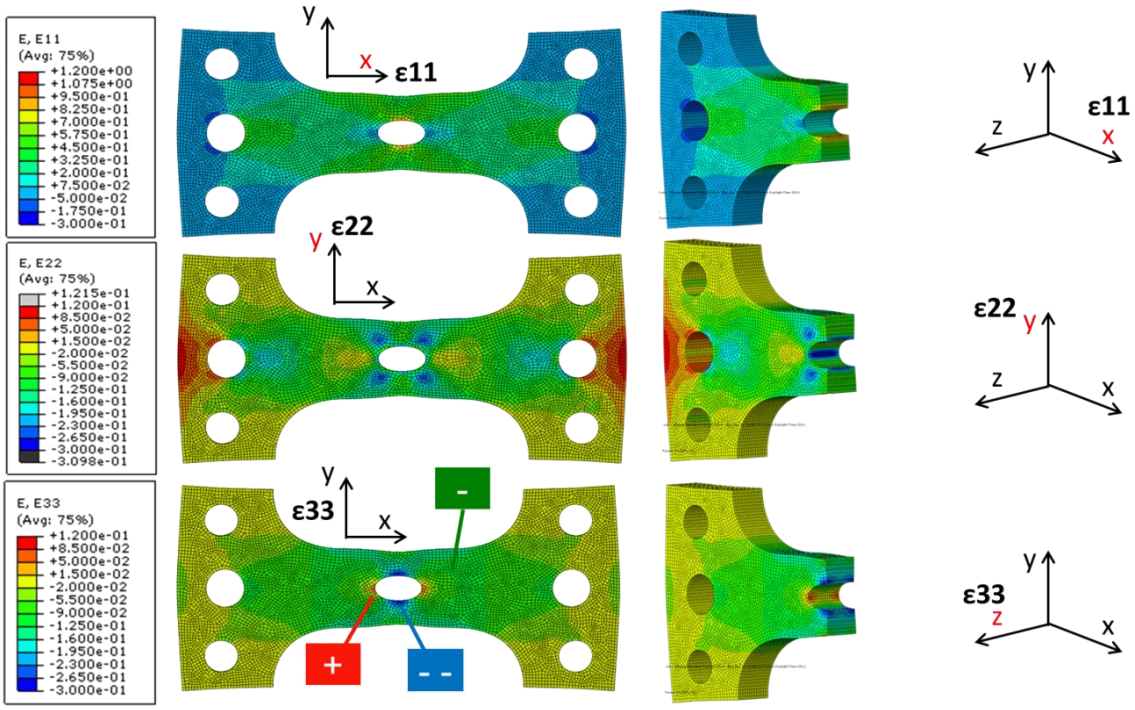

Figure 5-3. Finite Element Model (FEM) and strain state for of the a proposed (thick (9.5 mm)) steel sample geometry. The strain component ε33 will be probed during the transmission measurement and varies in the z-direction (along thickness direction) as can be seen.

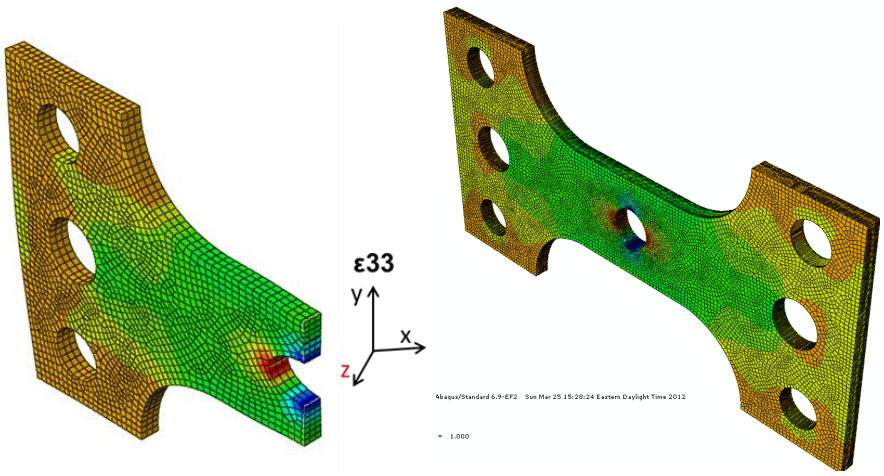

Figure 5-4. Finite Element Model (FEM) and strain state of a thin (3 mm) steel sample. The strain component ε33 is relatively uniform in the z-direction.

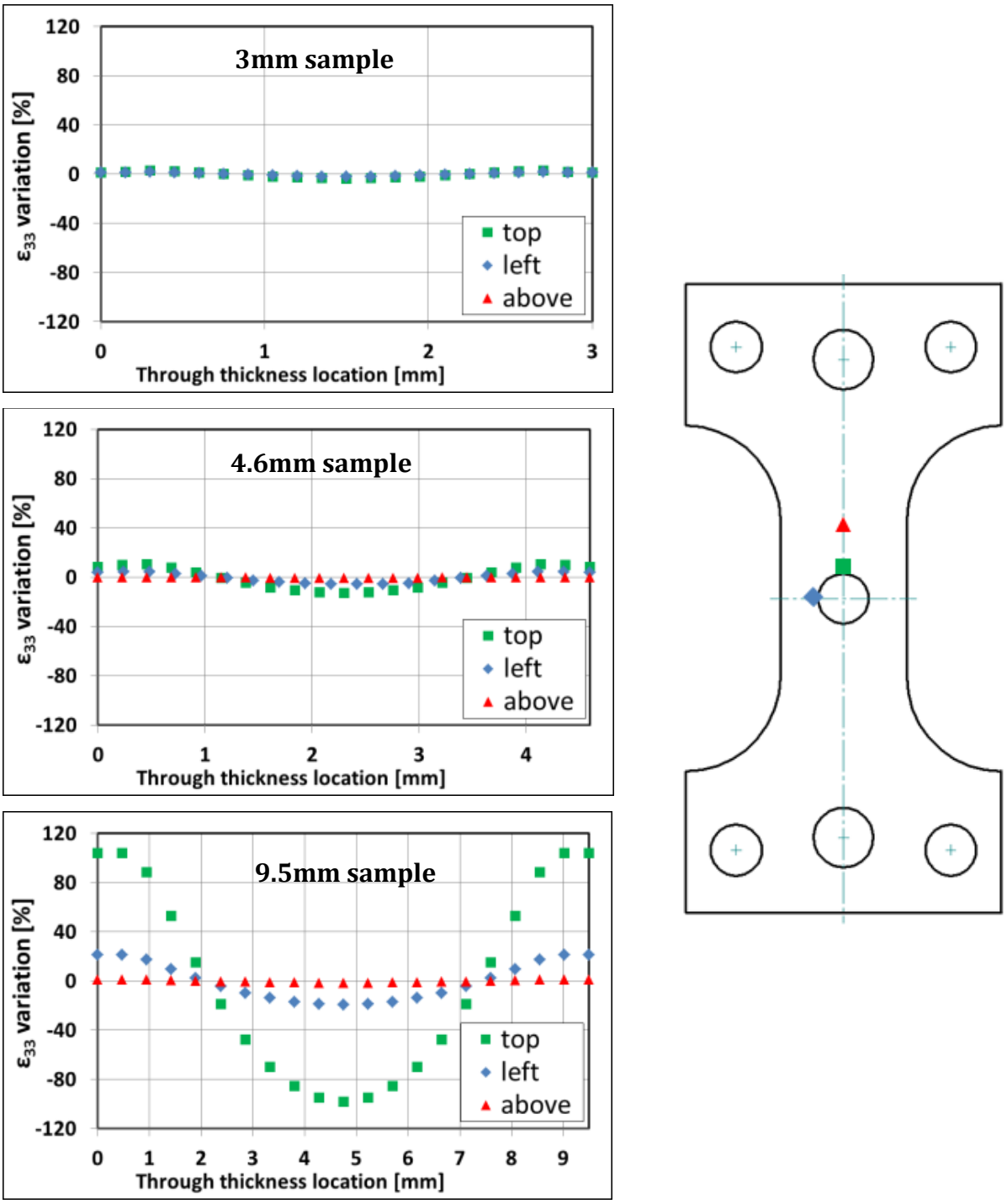

Figure 5-5. Variation of strain component ε_{33} from FEM: The strain variation at three different locations through the thickness relative to the integral (sum averaged) strain in that direction.

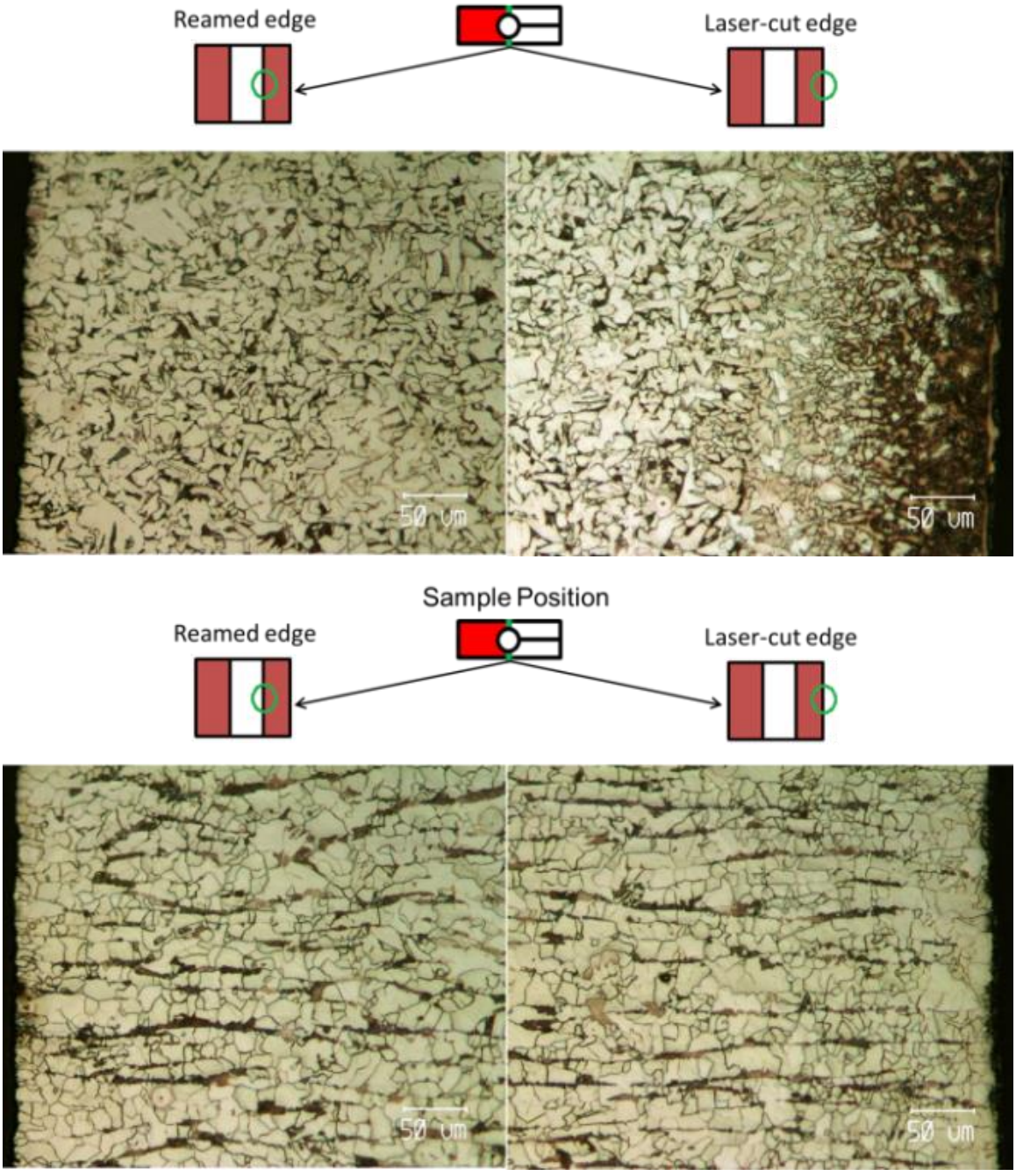

Figure 5-6. Microstructure of the machined samples, before (top) and after the annealing process (below). Magnification corresponds to ruler size of 50 µm.

5.3 Mechanical Deformation and Surface Strains

To monitor the macroscopic strains on the surface of the samples during tensile deformation, resistance based strain gauges were installed. In addition suitable speckle pattern was applied to optically measure surface strain using 3-D digital image correlation using a commercial system called VIC-3D. For performing Bragg edge based neutron imaging measurements, the deformation was halted for the time of data collection at a target state of stress. The discrete steps were maintained to be similar for both sample thicknesses corresponding to similar stress magnitudes. For ease of comparison, they are given the following nomenclature as follows (even though they were slightly different):

- S1 (10 MPa for thin sample, 20 MPa for thick sample; this is used in each case as the stress-free or d0 reference stress state)
- S3 (160 MPa for both samples)
- S4 (300 MPa for thin sample, 315 MPa for thick sample)

The small load at stress state S1 was used to fix the sample in the loading system (seating load). For both sample types, additional data was acquired, besides the three states of stress corresponding to neutron imaging experiment, using the same type of sample, the same loading system and identical boundary or deformation conditions as described in the following sections.

5.3.1 Strain Gauge Results

Electrical resistance based strain gauges were used to measure the surface strains during the tensile loading. The strain gauges were mounted along the loading direction and hence probe strain in the direction along component $\varepsilon_{11.}$ However, in many cases the strain gauge interface failed after the material was subjected to plastic deformation. Strain gauge data is only reliable for elastic loading.

Thin sample (i)

During the neutron imaging experiment, four electrical resistance based strain gauges were mounted around the hole on each side of the sample to obtain surface strains at four locations for comparison purposes and to evaluate the resolution of Bragg edge based bulk material strain measurement method. By mounting strain gauges on both sides, it was ensured that bending in the sample was minimal and that a uniform load is applied on both sides. Measurements indicate large strains on the left and right side of the holes and a relatively small amount of strain on top and bottom of the hole (approximately a factor of eight).

For example, the following strain values were recorded at a tensile stress of 160 MPa (S3): On side A (front side), the strains on top (st5) and bottom (st1) of the hole were 90 με and on the sides (st6 and st2) 650 με. On side B (back side), the strain values were similar with values at 84 με on the top/bottom (st7 and st3) and 600 με on the sides (st8 and st4). The engineering stress-deformation curve and the strain gauge results are shown in Figure 5-7. For this plot, stress corresponds to tensile force divided by the smallest cross-sectional area, and deformation is the applied deformation through stepper motor, thus not true deformation.

It should be noted that the front of the sample (Side A) was also painted with a speckle pattern, with the goal to obtain surface strains by means of Digital Image Correlation simultaneously (see chapter 5.3.2). The paint was applied on top of the strain gauges, which were unaffected by the paint.

Thick sample (ii)

During the in-situ neutron imaging experiment, two electrical resistance based strain gauges were mounted around the hole on both sides of the sample. Again, with a goal to monitor and adjust sample alignment to minimize any bending and ensuring that a uniform tensile stress is applied throughout the cross-section. It was found that the strain magnitude can indeed vary vastly between the two sides due to any sample misalignment after mechanical gripping process. Unfortunately, the strain gauges on one side failed

during the in-situ neutron experiment and uniformity of strain distribution could not be fully ensured (which would have been done by adjusting the sample alignment within the loading/gripping system).

For example, the measured strain values during the neutron experiment at 160 MPa (S3) on side A (front side) were measured as: 230 με on bottom of the hole (st1) and 990 με on the side of the hole (st6). Compared to the thin sample (where bending and misalignment could be ensured to be minimal), the strain values are significant higher in this case. This in return indicates that the strain magnitude on side B is lower and that the loading is not uniform through the cross-section. As long as the material is within the elastic regime, the averaged strain over the complete cross section will be of the same magnitude. This can be seen in the global stress-deformation curves, which are very comparable for both cases. However, as a result of this problem, the gripping and alignment system was improved and was implemented for all tests that took place afterwards (including all testing involving the thin sample geometry that was described above but was chronologically performed later).

A thick sample was also investigated at the E3 neutron diffractometer (sample R#105; details will be described in section 5.6). In this experiment, the new and improved gripping system was utilized. Eight strain gauges were mounted (four on each side) around the hole of the sample. It was shown that in this case the loading was relatively uniform on both sides. For example, the following strain values were recorded at a global stress of 160 MPa (S3): On side A, the strains on top (st5) and bottom (st1) of the hole were 95 με and on the sides (st6 and st2) 530με. On side B, the strain values were close with values at 100με on the top/bottom (st7 and st3) and 610με on the sides (st8 and st4). These values compare well with the ones from the thin sample. The stress-deformation curve and the strain gauge results for are shown in Figure 5-8. The strain results from the two strain gauges that worked during the neutron imaging experiment are included in this figure.

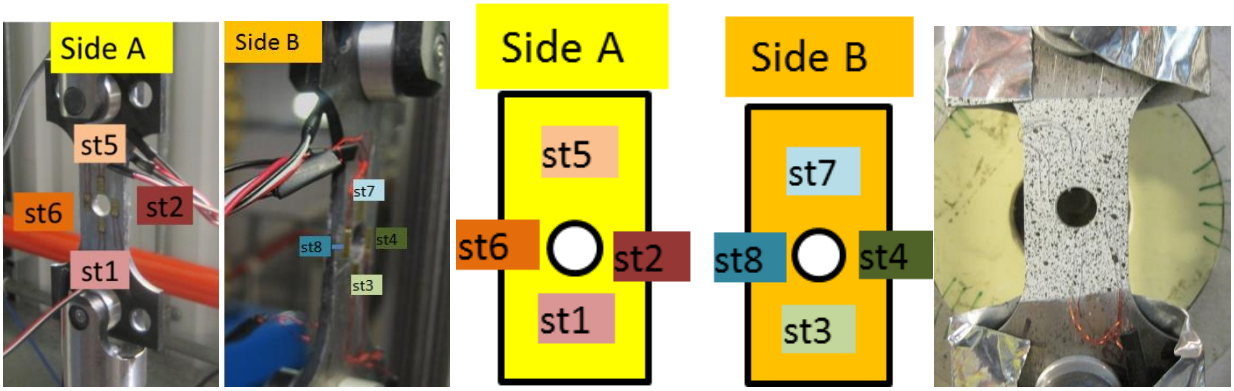

(a) (b) (c)

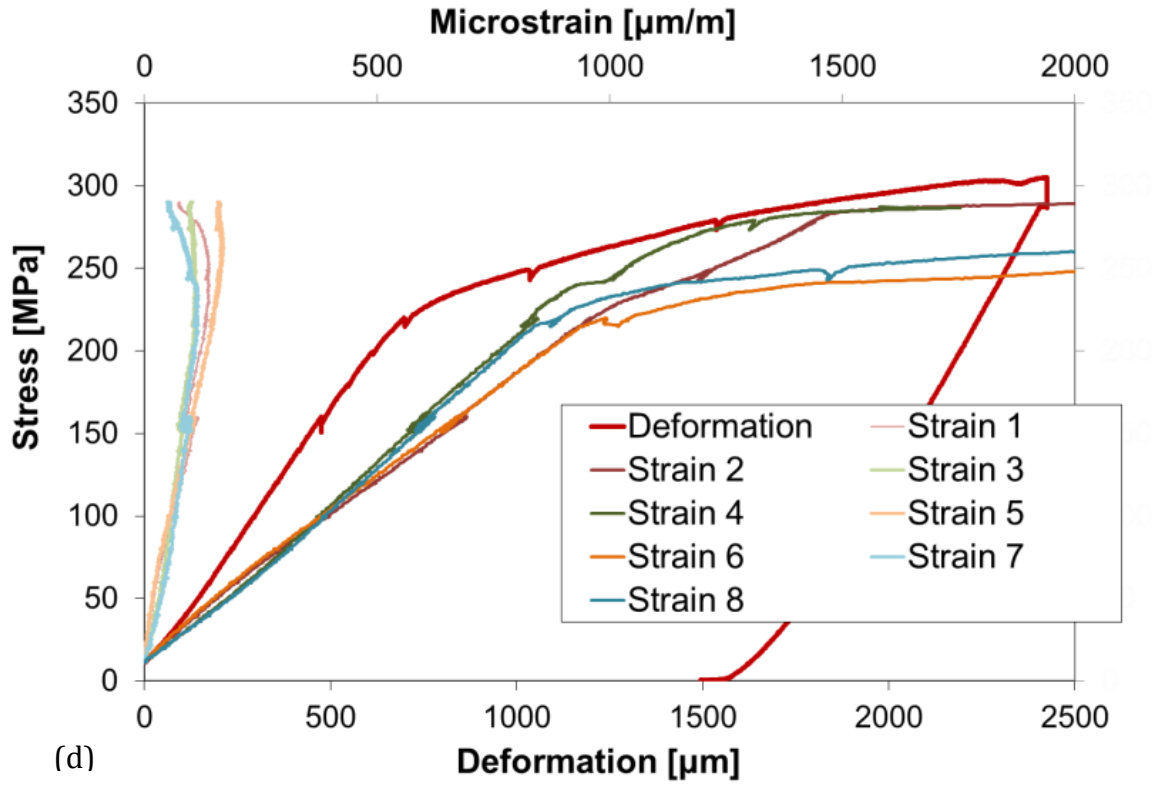

(d)

Figure 5-7. (a) Strain gauges mounted around the hole on both sides (b) Notation of strain gauges (c) The same sample painted for Digital Image Correlation (d) Stress-Deformation and Stress-Strain results as recorded during the transmission measurements (for sample R#124) at ENGIN-X, where eight strain gauges were positioned as indicated above.

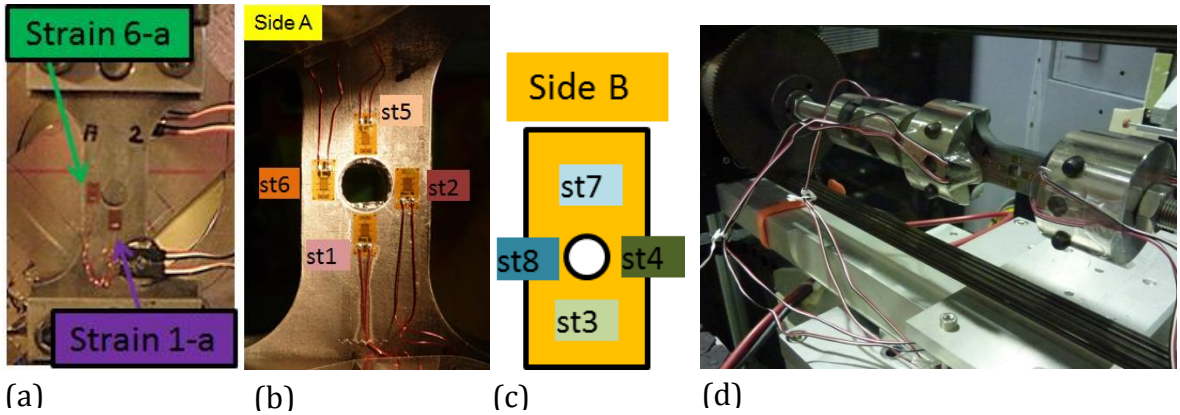

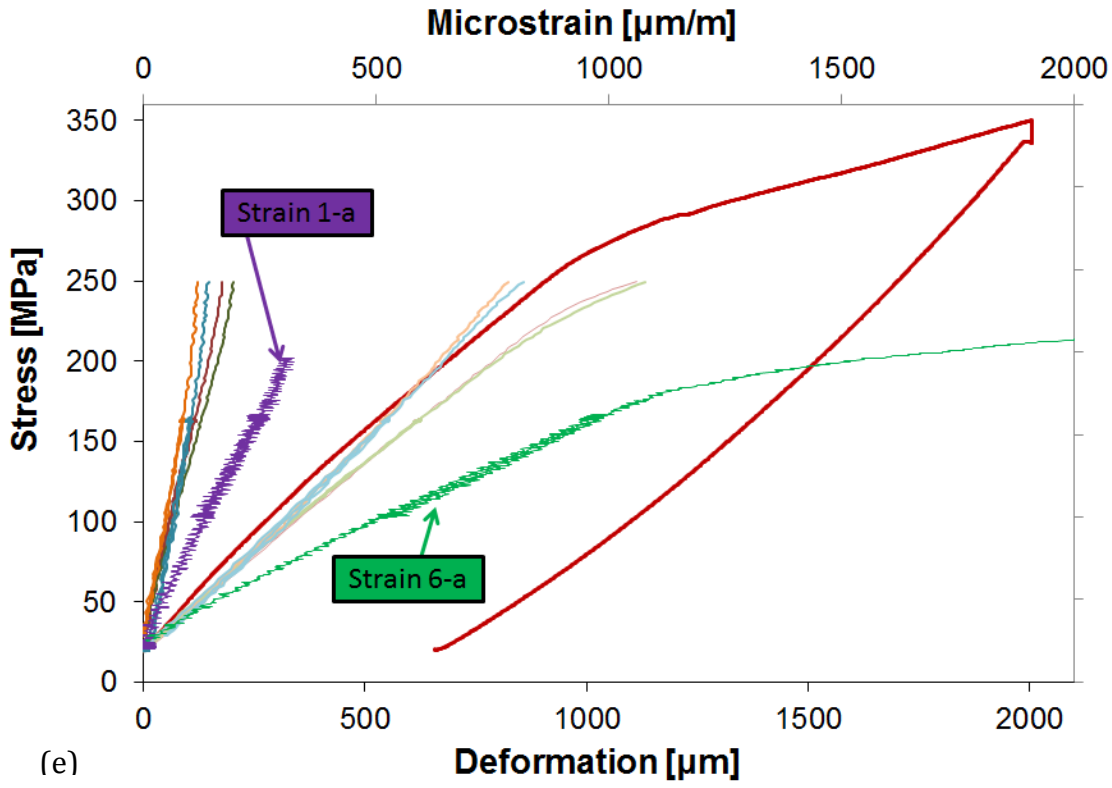

Figure 5-8. (a) Two strain gauges mounted around the hole of the thick sample during the imaging experiment (I20-2) (b-d) Notation and layout of strain gauges mounted around the hole of the thick sample during the diffraction experiment. The notation is same as in Figure 5-7 (e) Stress-Deformation and Stress-Strain results as recorded during the imaging and diffraction measurements (including strain gauge data from samples I20-2 and R#105).

5.3.2 Digital Image Correlation

On-specimen strain mapping by digital image correlation (DIC) has recently seen significant research and application in mechanically performed testing (*Sutton et al. 2008,[243]; Kaschner et al. 2010,[244]; Savic et al. 2010,[245]*). For this study, digital image correlation using the commercially available VIC-3D and VIC-2D system (Correlated Solutions) was implemented to determine surface deformation patterns for strain mapping. The VIC-3D system uses dual-cameras (whereas the VIC-2D uses only one camera) to measure the shape of an object, displacements, and full-field strains in three dimensions (see Figure 5-9). The region wherein displacements are calculated for a single, central point is called a subset, which in this case was between 33 and 35 pixels. The general motion of these subsets is tracked from image to image using numerical algorithms. The resulting displacement defines the motion of the center pixel in a given subset. The software locates, for each subset center, a specific number of pixels apart, called the step size. The relative motion between steps is then used to calculate strain on the sample surface. Surface features that are required for mapping were introduced by careful painting of speckle patterns on the surface. Samples were first painted white using nonglossy paint and lightly speckled with small black features in a random fashion.

<u>Thin sample (i)</u>

At the time of the experiment at the ENGIN-X beamline, there was only one camera available and hence VIC-2D instead of VIC-3D needed to be performed. VIC-2D is normally fully suitable for the plate sample geometry as used in this study. However, because the goal was to obtain the VIC-2D data simultaneously with the neutron data, the camera needed to be positioned slightly to the side of the sample (instead of centered). It was found that the data obtained from this camera angle did not yield reliable strain results, due to lens distortion of the image (*Sutton et al. 2008,[243]*). Using two cameras in future experiments will allow the simultaneous measurement, as they can both be positioned towards the side and hence won't be in the way of the neutron beam.

Thick sample (ii)

For the thick sample geometry, VIC-3D was carried out separately (without neutrons simultaneously), using an identical sample and loading conditions. The corresponding surface strains are shown in Figure 5-10 and the observed strain profiles agree very well with the FEM results shown in Figure 5-3.

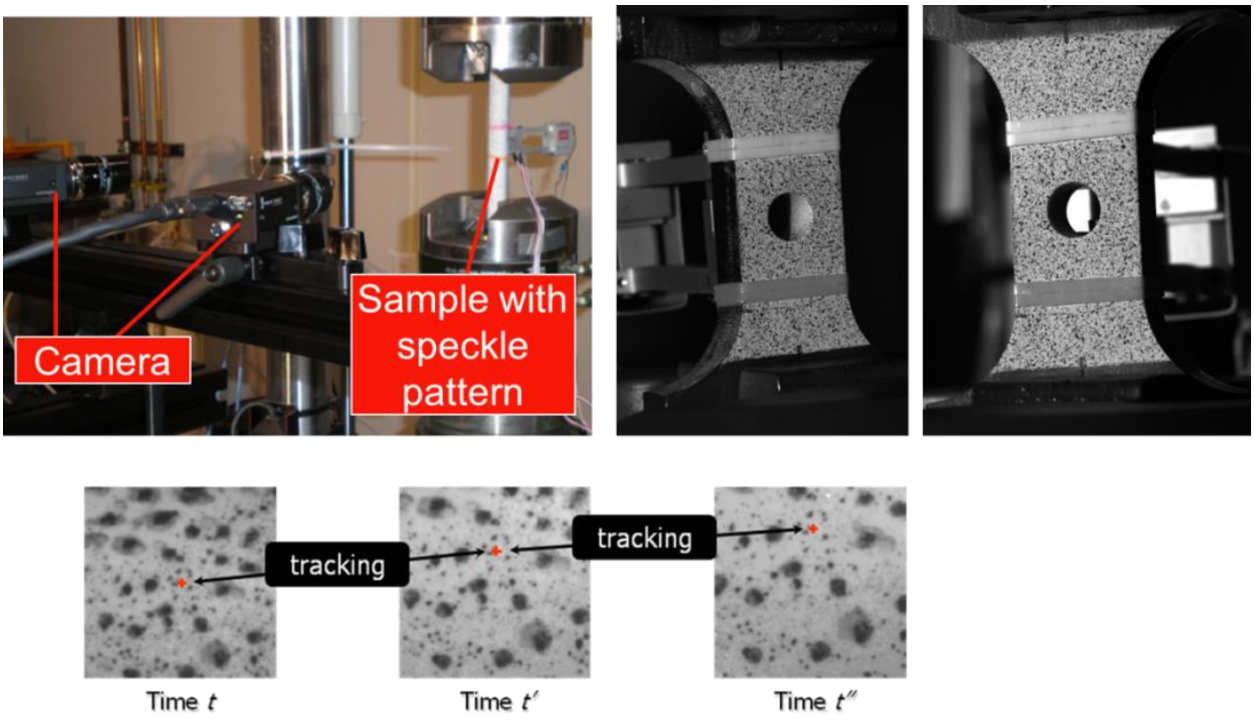

Figure 5-9. Principle of digital image correlation (here VIC-3D). The example shows the dual camera setup and the speckle pattern that is used to calculate the strains on the surface of the sample.

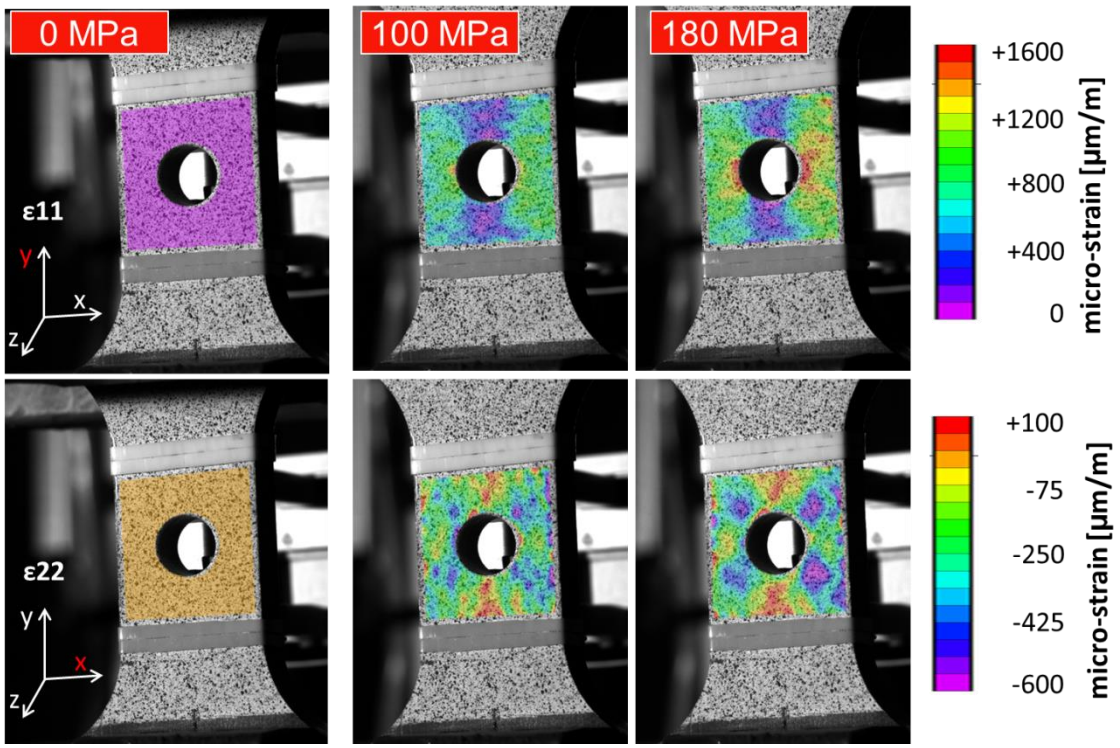

Figure 5-10. Surface strain (2 strain components in x- (ε_{11}) and y- (ε_{22}) direction) measured by digital image correlation on the thick sample. (Note: The neutron transmission measurement will probe the strain component in the z-(ε_{33}) direction.)

5.4 Neutron Transmission Experiment

5.4.1 ENGIN-X Beamline

The portable loading system was integrated at the ISIS spallation neutron source (UK) at the Engineering materials beamline ENGIN-X. This instrument is optimized for the measurement of strain in diffraction geometry. It is designed to precisely measure the lattice parameter of the sample and hence provides the required wavelength resolution that is also necessary for the imaging experiment. ENGIN-X is situated at target station 1 (producing neutron pules at 50 Hz frequency) after a 50 m flight path using a curved 'supermirror' neutron guide. The available wavelength range is between 0.5 – 6 Å. The incident beam can be defined to a size of 0.2 – 20 mm in the vertical direction and 0.2 – 10 mm in the horizontal direction. Frame overlap is avoided by using two choppers, operating

at 25 HZ or lower frequencies. The integrated beam intensity is on the order of 10^6 n cm^{-2} s^{-1}. The dedicated strain scanner has two large detector banks at $2\theta^B=90°$ for the standard operation. The general layout of the instrument is sown in Figure 5-11, while detailed information about the instrument can be found in (*Santisteban et al. 2006,*[71]; *ISIS 2015,*[246]). For the herein described experiment, the detector banks for diffraction are not used and instead a transmission detector is positioned as close as feasible behind the sample/loading system, in order to minimize image blur due to divergence of the neutron beam. The distance between the center of the sample and the detector was ~20 mm.

5.4.2 MCP Detector

In cooperation with the UC Berkley (UCB), a relatively novel neutron-sensitive Microchannel Plate (MCP) detector was used.(*Tremsin et al. 2013,*[247]) In addition to providing a 55 micron spatial resolution with high detection efficiency, this detector has very high temporal resolution thus allowing accurate energy selection in TOF experiments on a pulsed neutron source.

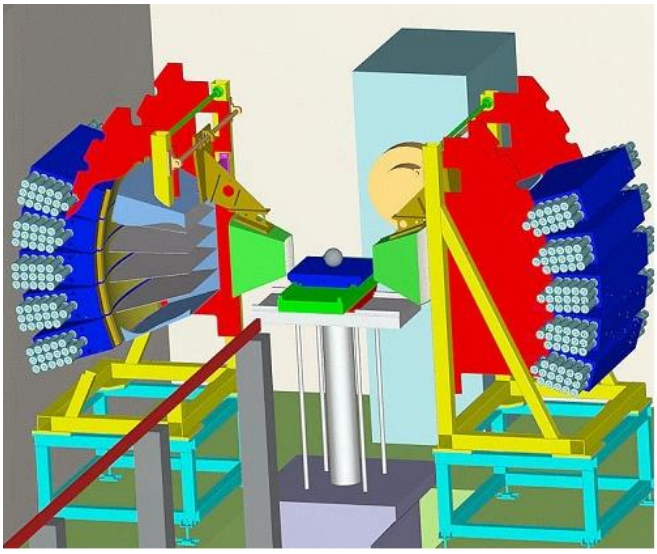

Figure 5-11. Schematic of the ENGIN-X beamline. *From* (*ISIS 2015,*[246])

It is principally the same detector as used in the earlier study (*Tremsin et al. 2005,*[105; *Tremsin et al. 2012,*[221]), but now provides larger detector spatial coverage 512 x 512 pixel (256 x 256 before). The detector consists of a Z-stack of MCP's and (2 x 2) Timepix readout chips. The MCP glass structure is doped with ^{10}B to enhance the neutron interaction within the MCP through the $^{10}B(n,\alpha)^{7}Li$ reaction. The energetic charged particle reaction products release secondary electrons directly into MCP channels, initiating an electron avalanche and a subsequent strong output pulse. The pixel size of the detector is 55 μm, the active area hence 28 x 28 mm^2. A more detailed description of the detection system can be found in the references mentioned above.

The experimental setup for both sets of experiments (thin sample and thick sample) is shown in the following figures. As mentioned above, the experiment involving the thick sample geometry was chronologically performed before the experiment involving the thin sample. In the meantime, some changes were done to the loading system concerning improved sample alignment and gripping procedures.

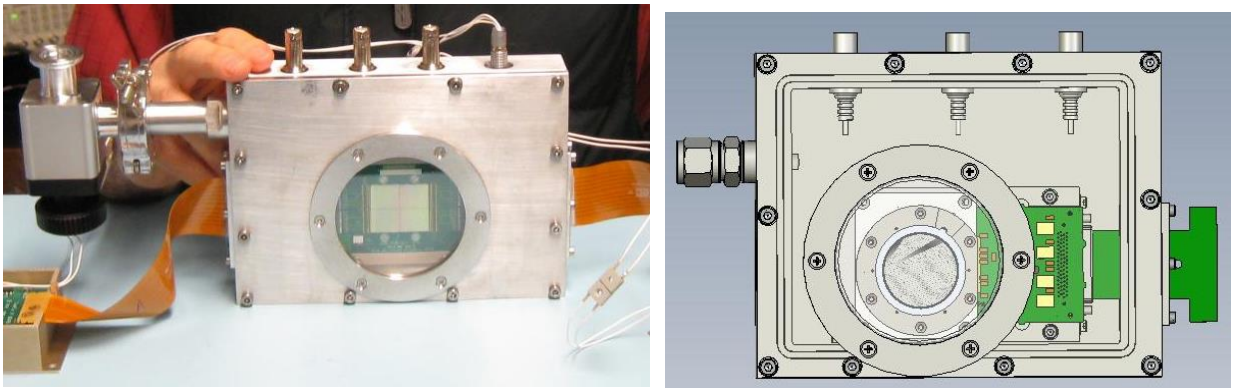

Figure 5-12. Microchannel Plate (MCP) detector that was used for the transmission measurements. It features a Medipix-Timepix readout and an of 512 x 512 pixels, with a pixel size of 55 μm.

Figure 5-13. Experimental setup at ENGIN-X for measurement of the thin sample gemeotry. The Microchannel Plate (MCP) detector is positioned behind the sample for the transmission measurement. An improved gripping system was used, compared to measurement of the thick sample (done several months before). VIC-2D was attemped to be carried out simultaniously.

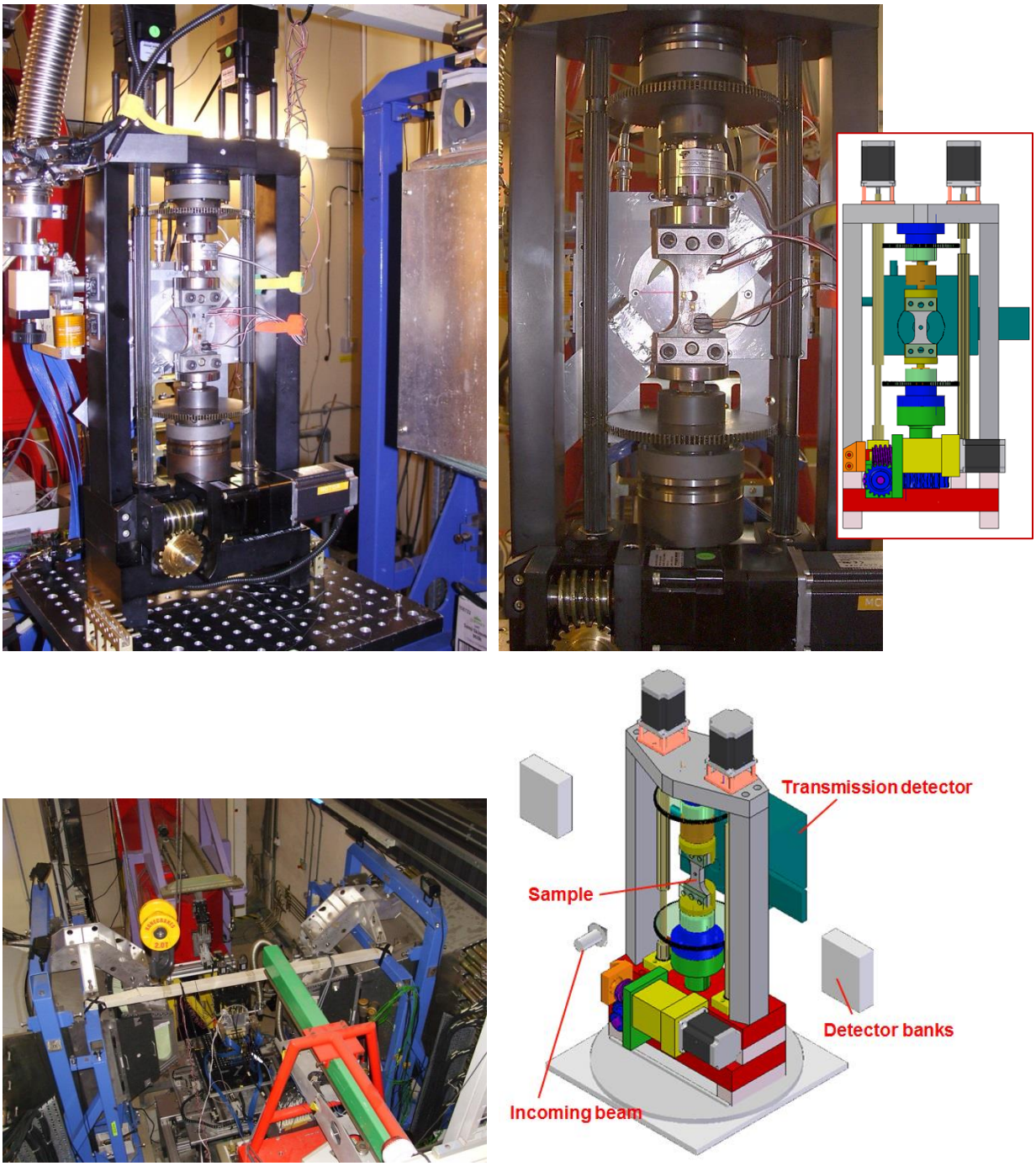

Figure 5-14. Experimental setup at ENGIN-X for measurement of the thick sample geometry.

5.5 Neutron Bragg Edge Imaging Results

5.5.1 Collected Data and Analysis

Neutron transmission data for the sample (alpha iron) was recorded with high temporal resolution around six different Bragg edges simultaneously, contrary to the earlier study (*Tremsin et al. 2012,*[221]) where only data for one Bragg edge could be recorded. The corresponding position of the Bragg edge for each reflecting lattice plane family is presented in Table 5-1, while Figure 5-15 is depicting the lattice planes for the first three reflections. A transmission spectrum was recorded for both samples at each of the three stress states defined in section 5.3. The data set for each stress state consists of a stack of 2452 individual images (each 512 x 512 pixel), where every image corresponds to a certain time of flight, i.e. wavelength. In the case of strain mapping, a high accuracy of the detected wavelength is desired and hence the data was collected only around the Bragg edges itself, so the time in between could be used for the detector readout. The timing between each image was 4.16 µs, corresponding to a wavelength interval of 0.00033 Å. The ranges during which data were recorded are included in Table 5-1, both in time of flight and wavelength.

Table 5-1. Reflections for which Bragg edges were recorded, with correspodning lattice spacing, the position of the Bragg edge and the range of the recorded data.

hkl	**d_{hkl}**	**Bragg Edge Position [Å]**	**Data Collected [ms, Å]**	
			from	**to**
(110)	2.0269	4.05	50.160 ms 3.9687 Å	52.157 ms 4.1266 Å
(200)	1.4332	2.87	35.160 ms 2.7819 Å	37.157 ms 2.9398 Å
(211)	1.1702	2.34	28.560 ms 2.2597 Å	30.557 ms 2.4177 Å
(220)	1.0135	2.03	24.760 ms 1.9590 Å	26.357 ms 2.0854 Å
(310)	0.9065	1.81	22.160 ms 1.7533 Å	23.558 ms 1.8639 Å
(222)	0.8275	1.66	20.260 ms 1.6030 Å	21.458 ms 1.6978 Å

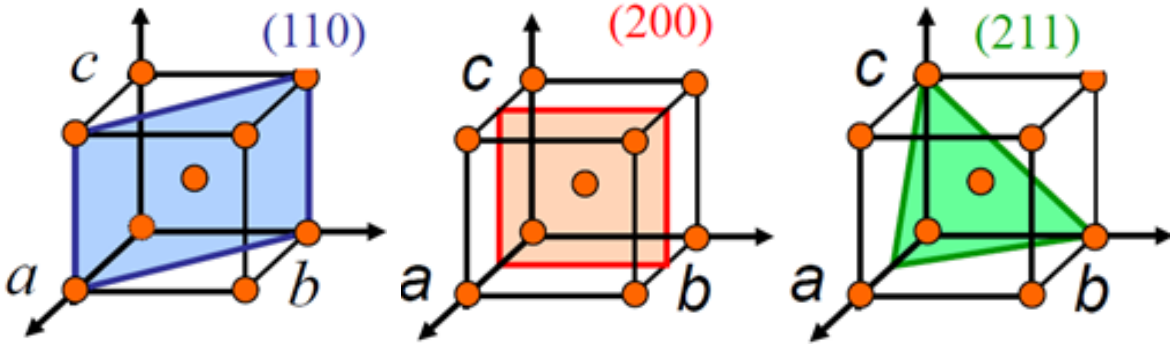

Figure 5-15. Lattice planes for the first three reflections of a bcc unit cell.

In order to obtain data of comparable quality for both samples, the data collection times for the thin sample were significantly longer compared to the thick sample. While the integration times were 3 h for each stress state (S1, S2 and S4) of the thick sample, the times varied for the thin sample. The integration times for the thin sample geometry were 8 h for stress state S1, 9.2 h for stress state S2, and only ~2 h for stress state S4, due to the fact that the neutron beam had an unexpected outage. One individual image of each stack (in this case corresponding to 2.318 Å) is shown in Figure 5-16. In order to calculate the transmitted neutron intensity, each neutron spectrum (at the pixel level) was normalized by an area of the same image stack with no sample. Due to the fact that there is some variation of the neutron intensity across the detector area (also visible in Figure 5-16, especially for the experiment with the thin sample), it would be better to normalize to a data set (spectrum) which was recorded without a sample, but this was not possible in the present experiment due to time constraints. Figure 5-16 also shows the neutron spectrum for an area corresponding to the sample and another one corresponding to an area without a sample (the example is for the thin sample and the spectrum is built from an area of 100 x 100 pixels, corresponding to 5.5 x 5.5 mm^2).

The most important parameter for measuring strain is the lattice parameter, which is determined by fitting the individual Bragg edges with a five parameter analytical function. This functions was previously proposed for transmission experiments at ISIS (*Santisteban et al. 2001,[179] Santisteban et al. 2002,[167] Steuwer et al. 2003,[23] Tremsin et al. 2012,[221]*).

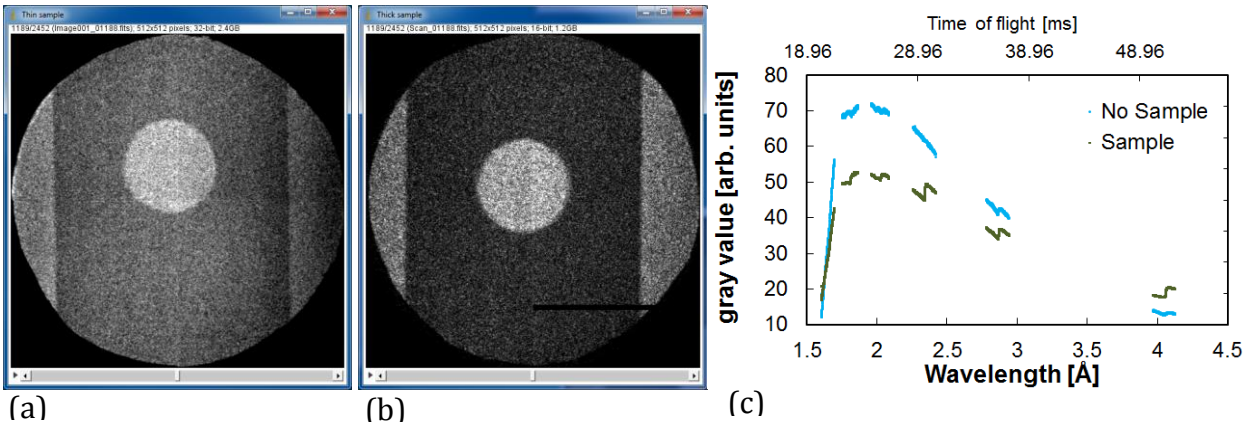

Figure 5-16. One slice of the image stack (containing 2452 images), where every slice corresponds to a certain time of flight (wavelength) for (a) the thin sample and (b) the thick sample. (c) Example neutron spectra for the thin sample image stack, where the spectrum is built from an area of 100 x 100 pixels, corresponding to 5.5 x 5.5 mm^2.

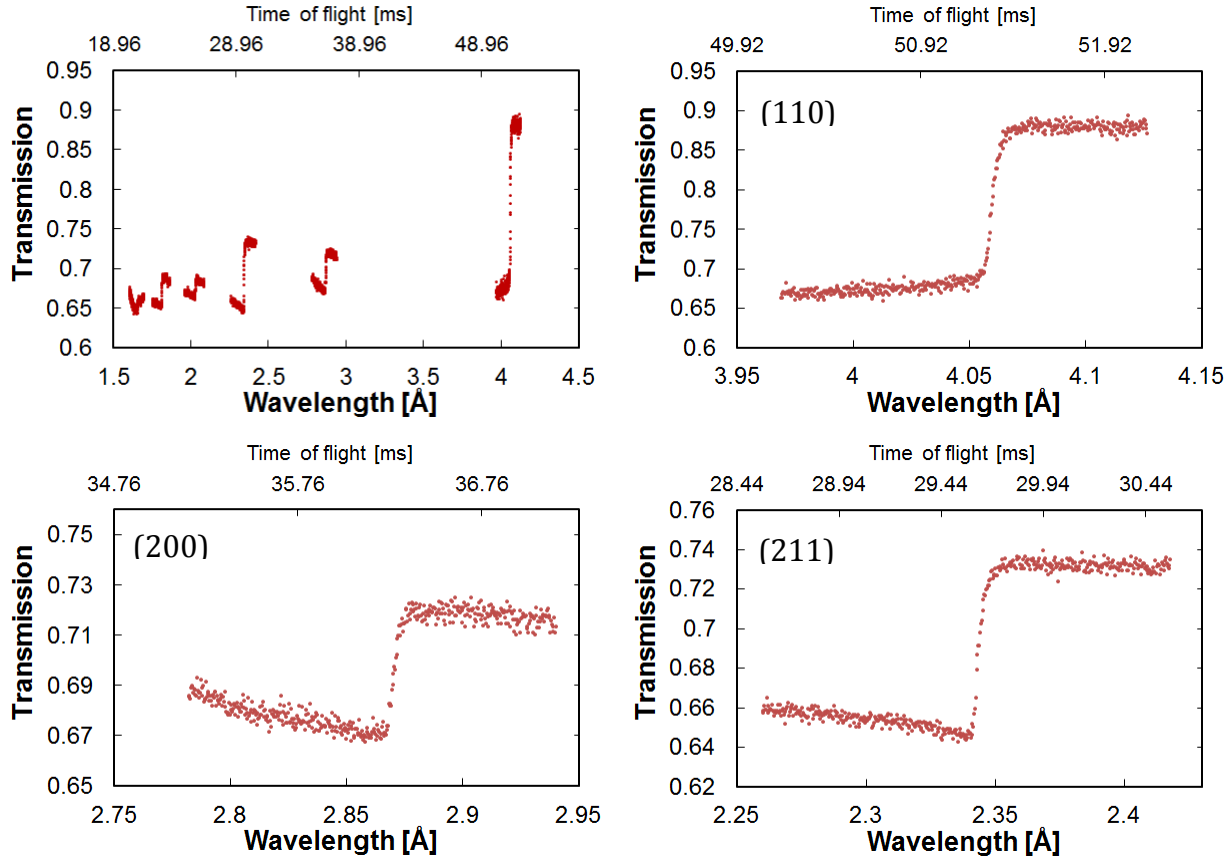

Figure 5-17. Transmission spectrum recorded around the Bragg edges for the thin sample.

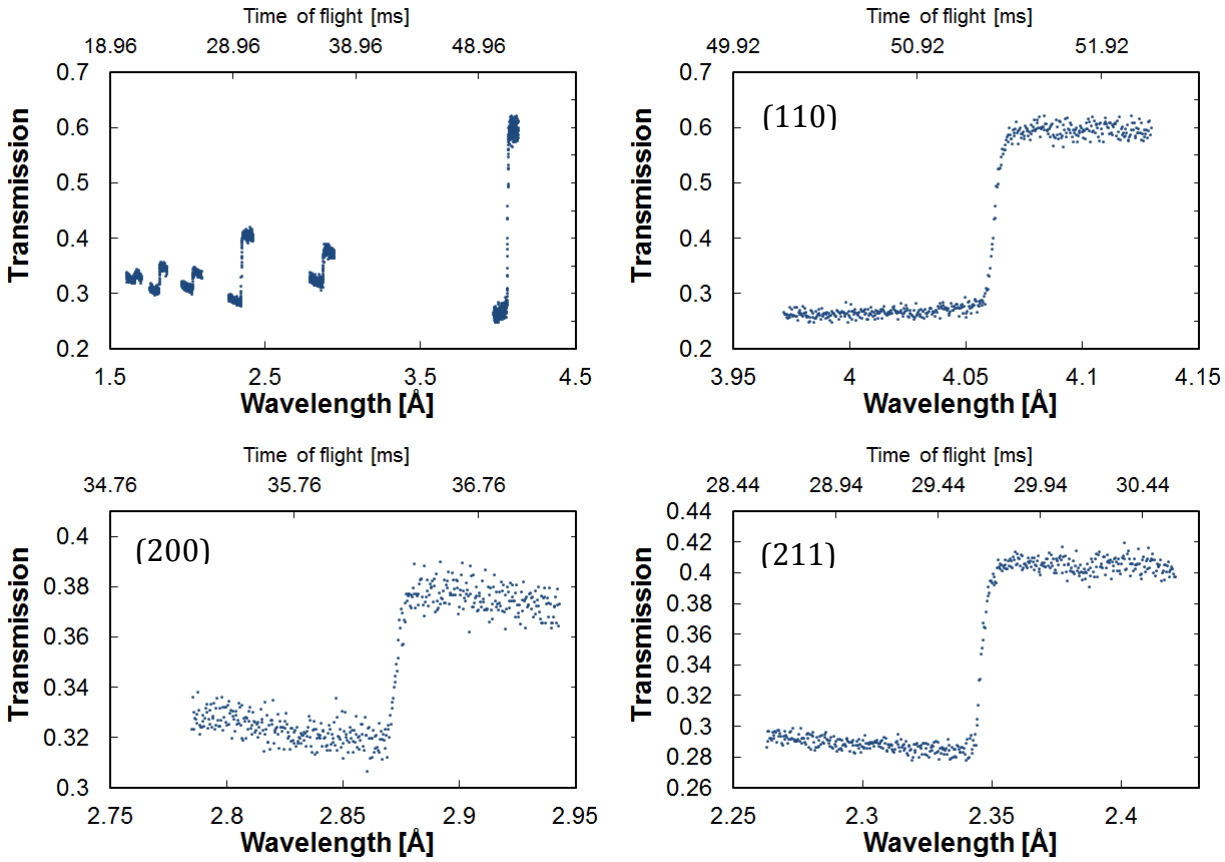

Figure 5-18. Transmission spectrum recorded around the Bragg edges for the thick sample.

The underlying profile function (Gaussian convoluted with an exponential) for the fit, describing the diffraction profiles at spallation sources, are discussed in detail by earlier research (*Kropff et al. 1982,[248]; Von Dreele et al. 1982,[249]*) with the applications for transmission measurements described in (*Santisteban et al. 2001,[179]*). By using an analytical fit, the accuracy of the determined Bragg edge position can be significantly improved, an approach routinely employed for analyzing the data obtained at neutron diffraction instruments. The following parameters of the Bragg edge are obtained: position, height, width, offset, and asymmetry.

In order to determine these parameters with adequate certainty, sufficient counting statistics are required. The counting statistics are obviously influenced by several factors (incident neutron intensity, counting efficiency, and exposure times, among others). The

limited neutron counting statistics per single pixel in the present measurement were improved by grouping several (surrounding) image pixels together and the resultant spectrum was fitted. For the data herein, 40 x 40 pixels were grouped together and the obtained value from the fitting routine was assigned to the single pixel to form a new image for each of the fitting parameters. By doing this, the spatial resolution was effectively smoothed with a 2.2 x 2.2 mm^2 'top hat' function. An example of the optimized parameter based analytical fit function for the measured Bragg edge is shown in Figure 5-19.

The first stress state was measured to provide Bragg edges that represent an accurate lattice d-spacing for the sample in a an unstressed state. After determining the position of the Bragg edge for each pixel at all three stress states, the corresponding strains can be calculated from the shifts of the Bragg edge position. For example, the strain of stress state S3 and S4 with respect to initial stress state S1 is calculated as:

$$\varepsilon^{S2,S3} = (d^{S2,S3}_{hkl} - d^{S1}_{hkl}) \,/\, d^{S1}_{hkl} \qquad (5\text{-}3)$$

In the results section below, the average d-spacing from stress state S1 (over the complete sample volume) was used for the reference d-spacing, instead of every single pixel. This allows to visualize the uniformity of determined strain values spatially for stress state S1 itself and if large gradients (for example due to residual strain) are present. Examples and quantification of the resulting strain maps will be presented in the next section.

It should be noted for completeness that more data (beyond the scope of this dissertation) for the thick sample was recorded during the experiment. For instance, several stress states with the sample rotated by 90 degrees inside the loading system were measured (Figure 5-20), with the aim to obtain average strain values for a different strain component.

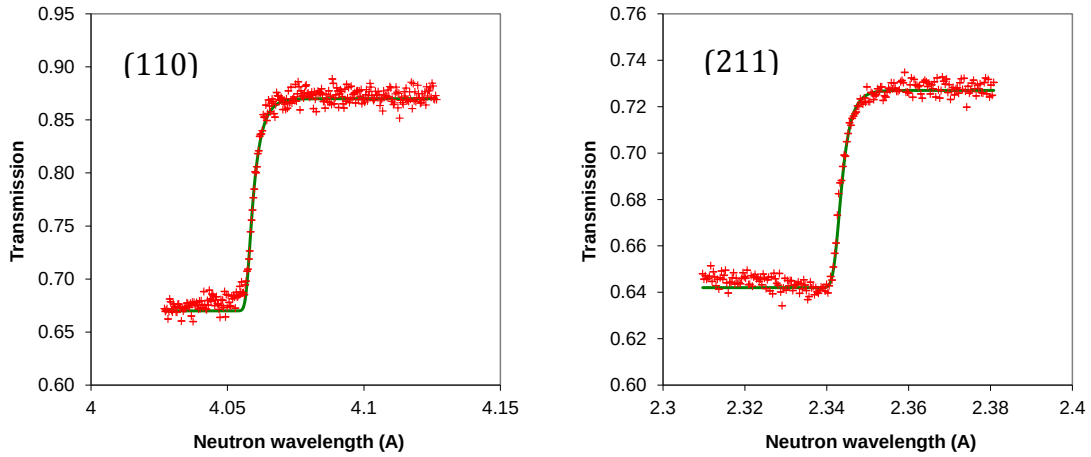

Figure 5-19. Examples of the analytical fitting functions for two measured Bragg edges for the thin sample.

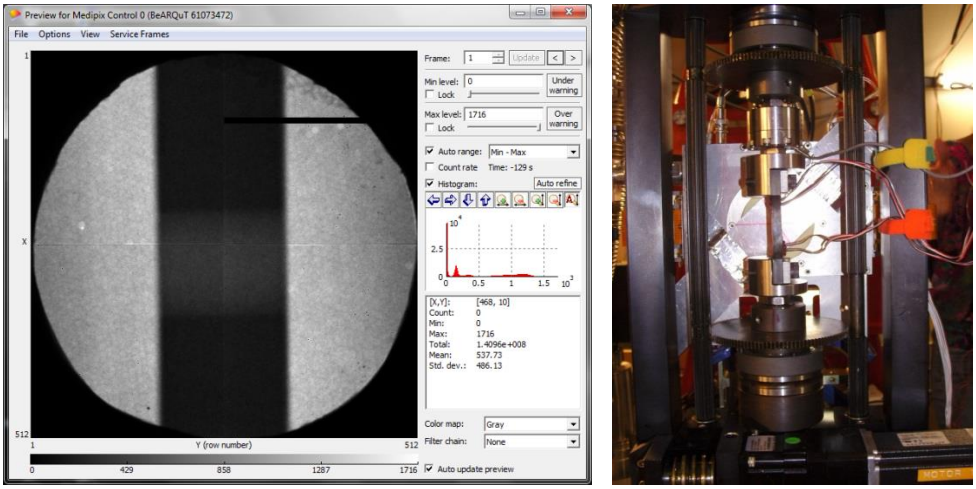

Figure 5-20. Example transmission image and picture for the sample rotated 90 degrees with respect to the neutron beam, resulting in strain component along the width direction.

5.5.2 Strain Maps and Comparison

As mentioned above, for a given sample thickness, the integration times have a significant influence on the counting statistics and hence the precision of the determined lattice parameter. Figure 5-21 is showing an example of the same data set, but with consecutively increasing counting statistics. As can be seen from these images, for the thin sample geometry, the variation of the determined lattice parameter (and strain) after three hours of acquisition time is still fairly large. For the thick sample geometry on the other hand, three hours were considered sufficient. The strain maps for the two sample thicknesses, derived from the Bragg edges corresponding to the (110) and (211) lattice planes, are presented in Figure 5-22 and Figure 5-23.

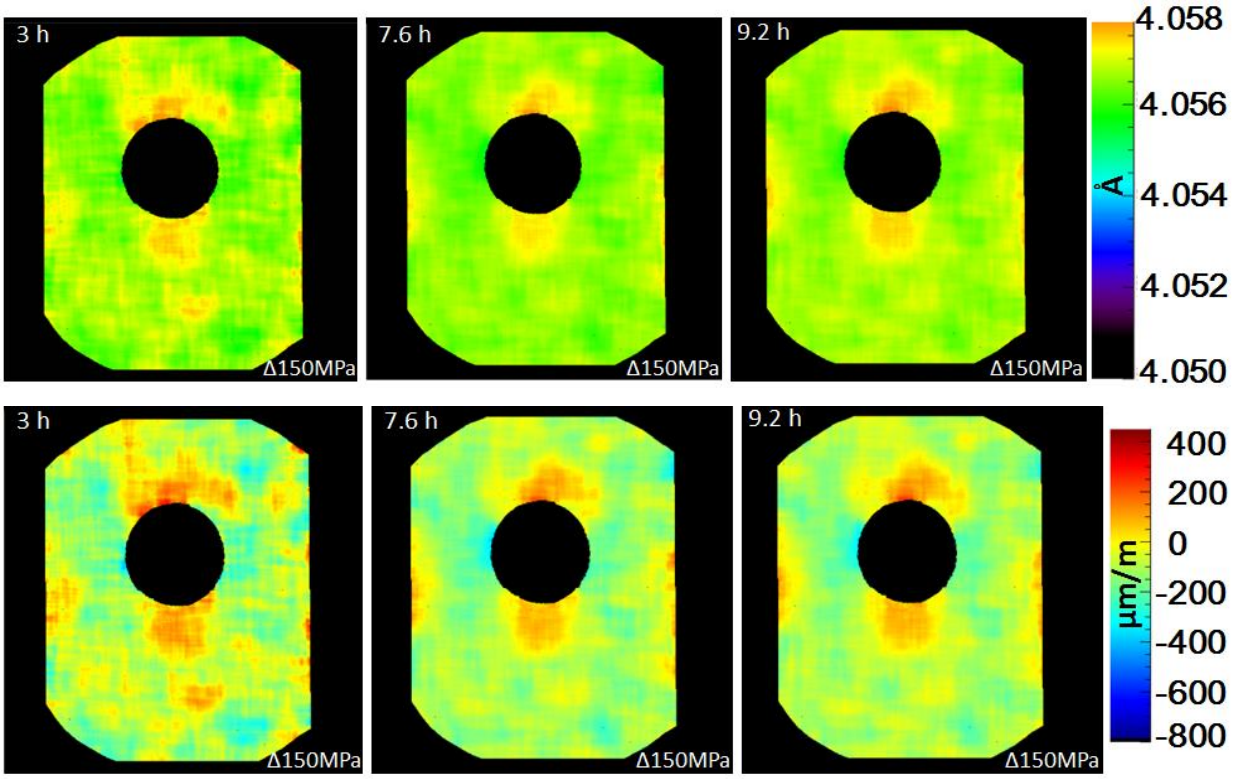

Figure 5-21. Example of the influence of integration times in the present experiment for the thin sample geometry. (a) Derived maps of the Bragg edge position corresponding to the (110) lattice planes (in this case for stress state S3). (b) The strain maps that are obtained after these acquisition times, using the average lattice paramter that was determined for stress state S1.

Since the reference stress state S1 is used in the strain calculations to determine the unstressed lattice parameter d_0, the effective stress magnitude corresponding to each strain map is slightly different as indicated. The resulting strain maps (for stress state S3 and S4) are visually nearly identical – when using an average of the lattice parameter determined from stress state S1 – vs using every pixel of stress state S1. The figures therefore show the results using the pixel average for d_0, as one can also see how uniform the determined strain maps are for stress state S1. Since the sample was stress-relieved by annealing and slow cooling, it is expected to be nearly stress-free. Any non-uniformity in the strain map for S1 could hence be seen as an indication of uncertainty in the experiment.

When investigating strain magnitudes under applied load, the following consideration should be made: Knowing the macroscopic yield stress for the material (250 MPa) and the elastic modulus E (200 GPa), one can deduce the maximum strain magnitude that can be considered to be within the elastic regime: ε_{max} = 250 MPa / 200000 MPa = 1250 με. For the Poisson direction this corresponds to ~ -375 με. Any Poisson direction strain values exceeding this magnitude must be considered carefully, as it is likely that the material has yielded at that location. Even though the above consideration is somewhat simplified (as around the hole for example, the strain at a certain point is triaxial and hence not solely related through Poisson's ratio), it serves as a good approximation for ensuring the potential for a local point in the material reaching or exceeding yield stress. In the case of diffraction (including Bragg edge imaging) based methods, the strain response of individual lattice plane families is probed. Due to elastic anisotropy of the crystal structure, the stiffness and Poisson ratio is specific to the lattice plane family (described by E_{hkl} and ν_{hkl}).[1] Using the lattice specific elastic constants for the (110) and (211) planes (E_{110} = E_{221} = 220 GPa and ν_{110} = ν_{221} = 0.28) (*Eigenmann et al. 1996,*[7]), the maximum Poisson strain

[1] It should be noted that individual grains exhibit crystalline anisotropy and symmetry, but when they form a poly-crystalline aggregate and are randomly oriented, the material can be considered to be macroscopically isotropic. If the grains forming the poly-crystalline aggregate have preferred orientation, the material is microscopically anisotropic. In polycrystalline materials, elastic anisotropy can lead to stress concentrations and inhomogeneities during plastic deformation. Beyond yield, the differences are even more significant, which can be explained by intergranular or, more precisely, grain-orientation dependent strains.

becomes ~ -320 με. However, it should be noted that the yield point for the individual hkl' s might be different from the macroscopic one as well.

Diffraction methods are specifically used to study elastic anisotropy and results are used to develop deformation models. In analogy to diffraction peaks in a diffraction experiment, the position of the Bragg edge only represents the elastic portion of the strain. When the material has yielded, plastic strain effects (like dislocation glide, grain boundary sliding, grain rotation, etc.) are not detected by only looking at the position of Bragg edge.

Thin sample (i)

The results for thin sample show some variation of the lattice parameter at stress S1 (both for (110) and (211)), visible as strain differences in Figure 5-22. It appears that there is a slight gradient from left to right. One might speculate that this could result from the non-uniform beam intensity (compare Figure 5-16): When building the corrected neutron spectra (based on an area with no sample of the same image), the Bragg edge has slightly different height. Even though the position of the Bragg edge shall be unaffected by the height, in practicality the determined position may be shifted slightly as well.

The stress variation around the hole is clearly resolved for stress state S3 and S4. For stress state S3, the transmission results are compared with the results from the finite element model. For the area away from the hole, that is purely elastic, the determined values are in very good agreement. Also for the region on top of the hole, excellent agreement between measured and predicted results is found. For the region on the side of the hole, at a first glance, the agreement is less favorable. However, as discussed above, the strain value from the FE model exceeds the limit of what can be considered elastic (the model does not consider plasticity). It can hence be expected that the material has yielded in this location and that the measured strain magnitude will be lower than if the material would still be elastic. It can therefore be concluded that the interpreted strain value of ~ 400 με appears to be reasonable. The quality of the data at stress state S4 suffers from the fact that the effective acquisition time was only ~2 hours. The strain magnitudes are higher than for stress S3 as can expected.

Overall there is very good agreement between the determined lattice strain for the (110) and (211) lattice planes. This is conform with the lattice elastic constants, which are the same for both lattice planes ($E_{110} = E_{221} = 220$ GPa and $\nu_{110} = \nu_{221} = 0.28$).(*Eigenmann et al. 1996,*[7]) Data was also collected for other Bragg edges as described above and the maps can be produced in the same manner. However, given the same experimental parameters, the less pronounced Bragg edges will result in larger uncertainties of the fit.

The finite element model suggests that the strain is very uniform through the sample thickness. Providing that the sample is within the elastic regime, the uniform strain should cause only a simple shift of the Bragg edge, while the width remains unchanged. For this purpose, a map of the Bragg edge width parameter is depicted in Figure 5-24 for all three stress states, corresponding to the (110) edge. The overall width for stress S1 and S3 appears to very similar, as expected. But if the material exceeds the elastic range, in analogy to peak broadening in a diffraction experiment, it is expected that the Bragg edge widens. As discussed above, it is suspected that at the side of the hole the material has already started to yield at stress state S3. An indication of this can be seen in Figure 5-24, where the line profile for S3 displays an increase of the width parameter. A strong increase of the width can be seen for stress state S4, but the data needs to be considered less reliable due to the low counting statistics. The trend of the increased width at the side of the hole however is clearly observed.

<u>Thick sample (ii)</u>

For the thick sample, the lattice parameter (see Figure 5-23) determined for the (110) planes appears more uniform than for the thin sample. The incident beam intensity and hence normalization was also more uniform in this case. A slightly larger variation is observed for the (211) lattice planes, which is likely due to the slightly larger uncertainty for the fit of the (211) edge vs the (110) edge.

The FE model predicts a uniform strain magnitude of -126 με through the sample thickness at a location away from the hole and the measured results are in very good agreement. The stress variation around the hole is again clearly resolved for stress state S3. Comparing the

transmission results with the FEM results for stress state S3 (which is effectively 10 MPa lower than S3 for the thin sample) reveals excellent agreement between the two. Since the FE model predicts a variation of the strain magnitude through the sample thickness for these locations, the average magnitude is included in the graph in Figure 5-23 (remember that the transmission method effectively measures the average strain through the sample thickness). Due to this strain gradient, it is expected that a widening effect is introduced to the Bragg edge. With the aim to potentially quantify this effect, corresponding edge width maps are presented in Figure 5-25. Indeed a sharp increase of the width can be observed for top of the hole at stress state S3 (compared to S1). However, the overall edge width at S3 is slightly higher than at S1 (even at locations where uniform through-thickness strain is predicted). This can be explained by the fact that the sample additionally might have experienced bending during the tensile test (due to misalignment) as was discussed in section 5.3.1. As was mentioned in this section as well, the average strain values though the thickness will be comparable even if some bending occurs, as long as the sample is within the elastic regime.[2] The predicted strains for stress state S3 are barely exceed the expected elastic limit and hence are close to the 'true' elastic strain magnitude to be expected.

The strain map for stress state S4 shows much higher strain magnitudes than at S3. A pronounced tensile strain is observed on top and bottom of the hole (up to 190 με), while strong compressive strains are observed throughout the rest of the sample and are not necessarily concentrated at the sides of the hole. The largest recorded compressive strains are ~ -420 με (besides some outliers towards the edge of the sample). The most interesting phenomenon however is observed for the Bragg edge width at stress state S4, which is significantly increased at the sides of the hole, but extending all the way across the sample width. This indicates that after the material has yielded at the sides of the hole, the stress further concentrated in this area and caused the material to yield across the width.

[2] This has actually been verified in additional mechanical tests where strain gauges were mounted on both sides and where an additional extensometer was used. The average strain between the strain gauges of both sides was of the same magnitude as the one measured using the extensometer, even if the individual strain gauges showed varying values due to bending.

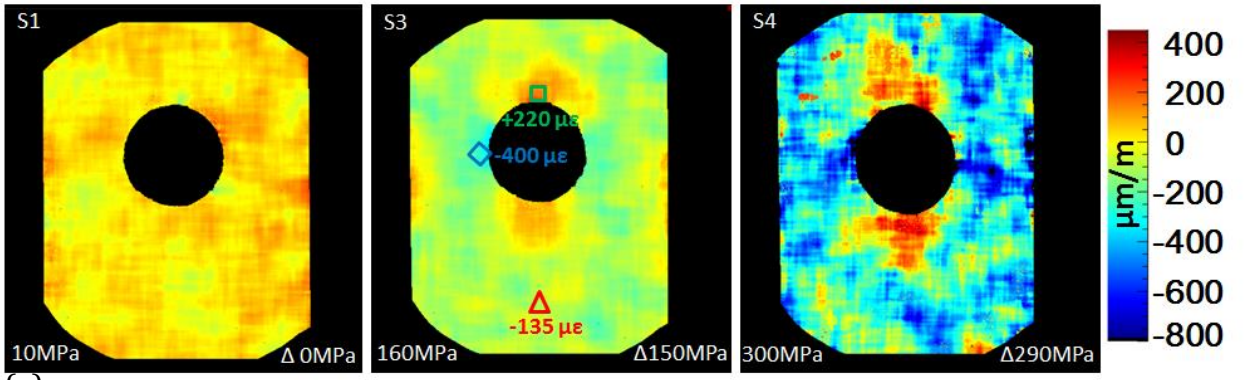

(a)

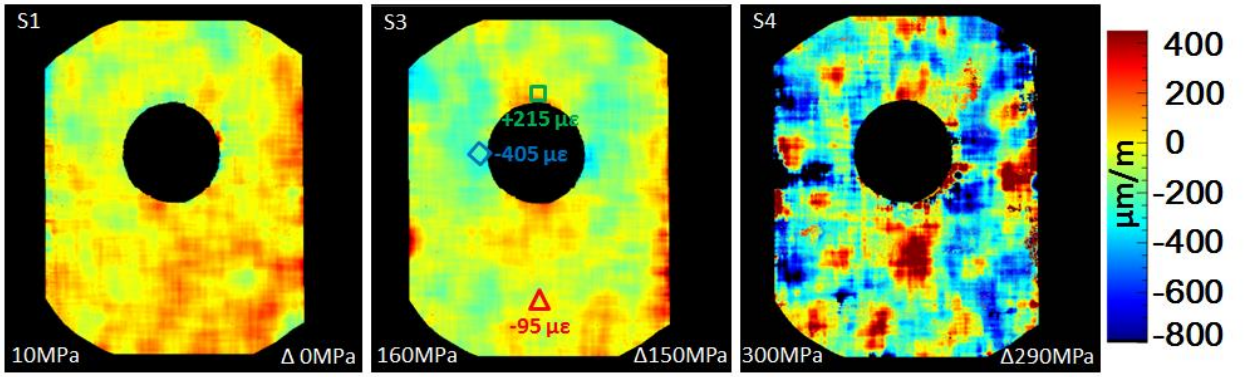

(b)

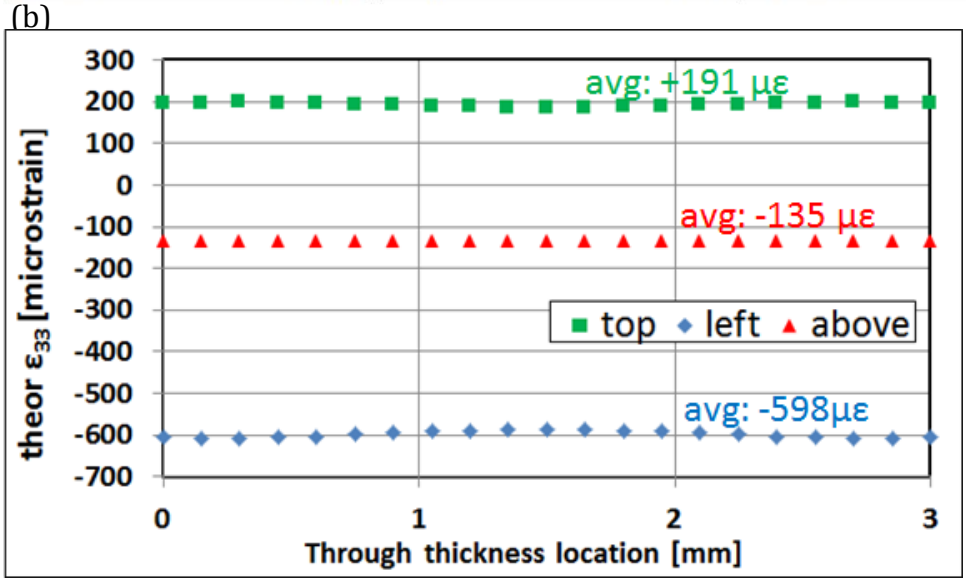

(c)

Figure 5-22. (a) Strain maps for the thin sample, derived from the Bragg edges corresponding to (a) the (110) lattice planes and (b) the (211) lattice planes. (c) FEM results for three locations (indicated above) at stress state S3 (effective stress of 150 MPa) showing the strain variation through the sample thickness (9.5 mm). It must be noted that the FE model does not consider plasticity (see discussion in text).

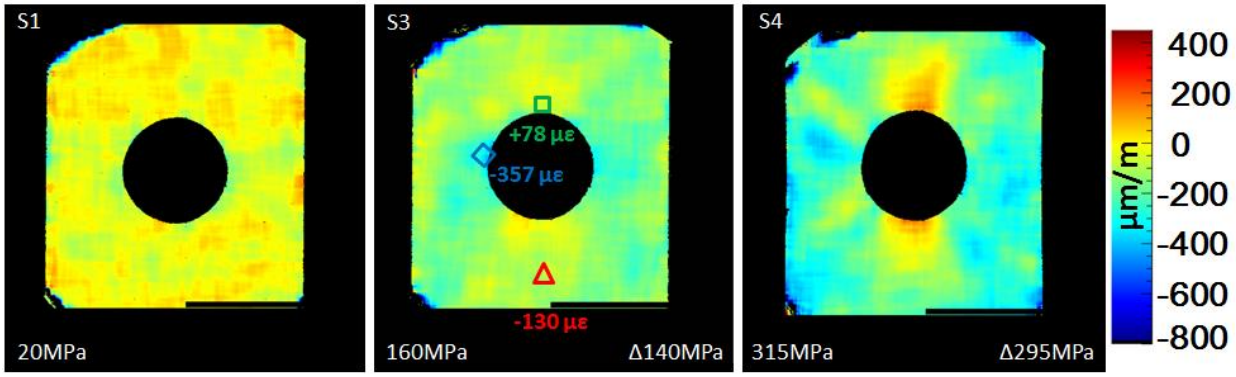

(a)

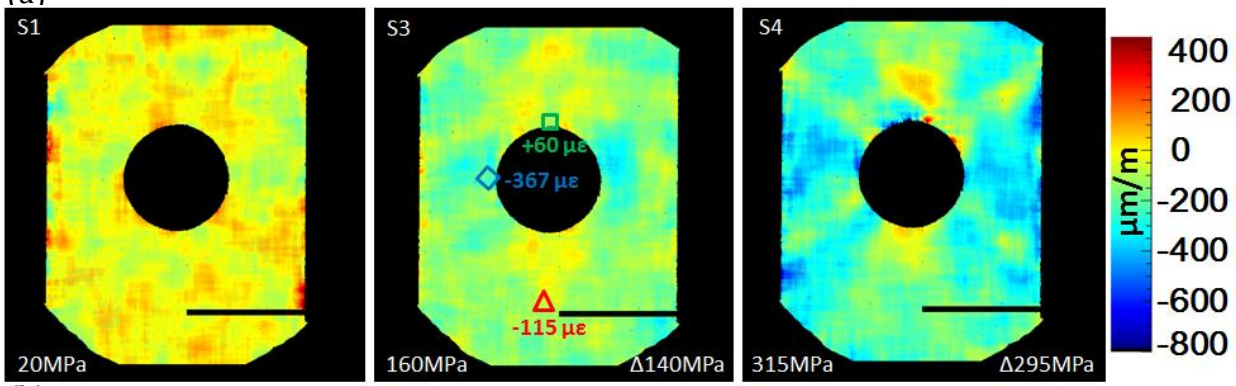

(b)

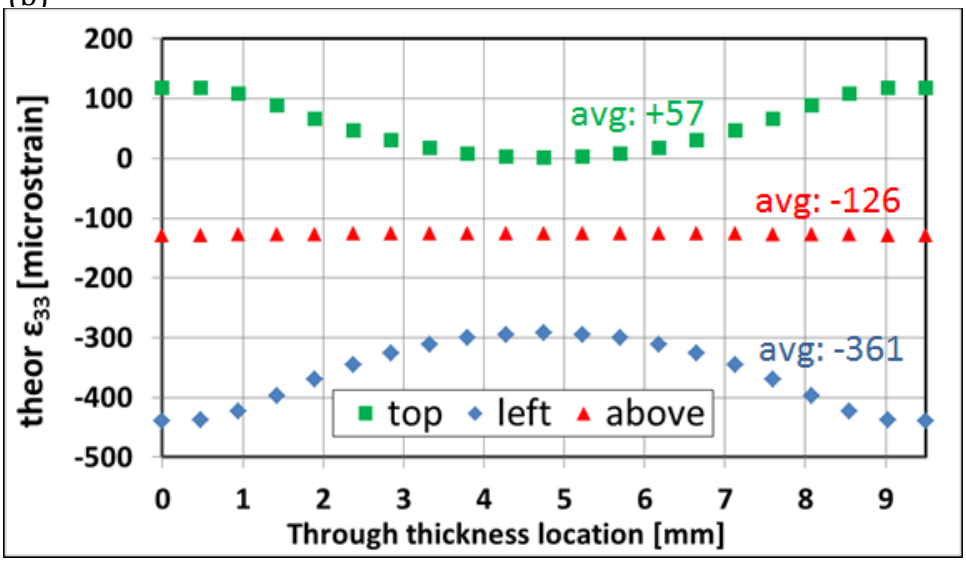

(c)

Figure 5-23. Strain maps for the thick sample, derived from the Bragg edges corresponding to (a) the (110) lattice planes and (b) the (211) lattice planes. (c) FEM results for three locations (indicated above) at stress state S3 (effective stress of 140 MPa) showing the strain variation through the sample thickness (9.5 mm). It must be noted that the FE model does not consider plasticity (see discussion in text).

This could not be deduced form the strain map alone, as the strain value is around ~ -420 με also at other locations. Observing the associated changes in the Edge width at S4, this observation could also explain the occurrence of tensile strains that are observed in the strain map away from the hole (most pronounced on the left side of the sample). These positive strains occur right above/below where the material is expected to have fully yielded. To fully conclude that these values are in agreement with plasticity and stress concentration theories, one would need to elaborate on the numerical model for this case. Either way, this example shows the potential of the Bragg edge method for strain mapping even beyond the elastic regime and to detect where large plastic strains have accumulated.

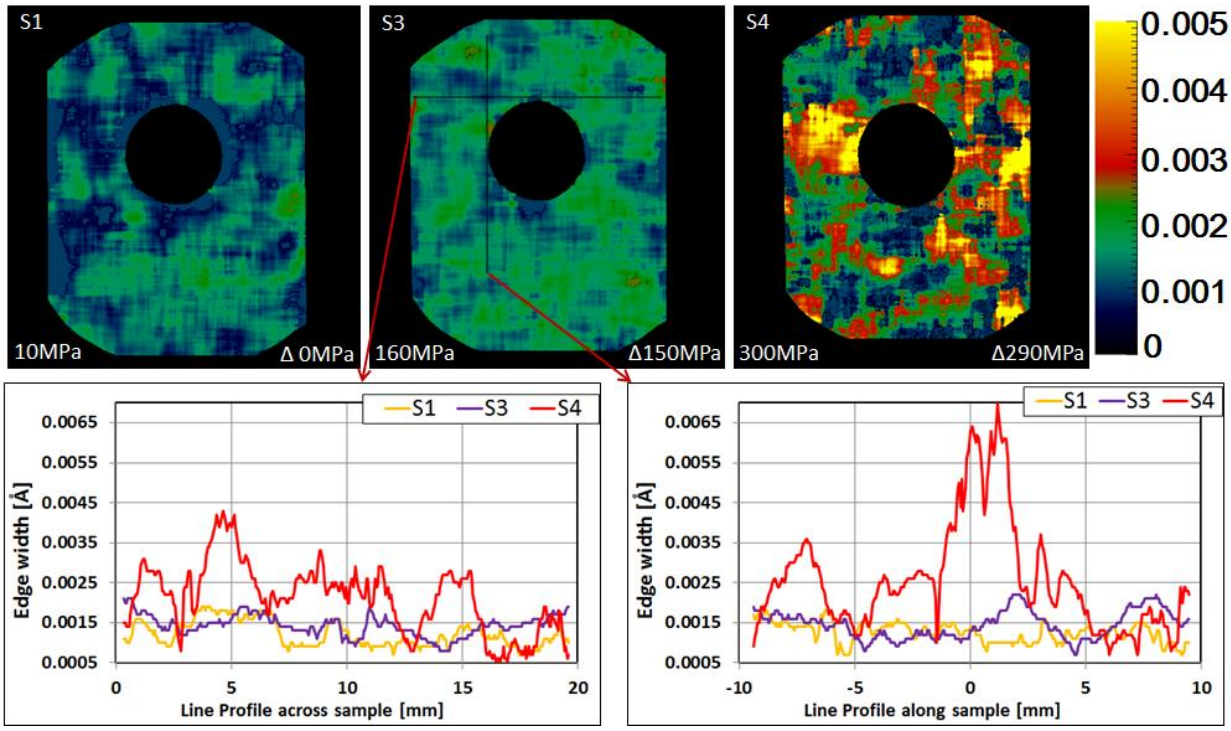

Figure 5-24. Thin sample (i): The edge width parameter for the (110) lattice obtained using the fitting routine. Spatial maps are shown on top. The graphs show a line profile across (the hole center is at 10 mm in this case) and along (the hole center is at 0 mm in this case) the sample for all three stress states, as indicated in the above map. An increase of the width can be noticed at the side of the hole for stress state S3. A strong increase of the width is noticed for stress state S4.

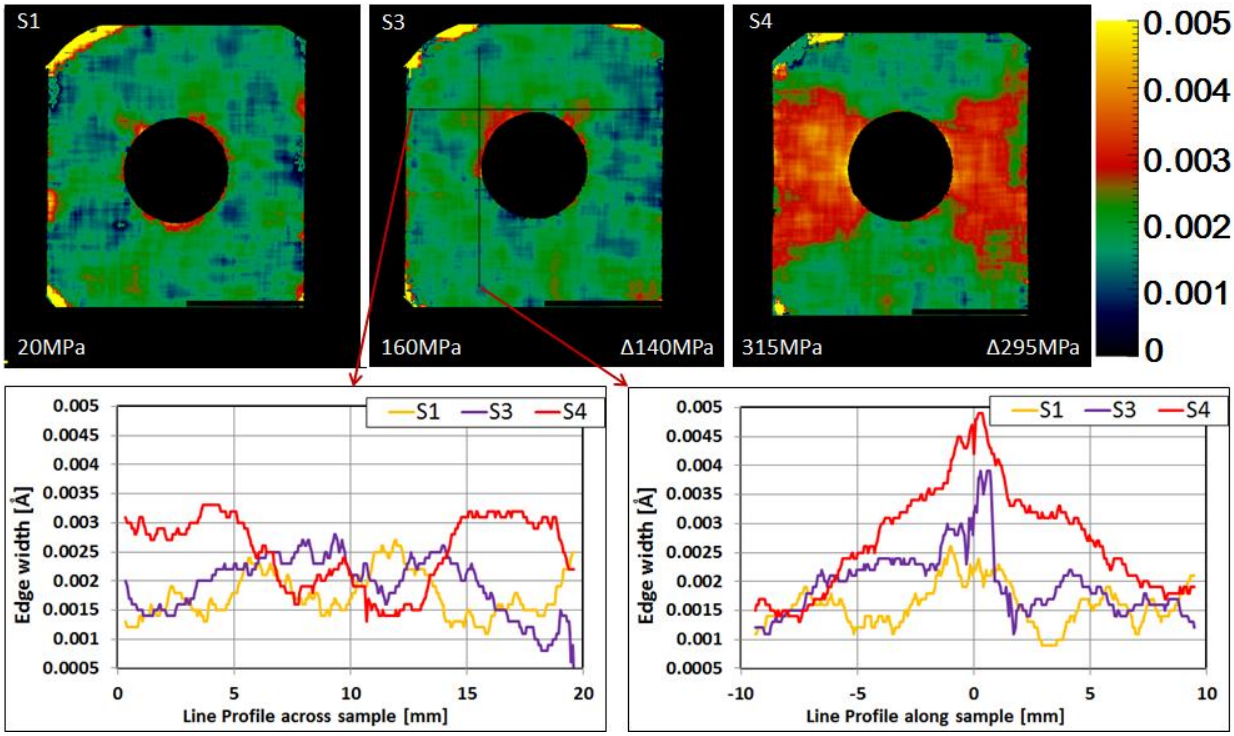

Figure 5-25. Thick sample (ii): The edge width parameter for the (110) lattice plane. Spatial maps are shown on top. The graphs show a line profile across (the hole center is at 10 mm in this case) and along (the hole center is at 0 mm in this case) the sample for all three stress states, as indicated in the above map. A significant increase of the width can be detected at the sides of the hole for stress state S4. It appears that an effect is also visible for the side of the hole at S3 (however some effect is also visible under S1, so it might also just be due to poorer counting statistics close to the hole).

5.6 Neutron Diffraction Results from E3

Neutron diffraction measurements were carried out for the 9.5 mm (thick) sample at the engineering diffractometer E3 at HZB with the goal to measure the strain gradient through the sample thickness. For these measurements, the gauge volume was to set to 1mm x 1mm x 1mm, using slits in the incident and diffracted beam direction. The loading system was positioned on its side (see Figure 5-26) and the scattering geometry chosen so that the through thickness strain component (ε_{33}) was measured. A fixed wavelength of 1.19 Å was

used and the detector scattering angle 2θ was set at 95°, so effectively the (220) lattice plane spacing was probed. The integration time for each measurement point was 1 h.

Three spatial locations were probed, in analogy to the examples that are presented above for the finite element and transmission data (side and top of the hole and away from the hole). It was attempted to position the gauge volume close to the hole, but still completely inside the material (for the points close to the hole, the center was positioned 4.5 mm away from the sample center). For all three positions, five locations though the sample thickness were probed at a step size of 1.7 mm. Again, care was taken to position every measurement position inside the sample, in order to avoid surface scattering effects which may artificially shift the position of the diffraction peak.

The stress states S1 and S3 correspond exactly to the same stresses as were applied during the transmission experiment for the thick sample (S1 = 20 MPa and S3 = 160 MPa). The measured lattice parameter from S1 (at each location) was used as the reference d-spacing and to calculate the strain values at S3. Positioning

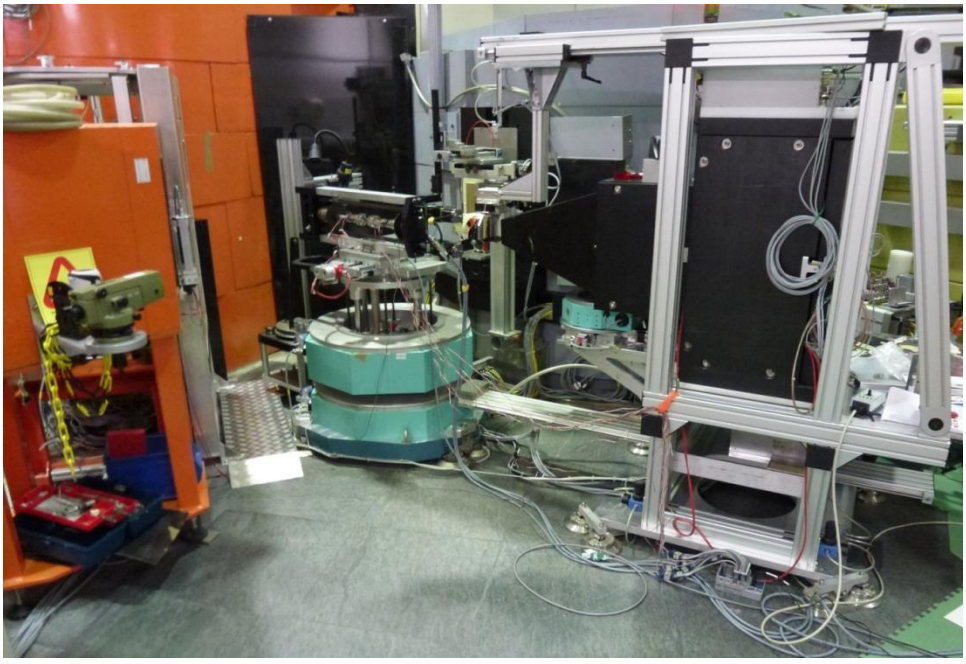

Figure 5-26. Experimental setup at E3, with the loading system positioned sideways on top of the sample positioning table.

For stress S3, the strain values obtained for the location close to the top side of the hole are of the same sign (tensile) and magnitude as was predicted by the FEM model. Expected strain gradient – with lower strain magnitude towards the center of the sample – were confirmed. The values obtained for the location at the side of the hole also agree with the FEM results, as they are of the correct sign (compressive) and resulting magnitude within the uncertainties of the experiment. However, a clear trend of the gradient is not revealed here. The results for the location away from the hole appear even less accurate at a first glance, however besides one outlier (at 3 mm), the values are still nearly within the predicted values from the FE model. The neutron counting statistics for the measurement position at the far end of the sample thickness relative to neutron beam (in Figure 5-27correspond to 0 mm), were very poor and even doubling the counting time still resulted in large uncertainties for the fit. Especially the data points collected for all three locations at ~ 3 mm into the sample may have been prone to an unknown experimental error, as they mutually shows less agreement. Overall, the results agree fairly well with the predicted FEM results, even though the uncertainties are relatively large.

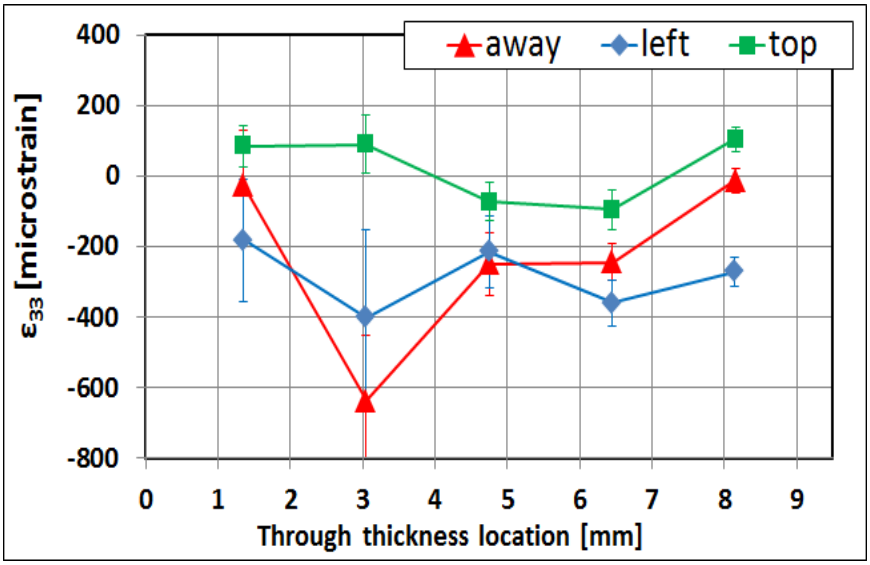

Figure 5-27. Strain results from neutron diffraction for strain component in through-thickness Poisson direction (ε_{33}) measured at three locations (A, B, C) for stress states S3 and S4 (where S1 was used as the d0 reference).

5.7 Conclusion

Many proof-of-principle measurements have demonstrated that wavelength dependent neutron imaging can be used to spatially resolve effects of texture, crystallographic phase and lattice strain, by analysis of Bragg edges. This chapter presented a detailed case study for strain mapping using the Bragg edge transmission technique. Two sets of flat tensile samples, one being relatively thin and one being relatively thick, were investigated. Both samples had a center of hole (d = 8 mm) which introduced a stress concentration under applied load. The macroscopic strain on the surface was additionally monitored using resistance based strain gauges and digital image correlation, both in separate mechanical tests and in-situ with the neutron imaging experiment. Finite element modelling was initially used to determine the expected strain variations at sample geometries of varying thicknesses. The results from the FE model were used for comparison with the experimental results. Furthermore, 'traditional' neutron diffraction was used with the goal to probe the strain gradients – that are present close to the hole – within the thick sample geometry.

By using the time-of-flight mode at the spallation source ISIS, unique advantages were exploited due to the fact that several Bragg edges could be recorded simultaneously. This can be extremely useful if phase transitions are to be studied simultaneously, as new edges will appear and others becoming weaker. For strain mapping, the elastic and plastic anisotropy can be studied efficiently. Moreover by fitting all edges simultaneously, more precise strain maps could even be obtained. At a reactor source using a tunable monochromator, such measurements will take significantly longer amount of measurement time. It should be noted in this respect, that most of the conclusions that are applicable when comparing (engineering) diffraction experiment for both approaches (TOF vs monochromator) are also applicable for Bragg edge imaging as well.

The MCP detector technology with Timepix readout (*Tremsin et al. 2013,*[247]) proved to be very suitable to obtain high wavelength resolution in order to determine the position of the Bragg edges with needed precision. Despite the good spatial resolution for a neutron detection system, the active area of such a MCP detector is (due to the size of the Timepix

readout chips) relatively small as of now – especially compared to standard neutron imaging scintillation-based and lens-coupled detectors. But further improvements of the readout electronics are expected to lead to larger active area. Compared to an earlier study (*Tremsin et al. 2012,*[221]), the area increased from 256 x 256 pixels to four times the size, even within a few years.

It was shown that the varying strain distribution due to the stress concentration can be resolved and that the determined strain values are in excellent agreement with the results predicted from the finite element model. The analysis and interpretation of the thin sample geometry is straight forward and unambiguous. Once the material exceeds the elastic limit, an interpretation is analogue to a diffraction experiment. However, while many loading points are usually measured in a diffraction experiment to describe the stress-strain response, this would take significantly longer in transmission, which on the other hand obviously provides spatial resolution.

The thick sample showcases one important shortcoming of the Bragg edge transmission method: Since an average value through the complete sample in the direction of the incident beam is measured, peak value of strains will be easily missed if strain gradients are present, which is the case for the majority of samples. It was shown that the Bragg edge width can provide important information regarding strain gradients with spatial resolution in one plane. The analysis of the edge width maps is especially crucial if no detailed additional information is available (such as was available through the FE model in this case). In analogy to peak broadening in a diffraction experiment (*Todd et al. 1995,*[250]*; Withers et al. 2001,*[251]*; Hutchings et al. 2005,*[1]), the increase of the width can be used to study plasticity effects. The practicality and usefulness of this became apparent for the thick sample at stress state S4, where the width drastically increased from the sides of the hole all the way toward the edges, indicating local plasticity and yielding near the hole and along the width. By observing a complete map of the sample, such widening effects can be unambiguously attributed to the sample, while in diffraction experiments, a widening of the diffraction peak may not be explainable at first (if it appears unexpected). The imaging

data can serve in such cases uniquely as complementary for successful planning of a diffraction experiment.

In the framework of this study, neutron diffraction was undertaken with the motivation to verify the predicted values from the finite element model, especially mapping the strain gradients. Even though the overall trends of the results agree well, the results also demonstrate the challenges to resolve strains in this sample (and similar samples) using a diffractometer, even though it is optimized for strain scanning. The complicated experimental setup requires a lot of care to be taken and resulting count times are fairly long if small volumes are to be measured. In such cases, Bragg edge imaging measurements could indeed be very beneficial. Furthermore it is envisaged that the Bragg edge method will be extremely useful if a phase transformation is to be observed simultaneously to the strain measurement, as the spatial information could detect any in homogeneities. The additional use of far field diffraction detectors is foreseen to be used with the analysis of Bragg edges using a single instrument in the future. In such a case, advantage can be taken of spatially resolving strain, phase and texture distributions using the imaging detector, while being able to obtain more detailed crystallographic parameters from the diffraction detectors based on a coupled data analysis.

Chapter 6

Method to Determine hkl Strains and Shear Moduli under Torsion Using Neutron Diffraction

The following chapter is written based on a paper published by Robin Woracek et al.(*Woracek et al. 2012,*[252]) with only minor modifications (subheadings):

> Woracek, R., Bunn, J. R., Penumadu, D. & Hubbard, C. R. Method to determine hkl strains and shear moduli under torsion using neutron diffraction. Applied Physics Letters 100, 191904 (2012).

As the first author, my primary contributions include (1) proposing the experimental setup for the study (based on preliminary experiments I performed at the E3 diffractometer at HZB) (2) design of the used loading system and inclination system (3) design and conducting the experiments in collaboration with fellow PhD student Jeffrey Bunn (4) data processing in collaboration with fellow PhD student Jeffrey Bunn (Jeffrey Bunn performed most of the raw diffraction data, while I focused on the strain conversions) (5) data interpretation, and (6) writing the paper.

Preface:

So far, this dissertation was mainly concerned with developing and improving neutron imaging methods, largely based on diffraction contrast (Bragg edge imaging). Another fundamental motivation for this dissertation is the investigation of materials under multi-axial loading conditions. From an engineering perspective, multi-axial stress states resemble realistic conditions more closely, but have been largely neglected in diffraction studies so far, largely due to its complex nature. Since Bragg edge imaging needs to be seen as a method in a developmental state, where possibilities and limitations are still being exploited, in the previous chapters only cases of applied uni-axial tension were considered, as the state of strain and stress is much easier to interpret. Moreover, the Bragg edge imaging method is (so far) only suitable to plane stress problems (until/unless a more universal procedure and analysis will be developed).

It is of great interest to study materials under more complex stress states, including shear stresses, as shear is the predominant failure mechanism in many applications. However, there are only a few diffraction based studies (and no Bragg edge experiments) that investigate applied stresses other than tensile or compressive loading, and – to the authors

knowledge – none of these studies were aimed to measure lattice strains. The following research was undertaken with the goal to measure lattice strain under applied torsion for the first time. The established neutron diffractometer NRSF2 at the High Flux Isotope Reactor at ORNL was used for this study (with some preliminary experiments being conducted using the engineering diffractometer E3 at HZB).

Abstract:
An experimental method, using *in-situ* neutron diffraction for the measurement of shear strain, based on (*hkl)* lattice spacing changes under torsional loading, is described. This method provides the ability to probe the response of crystallographic planes to application of shear stress, inside the bulk of samples that are subjected to torsion. To demonstrate the method, shear moduli corresponding to bcc (211), (200) and (110) were experimentally determined for a solid cylinder of ferritic alloy 12L14 under elastic loading. Results indicate that the elastic constants determined under torsional shear show a different degree of anisotropy than those obtained from tensile loading.

6.1 Introduction

The lattice strain response of polycrystalline materials under deformation is usually characteristic for each lattice plane family *hkl*, because the stiffness of a crystal is generally anisotropic.(*Chung et al. 1967,[224;] Hutchings et al. 2005,[1]*) In polycrystalline materials, elastic anisotropy can lead to stress concentrations and inhomogeneities during plastic deformation.(*Dieter 1986,[6]*) X-ray and neutron diffraction have been used extensively to determine the elastic constants (E_{hkl}, ν_{hkl}) for different crystallographic planes, in single crystals and polycrystalline materials.(*Clausen et al. 1999,[8;] Choo et al. 2004,[24;] Rajagopalan et al. 2005,[25]*) Such measurements are important for understanding the effects of anisotropy and texture on the macroscopic mechanical properties. Models and theoretical considerations can be found in past and recent literature, relating Young's modulus E and Shear modulus G to single crystal elastic constants.(*Hill 1952,[9;] Kröner 1958,[10;] Nye 1985,[11;] Hutchings et al. 2005,[1;] Singh 2009,[12]*)

A majority of the published experimental data associated with the lattice strain response of polycrystalline materials has been obtained using uni-axial tensile loading. In practical applications however, shear is often the predominant loading case and leads to dominant failure mechanism(*Yu 2002,*[18]), but only a few detailed diffraction studies under direct application of shear stress have been carried out.(*Martins et al. 2005,*[31]; *Bunn et al. 2010,*[85]; *Cakmak et al. 2011,*[32]) Recently, Bunn et al. have shown that residual intergranular strains generated by the application of shear deformation behave differently than those generated by tensile deformation when explored on an ex-situ basis for hollow cylinders made from 12L14 steel alloy.(*Bunn et al. 2010,*[85])

When isotropic solid cylinders are subjected to torsion within the elastic range, the maximum normal stresses (tensile and compressive) act at 45° to the longitudinal axis. The maximum shear stress and strain occur at the outer radius of the cylinder and are zero at its center.(*Dieter 1986,*[6]; *Martins et al. 2005,*[31]) The maximum shear stress of a cylinder under torsion can be calculated as $\tau = T \cdot r / J$, where T is the applied torque, r is the radius and J the polar moment of inertia of the cylinder. In the case of pure shear, the magnitude of the principal strains on the surface of a cylinder relates directly to the magnitude of shear strain based on the strain rotation principle.(*Nye 1985,*[11]; *Bickford 1998,*[14]) During elastic deformation in torsion, it can further be assumed that plane sections perpendicular to the longitudinal axis of the cylinder remain plane and radial lines remain straight.(*Bickford 1998,*[14]; *Young 2002,*[238]) Therefore no significant radial and circumferential strains and stresses are generated, thus the state of strain is two-dimensional (plane strain). Prior measurements by the authors at the Neutron Residual Stress Mapping Facility (NRSF2) at Oak Ridge National Laboratory (ORNL) and at the Residual Stress Analysis and Texture Diffractometer (E3) at Helmholtz Zentrum Berlin, using identical samples and setup as used in this study, confirmed that the strains in the radial, axial and circumferential direction of a cylinder remain small (within ±50 με, approximately the limits of measurement resolution) while the samples were elastically loaded in pure torsion to a maximum shear stress of 120 MPa.

In the present study, an experimental approach is reported using in-situ neutron diffraction for determining lattice plane (*hkl*) specific shear strains while subjecting a cylinder to a state of pure shear stress by torsional loading. The measurement principle and experimental requirements will be described in the first section of this letter. Then the method is illustrated by an example measurement at NRSF2, using a solid cylinder sample (d = 6 mm) made from a ferritic steel alloy (12L14), and results are reported. The presented technique allows probing shear strains within the interior of a sample, in contrast to other techniques, which are limited to the (near) surface, e.g. use of resistance based strain gauges.(*Perry 1969,*[223]) Digital Image Correlation.(*Chu et al. 1985,*[253]) Moiré Interferometry(*Post 1991,*[254]), photo elastic methods (*Zandman 1961,*[255]) and Electron Backscatter Diffraction (EBSD).(*Wilkinson et al. 2006,*[256])

6.2 Experimental Procedure

6.2.1 Neutron Diffraction Considerations

For the neutron diffraction method described herein, *hkl* specific interplanar spacings (d_{hkl}) have to be measured for a given gauge volume in (at least three) independent directions, all lying in the "axial-circumferential" plane of the cylindrical sample, while incrementally subjecting the sample to pure torsion (within the elastic limit). The interplanar spacings are then converted to strains using the d_{hkl} values measured at zero torque (d^0_{hkl}). The subset of grains within the neutron scattering gauge volume which are aligned such that the normal of the lattice plane is parallel to the diffraction vector are used as internal strain gauges to measure the *hkl* specific response to torsional shear. The principal strains (ε_1 and ε_2) and the maximum shear strain (γ_{xy}), at the measurement location, are calculated using the strain transformation suitable for a plane strain condition (*Perry 1969,*[223]*; Nye 1985,*[11]*; Young 2002,*[238]), and the previously measured elastic strain components ($\varepsilon_{\psi(hkl)}$):

$$\varepsilon_{\psi} = \frac{\varepsilon_x + \varepsilon_y}{2} + \frac{\varepsilon_x - \varepsilon_y}{2} \cdot \cos 2(90° - \psi) + \frac{\gamma_{xy}}{2} \cdot \sin 2(90° - \psi) \tag{6-1}$$

In order to measure the strain in three directions (three values of ψ yielding three ε_ψ) for a single spatial location within the solid cylinder, the loading system (Figure 6-1a) and therefore sample (Figure 6-1b) axis are inclined at angles between 0° and at 45° with respect to the horizontal (X-Y) plane defined by the incident and diffracted neutron beams. The highest sensitivity (i.e. lowest relative error) will be achieved at 45° where the lattice strains are at maximum. For the described experiment at NRSF2, the maximum inclination was limited to 41.3° due to interferences with slit holders. The derived shear strains are independent of the specific inclination used (authors have obtained similar results for an inclination of 31.5°), as long as the strains in that direction are non-zero.

The gauge volume was positioned at a radial offset from the sample's cylinder axis, as shown in Figure 6-1 and Figure 6-2, to ensure the gauge volume was fully within the cylindrical sample. While inclining the loading system at 41.3°, one can measure the strain component corresponding to $\psi = +41.3°$ as well as $\psi = -41.3°$. To measure the latter, the sample is rotated inside the loading system by $\varphi = 180°$ and the entire loading system is translated in the x-direction, such that the gauge volume resides at the same spatial location of the cylinder. It should be noted that measurement of the described strain components could also be achieved by rotating the sample stage (usually termed Ω) and without inclining the loading system, but for many diffraction instruments the range of rotation movement is typically restricted by slit/collimator interferences with the load frame.

In neutron diffraction, a volumetric averaging is used to achieve useful counting rates and grain averaging. However, to minimize impact of radial and circumferential variation of strains (for both see Figure 6-1) the gauge volume has to be small compared to the sample dimensions. For the herein described experiments, the gauge volume (established by gadolinium slits) was chosen to be 1x1x1 mm^3. The impact of strain variation was explored using an even smaller gauge volume (0.7x0.7x0.7 mm^3), which resulted in much longer count times, with the conclusion that similar results were obtained. For the herein reported experiment, the gauge volume center was fixed at a radial distance of 2 mm from the axis of the sample. The shear stress and strain at this location is 2/3 of the maximum shear stress

and strain experienced on the surface of the cylinder. Due to the radial gradient of the shear stress/strain, a careful and precise alignment procedure is crucial in order to assure that the same gauge volume location is irradiated for each measurement condition. A positioning accuracy of the gauge volume location below 100 μm is required to achieve an uncertainty of < 5% in the calculated shear stress. The required accuracy was reached by using a laser alignment system, consisting of a FARO laser tracker and SScanSS software(*James et al. 2007,*[257]) to align the sample within 50 μm accuracy for gauge volume location. The gauge volume alignment procedure was repeated for every inclination of the loading system, prior to each loading experiment.

6.2.2 Mechanical Loading and Sample

A portable axial/torsional loading system (Figure 6-1a) was utilized for the particular measurements, offering an axial force capacity of 50 kN, a torque capacity of 12 Nm and the ability to rotate a specimen under an applied load.(*Woracek et al. 2011,*[207])

The solid cylinder sample (Figure 6-1b) was machined from a hexagonal bar of a low carbon BCC steel (12L14, Table 6-1). Significant strain gradients as function of radius were observed in an as-machined, unstressed sample. To relieve these internal stresses, the sample was annealed at 870°C for 15 minutes and slowly cooled. Using neutron diffraction, it was confirmed that the residual strain gradient for the stress-relieved sample was significantly reduced. Optical micrographs indicated a resulting average grain size of 25 μm. Texture measurements of the undeformed sample, carried out at the HIPPO instrument(*Vogel et al. 2004,*[258]) at Lujan Neutron Scattering Center (LANSCE), indicated mild to no bulk texture. (Figure 6-3)

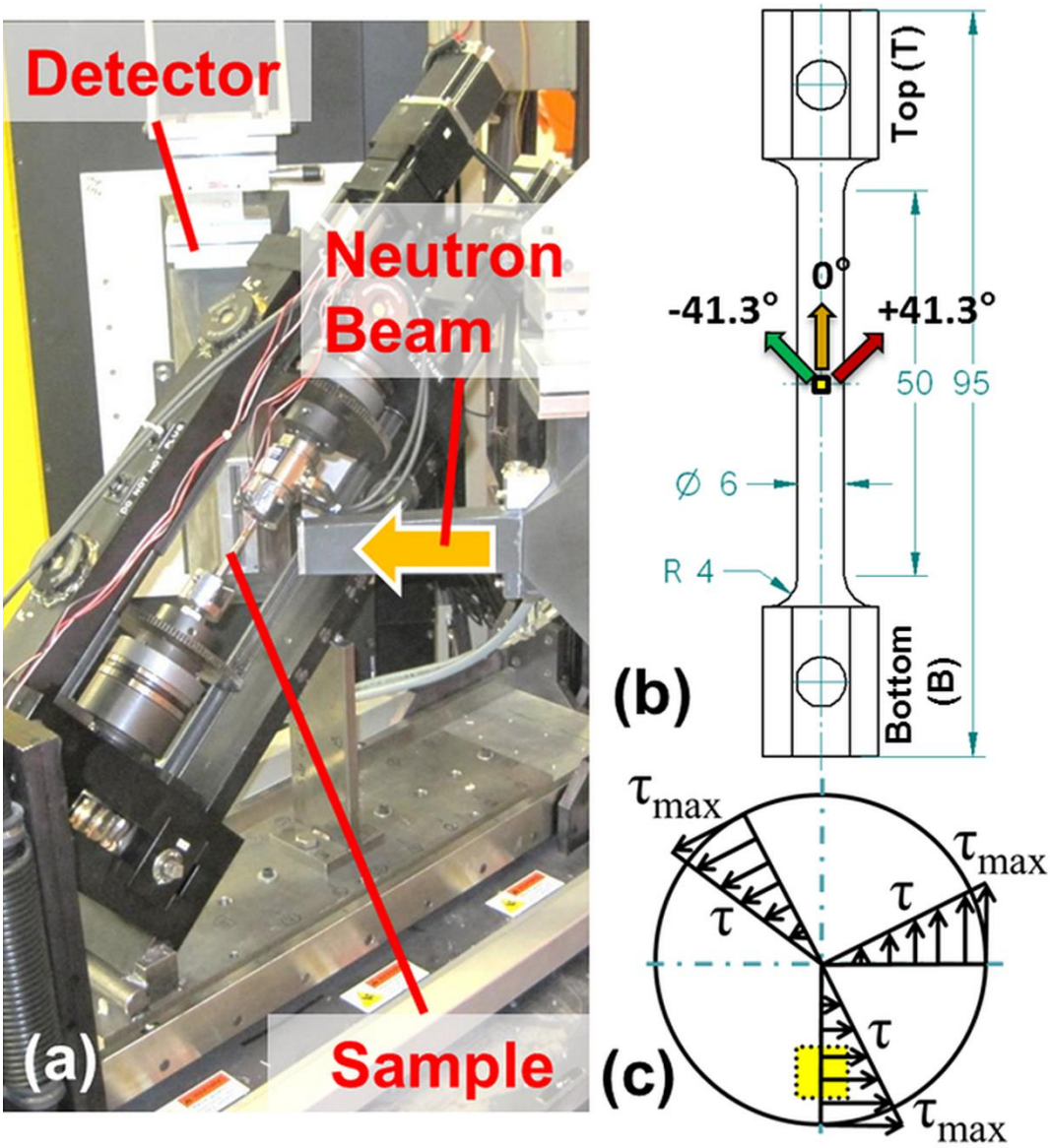

Figure 6-1. (a) Experimental setup at NRSF2 with loading system shown at 41.3° inclination (b) Sample dimensions (mm) and directions of measured strains at a gauge location 2 mm from the cylinder axis (B = bottom and T = top of sample) (c) Linear variation of shear stress along each radial line of the cylinder cross section with gauge location shown as yellow square.

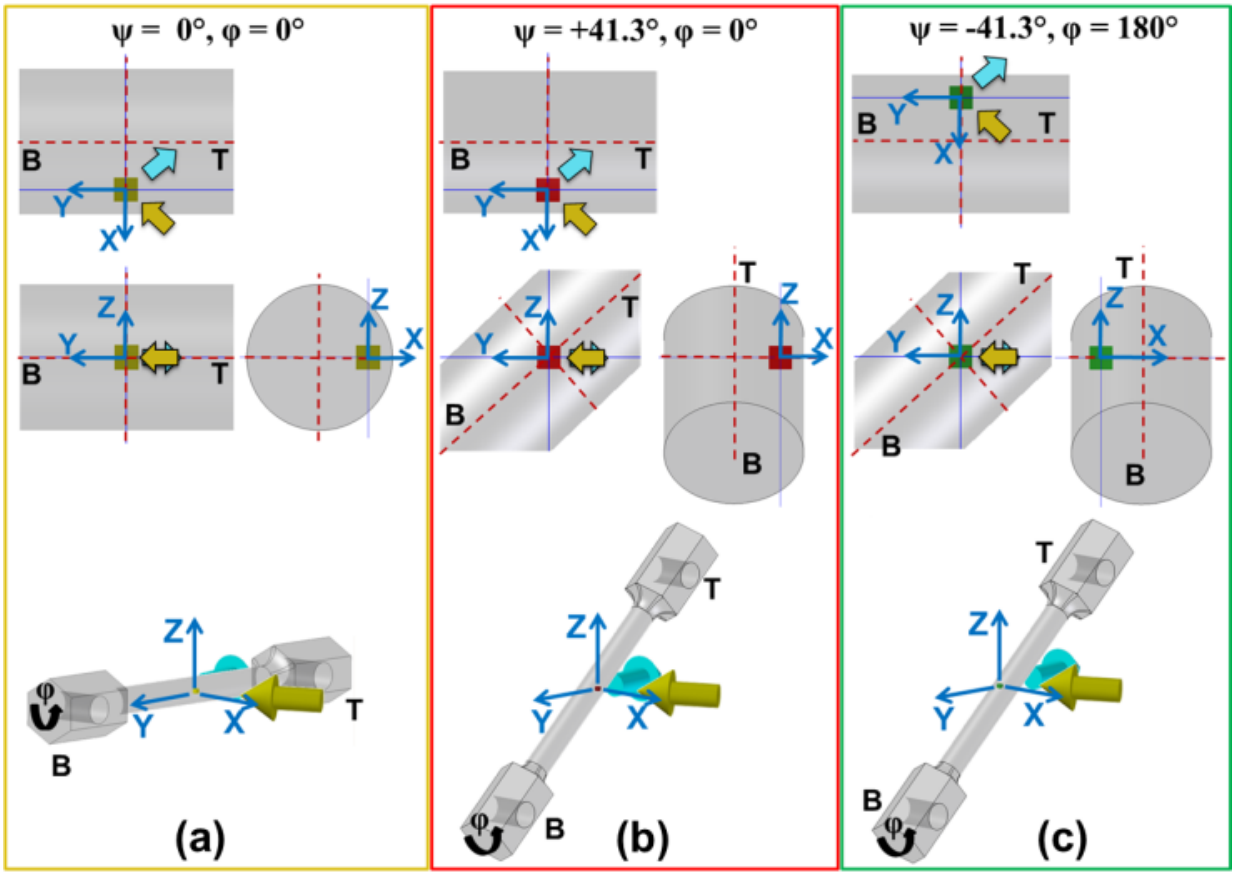

Figure 6-2. Sample positioning to obtain the three strain components. The yellow arrow represents the incident neutron beam; the cyan arrow represents the diffracted beam (the direction of measured strains bisects these two). The sample coordinate system is denoted by the dashed red lines and the instrumental coordinate system is shown in blue. The angle φ denotes the sample rotation inside the loading system. The gauge volumes are shown by yellow, red, green squares, respectively. **(a)** For ψ=0° the loading system is lying on its side, while **(b, c)** in the other two cases it is inclined at 41.3°. For measurement of the strain component corresponding to ψ=-41.3°, **(c)** the sample is rotated inside the loading system by 180° and the loading system is translated in x-direction, so the same spatial location within the sample is measured.

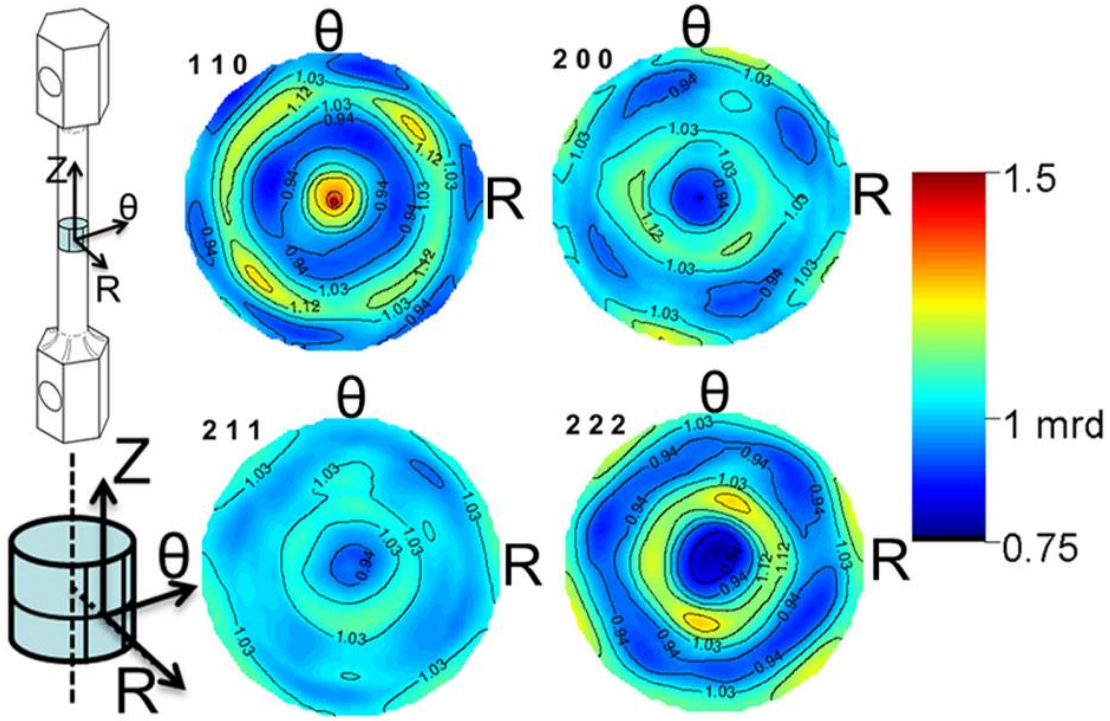

Figure 6-3. Pole Figures for the sample indicate mild to no bulk texture.

An electrical resistance based rosette strain gauge was attached to the sample surface in the gauge section, 10 mm above the center to prevent interference with the incident neutron beam. The sample was connected to the load frame grips using a pin arrangement. Proper mechanical alignment of the sample in the load frame was verified by applying elastic loading in tension and torsion and calculating the principal strains. In the case of pure tension, shear strain γ_{xy} was observed to be essentially zero and for pure torsion, the out-of-plane bending strains were negligible.

Different neutron monochromator settings were used at NRSF2 to select the wavelength of neutrons. Changing the wavelength allowed investigation of several different lattice planes in the near 90° 2θ range. For the two strain components corresponding to a ψ value of +41.3° and -41.3°, neutron measurements were performed while applying a macroscopic shear stress between 0 MPa and 120 MPa, at 10 MPa increments. For ψ = 0°, measurements

were performed only at 60 MPa increments, as the measurements are mainly used to verify proper load frame alignment. The axial stress was kept constant (using PID control) at a nominal tensile seating stress of 20 MPa for all measurements of shear stress. During data acquisition (10-40 minutes depending on investigated lattice plane) the angular twist and axial deformation were held at fixed positions.

The reference interplanar lattice spacings d^0_{hkl} were determined at the same axial stress of 20 MPa and zero shear stress. The monochromator was changed following the loading/unloading cycles for a given *hkl*.

The macroscopic surface principal strains and shear strains were monitored throughout the neutron diffraction experiments via the strain gauge rosette. Nearly identical macroscopic stress-strain behavior was seen in each loading/unloading cycle of the same sample and also for measurements on replicate samples. The macroscopic shear modulus under torsional loading was measured as 73 (± 1) GPa. No creep behavior was observed. The bulk average shear modulus predicted by the Reuss model is closest to the measured value (Table 6-2).

Table 6-1. Chemical composition (weight percent) and mechanical properties of annealed (stress relieved) 12L14.

C	Mn	P	Pb	S	Yield Strength [MPa] under Tension[a]	Shear Strength [MPa] under Torsion[a]
0.15 (max)	0.85 – 1.15	0.04 – 0.09	0.15 – 0.35	0.26 – 0.35	250	160

[a] Measured with portable loading system and verified separately with MTS servo-hydraulic loading system

Table 6-2. Macroscopic values of shear moduli G [GPa] as calculated for α-Fe and experimentally determined (via strain gauge rosette) for 12L14.

α-Fe		12L14	
acc. to Voigt (*Hutchings et al. 2005,*[1])	acc. to Reuss (*Hutchings et al. 2005,*[1])	acc. to Kröner (*Hutchings et al. 2005,*[1])	Experimental
88.8	72.5	82.1	73 (± 1)

6.3 Experimental Results

The strain components for three tilts for the bcc (211) plane, measured by neutron diffraction as a function of applied shear stress, are shown in Figure 6-4. The error bars represent the 2 x rms deviation of the determined strain values from four repeated loading experiments using the same sample. Note that strains $\varepsilon_{+41.3^\circ}$ are positive (tensile), strains $\varepsilon_{-41.3^\circ}$ are negative (compressive) and strains ε_{0° are essentially zero, as expected. Fig. 3 also shows results obtained for spatial locations at a radial distance of r = 1 mm and the sample center (r = 0 mm). These additional data points confirm that the diffraction based measurements agree with the predicted radial variation of shear strain using elasticity theory. A significant change of lattice strain in the axial direction (ε_{0°) due to length change under application of (elastic) torsional stress (*Young 2002,*[238]) was not observed.

For the three measured strain components (ε_{0°, $\varepsilon_{+41.3^\circ}$, $\varepsilon_{-41.3^\circ}$), the shear strain can be obtained by using Equ. 6-1 as $\gamma_{xy} = (\varepsilon_{+41.3^\circ} - \varepsilon_{-41.3^\circ}) / \sin(97.4°)$. The shear stress versus shear strain response is shown in Figure 6-5 for the three lattice planes. For bcc (200), it was observed that the shear stress *vs.* lattice strain response behaves non-linearly from about 40 MPa onwards, which typically indicates the onset of plastic flow, a feature also commonly observed in tensile mode(*Clausen et al. 1999,*[8]; *Hutchings et al. 2005,*[1]). A similar but much less pronounced shift is noticed from this figure for the other two *hkl's*.

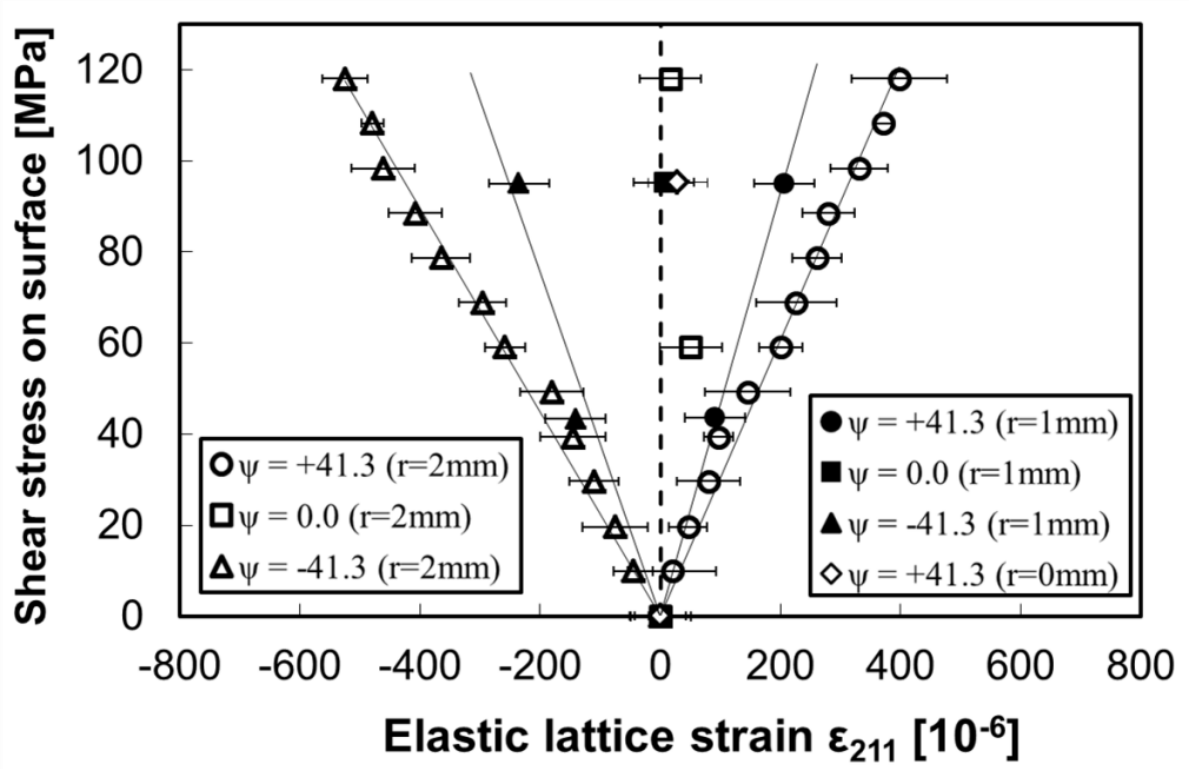

Figure 6-4. Measured strain components for ferritic bcc (211) lattice plane during elastic loading in torsion for three separate spatial locations along the same radial line (r = 2 mm, r = 1 mm, r = 0 mm). Shear stress corresponds to the maximum shear stress at the surface of the sample.

However, the non-linearity occurs at an unexpectedly low shear stress amplitude for all three *hkl's* (considering the macroscopic shear strength) and identical inference was observed for repeated loading cycles of the same sample for stress amplitudes well below yield stress in shear. Additionally, it appears that the bcc (200) planes start to soften again at approximately 60 MPa and this observation is perplexing and needs further investigation. The break in slope was not seen in the macro strain data from the attached strain gauge rosette where the surface shear strain response indicates perfectly linear elastic macroscopic strain behavior. It is further interesting to note that lattice strain data from a tensile test (which was performed using the same alloy, sample dimensions and setup; table III) behaved perfectly linear.

The shear moduli G_{hkl} was determined using linear regression between 0 MPa and ≈ 33 MPa shear, because of the non-linearity of the data based on lattice specific shear strains for stress amplitudes above 33 MPa. The shear moduli corresponding to the ferritic bcc (211) and bcc (110) planes are significantly larger than that for the bcc (200) (Table III). Under tensile loading, the bcc (211) and bcc (110) planes show a similar order of stiffness and it appears that these two *hkl's* behave similarly for pure shear stress application under torsion. The crossover at about 40 MPa in Fig. 4 for those two lattice planes cannot be fully rationalized at this stage due to relatively large error bars relative to the changes near the crossover. The bcc (200) planes are found to be much weaker under torsion than would be expected from tensile results, when comparing on a relative scale. The *hkl* specific Youngs's moduli E_{hkl} and Shear moduli G_{hkl} following the Reuss (stress continuity) and Kröner modeling schemes are presented in Table III. The experimentally determined values for E_{hkl} are closer to the Reuss values than to the Kröner, but the experimentally determined G_{hkl} values for bcc (211) and bcc (110) are much closer to the values predicted by Kröner/deWitt(*Singh 2009,*[12]). For the bcc (200) plane however, it is difficult to interpret a single value of shear modulus due to the pronounced non-linearity starting at shear stress value of 40 MPa. Using the initial linear part of the slope, yields G_{200} to be 32 GPa, while linear regression of the entire data set yields a value of 50 GPa.

6.4 Conclusion

This study presents a neutron diffraction method to obtain the lattice specific shear modulus of polycrystalline materials. The in-situ tests with ferritic 12L14 alloy confirmed the method. The 12L14 results are a first step in understanding effects of the application of shear stress on the mechanical behavior of polycrystalline materials and associated elastic anisotropy. Results suggest that, when applying pure torsion within the elastic regime to a cylinder, it can be sufficient to measure only one strain component (close to 45°) and use the assumption of symmetry to calculate shear strain. Initial results, obtained for 12L14 ferritic steel alloy, indicate that the (200) lattice planes show a different behavior under

torsional shear than would be expected from properties determined under uni-axial tensile loading. The phenomenon of early onset of non-linearity in measured shear modulus due to direct application of shear stress will need to be studied in more detail for bcc materials and explored for polycrystalline materials with complex slip systems (fcc, hcp).

The described experiments were performed at a high flux steady state neutron source, however there are potential advantages to conduct future experiments at pulsed sources with adequate spatial resolution. This can be particularly advantageous for exploring plastic and time dependent strain (while the need of measuring more strain components must be considered for correct interpretation of the strain tensor in this case).

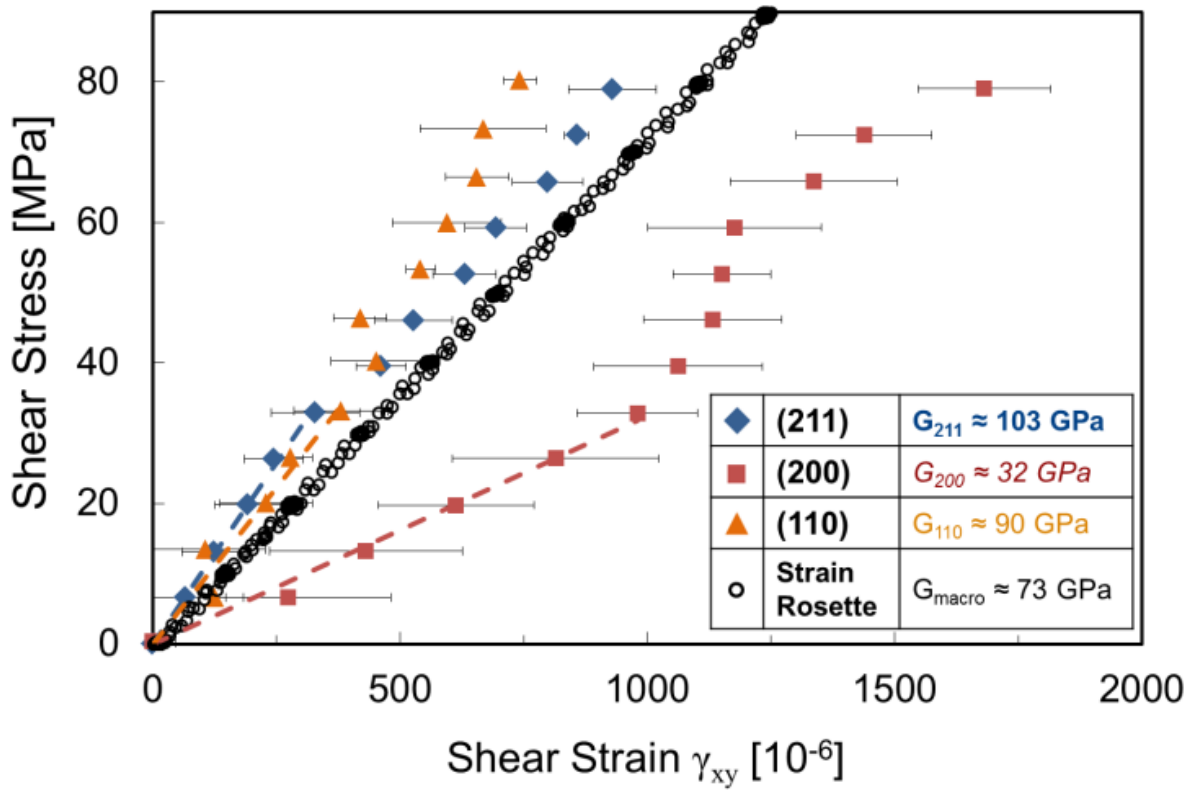

Figure 6-5. Shear Stress (at r = 2 mm for three *hkl's* and the surface for the strain rosette) *vs.* obtained Shear Strain (for the investigated lattice planes and strain rosette) with shear modulus ($G_{hkl} = \tau/\gamma_{xy}$) determined using a linear fit to the initial slope.

Acknowledgements

The authors would like to acknowledge the help of Dr. A. Siriruk and Mr. K.G. Thomas who performed accompanying testing using a MTS tension-torsion loading system at the University of Tennessee. Gratefully appreciated is the support of Mr. B. Cady and Mr. P. Cornwell who assisted with the experiments at NRSF2. Also, we would like to express appreciation to Dr. R.C. Wimpory and Dr. N. Kardjilov for their support during experiments performed at Helmholtz Zentrum Berlin. The authors further acknowledge the help of Mr. Matthew Kant at the University of Tennessee and Dr. S.C. Vogel for texture measurements at HIPPO instrument of LANSCE. Research at the 2nd Generation Neutron Residual Stress Mapping Facility at the High Flux Isotope Reactor was partially sponsored by the U.S. Department of Energy, Office of Energy Efficiency and Renewable Energy, Vehicle Technologies Program, through the Oak Ridge National Laboratory's High Temperature Materials Laboratory User Program and by the Scientific User Facilities Division, Office of Basic Energy Sciences, U.S. Department of Energy. This material is based upon work partially supported by the US National Science Foundation under Grant No. #0801470 to Dr. D. Penumadu for supporting IGERT student, Mr. J. Bunn.

Table 6-3. Calculated values of Young's moduli E_{hkl} and shear moduli G_{hkl} for α-Fe and experimentally determined E_{hkl} and G_{hkl} for 12L14.

	α-Fe		α-Fe		12L14	
Lattice Plane hkl	E_{hkl} [GPa] acc. to Reuss (*Hutchings et al. 2005,[1]*)	G_{hkl} [GPa] acc. to Reuss (*Singh 2009,[12]*) [a]	E_{hkl} [GPa] acc. to Kröner (*Hutchings et al. 2005,[1]*)	G_{hkl} [GPa] acc. to Kröner/deWitt (*Singh 2009,[12]*)	Experimental E_{hkl} [GPa] [b]	Experimental G_{hkl} [GPa]
bcc (211)	210.5	84.4	225.5	96.9	208	103
bcc (200)	125	46.3	173.3	70.8	146	32-50
bcc (110)	210.5	84.4	225.5	96.9	197	90

[a] Calculated using stiffness constants presented in (*Hutchings et al. 2005,[1]*) (page 220)

[b] Tensile measurements were performed using the same alloy, sample dimensions and setup, while subjecting the sample to axial stresses between 20 MPa and 100 MPa, at 10 MPa increments, and keeping the shear stress at 0 MPa.

Chapter 7

Neutron Bragg Edge Imaging for Crystallographic Phase Mapping

The majority of the following chapter (sections 7.2 – 7.6) is written based on a journal paper published by Robin Woracek et al. (*Woracek et al. 2014,*[234])

> R. Woracek, D. Penumadu, N. Kardjilov, A. Hilger, M. Boin, J. Banhart, I. Manke, "3D Mapping of Crystallographic Phase Distribution using Energy-Selective Neutron Tomography". Advanced Materials 26, 4069-4073 (2014).

As the first author, my primary contributions include (1) proposing the study and identifying its importance, (2) design and conducting the experiments, (3) data analysis and interpretation, and (4) writing the paper.

Preface:

Beyond the published work, section 7.1 is intended to provide more background information on previous related work by others. Section 7.7 shows and discusses additional and complimentary data that was taken and is relevant to this chapter. In addition, section 7.8 is presenting results of related experiments, where the same type of samples was studied but exhibiting pronounced texture effects.

Abstract:

This paper introduces nondestructive three-dimensional (3D) mapping of crystallographic phases providing distribution of phase fractions within the bulk (centimeter range) of samples with micrometer-scale resolution. The technique leverages diffraction contrast due to Bragg scattering and the large penetration power of neutrons through high-atomic-number-element-based structural materials. Our tomographic approach overcomes critical limitations of existing techniques by allowing spatially resolved phase mapping in bulk samples and offers a wide range of potential applications. The technique is demonstrated for (metastable 304L stainless) steel samples that exhibit strain-induced martensitic phase transformation after being subjected to tensile and torsional deformation. The distribution of phase fractions within the 3D reconstructed volumes was verified at selected locations using neutron-diffraction-based measurements, and results agree with transformation kinetics theory.

7.1 Motivation and Related Work

As described in previous chapters, using neutrons of particular wavelengths, it is possible to probe the energy dependence of the sample's attenuation coefficient and to record the characteristic Bragg edge spectra for polycrystalline materials. Figure 7-6 is showing the characteristic Bragg edges for bcc and fcc phases of iron. (*Boin 2012,*[191]) This methodology has been used by others to determine crystallographic phase fractions (*Bourke et al. 1996,*[172]*; Santisteban et al. 2002,*[167]*; Steuwer et al. 2004,*[173]*; Steuwer et al. 2005,*[174]*; Huang et al. 2007,*[175]), but without providing spatial resolution. In 1996, Bourke et al. have shown how the transmission Bragg edge spectrum is changing in real time, while reversing the phase transformation in austenitic stainless steel. (*Bourke et al. 1996,*[172]) The reference neutron diffraction data and the corresponding transmission spectra are shown in Figure 7-1.

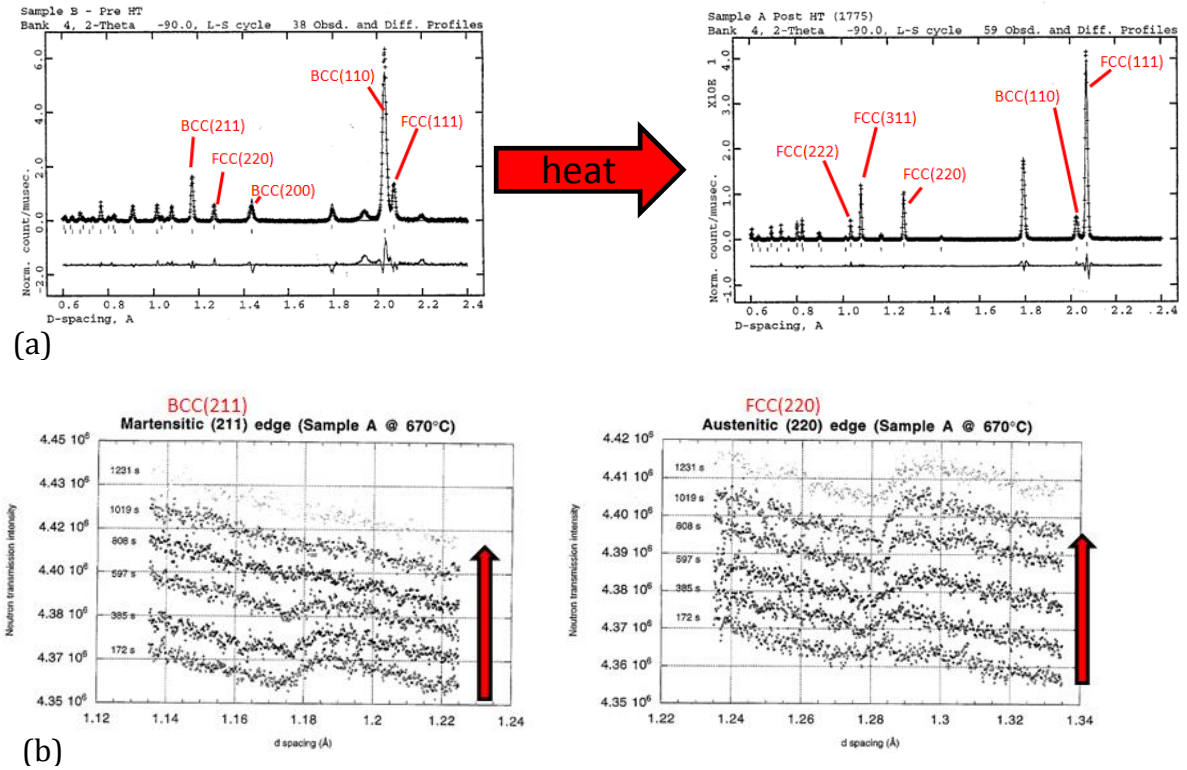

Figure 7-1. (a) Neutron diffraction spectrum of reversed phase transformation (by heating) in austenitic stainless steel. (b) Corresponding transmission spectrum. *From* (*Bourke et al. 1996,*[172])**.**

In 2008, the group at HZB (N. Kardjilov, I. Manke, T. Kandemir) demonstrated tomographic reconstructions of metallic samples (Figure 2-30), which consisted of varying amount of martensite and bainite, but the work has not been published. Motivated by these results, the experiments reported in this chapter were designed, with the goal to produce a quantifiable tomographic reconstruction of two phases in a metastable austenitic stainless steel. This steel exhibits the TRansformation Induced Plasticity (TRIP) effect, where the metastable fcc austenite transforms to hcp and bcc martensites under applied strain.

Tensile testing is ideal to apply a well-known amount of deformation. However for ductile materials (such as TRIP steel), necking often occurs in the center of the gauge area in tensile samples during increased plastic deformation and causes the stress to further concentrate in this region. The torsion test on the other hand allows applying large amounts of deformation without necking. In a cylindrical torsion sample, the maximum shear stress and strain occur towards the outer radius of the cylinder and are zero at its center. The regions of highest strains are expected to exhibit the largest martensitic phase transformation, and torsion provides an elegant way of controlling the amount of phase transformation in the radial direction.

Cakmak, Choo et al, have recently published results from a synchrotron diffraction study, and related results are ideally suited to be used as a reference for Bragg edge based measurements. They studied the phase changes from FCC to BCC under torsional loading in 304L stainless steel.(*Cakmak et al. 2011,*[32]) In their study, they used nine separate samples which were plastically deformed to different strain rates and subsequently extracted small portions of the sample for synchrotron diffraction measurements. The phase fractions were then mapped as a function of radial distance from the sample center, and the reported results are presented in Table 7-1 and Figure 7-2.

The results from the proposed neutron transmission study are expected to be less precise in phase fraction determination, but they will have the advantage of being non-destructive and also cover large sample volumes.

Table 7-1. Phase fractions near the outer diameter, reported for nine samples of austenitic stainless steel that were subjected to torsion. *From* (*Cakmak et al. 2011,*[32])

Sample code	Shear strain	fcc wt.%	bcc wt.%	hcp wt.%
T1	0.17	93.1	0.8	6.1
T2	0.35	90.9	3.9	5.2
T3	0.52	84.4	8.0	7.6
T4	0.70	78.2	12.6	9.2
T5	1.04	64.4	25.9	9.7
T6	1.40	51.7	39.7	8.6
T7	1.74	41.0	48.3	10.7
T8	2.09	37.8	56.0	6.2
T9	2.55	31.6	63.5	4.9

More strain

From mostly Austenite to mostly Martensite

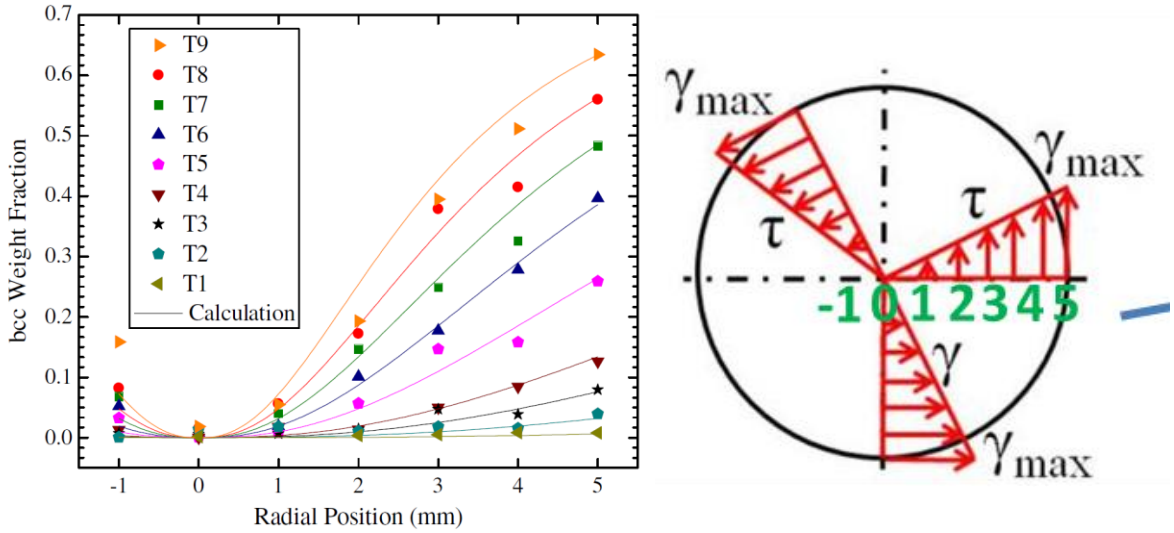

Figure 7-2. Phase fractions for the nine samples as a function of radius, measured at 7 different locations. *From (Cakmak et al. 2011,*[32]*)*

7.2 Introduction

Recently demonstrated diffraction-based imaging using X-rays and transmitted electrons offers exciting prospects for non-destructive three-dimensional (3D) microstructural characterization of crystalline materials.(*Larson et al. 2002,*[47]; *Poulsen 2004,*[48]; *Pfeifer et al. 2006,*[49]; *Bleuet et al. 2008,*[50]; *King et al. 2008,*[51]; *Liu et al. 2011,*[52]) However, because of the limited penetration power of X-rays and electrons into structural alloys, neutrons are required for bulk investigations,(*Banhart 2008,*[54]) which are crucial to understand the meso-scale effects for polycrystalline materials.(*Doherty et al. 1997,*[55]) Here we introduce a tomography method for non-destructive 3D mapping of crystallographic phases that overcomes critical limitations of existing methods by providing spatially resolved phase fractions within the bulk (centimeter range) of samples with micrometer-scale resolution. We demonstrate spatial mapping of two phases in (metastable 304L stainless) steel samples that exhibit strain-induced martensitic phase transformation after being subjected to tensile and torsional deformation. The technique leverages diffraction contrast due to Bragg scattering and the large penetration power of neutrons through high-atomic-number-element-based structural materials, offering a wide range of potential applications for characterization of natural and advanced materials.

Studying crystallographic phase distributions and phase transformations is important, as these microstructural properties largely govern the global mechanical properties of these materials. Understanding the relation between dislocation density evolution and phase transformations is essential for developing the theoretical framework in computational materials science, especially as it relates to the Materials Genome Initiative. There has been extensive research of phase-transformed materials, e.g., shape-memory alloys,(*Ma et al. 2010,*[259]) recrystallization processes,(*Offerman et al. 2002,*[260]) and materials exhibiting the transformation induced plasticity (TRIP) effect.(*Militzer 2002,*[261]) "Further understanding of the transformation mechanisms depends critically on the available characterization techniques," which is "crucial for the development of fundamental phase transformation models and to develop steels with superior properties."(*Militzer 2002,*[261]) Existing techniques (e.g., electron backscatter diffraction, electron microscopy, X-ray and

synchrotron diffraction, optical microscopy, magnetic and ultrasonic measurements) are destructive and/or limited to the surface or to small-sized specimens. Diffraction contrast tomography(*King et al. 2008,*[51]) and 3D-XRD,(*Poulsen 2004,*[48]) as employed at synchrotron sources, use the diffraction signal of individual grains to produce 3D maps of grain shape and crystallographic orientation and are, in principle, capable of non-destructive phase mapping. However, those techniques are usually constrained to small sample sizes consisting of a limited number of grains and limited degree of mosaicity, which is not the case for plastically deformed materials. Our energy-selective neutron tomography approach provides a non-destructive 3D representation of phase fractions in large-specimen volumes (cm^3 range). The best currently achievable spatial resolution (approximately $50\times50\times50\ \mu m^3$ voxel volume) and sensitivity for quantifying phase fractions, which also is determined by the grain size, is at least three orders of magnitude more precise than what is possible with neutron diffraction instruments ($> 500\times500\times500\ \mu m^3$).

Using neutrons of particular wavelengths (energy), it is possible to probe the energy dependence of the sample's attenuation coefficient. The elastic coherent scattering cross section changes suddenly at well-defined wavelengths λ, defined by Bragg's law ($\lambda = 2d_{hkl}\sin\theta^B$; d_{hkl}: lattice spacing, θ^B: Bragg angle). In monochromatic transmission measurements, the "missing" portion of the neutron beam is observed while neutrons are scattered at certain angles θ^B (typically detected in a diffraction instrument). If the wavelength is increased to larger than $\lambda = 2d_{hkl}\sin90° = 2d_{hkl}$, Bragg scattering for the corresponding lattice planes *hkl* cannot occur, and the transmitted intensity increases suddenly, corresponding to a well-defined Bragg edge (see Figure 7-3 and Supplementary Figure S1 for austenite and α-martensite phases of iron(*Boin 2012,*[191])). This methodology has been used to produce 2D strain(*Santisteban et al. 2002,*[167]; *Steuwer et al. 2003,*[23]; *Woracek et al. 2011,*[207]) and texture(*Santisteban et al. 2006,*[176]; *Santisteban et al. 2011,*[184]) maps. The transmission method has also been used to determine crystallographic phase fractions, but without spatial resolution.(*Bourke et al. 1996,*[172]; *Santisteban et al. 2002,*[167]; *Steuwer et al. 2004,*[173]; *Steuwer et al. 2005,*[174]; *Huang et al. 2007,*[175])

7.3 Experimental

To demonstrate the transmission technique for 3D phase mapping, we studied metastable stainless steel (ASTM standard 304L) exhibiting the TRIP effect, where austenite (having a face-centered cubic structure, fcc) transforms to martensite (consisting of body-centered cubic, bcc, and hexagonal closest packed, hcp, structures), when subjected beyond a certain plastic strain.(*Bayerlein et al. 1989,*[262]) For this class of materials, there is a significant amount of literature regarding uni-axial deformation,(*Venables 1962,*[263]; *Tomota et al. 2004,*[83]) and recently, more complex loading in torsional shear has been investigated.(*Cakmak et al. 2011,*[32]; *Cakmak et al. 2012,*[33]) A previous study indicates that the degree of elastic anisotropy varies depending on whether a sample is loaded in pure torsion or pure tension.(*Woracek et al. 2012,*[252]) Any plastic deformation is prone to inhomogeneity that, due to anisotropy, can result in distinct failure mechanisms; therefore, the comparison of loading paths is of significant interest.

Five samples were investigated (see radiographs in Figure 7-3; detailed dimensions in Supplementary Figure S2). Two samples were deformed in pure tension to a theoretical engineering strain of 108% ("TEN-med"; 5.4 mm axial deformation) and 144% ("TEN-max"; 7.2 mm axial deformation). Two samples were deformed in pure torsion to a maximum shear stress of 100% ("TOR-med"; 71.5° twist) and 250% ("TOR-max"; 179° twist). The non-deformed sample ("VIR") was used as a reference corresponding to no external mechanical stress. Additional details on samples and mechanical testing are described in the Supplementary Methods (stress vs. strain curves are shown in Supplementary Figure S3). We expected the regions of highest strains to exhibit the largest martensitic phase transformation, and torsion provides an elegant way of controlling the amount of phase transformation in the radial direction (Supplementary Figure S4).

Energy-selective neutron transmission measurements can be performed at spallation sources using the time-of-flight information and a suitable time-resolving detector or at reactor sources, if the wavelength can be chosen accordingly. For the results presented herein, we used the dedicated neutron-imaging beamline CONRAD at the reactor source at

Helmholtz-Zentrum Berlin and a tunable double-crystal monochromator (details in Experimental Section).

7.3.1 Radiography

For initial investigation, Bragg edge spectra were obtained for all five samples simultaneously in one orientation (see Figure 7-3a). The Bragg edge spectra were normalized by the open beam (no sample) spectrum, and the resulting spectra for a region of interest (ROI) are shown in Figure 7-3b.

7.3.2 Tomography

Tomographic scans were performed by recording 180 projections over a 360° range before (4.1 Å) and after (4.3 Å) the 'Bragg cut-off' corresponding to the austenitic phase. The 'Bragg cut-off' for the martensitic phase is slightly shifted towards smaller wavelengths compared to the austenitic phase, resulting in attenuation differences between the two phases in the data taken at 4.1 Å. We used filtered back-projection algorithms for parallel beam reconstruction to individually reconstruct the tomographic data sets for each wavelength.

Figure 7-4a shows a cut through the middle of the 3D-reconstructed volume data (center of the samples) taken at 4.3 Å. The attenuation coefficient is uniform throughout the samples and unaffected by differences in the elastic coherent scattering cross section. In contrast, the reconstructed volume of the measurement at 4.1 Å (Figure 2b) shows distinct differences in the reconstructed attenuation coefficient. The transmitted intensity is higher for regions with larger martensitic phase content due to the different Bragg edge position. The reconstructed data taken at 4.1 Å already provides the 3D crystallographic phase distribution of austenite and martensite. However, for optimal quantification and to exclude any possible influence of slight material or signal inhomogeneities, the reconstructed slices belonging to 4.1 Å were individually normalized by the reconstructed slices belonging to 4.3 Å (Figure 2c-e). In this case, if mostly austenite is present, the

resulting voxel value will be small (e.g., the pure austenitic phase in the virgin sample has a gray value of ~0.7, indicated as blue in Figure 2c-e) while the values will be closer to 1 if primarily martensite is present (i.e., pure martensitic phase in center of the maximum tensile sample has a gray value of 0.97, indicated as red). An assigned linear weighting factor corresponds to a known weight fraction for each voxel of the reconstructed volume.
Line profiles, presented in Figure 7-5, show the phase distribution across the diameter of the torsion samples and along the height of the tensile samples. There is good agreement when the phase fraction values are compared to previously published data(*Cakmak et al. 2011,*[32]) (see Supporting Information) that describe torsion samples of the same material (304L) investigated by synchrotron diffraction, using small specimen extracted from the deformed samples. Figure 3 includes derived phase fractions from complementary neutron diffraction measurements performed at the E3 instrument at HZB (see Experimental Section), and the results for the tensile samples are in good agreement with the information derived from the tomography data. For the torsion samples, the diffraction results show a trend identical to the tomography data; however, sharp gradients could not be captured because of the relatively large gauge volume used in neutron diffraction. For sample "TOR-max", the theoretical α-martensite phase evolution is shown using the Olson–Cohen model(*Olson et al. 1975,*[264]) and parameters described in (*Cakmak et al. 2011,*[32]) (see Supporting Information) with good agreement between the model and experiment.

7.4 Conclusion

This study presents a new non-destructive characterization method that allows the spatial distribution and volumetric extent of crystallographic phases within the bulk of large sample volumes to be determined *with superior spatial resolution*. It has the invaluable advantage of being able to reveal inhomogeneities within the measured volume, which otherwise may remain undetected. The tomographic reconstruction allows the visualization of geometric differences such as cracks and holes simultaneously with the crystallographic phase identification.

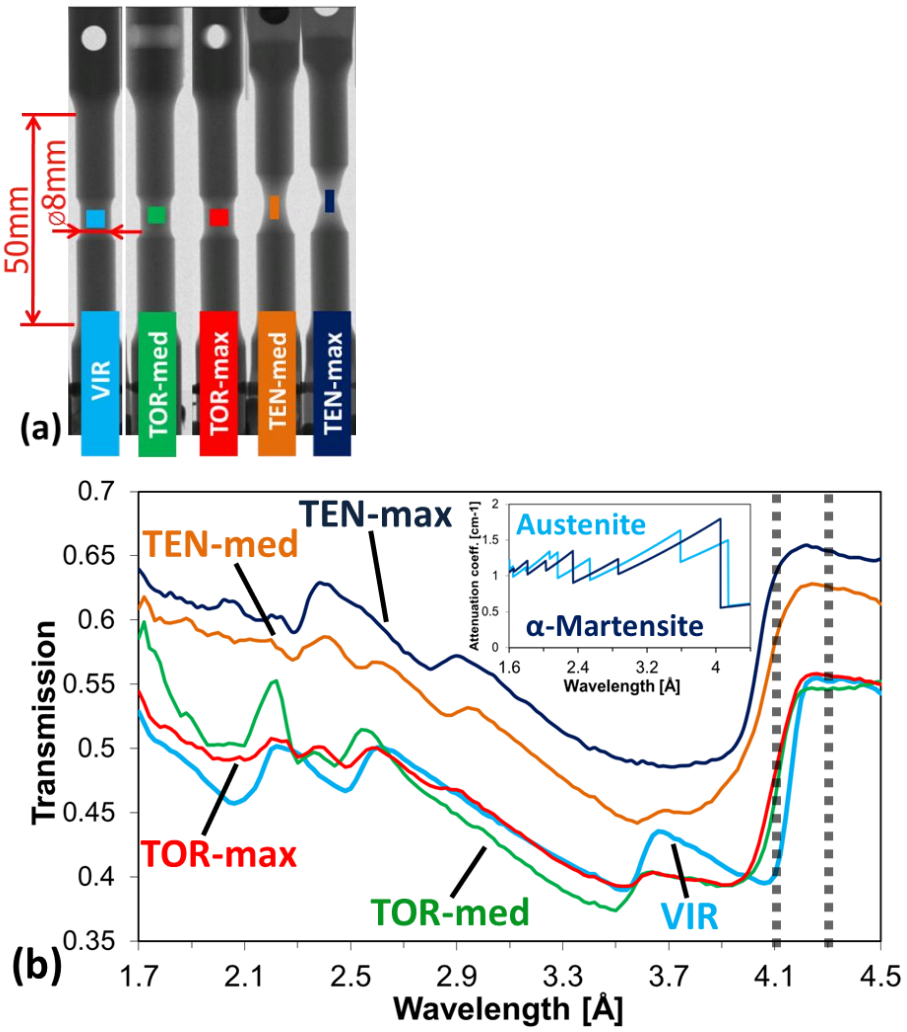

Figure 7-3. Transmission image and transmission spectra: (a) Radiograph of samples with region of interest (ROI) depicted, which was used for the plot in Figure 1b. (b**)** Bragg edge transmission spectra (131 mono-energetic radiographic projections between 1.7 Å and 4.5 Å with an exposure time of 240 seconds/projection) for the center gauge area of the five samples. The non-deformed sample "VIR" is purely austenitic, and only Bragg edges corresponding to austenite are visible. The center of tensile sample "TEN-max" is fully transformed to martensite (compare to theoretical attenuation coefficients depicted in inset and Figure S1) while "TEN-med" is only partially transformed over the selected ROI. The two torsion samples show Bragg edges of both crystallographic phases in the gauge area, which is anticipated, as the center of the sample is not expected to transform to martensite since the applied shear stress there is zero; hence tomographic reconstruction is needed for further quantification. Investigating regions outside the gauge area, the Bragg edge spectra are identical to those of the virgin sample, proving that no (significant) deformation occurred. The dotted vertical lines indicate the wavelengths where tomographic scans were performed.

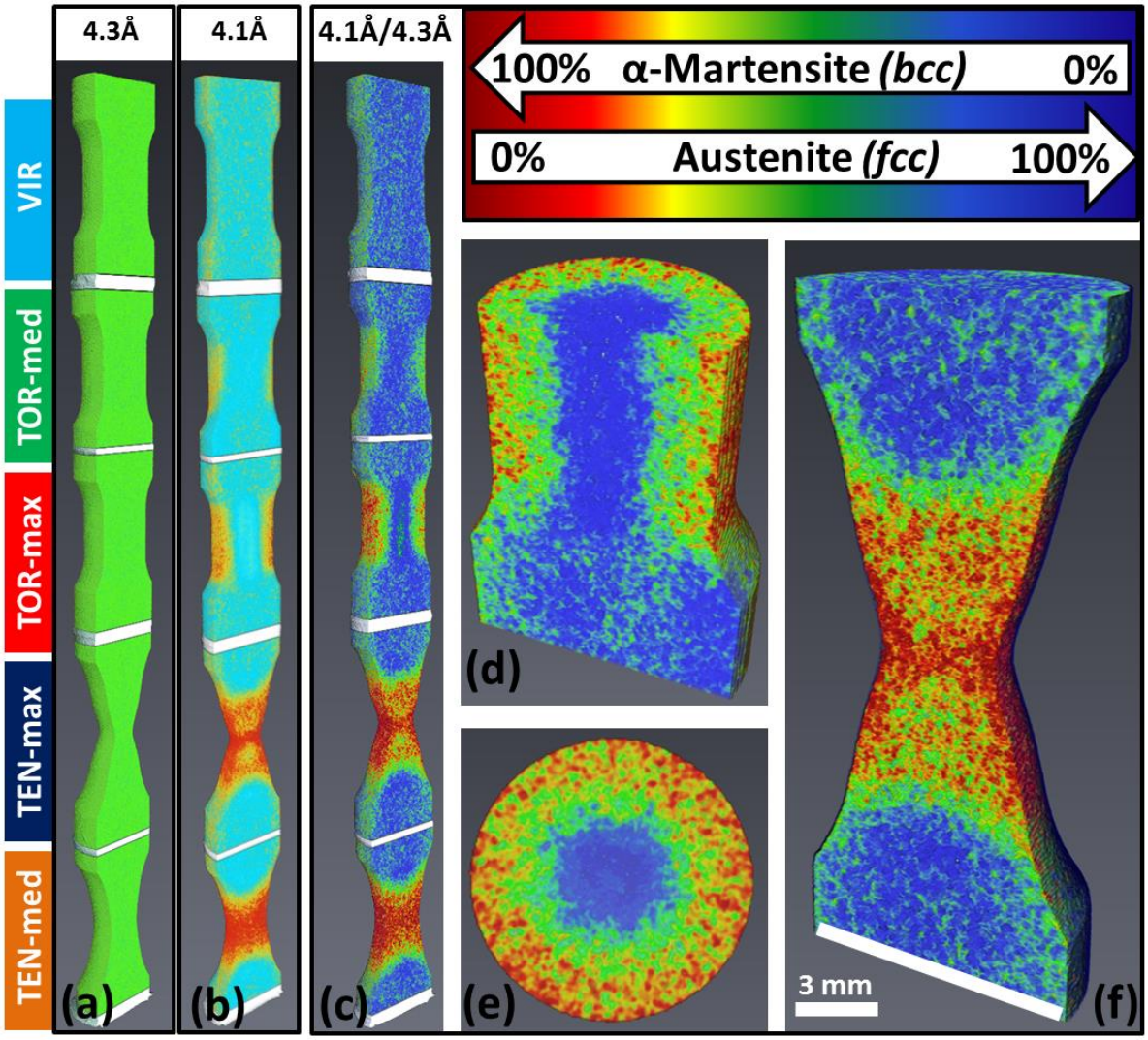

Figure 7-4. Tomographic reconstructions:

(a,b) Center slice of the tomographic reconstruction of the five samples (samples were cut to a region around the gauge area and glued atop one another to be measured simultaneously) for wavelengths before (4.1 Å) and after (4.3 Å) the 'Bragg cut-off' of austenite.

(c-f) The reconstructed data sets were divided to accentuate the transmission intensities due to Bragg diffraction (4.1 Å/4.3 Å), and phase fractions were assigned.

(d,e) The radial dependence of the phase transformation in the torsion sample "TOR-max" is clearly visible in the tomographic reconstruction when viewing the cross section. f) Close-up of the tensile sample "TEN-max" showing that the necking region and regions close to the gauge area surface have the highest martensitic phase contents.

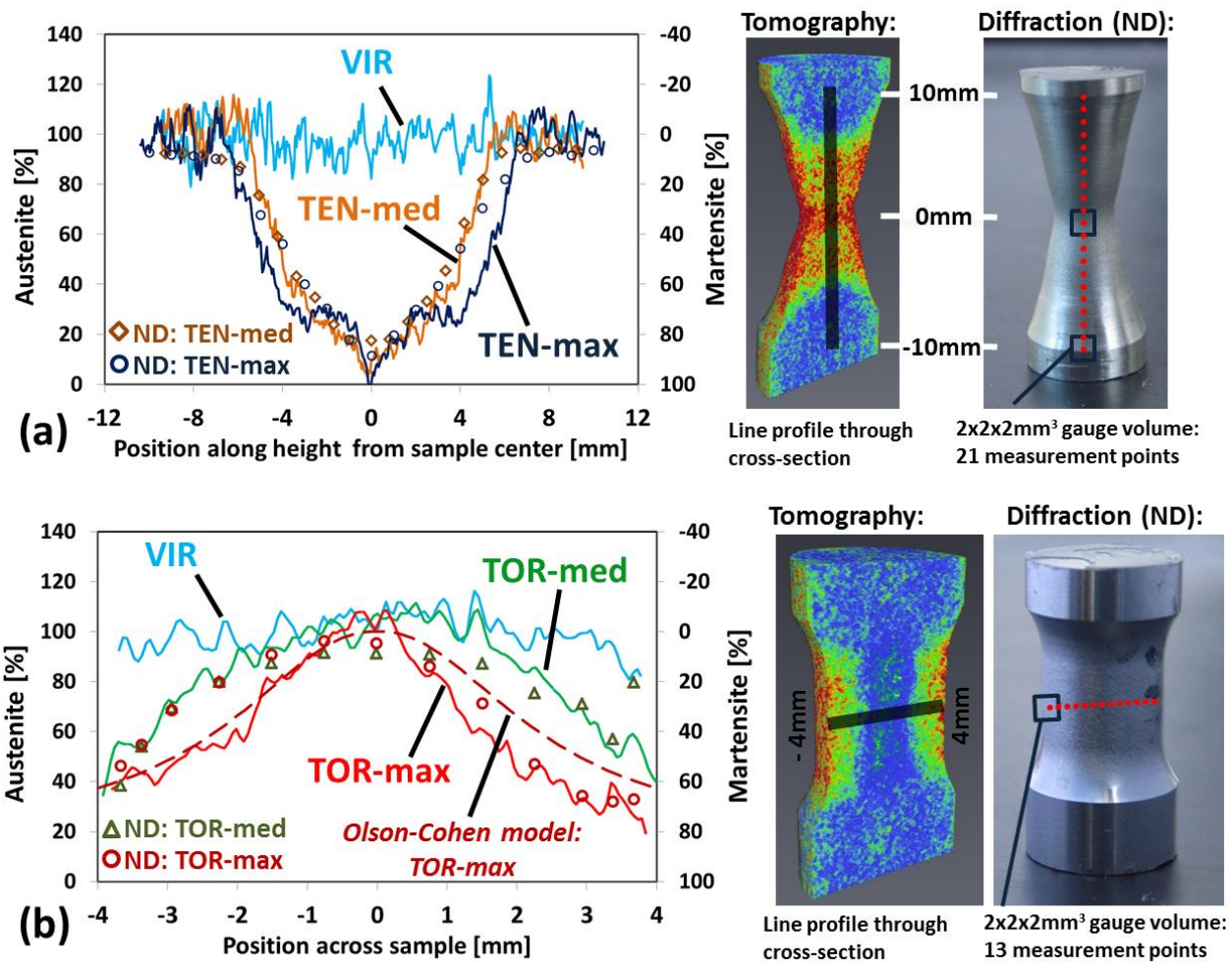

Figure 7-5. Line profiles along and across the reconstructed tomographic data showing the austenitic and martensitic phase fractions. Neutron-diffraction-based results (labeled "ND") are also included to refer to a standardized characterization method. The diffraction results were obtained using a 2×2×2 mm^3 gauge volume and by scanning along/across the samples. (a) Phase fractions along the height of the tensile samples and the virgin sample. Both samples subjected to tensile loading were fully transformed to martensite in the necking region. (b) Phase fractions across the center of the torsion samples and the virgin sample. For the torsion samples, the maximum phase changes occurred in the region near the outer diameter as expected, and no transformation occurred in the sample center. For "TOR-max", the theoretical α-martensite phase evolution is predicted using the Olson–Cohen model (*Olson et al. 1975,*[264]*; Cakmak et al. 2011,*[32]).

The technique opens up new paths for investigations of materials in various fields of science, e.g. physical sciences, materials research, geosciences and even biology or medical sciences (e.g. bone structures using ultra-cold neutrons). By investigating several Bragg edges simultaneously (either using the time-of-flight or monochromator approach), the accuracy of such measurements can be further improved, while even allowing more than two phases to be mapped.

7.5 Technical Experimental Details

Neutron Imaging Instrumentation

The energy selectivity at the cold neutron imaging beamline CONRAD at the reactor source at Helmholtz-Zentrum Berlin (HZB, Germany) was achieved by employing a tunable double-crystal monochromator consisting of one pyrolytic graphite crystal (PCG) monochromator in the upper and lower position, each with a mosaic spread of 0.8°. The wavelength band has an approximate resolution of $\Delta\lambda/\lambda=3\%$ and can be tuned freely between 2.0 and 6.5 Å while the beam position remains unchanged(*Treimer et al. 2006,*[125]). The neutron detector used at HZB consisted of a Li6F scintillator screen of 200 µm thicknesses and an optical CCD camera (2048×2048 pixels) with an objective lens. The effective pixel size in the presented data was 53.6 µm, resulting in a 11×11 cm^2 field of view (FOV), which allowed all five samples to be accommodated. For the experimental data in this paper, the resulting spatial resolution with which the two phases can be distinguished is estimated to be ≈ 100-300 µm, and largely depends on the grain size and microstructural features of the sample. It should be noted that the presented neutron-imaging-based approach is capable of spatial resolutions below 20 µm(*Williams et al. 2012,*[265]) if only the sample grains are small enough to provide sufficient statistics.

Complementary Neutron Diffraction

Complementary neutron diffraction measurements were performed at the constant wavelength diffractometer E3 at HZB ($\lambda = 1.486$Å) with the goal of verifying the

transmission-based results. A primary slit of 2×2 mm^2 and a 2 mm radial collimator (oscillating) were used to define the probed volume within the sample. The tensile samples were incrementally scanned along the height over approximately 20 mm around the sample center. The torsion samples were scanned at 13 locations along the sample cross section, starting from the sample center and going 4.5 mm in both directions. In each case, three bcc reflections (110, 200, 211) and three fcc reflections (111, 200, 220) were recorded. The neutron ray tracing package McStas(*Lefmann et al. 1999,*[266]) was used to correct for the variation in detected neutron intensities due to the different neutron path lengths and partially filled gauge volumes (close to the surface) by simulating an ideal powder sample and normalizing the measured data to the simulated data. From this information, the phase fractions were determined by weighting all bcc and fcc peak intensities. The resulting plots are included in Figure 3.

7.6 Supplement to Chapter 7

This section corresponds to the supporting online information belonging to the article. For the published article is available from the Wiley Online Library.

7.6.1 Supplementary Discussion

Comparison to previous diffraction study of torsion samples Cakmak et al. (*Cakmak et al. 2011,*[32]) have subjected separate samples of the same material (304L) to nine different levels of shear strain and subsequently extracted pins from each deformed specimen along the radial direction, which were then measured using synchrotron X-ray diffraction. For a torsion sample that has undergone a shear strain of 250%, they reported 32% fcc austenitic phase content near the surface. This value is in good agreement with sample "TOR-max" (250% shear strain) where the tomographic data yield a value between 25–35%. For a sample undergoing 104% shear strain, the synchrotron study reported 64.4% austenitic phase content near the surface, while we observed volume fractions between 40–60% for sample "TOR-med" (100% shear strain).

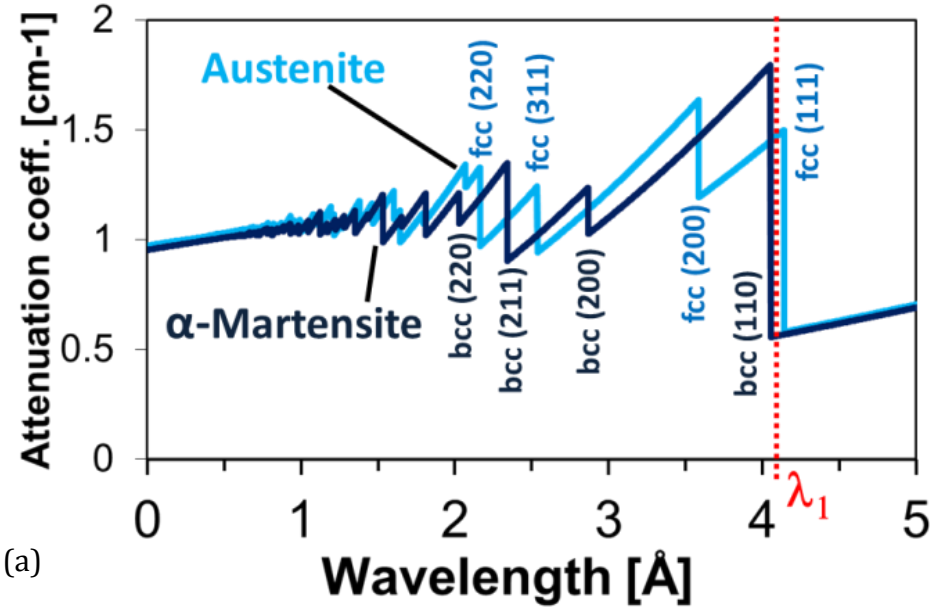

(a)

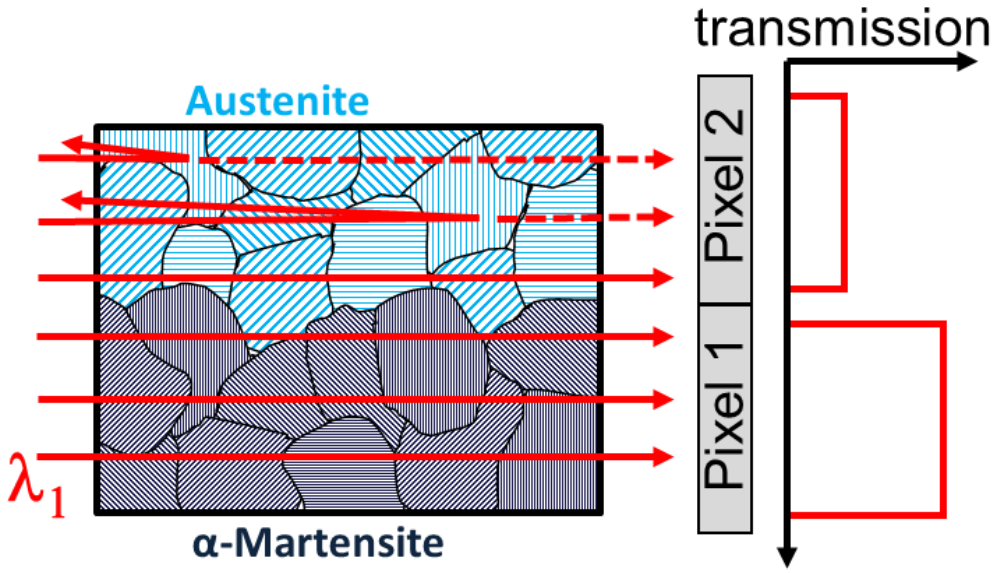

(b)

Figure 7-6. Supplementary Figure S1. (a) Theoretical attenuation coefficients for austenite (fcc structure) and α-martensite (bcc structure) in comparison. (b) Schematic drawings on the principle of Bragg edge tomography: Choosing a wavelength before the Bragg cut-off for austenite and after the Bragg cut-off for martensite results in differences of transmitted intensities.

Comparison to Olson–Cohen model

In Figure 3 for sample "TOR-max," we have included the expected bcc phase evolution across the radius based on the Olson–Cohen model (*Olson et al. 1975,*[264]) and fitting parameters described in(*Cakmak et al. 2011,*[32]):

$$f_{bcc} = 1 - \exp\left\{-\beta \cdot \left[1 - \exp\left(-\alpha \cdot \gamma\right)\right]^{n}\right\}$$
$$\alpha = 0.73; \beta = 1.55, n = 2.59 \quad \text{(S1)}$$

where f_{bcc} is the α-martensite (bcc) fraction, α is a parameter representing the rate of shear band formation with respect to strain, β is related to the probability that a shear-band intersection will generate a martensitic embryo, n is an exponential constant, and γ is the engineering shear strain.

Reconstruction Algorithm

The filtered back-projection algorithm, which was used for the current study, only takes the attenuation differences into account that can be detected in the straight path transmission mode for a given wavelength. In the case of polycrystalline samples with only little texture (as in our case) this works very well. However if strong textures are present, the measured attenuation will vary depending on the sample orientation. Depending on the degree of texture, this effect can just be neglected or corrected for a majority of cases. In order to address the effect of texture, authors propose using additional detectors to detect the diffracted intensities for suitable correction of texture related effects. Furthermore, recording the full Bragg edge spectrum (which is effectively done at Time-of-Flight neutron sources) in conjunction with model predictions is expected to further improve the phase mapping and related future reconstruction algorithms, and might even contribute to the development of new tools for 3D texture analysis.

7.6.2 Supplementary Experimental Section

Samples and Mechanical Deformation

The samples (Figure S2) were made from commercially available 304L (ASTM standard; corresponds to EN 1.4307) stainless steel with an average grain size of 35 μm before deformation. The samples were deformed before the neutron experiment with a custom built tension-torsion loading system,(*Woracek et al. 2011,*[207]) while the surface strains were monitored with a digital image correlation system (VIC-3D). Two of the samples were deformed in pure torsion (tensile stress kept at constant holding load of 20 MPa) to a maximum shear stress of 100% (sample "TOR-med"; 71.5° twist) and 250% (sample "TOR-max"; 179° twist). For comparison among various loading paths, the invariants of the strain tensor are calculated as octahedral shear stain, described by:

$$\gamma_{oct} = \frac{2}{3}\sqrt{(\varepsilon_x - \varepsilon_y)^2 + (\varepsilon_y - \varepsilon_z)^2 + (\varepsilon_z - \varepsilon_x)^2 + 6\cdot(\varepsilon_{xy} + \varepsilon_{yz} + \varepsilon_{zx})^2} \qquad \text{(S2)}$$

yielding an octahedral shear strain of 82% for sample "TOR-med" and 204% for sample "TOR-max." Two samples were deformed in pure tension to 5.4 mm ("TEN-med") and 7.2 mm ("TEN-max") axial deformation, corresponding to theoretical octahedral shear strains of 101% and 136%. The corresponding stress vs. engineering strain curves are shown in Figure 7-8, S3. One sample, "VIR," was kept un-deformed as a reference.

For a sample subjected to tensile loading, the stress – and hence strain – is uniform across the cross section of the sample during elastic loading (see Figure 7-9, S4). For ductile materials, necking often occurs in the center of the gauge area during increased plastic deformation and causes the stress to further concentrate in this region (note that the transmitted neutron intensity for the center of the tensile samples is higher than for the torsion and virgin samples due to the reduced attenuation/path length of the neutrons). In a cylindrical torsion sample, the maximum shear stress and strain occur towards the outer radius of the cylinder and are zero at its center (see Figure 7-9, S4).

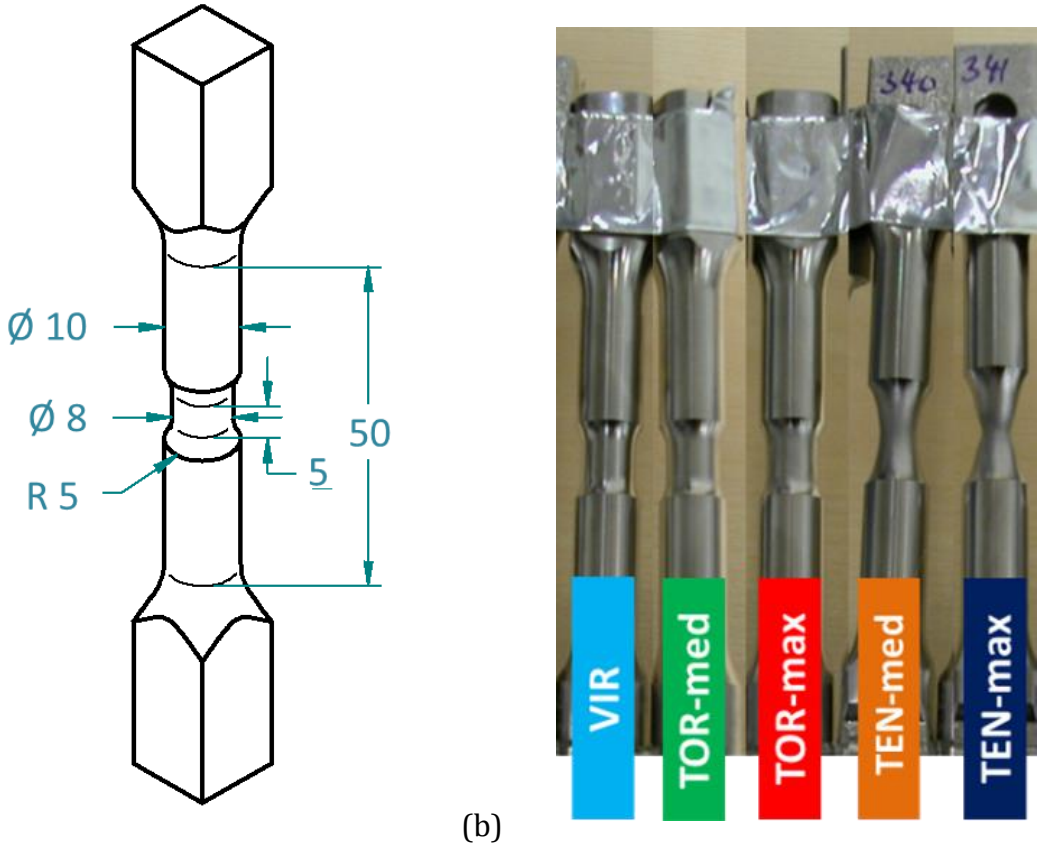

(a) (b)

Figure 7-7 Supplementary Figure S2. (a) Sample dimensions in mm. (b) Photograph of the five samples after deformation.

(a)

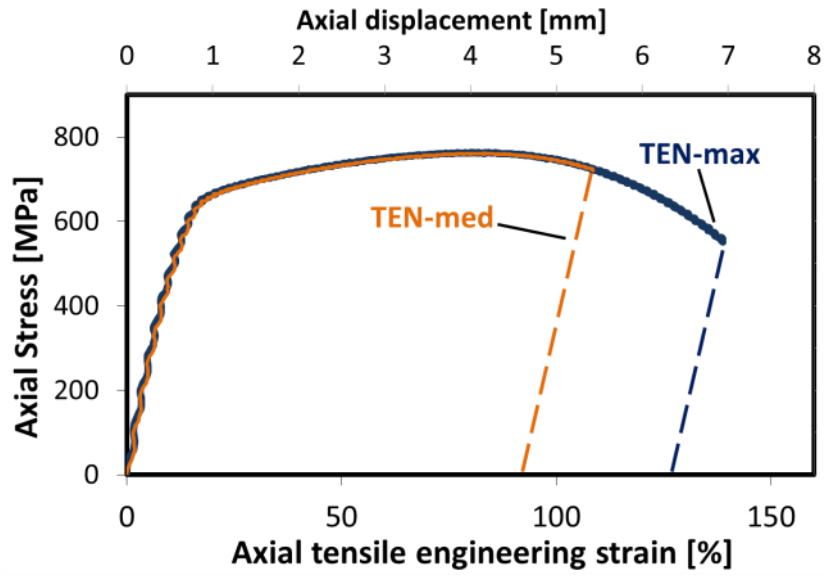

(b)

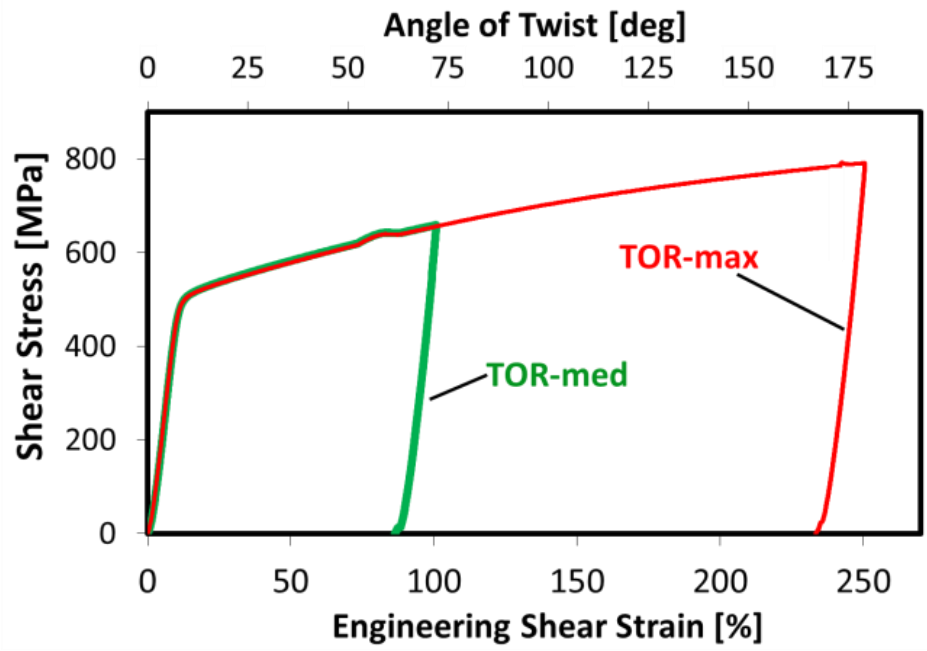

Figure 7-8. Supplementary Figure S3. Stress-strain and stress-deformation relationships for the (a) tensile and (b) torsion test.

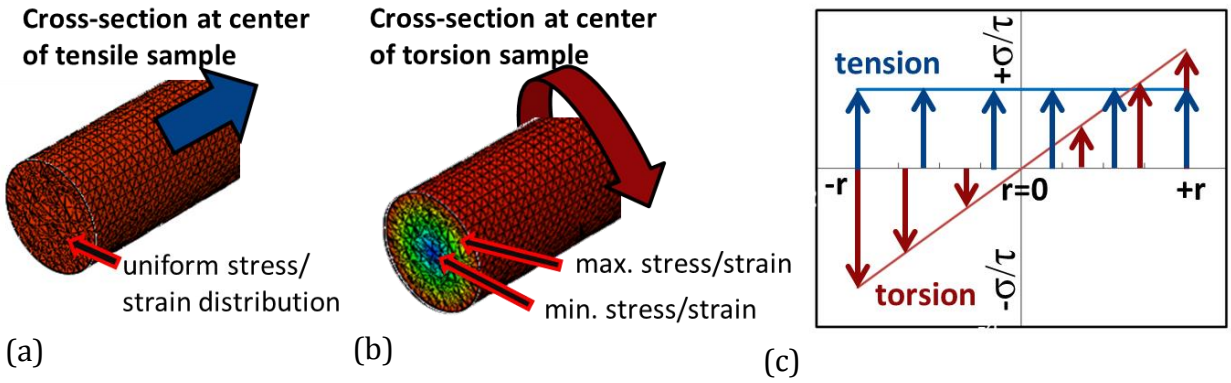

Figure 7-9. Supplementary Figure S4. Elastic loading (up to yielding only): (a) The stress (and strain) during tensile loading is uniform in magnitude and direction while (b) the shear stress changes with radial distance r under torsion. (c) Variation with radius r of axial stress (σ) during tension and shear stress (τ) during torsion.

7.7 Complementary Experimental Data

This section presents additional data that was not published in the journal paper. It will discuss the experimental parameters in more detail,

7.7.1 Surface Strains by Strain Gauges and VIC-3D

The surface strains were monitored during the torsion test by using resistance based rosette strain gauges and by Digital Image Correlation (VIC-3D). Due to compliance in the loading system, there is a discrepancy between the theoretical calculated shear strain based on the twist angle (from the stepper motor position) and the recorded shear strain by strain gauges/VIC-3D. The compliance of the system, i.e. the twist angle based on the stepper motor, has been corrected with a compliance factor, as is shown in Figure 7-10 for a typical torsion test of the 8 mm diameter samples (strain magnitude shown corresponds to sample TOR-max). Since the strain gauge and VIC-3D will not provide meaningful results beyond a certain plastic strain, the corrected twist angle was used to plot the engineering

stress-strain curve as depicted in Figure 7-11. It should be noted that the maximum plastic strain magnitudes are approximately the same for the corrected engineering shear strain and the strain derived from the stepper motor directly. The surface strains from VIC-3D during the torsion test indicate a uniform deformation inside the gauge area (Figure 7-12).

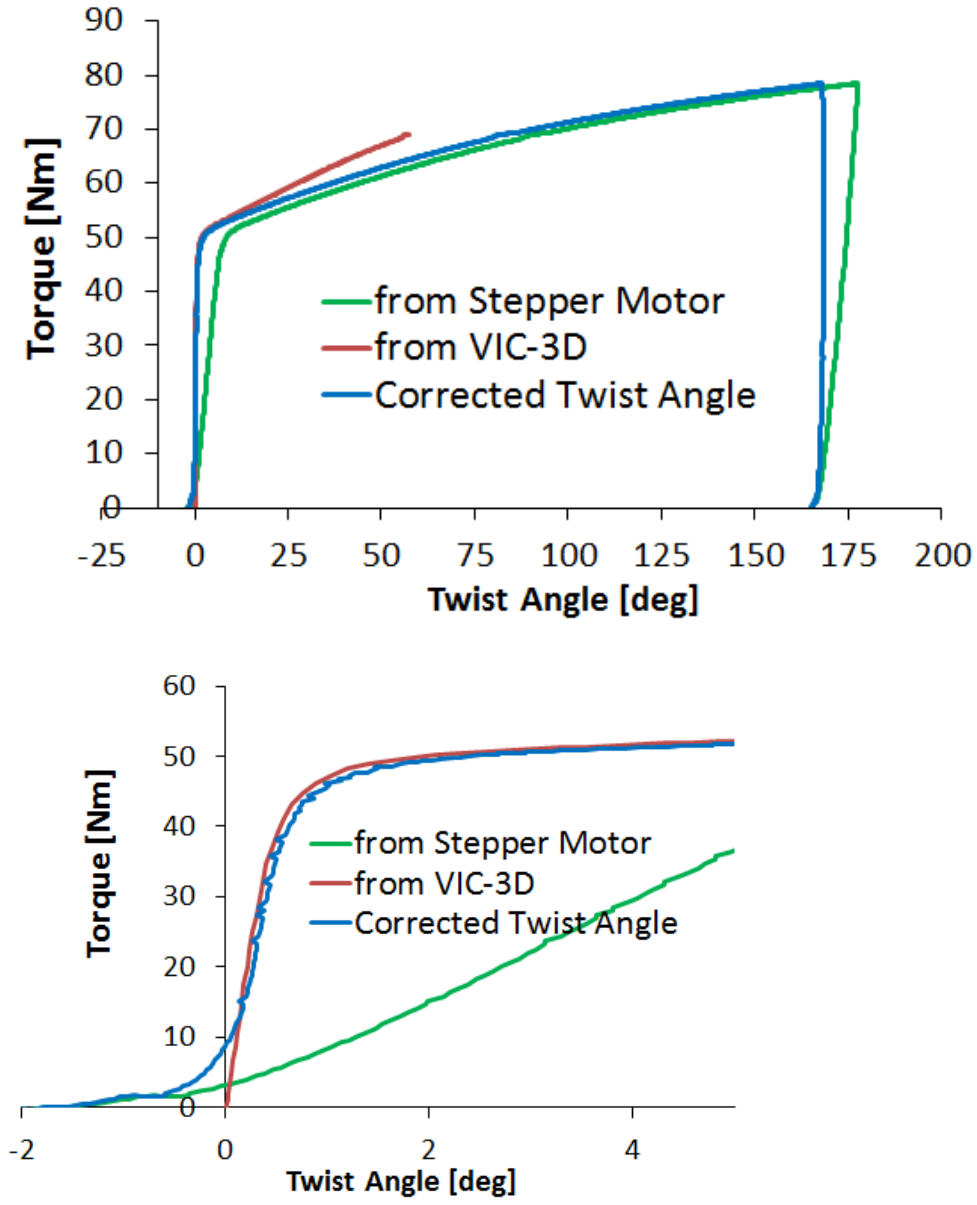

Figure 7-10. Compliance Correction of the loading system for torsion testing of sample TOR-max (d=8 mm).

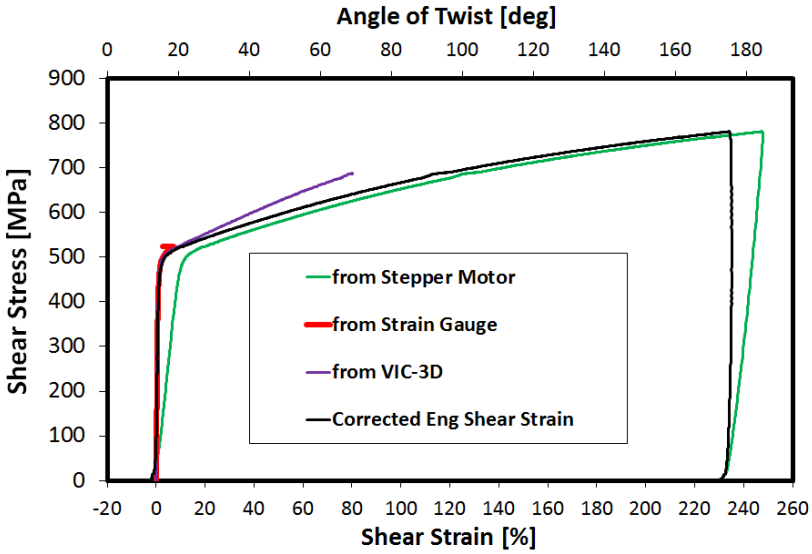

Figure 7-11. Shear Stress vs. Shear Strain and Angle of Twist for torsion sample "TOR-max). The angle of twist (and the engineering shear strain based on this value) needs to be corrected especially in the elastic sample regime due to compliance of the loading system. The corresponding uncorrected and corrected curves are shown. Surface based strain measurements by rosette strain gauges and VIC-3D are in excellent agreement (up to the onset of plasticity).

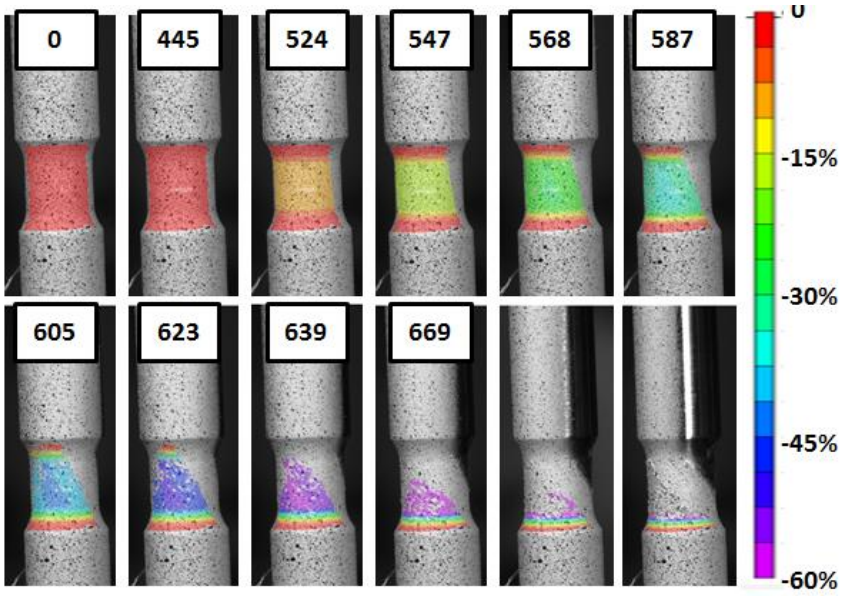

Figure 7-12. Shear Strain on the surface from VIC-3D: It can be seen that the gauge section undergoes a uniform strain on the surface. The numbers refer to shear stress in MPa (the last 2 images are recorded beyond 669MPa).

7.7.2 Texture and Phase Measurements using Neutron Diffraction

Texture measurements were performed at the GEM beamline of the ISIS spallation neutron source at Rutherford Appleton Laboratory (*Kockelmann et al. 2006,*[267]) and at the HIPPO beamline of the LANSCE spallation neutron source (*Vogel et al. 2004,*[258]). The instruments are depicted in Figure 10-11. The beam was defined by incident slits to irradiate the gauge section of the samples. At HIPPO, where all five samples were measured, the incident beam was defined to a height of 2 mm around the gauge center. At GEM, only the virgin sample (R#344) and the TOR-med (R#348) sample were measured, with the incident beam defined to a height of 5 mm, spanning about the complete gauge center.

- The undeformed (virgin) samples were determined to be 100% austenitic at both instruments, as was determined from the tomography approach. Contrary to EBSD (see next section), this is expected as bulk neutron diffraction is usually not sensitive enough for small amounts of phase fractions, while it should be kept in mind that EBSD also only probes a very small portion of the sample and hence may not be fully representative.
- For the TOR-med (R#348) sample, the averaged phase fraction in the sample volume was determined to be 86.7% at GEM and 88.5% at HIPPO. The bulk average based on the Olsen Cohen model is predicted in this case to be 91% Austenite, whereas the line profile from the tomography data suggests 84%.
- For the TOR-max (R#347), the bulk average based on the Olsen Cohen model is predicted to be 68%, while at HIPPO 59.9% were measured. The neutron tomography line profile measures exactly 60% Austenite.

The texture results of HIPPO and GEM agree well and show that the samples exhibited only a mild texture before and after the deformation. Pole Figures are shown in Table 7-2, Table 7-3 and Table 7-4. The orientation of the pole figures is such that the marked line faces to 12 o'clock.

Table 7-2. Pole Figures for the undeformed and Torsion samples measured at HIPPO.

• **Sample name** • **Shear strain experienced**	**Phase**	**Pole Figures**
• R#344 (VIRGIN) • 0 % 	Austenite (100 wt%)	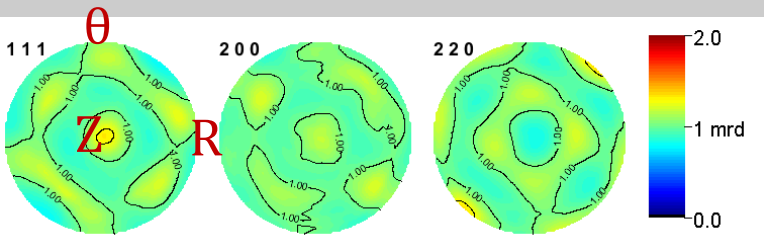
	Ferrite	-
• R#348 (TOR-med) • 100 % 	Austenite (88.5 wt%)	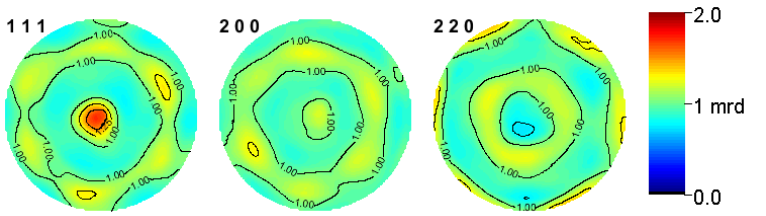
	Ferrite	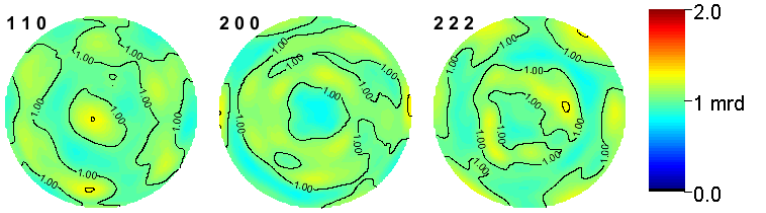
• R#347 (TOR-max) • 250 % 	Austenite (59.9 wt%)	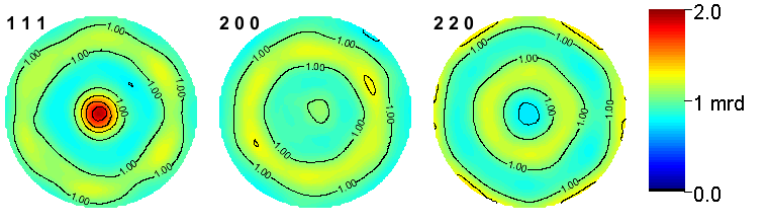
	Ferrite	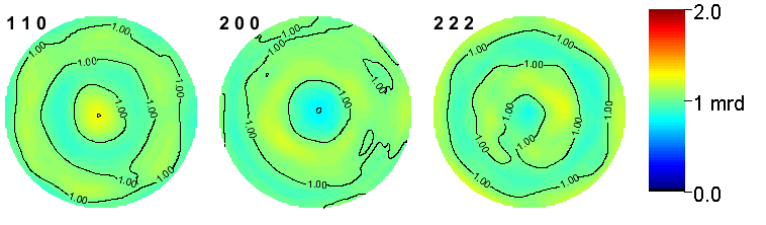

Table 7-3. Pole Figures for Tensile samples measured at HIPPO.

• Sample name	Phase	Pole Figures
• R#340 (TEN-med) 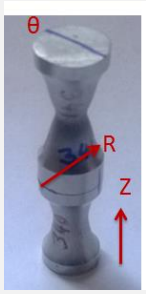	Austenite (65.2 wt%)	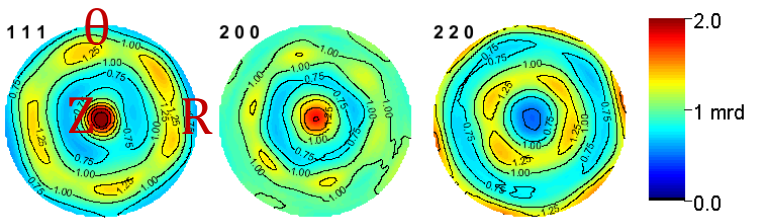
	Ferrite	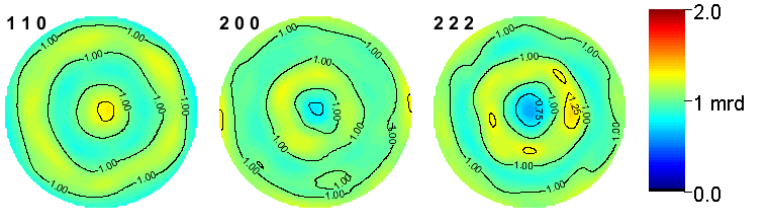
• R#341 (TEN-max) 	Austenite (12.8 wt%)	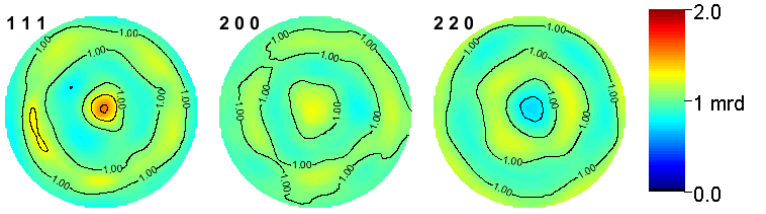
	Ferrite	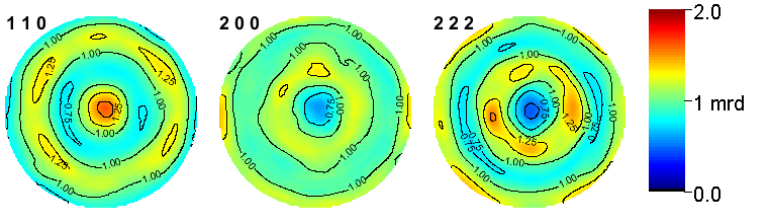

Table 7-4. Pole Figures for the undeformed and one Torsion sample measured at GEM.

• **Sample name** • **Shear strain experienced**	**Phase**	**Pole Figures**
• R#344 (VIRGIN) • 0 % 	Austenite (100 wt%)	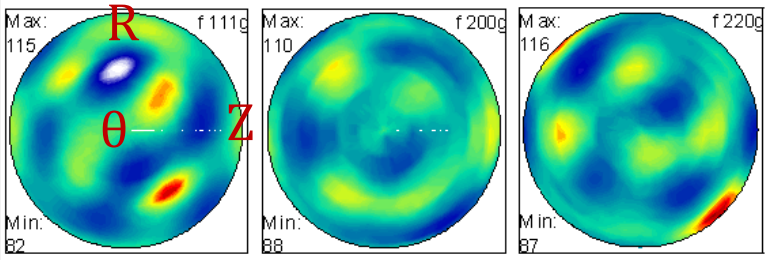
	Ferrite	-
• R#348 (TOR-med) • 100 % 	Austenite (86.7 wt%)	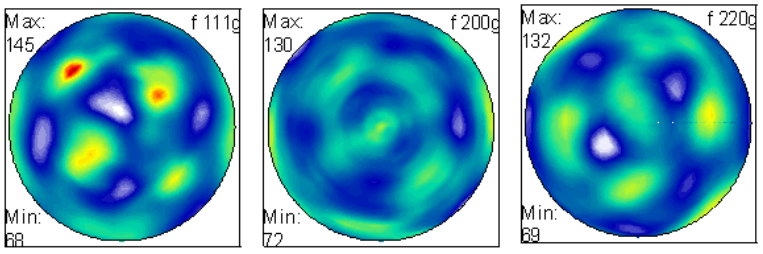
	Ferrite	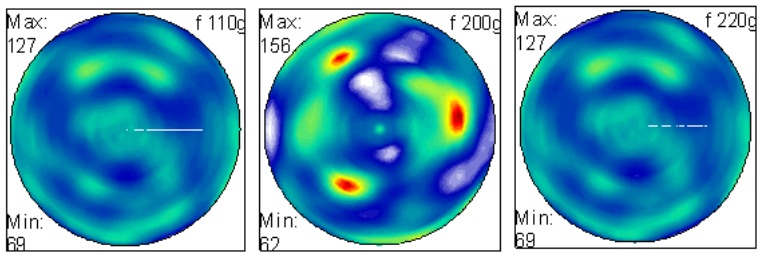

Note: Pole Figures will be updated to change the orientation to be the same as for HIPPO

7.7.3 EBSD Mapping

With the aim to verify the phase transformation using another alternative method, Electron Backscatter Diffraction (EBSD) was performed on samples of the same stock material, on samples that were deformed to the same amount of shear strain. To produce specimen for EBSD investigation, the samples were cut by a slow cutting saw with a diamond blade. The samples were mounted in Epoxy and mechanically polished according to (*Vander Voort et al. 2007,*[268]), followed by vibratory polishing for 25 minutes. Afterwards the samples were removed from the Epoxy mount (by heating in an oven to 80°C) to be mounted to a sample holder for the SEM. Specimens that were cut from the cross section outside of the gauge section (d=10 mm instead of d=8 mm) were assumed to be non-transformed.

EBSD maps were obtained for the various samples, where the non-deformed specimen sections yielded Kikuchi patterns of good quality consistently (>90% indexing success). The scan time to produce an EBSD maps as presented in Figure 7-13 was approximately 45 minutes. The non-deformed samples were mostly austenitic, but some martensite was shown to be present as well, which is expected in such a material. The fractions however may not have been enough to be measured by neutron diffraction. Besides the phase determination, the grain size can be seen nicely as well as the grain orientation, also indicating only a low degree of preferred orientation.

When investigating areas that are slightly away from the center line of the deformed samples, patches of martensite become apparent. The Kikuchi patterns obtained in regions of the sample that had experienced more strain were of less quality and could often not be indexed. For one region, presented in Figure 7-14c, a scan was performed at a radial distance of 2 mm from the center. In order to obtain data that could be indexed, the electron voltage was reduced, increasing the scan time to over 9 hours. The determined phase fractions at 2 mm (45% Austenite) agree reasonably well with the ones shown in Figure 7-5, determined by Bragg edge tomography (one side ≈55%, the other ≈45%) and diffraction (one side ≈79%, the other ≈47%). One needs to keep in mind that the phase transformation may not happen uniformly throughout and different locations/samples were probed.

It should be noted that eventually, with more careful preparation and more time consuming scanning procedures (for example further reducing the electron voltage), better EBSD patterns could maybe be obtained in even higher strained regions. Papers addressing deformation of 304 grade stainless steel using EBSD are for example (*Gey et al. 2005,*[269]; *Petit et al. 2007,*[270]; *Rodríguez-Martínez et al. 2011,*[271]; *Shen et al. 2012,*[272]). However, this needs to be considered beyond standard EBSD operation and as such would be methodological development itself. Hence, the neutron imaging approach has a significant advantage of resolving phase fractions in highly strained regions.

Table 7-5. Overview of samples for EBSD analysis.

Sample name	• **Shear strain experienced** • **Cross section**	**As-cut specimen from Torsion sample**	**Polished and mounted specimen for EBSD**
R#343D	• 0 % • across	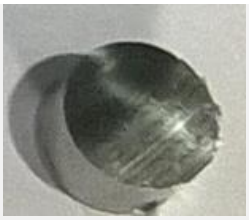	
R#411C	• 0 % • along		
R#410A	• 250 % (corresponds to TOR-max) • across	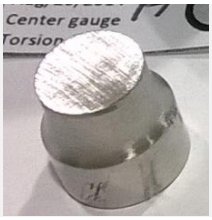	
R#411B	• 250 % (corresponds to TOR-max) • along		

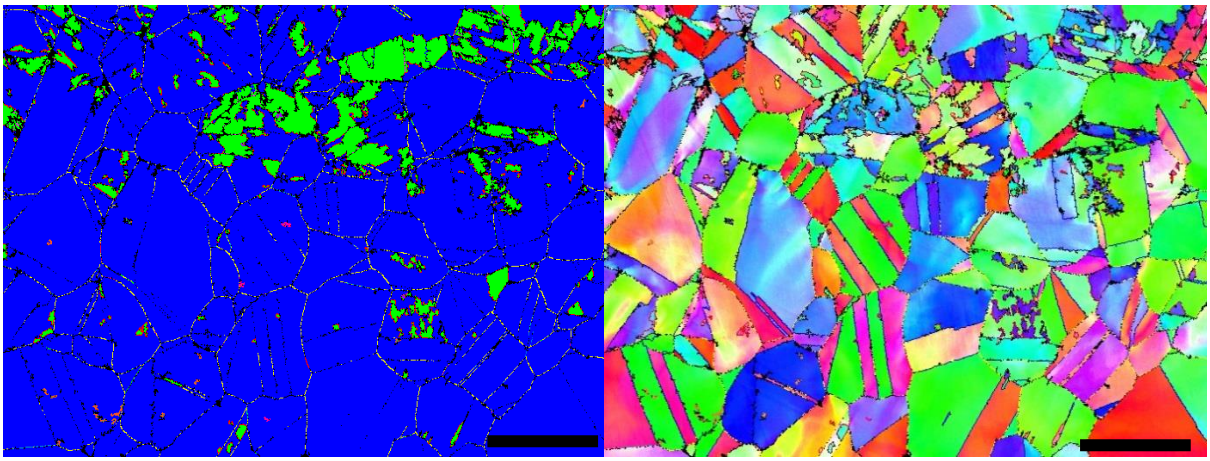

(a) Sample R#343D. Measured at sample center.

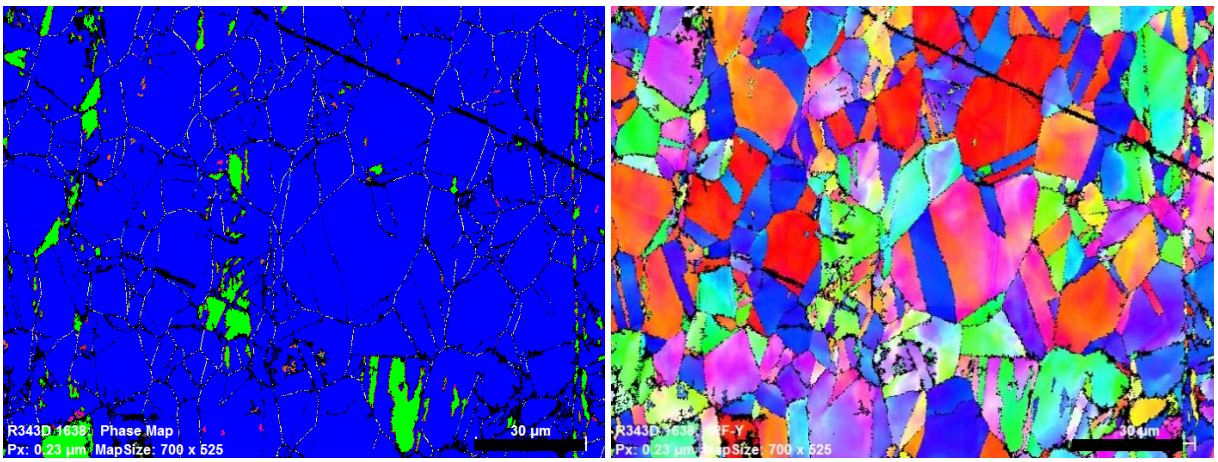

(b) Sample R#411C. Measured at sample center. Phase: 85% FCC, 7%hcp, 6%bcc

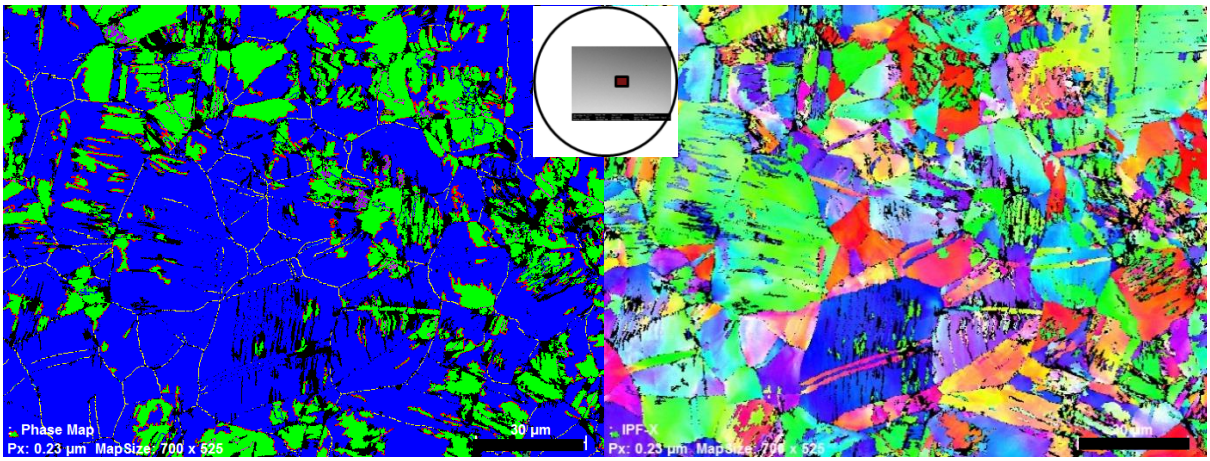

(c) Sample R#410A: close to center (slightly off to the side)

Figure 7-13. EBSD phase maps and grain orientation maps PART I. Magnification bar = 30 µm.

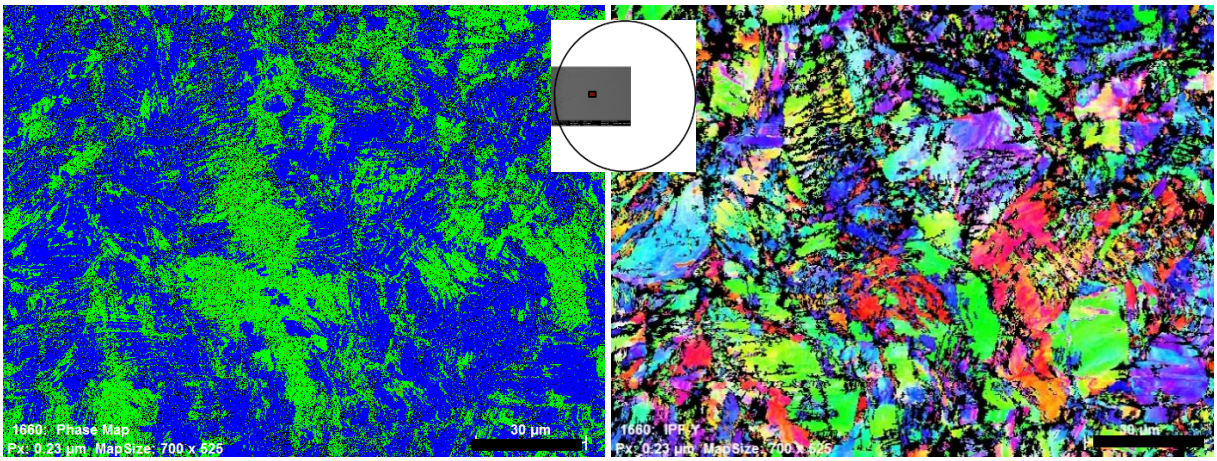

(a) Sample R#410A. Measured towards side of the sample (not precisely defined).

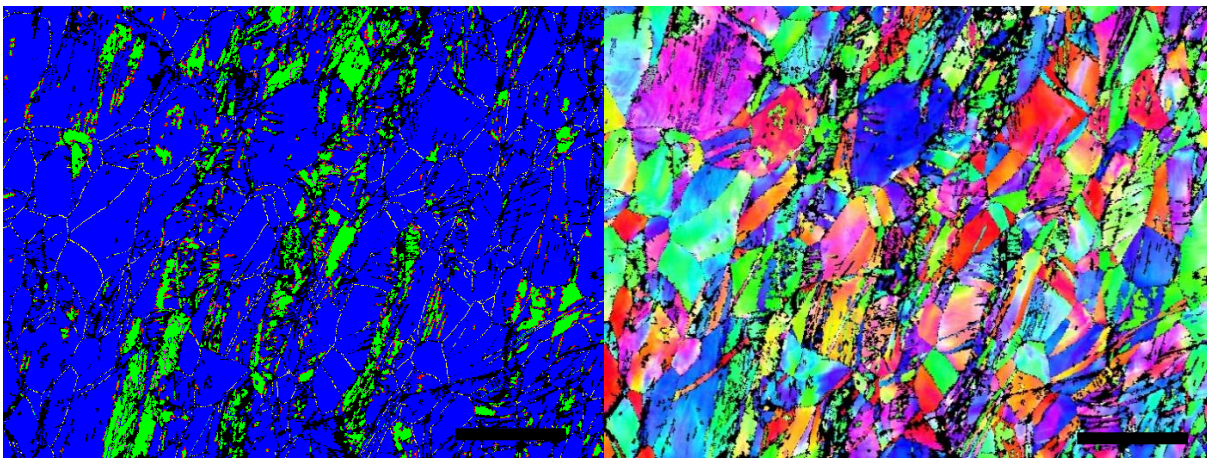

(b) Sample R#411B: center (slightly off to the side). Phase: 75% FCC, 8%hcp, 15%bcc

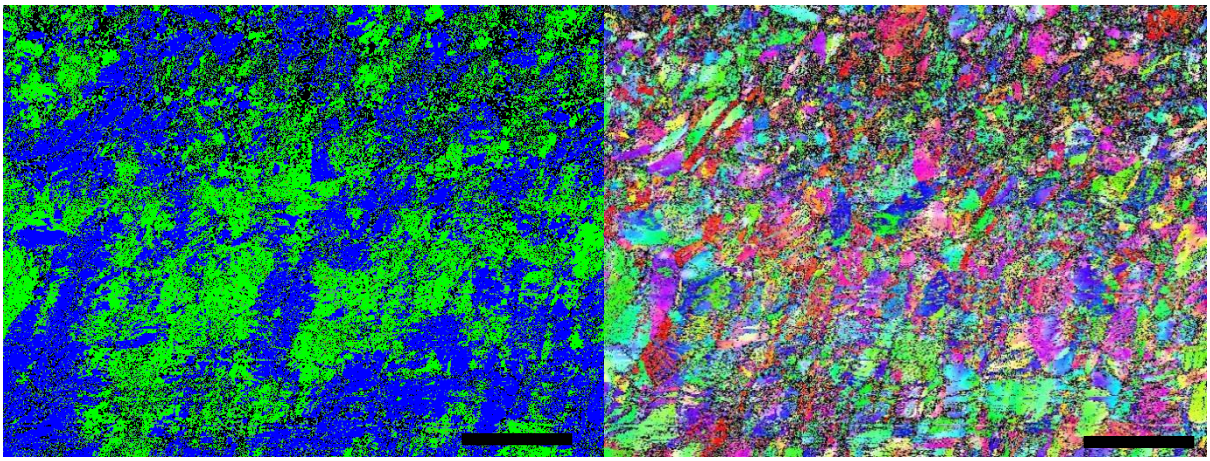

(c) Sample R#411B: 2mm from the center. Phase: 45% FCC, 15%hcp, 39%bcc

Figure 7-14. EBSD phase maps and grain orientation maps PART II. Magnification bar = 30 µm.

7.7.4 Time-Of-Flight Bragg Edge Measurements

Two of the samples, TEN-max (R#341) and TOR-max (R#347), were investigated by transmission measurements at the engineering TOF diffractometer ENGIN-X at ISIS, using the MCP detector described earlier. Using this setup it is possible to record a broad wavelength spectrum for every pulse, while counting statistics are being improved by adding multiple pulses. Due to the instrument length and the high time sensitivity of the detector, the achievable wavelength resolution allows recording the Bragg edges with high precision. It can be observed that the Bragg edges are sharper compared to CONRAD, because of the superior wavelength resolution.

A phase determination can be achieved even after short exposure times (<30 minutes; this of course depends on sample size and region of interest) since the complete spectrum becomes visible. Figure 7-15 depicts the transmission data for the tensile sample "TEN-max" and clearly shows the phase transformation in the gauge area (data obtained after 5h integration time). A comparison of exposure times can be found in the appendix 10.7. This in particular allows obtaining transmission spectra for various sample orientations which in return gives an indication if a sample exhibits texture or not. This is included in Figure 7-15, showing that a sample rotation of 30 degrees results in a similar spectrum, indicating that no strong texture is present (compare this to section 7.8, where examples of texture are given). More sample orientations will help to support and verify this indication. Obviously a cylindrical sample is the simplest case, as the beam path length is the same for different sample orientations.

For the torsion sample TOR-max, the better wavelength resolution and the ability to measure Bragg edges more precisely is apparent: When both phase are present in the measured beam path, the Bragg edge correspond to the austenitic phase, fcc(111), and the Bragg edge correspond to the martensitic phase, bcc(110), were convoluted/smeared in only one – widened – Bragg edge at CONRAD, while here it becomes clear that two individual edges are present, visible as a "shoulder in Figure 7-16. The black vertical lines in 7-15 and Figure 7-16 correspond to detector read-out times, after which the detection

efficiency is slightly changed and hence the offset of the transmission value (this can be corrected for and will be done in the future).

Despite all these advantages that are apparent using the TOF technique at a spallation source, there are still many challenges associated with such measurements, especially if the goal is to perform a tomography reconstruction as was done at CONRAD. Tomography with "many" projections seems less feasible than using monochromator at this stage. The challenges that need to be addressed are how to combine the individual images (in this case each projection consist of a spectrum with ≈2000 images) most effectively for reconstruction. If using only one or few images, the image quality is not sufficient for a tomographic reconstruction and obviously, the available information from TOF would not be used efficiently. The easiest possibility could be to sum images before and after Bragg edges of interest in order to obtain individual images of reasonable quality. However, in the case of the last Bragg edge this will not be suitable as there not enough images at distinct wavelengths that would clearly belong to one phase. The most promising approach would be to apply a fitting routine to the Bragg edge spectrum. The fitting parameter would deliver the phase fractions for every curve and pixel, from which a new images would need to be assembled for every projection. Then this new image would be the one to be reconstructed. Since the fitting parameter would not be the attenuation value, thought needs to be given on how to quantify the reconstruction. In order to fit the spectra successfully at small regions (only a few pixels) long count times are needed, as can be seen from the figures in appendix 10.7.

For the torsion sample "TOR-max", 28 tomographic projections were recorded at ENGIN-X, each using one hour exposure time. This limited number of projections and the relatively poor statistics pose a significant challenge to successfully obtain a tomographic reconstruction. The detailed data treatment is beyond the scope of this dissertation, but is planned to be continued. For comparison, in the same amount of time, at CONRAD 180 projections were obtained and standard data processing and reconstruction tools could be used.

The next generation of instruments at spallation sources, optimized for imaging experiments, could overcome some of the problems, especially if effort is dedicated for suitable data processing.

Table 7-6. Overview of experimental parameters for energy scan at CONRAD and ENGIN-X for the same samples.

	Energy Scan CONRAD	**Energy Scan ENGIN-X**
Samples	6 samples (full length)	2-3 samples (cut)
Pixel Size	54um	55um pixels
FOV	11x11cm2	2.8cmx2.8cm2
Wavelength spectrum	1.6Å to 4.4Å	1.4Å to 4.4Å
Wavelength increments	0.02Å increments	0.0014 Å increments
Time	• Parameters need to be decided before Energy Scan • 10h +10h FF (3x80sec/ λ)	• More flexible. Data saved in 1h intervals, up to 11h. • 11x1h (+1h FF)

Table 7-7. Overview of experimental parameters for tomography scan at CONRAD and ENGIN-X for the same samples.

	Tomography CONRAD	**Tomography ENGIN-X**
Samples	5 samples (cut)	2 samples (cut)
Wavelengths	6 single λ (2λ's sufficient in our case)	1.4Å to 4.4Å (0.0014 Å increments
Range	0-360deg	0-360deg
Projections	180	28 projections: golden ratio
Exposure	3x80sec/projection	1h/projection
Time	• 24h (12h/2 λ's) • 72h for 6 λ's	• 28h (+1h FF)

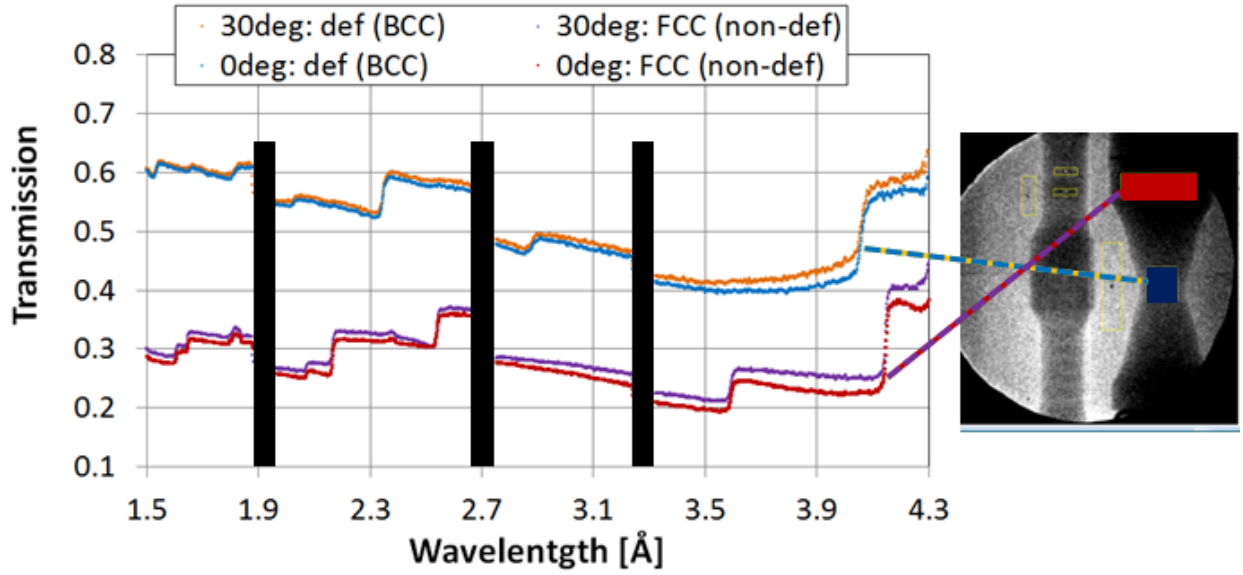

Figure 7-15. Bragg edge transmission spectra recorded by TOF for sample TEN-max . The region in the center of the gauge center shows a full transformation to Martensite, in analogy to the data taken at CONRAD. The region outside of the gauge area has not experienced plastic deformation and hence is still fully austenitic. Two sample orientations are presented and it can be observed that the Bragg edge spectra are very similar, indicating that no strong texture is present.

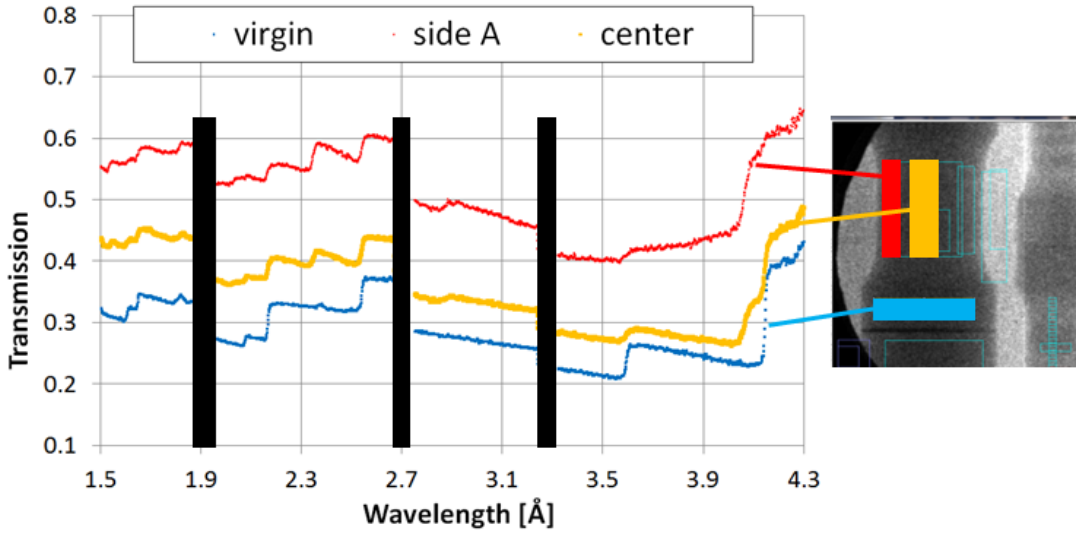

Figure 7-16. Bragg edge transmission spectra for sample TOR-max. It can be seen that the transition from Austenite to Martensite for the last Bragg edge is resolved much more detailed than at CONRAD.

7.8 Outlook: Further Work on Textured Samples

Torsion samples were made from another stock of same type of alloy (304L) with the same initial goal of phase mapping. However, it shows that these samples exhibited a significant amount of texture, before and after the deformation. This sub-chapter is intended to give a brief overview of the experiments and the observations, but the complete analysis of this data is beyond the scope of this dissertation. Especially analyzing the texture in more detail and more quantitatively would require a significant effort, and is being discussed for example by Santisteban (*Santisteban et al. 2006,[176]; Santisteban et al. 2011,[184]; Malamud et al. 2014,[233]*).

The measurements that were made showcase the strength of Bragg edge neutron imaging to reveal spatial variations of texture, that otherwise easily would remain undetected using destructive surface or bulk measurement techniques. Three samples were investigated at CONRAD, as depicted in Figure 7-17: an undeformed sample (A), a torsion sample subjected to 100% shear strain (B) and a torsion sample subjected to 250% shear strain (C). Radiographs taken at CONRAD: (b) at 3.9 Å (c) at 4.2 Å and (d) Diffraction contrast by normalizing images taken at 3.9 Å by 4.2 Å.

From the radiographs that were taken using CONRAD (Figure 7-17) at 3.9 Å and at 4.2 Å, one can quickly observe distinct difference in the non-deformed (virgin) sample A. The thickest part of the sample (center diameter) in the radiographs at 3.9 Å is more transparent than the outer diameter. In the diffraction contrast enhanced images (when normalized by radiographs taken at 4.2 Å), this effect can be even seen much clearer. This could be explained by the fact that the sample exhibits a different crystallographic orientation of grains along the hoop vs radial direction, potentially – but not necessarily – due to a fiber texture. (In the radiograph, the center of the sample corresponds to the hoop directions, whereas the edge corresponds to the radial direction). For the given orientation in Figure 7-17, the grains of the bcc (110) family are orientated such that they are mostly aligned non-perpendicular to the incident beam in the hoop direction, where many more are aligned perpendicular to the incident beam in the radial direction. Texture differences in the as-processed material can hence quickly be discriminated.

Moreover, the radiographs revealed that the samples form a complicated texture after torsional deformation, appearing as horizontal lines in the radiographic projections. The samples were cut and stacked atop one another to record radiographs over a 360 degree rotation (as for a tomography).The different projections reveal how fast the texture varies and moreover indicate that the texture of the undeformed samples may not be (only) radially dependent, but instead be an artifact of rolling (in-plane texture). However, the careful analysis of the data is still to be performed and the discussion above is based only on first observations.

The same samples were also measured by Bragg edge transmission at ENGIN-X, using the MCP detector technology described in chapter 5. Figure 7-19 shows the rcorded Bragg edge patterns for torsion sample B. Investigating small regions within the horizontal bands reveals that the Bragg edge patterns vary along the height of the specimen. A a distance of approximately 3.2mm apart, the Bragg edge profile has the same shape again (compare the yellow and baby-blue curves in Figure 7-19). The figure also shows the Bragg edge pattern for the same region (indicated in dark blue), while the sample is rotated 15 dgrees around its center. One can already see from these few data sets, that valauble information about the texture variations can be deduced. It is planned to further analyze the existing data and eventually collect complemnatry data for a more detailed examination.

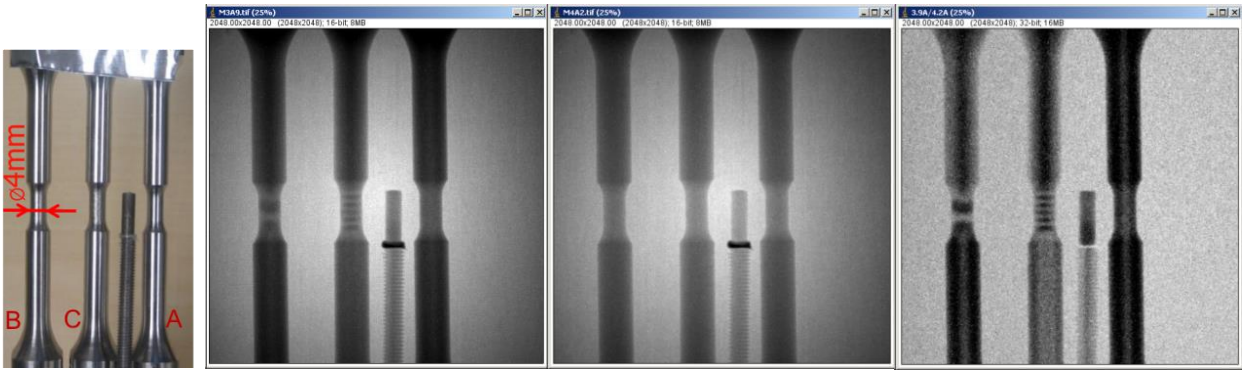

(a) (b) (c) (d)

Figure 7-17. (a) Photograph of three samples (A: undeformed, B: Torsion sample subjected to 100% shear strain, C: : Torsion sample subjected to 250% shear strain) that were investigated at CONRAD and ENGIN-X. Radiographs taken at CONRAD: (b) at 3.9 Å (c) at 4.2 Å and (d) Diffraction contrast by normalizing images taken at 3.9 Å by 4.2 Å.

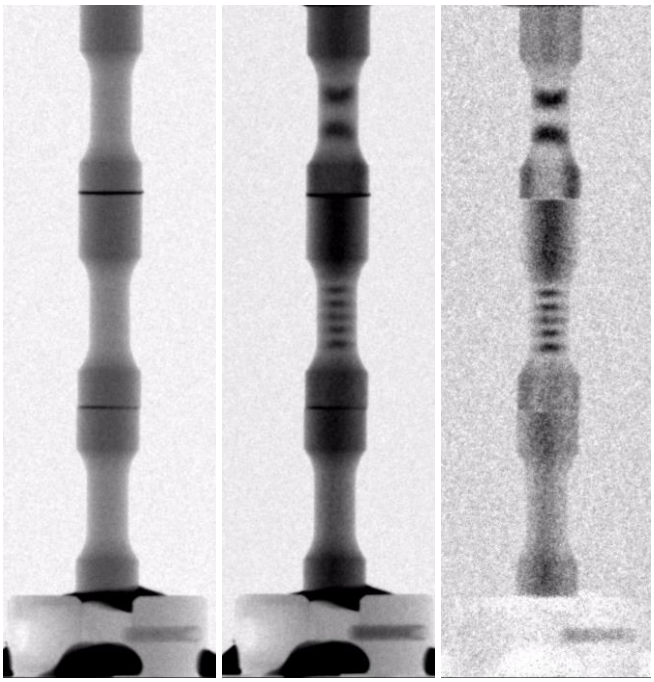

Figure 7-18. Screenshots from radiographs during 360 degree sample rotation: (a) at 3.9 Å (b) at 4.2 Å and (c) Diffraction contrast by normalizing images taken at 3.9 Å by 4.2 Å.

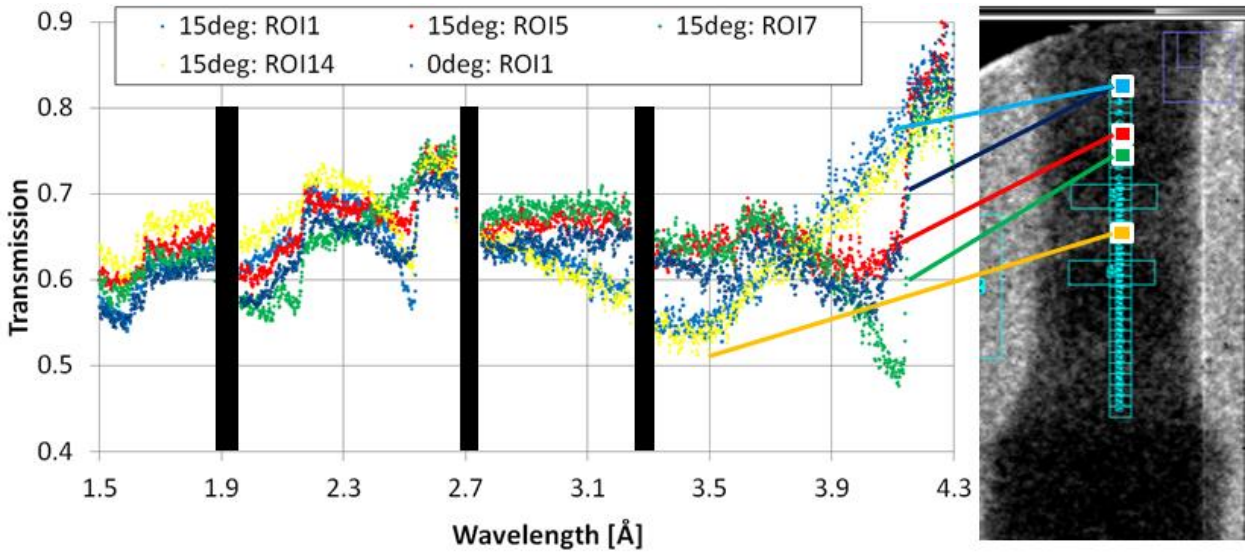

Figure 7-19. Bragg edge transmission profiles recorded in TOF mode at ENGIN-X reveal local differences in texture along the gauge section of the torsion sample.

Chapter 8

Summary, Conclusion & Outlook

8.1 Summary and Conclusion

Within the framework of this dissertation research, several advances have been made regarding methodological developments for the investigation of crystalline samples using neutron imaging and diffraction.

The given objectives have been successfully accomplished. A portable loading system was designed, built and integrated during diffraction and imaging experiments. This capability ensured that experiments could be conducted under the same conditions across different facilities, an important prerequisite for the comparison and quantification of results. A step forward was accomplished regarding the integration and evaluation of Bragg edge transmission imaging for quantitative strain investigations at a neutron reactor source. It was shown that quantification can be achieved for samples that are loaded in tension, both using a monochromator (at the imaging beamline CONRAD) and using a chopper system.

Next, a case study was presented to showcase and evaluate a potential application of strain mapping at a spallation neutron source using the neutron sensitive Micro-Channel-Plate (MCP) detector technology. Superior spatial resolution, compared to previous measurements, was obtained. Challenges and limitations for samples that possess more complicated strain distributions were discussed. From this, it could furthermore be seen that the study that was presented in chapter 6 could not have been conducted in transmission mode. In regard to strain mapping, it is hence concluded that diffraction methods will remain the method of choice for universal and precise strain mapping. Even if a universal mathematical solution for strain tomography would become available, it cannot be foreseen that it would automatically be suited for the majority of samples. Complex strain fields, not even to mention texture effects, will create Bragg edge profiles that will be very complicated to de-convolute unambiguously.

It was shown that the option to define small gauge volumes, the precise gauge volume alignment (achieved using the FARO laser tracker system and SScanSS software) and the measurement of several strain components (by orientating the sample – i.e. scattering vector – accordingly) are necessary to perform lattice strain measurements for a sample under torsional loading. These experiments were the first of its kind and hopefully will

inspire future work in the field of multi-axial deformation. Neutron diffractometers at FRM-2, PSI and SNS already have the capability of performing in-situ multi-axial mechanical testing.

A very promising application of Bragg edge imaging has been presented for the case of crystalline phase mapping. Quantitative phase investigations were extended from previous work, which was either spatially resolved but did not provide quantification or provided quantification but no spatial information, to quantitative radiography and even to three-dimensional tomography. This approach could become a standard methodology for several engineering and material science studies at existing neutron imaging beamlines with an energy selective option. Additional features could be visualized simultaneously, for example cracks, hydrogen inclusions in metals, or eventually even magnetic domains.

Furthermore complications were discussed if strongly textured samples are to be investigated. At the same time, the transmission method was shown to be capable of revealing texture inhomogeneities that would remain undetected if only diffraction or destructive surface techniques were to be used.

8.2 Outlook and Future Work

Significant progress was made in the last few years in the field of energy selective neutron imaging and promising applications were identified. Many of these applications will require a further development to make them more user-friendly and in particular to establish them as techniques that are taken serious across different communities. At the same time, the lessons that were learned over the past few years open numerous exciting opportunities. Some of the immediate tasks and possibilities that are foreseen with regard to this dissertation include:

- Develop approaches that could correct for texture during Bragg edge based phase tomography. These could include information from ODF's and/or data from additional detectors installed simultaneously to the tomography experiment (see discussion on 3D-ND).

- Simulations should be integrated more routinely into Bragg edge measurements – both for spallation and reactor sources – as they could help to better understand sample and instrumental effects. This could be built based on the nxs library developed by M. Boin. (*Boin 2010,[5]; Boin 2012,[191]; Boin et al. 2012,[232]*). This could be useful – if not crucial – for decoupling strain gradients and texture effects, especially with regard to the approach of strain tomography. An option to import results from Finite Element models into such simulations would be further helpful. However, also the existing simulation tool will need more development, as pointed out by Boin, since only certain cases are considered.
- 3D-ND: The combination of imaging and diffraction has been successfully shown for three dimensional crystallographic mapping at synchrotron sources, namely 3D-XRD and DCT (see chapter 2.5). The implementation of a similar approach for neutrons, hence termed 3D-ND, was investigated within the research effort of this dissertation this work, Two major sets of experiments were performed at NIST in September 2012 and at HZB in January 2013. The results and discussion of the experiment are still planned to be published. In this context, the reader is also referred to experiments that were performed around the same time and have been published by S. Peetermans and collaborators at PSI. (*Peetermans et al. 2013,[273]; Peetermans et al. 2013,[274]; King et al. 2014,[275]; Peetermans et al. 2014,[206]*) A modified version of this technique could be envisioned to be paired with the Bragg edge method for phase and texture evaluations, maybe even for strain mapping. This would be further merge between imaging and diffraction. Some neutron beamlines are currently planned and are being built where the combination of imaging and diffraction is a focus, namely IMAT at ISIS and ODIN at ESS.
- For Bragg edge imaging at spallation sources, there is a need for more efficient data processing and data treatment. This is not surprising as this methodology has just started to emerge. It is especially evident for the tomography data set that was recorded, presented in chapter 7.7.4.

Regarding the investigation of multi-axial deformation and stress states using neutron diffraction, numerous expansions are feasible and appear worthy to be undertaken, as they could aid the understanding of micromechanics in materials. The dissertation by former fellow PhD student J. Bunn should be mentioned in this context, as it focused on this topic described by its title "Neutron Diffraction Study of Engineering Materials Subjected to Complex Loadings" (*Bunn 2014,*[276]) and has addressed some of these tasks already. Further experiments and tasks that should be undertaken include:

- Strain tensor measurements of a cylindrical sample under torsion beyond elastic loading. This is best performed at a spallation source, where multiple hkl's could be investigated. The results could be used for comparison with results reported herein and be used for modelling purposes. (Note: An attempt was undertaken together with J. Bunn within the dissertation framework at the SMARTS engineering diffractometer in January 2012, but the small gauge volume possessed challenges to retrieve individual lattice strains. More information can be retrieved upon request.)
- Integrate the application of direct shear into existing deformation models, which have so far been limited to uni-axial loading.
- Probe the strain response of different material systems to the application of torsional shear. Materials of high interest include TRIP/Duplex steels and titanium alloys, while complex slip systems could be investigated for a better understanding of any load path dependencies that may exist.

List of References

1. M. T. Hutchings, P. J. Withers, T.M.Holden, T. Lorentzen, *Introduction to the Characterization of Residual Stress by Neutron Diffraction*. (CRC Press, 2005).
2. K. Meggers, "Echtzeit Neutronen-Transmissionsuntersuchung der Austenit-Bainit Phasenumwandlungskinetik in Gusseisen, Christian-Albrechts-Universität zu Kiel, (1995).
3. S. Vogel, "A Rietveld-Approach for the Analysis of Neutron Time-of-Flight Transmission Data, "Dissertation, Uni Kiel, Kiel (2000).
4. A. Steuwer, "Strain determination and imaging by pulsed neutron transmission, University of Cambridge, (2002).
5. M. Boin, "Developments Towards the Tomographic Imaging of Local Crystallographic Structures, Open University., (2010).
6. G. E. Dieter, *Mechanical Metallurgy* (McGraw-Hill, New York, NY, ed. Third Edition, 1986).
7. B. Eigenmann, E. Macherauch, Röntgenographische Untersuchung von Spannungszuständen in Werkstoffen. Teil III. Fortsetzung von Matwiss. und Werkstofftechn. Heft 3/1995, S. 148–160 und Heft 4/1995, S. 199–216. *Materialwissenschaft und Werkstofftechnik* **27**, 426-437 (1996).
8. B. Clausen, T. Lorentzen, M. A. M. Bourke, M. R. Daymond, Lattice strain evolution during uniaxial tensile loading of stainless steel. *Materials Science and Engineering: A* **259**, 17-24 (1999).
9. R. Hill, The Elastic Behaviour of a Crystalline Aggregate. *Proceedings of the Physical Society. Section A* **65**, 349 (1952).
10. E. Kröner, Berechnung der elastischen Konstanten des Vielkristalls aus den Konstanten des Einkristalls. *Zeitschrift für Physik A* **151**, 504-518 (1958).
11. J. F. Nye, *Physical properties of crystals: their representation by tensors and matrices*. (Clarendon Press, 1985).
12. A. K. Singh, Analysis of nonhydrostatic high-pressure diffraction data (cubic system): Assessment of various assumptions in the theory. *Journal of Applied Physics* **106**, 043514-043514-043518 (2009).
13. R. W. Hertzberg, *Deformation and Fracture Mechanics of Engineering Materials* (Wiley, New York, 1976).
14. W. Bickford, *Advanced mechanics of materials*. (Addison-Wesley, Menlo Park, CA, 1998).
15. M. Miller, D. McDowell, Modeling large strain multiaxial effects in FCC polycrystals. *International journal of plasticity* **12**, 875-902 (1996).
16. E. Cakmak, Investigation of the Phase Transformation Kinetics and Texture Evolution in a TRIP Steel under Complex Loads. (2014).
17. R. B. Ross, *Handbook of metal treatments and testing*. (Springer, 1988).
18. M. Yu, Advances in strength theories for materials under complex stress state in the 20th Century. *Applied Mechanics Reviews* **55**, 169-218 (2002).
19. R. D. Cook, W. C. Young, *Advanced Mechanics of Materials*. (Prentice Hall, 1999).
20. T. Hirano, K. Usami, Y. Tanaka, C. Masuda, In situ x-ray CT under tensile loading using synchrotron radiation. *Journal of materials research* **10**, 381-386 (1995).

21. S. Kruijver, L. Zhao, J. Sietsma, E. Offerman, N. van Dijk, L. Margulies, E. Lauridsen, S. Grigull, H. Poulsen, S. van der Zwaag, In situ observations on the austenite stability in TRIP-steel during tensile testing. *Steel research* **73**, 236-241 (2002).
22. J. W. L. Pang, T. M. Holden, T. E. Mason, In situ generation of intergranular strains in an A17050 alloy. *Acta Materialia* **46**, 1503-1518 (1998); published online EpubMar.
23. A. Steuwer, J. R. Santisteban, P. J. Withers, L. Edwards, M. E. Fitzpatrick, In situ determination of stresses from time-of-flight neutron transmission spectra. *Journal of Applied Crystallography* **36**, 1159-1168 (2003).
24. H. Choo, D. Seo, J. Beddoes, M. A. M. Bourke, D. W. Brown, In situ neutron diffraction studies on the elevated-temperature deformation behavior of a TiAl?W alloy. *Applied Physics Letters* **85**, 4654-4656 (2004).
25. S. Rajagopalan, A. L. Little, M. A. M. Bourke, R. Vaidyanathan, Elastic modulus of shape-memory NiTi from in situ neutron diffraction during macroscopic loading, instrumented indentation, and extensometry. *Applied Physics Letters* **86**, 081901 (2005).
26. S. Qiu, V. B. Krishnan, I. S. A. Padula, R. D. Noebe, D. W. Brown, B. Clausen, R. Vaidyanathan, *Measurement of the lattice plane strain and phase fraction evolution during heating and cooling in shape memory NiTi*. (AIP, 2009), vol. 95, pp. 141906.
27. K. An, H. Skorpenske, A. Stoica, D. Ma, X.-L. Wang, E. Cakmak, First In Situ Lattice Strains Measurements Under Load at VULCAN. *Metallurgical and Materials Transactions A* **42**, 95-99 (2011).
28. N. Wittridge, J. Jonas, The austenite-to-martensite transformation in Fe–30% Ni after deformation by simple shear. *Acta Materialia* **48**, 2737-2749 (2000).
29. R. V. Martins, U. Lienert, L. Margulies, A. Pyzalla, Residual Strain Tensor Determination within Highly Plastically Deformed Torsion Samples Using High Energy Synchrotron Radiation *Journal of Neutron Research*, 249-254 (2001).
30. R. V. Martins, U. Lienert, L. Margulies, A. Pyzalla, Dynamic in-situ investigation of the texture and strain state within a plastically deformed solid AlMg3 torsion sample using high energy synchrotron radiation. *Materials Science Forum* **404-407**, 115-120 (2002).
31. R. V. Martins, U. Lienert, L. Margulies, A. Pyzalla, Determination of the radial crystallite microstrain distribution within an AlMg3 torsion sample using monochromatic synchrotron radiation. *Materials Science and Engineering: A* **402**, 278-287 (2005).
32. E. Cakmak, H. Choo, K. An, Y. Ren, Radial distribution of martensitic phase transformation in a metastable stainless steel under torsional deformation: A synchrotron X-ray diffraction study. *Materials Letters* **65**, 3013-3015 (2011).
33. E. Cakmak, H. Choo, K. An, Y. Ren, A synchrotron X-ray diffraction study on the phase transformation kinetics and texture evolution of a TRIP steel subjected to torsional loading. *Acta Materialia* **60**, 6703-6713 (2012).
34. E. F. Byars, R. D. Snyder, *Engineering mechanics of deformable bodies*. R. D. j. a. Snyder, Ed., (New York, Intext Educational Publishers, New York, 1975).

35. T. Angel, Formation of martensite in austenitic stainless steels-effects of deformation, temperature, and composition. *Journal of the iron and steel institute* **177**, 165-& (1954).
36. J. R. Patel, M. Cohen, Criterion for the action of applied stress in the martensitic transformation. *Acta Metallurgica* **1**, 531-538 (1953); published online Epub9//.
37. K. H. Lo, C. H. Shek, J. K. L. Lai, Recent developments in stainless steels. *Materials Science and Engineering: R: Reports* **65**, 39-104 (2009); published online Epub5/29/.
38. V. F. Zackay, E. R. Parker, D. Fahr, R. Busch, The enhancement of ductility in high-strength steels. *ASM Trans Quart* **60**, 252-259 (1967).
39. P. Jacques, Q. Furnémont, A. Mertens, F. Delannay, On the sources of work hardening in multiphase steels assisted by transformation-induced plasticity. *Philosophical Magazine A* **81**, 1789-1812 (2001).
40. K. Tao, H. Choo, H. Li, B. Clausen, J.-E. Jin, Y.-K. Lee, Transformation-induced plasticity in an ultrafine-grained steel: An in situ neutron diffraction study. *Applied Physics Letters* **90**, 101911 (2007).
41. R. Ray, J. Jonas, Transformation textures in steels. *International Materials Reviews* **35**, 1-36 (1990).
42. R. Ray, J. Jonas, M. Butron-Guillen, J. Savoie, Transformation Textures in Steels. *ISIJ International* **34**, 927-942 (1994).
43. K. Tao, J. J. Wall, H. Li, D. W. Brown, S. C. Vogel, H. Choo, In situ neutron diffraction study of grain-orientation-dependent phase transformation in 304L stainless steel at a cryogenic temperature. *Journal of applied physics* **100**, 123515 (2006).
44. W. Ludwig, "Combined use of synchrotron radiation X-ray imaging and diffraction techniques for the characterization of polycrystalline materials, l'Institut National des Sciences Appliquées de Lyon et l'Université Claude Bernard LYON, (2011).
45. A. J. Allen, M. T. Hutchings, C. G. Windsor, C. Andreani, NEUTRON-DIFFRACTION METHODS FOR THE STUDY OF RESIDUAL-STRESS FIELDS. *Advances in Physics* **34**, 445-473 (1985).
46. B. Clausen, T. Leffers, T. Lorentzen, On the proper selection of reflections for the measurement of bulk residual stresses by diffraction methods. *Acta Materialia* **51**, 6181-6188 (2003); published online Epub12/8/.
47. B. C. Larson, W. Yang, G. E. Ice, J. D. Budai, J. Z. Tischler, Three-dimensional X-ray structural microscopy with submicrometre resolution. *Nature* **415**, 887-890 (2002); published online Epub02/21/print.
48. H. F. Poulsen, *Three-Dimensional X-Ray Diffraction Microscopy: Mapping Polycrystals and their Dynamics*. (Springer, Heidelberg, 2004).
49. M. A. Pfeifer, G. J. Williams, I. A. Vartanyants, R. Harder, I. K. Robinson, Three-dimensional mapping of a deformation field inside a nanocrystal. *Nature* **442**, 63-66 (2006); published online Epub07/06/print.
50. P. Bleuet, E. Welcomme, E. Dooryhee, J. Susini, J.-L. Hodeau, P. Walter, Probing the structure of heterogeneous diluted materials by diffraction tomography. *Nat Mater* **7**, 468-472 (2008); published online Epub06//print.

51. A. King, G. Johnson, D. Engelberg, W. Ludwig, J. Marrow, Observations of Intergranular Stress Corrosion Cracking in a Grain-Mapped Polycrystal. *Science* **321**, 382-385 (2008); published online EpubJuly 18, 2008.
52. H. H. Liu, S. Schmidt, H. F. Poulsen, A. Godfrey, Z. Q. Liu, J. A. Sharon, X. Huang, Three-Dimensional Orientation Mapping in the Transmission Electron Microscope. *Science* **332**, 833-834 (2011); published online EpubMay 13, 2011.
53. M. Strobl, I. Manke, N. Kardjilov, A. Hilger, M. Dawson, J. Banhart, Advances in neutron radiography and tomography. *Journal of Physics D: Applied Physics* **42**, 243001 (2009).
54. J. Banhart, *Advanced tomographic methods in materials research and engineering*. (Oxford University Press New York, 2008).
55. R. D. Doherty, D. A. Hughes, F. J. Humphreys, J. J. Jonas, D. J. Jensen, M. E. Kassner, W. E. King, T. R. McNelley, H. J. McQueen, A. D. Rollett, Current issues in recrystallization: a review. *Materials Science and Engineering: A* **238**, 219-274 (1997).
56. J. Goldstein, D. E. Newbury, D. C. Joy, C. E. Lyman, P. Echlin, E. Lifshin, L. Sawyer, J. R. Michael, *Scanning electron microscopy and X-ray microanalysis*. (Springer, 2003).
57. W. Ludwig, P. Reischig, A. King, M. Herbig, E. M. Lauridsen, G. Johnson, T. J. Marrow, J. Y. Buffière, *Three-dimensional grain mapping by x-ray diffraction contrast tomography and the use of Friedel pairs in diffraction data analysis*. (AIP, 2009), vol. 80, pp. 033905.
58. P. J. Withers, M. Turski, L. Edwards, P. J. Bouchard, D. J. Buttle, Recent advances in residual stress measurement. *International Journal of Pressure Vessels and Piping* **85**, 118-127 (2008); published online Epub3//.
59. R. Leggatt, D. Smith, S. Smith, F. Faure, Development and experimental validation of the deep hole method for residual stress measurement. *The Journal of Strain Analysis for Engineering Design* **31**, 177-186 (1996).
60. G. S. Schajer, *Practical Residual Stress Measurement Methods*. (John Wiley & Sons, 2013).
61. W. Bragg, W. Bragg, The reflection of X-rays by crystals. *Proceedings of the Royal Society of London. Series A* **88**, 428-438 (1913).
62. W. L. Bragg, The structure of some crystals as indicated by their diffraction of X-rays. *Proceedings of the Royal Society of London. Series A* **89**, 248-277 (1913).
63. M. Daymond, L. Edwards, Scientific Review: ENGIN-X: A Fully Refined Diffractometer Designed Specifically for Measurement of Stress. *Neutron News* **15**, 24-29 (2004).
64. T. Pirling, G. Bruno, P. J. Withers, SALSA—A new instrument for strain imaging in engineering materials and components. *Materials Science and Engineering: A* **437**, 139-144 (2006).
65. M. E. Fitzpatrick, A. Lodini, *Analysis of residual stress by diffraction using neutron and synchrotron radiation*. (CRC Press, 2003), pp. 354.

66. J. R. Bunn, D. Penumadu, X. Lou, C. R. Hubbard, Effect of Multi-Axial Loading on Residual Strain Tensor for 12L14 Steel Alloy. *Metallurgical and Materials Transactions A*, 1-8 (2014).
67. Webpage: http://www.veqter.co.uk/residual-stress-measurement/synchrotron-diffraction (www.veqter.co.uk), 2014
68. C. C. Aydıner, E. Üstündag, B. Clausen, J. C. Hanan, R. A. Winholtz, M. A. M. Bourke, A. Peker, Residual stresses in a bulk metallic glass–stainless steel composite. *Materials Science and Engineering: A* **399**, 107-113 (2005); published online Epub6/15/.
69. X.-L. Wang, The application of neutron diffraction to engineering problems. *JOM* **58**, 52-57 (2006); published online Epub2006/03/01.
70. M. A. M. Bourke, D. W. Brown, B. Clausen, H. Choo, P. Rancaswamy, R. Vaidyanathan, Neutron diffraction studies of polycrystalline deformation in engineering materials. *Neutron News* **10**, 24-30 (1999); published online Epub1999/01/01.
71. J. Santisteban, M. Daymond, J. James, L. Edwards, ENGIN-X: a third-generation neutron strain scanner. *Journal of Applied Crystallography* **39**, 812-825 (2006).
72. M. Bourke, D. Dunand, E. Ustundag, SMARTS–a spectrometer for strain measurement in engineering materials. *Applied Physics A* **74**, s1707-s1709 (2002).
73. M. Hofmann, G. A. Seidl, J. Rebelo-Kornmeier, U. Garbe, R. Schneider, R. C. Wimpory, U. Wasmuth, U. Noster, in *Materials science forum*. (Trans Tech Publ, 2006), vol. 524, pp. 211-216.
74. X. L. Wang, T. M. Holden, G. Q. Rennich, A. D. Stoica, P. K. Liaw, H. Choo, C. R. Hubbard, VULCAN—The engineering diffractometer at the SNS. *Physica B: Condensed Matter* **385–386, Part 1**, 673-675 (2006); published online Epub11/15/.
75. M. Boin, R. C. Wimpory, in *Materials Science Forum*. (Trans Tech Publ, 2014), vol. 768, pp. 31-35.
76. K. An, W. B. Bailey, S. O. Craig, H. Choo, C. R. Hubbard, D. L. Erdman III, NRSF2 load frame: design, control, and testing §. *Journal of Neutron Research* **15**, 207-213 (2007).
77. O. Kirstein, V. Luzin, A. Brule, H. Nguyen, D. Tawfik, Kowari–OPAL's Residual-Stress Diffractometer and its Application to Materials Science and Engineering. *Advanced Materials Research* **41**, 439-444 (2008).
78. S. Harjo, T. Ito, K. Aizawa, H. Arima, J. Abe, A. Moriai, T. Iwahashi, T. Kamiyama, in *Materials Science Forum*. (Trans Tech Publ, 2011), vol. 681, pp. 443-448.
79. B. Clausen, T. Lorentzen, T. Leffers, Self-consistent modelling of the plastic deformation of f.c.c. polycrystals and its implications for diffraction measurements of internal stresses. *Acta Materialia* **46**, 3087-3098 (1998); published online Epub5/22/.
80. M. Daymond, C. Tomé, M. Bourke, Measured and predicted intergranular strains in textured austenitic steel. *Acta materialia* **48**, 553-564 (2000).
81. M. R. Daymond, H. G. Priesmeyer, Elastoplastic deformation of ferritic steel and cementite studied by neutron diffraction and self-consistent modelling. *Acta Materialia* **50**, 1613-1626 (2002); published online EpubApr.

82. T. Holden, R. Holt, A. Clarke, Intergranular stresses in Incoloy-800. *Journal of Neutron Research* **5**, 241-264 (1997).
83. Y. Tomota, H. Tokuda, Y. Adachi, M. Wakita, N. Minakawa, A. Moriai, Y. Morii, Tensile behavior of TRIP-aided multi-phase steels studied by in situ neutron diffraction. *Acta Materialia* **52**, 5737-5745 (2004).
84. A. Lebedev, V. Kosarchuk, Influence of phase transformations on the mechanical properties of austenitic stainless steels. *International Journal of Plasticity* **16**, 749-767 (2000).
85. J. Bunn, D. Penumadu, C. Hubbard, Residual strain evolution in steel samples: tension versus torsion. *Applied Physics A* **99**, 571-578 (2010).
86. J. Chadwick, Possible existence of a neutron. *Nature* **129**, 312 (1932).
87. H. Kallmann, E. Kuhn. (1940), vol. US Patent No 2186 757
88. O. Peter, Neutronen-Durchleuchtung. *Zeitschrift Naturforschung Teil A* **1**, 557 (1946).
89. J. Thewlis, Neutron radiography. *British Journal of Applied Physics* **7**, 345 (1956).
90. R. Halmshaw, *Industrial radiology: theory and practice*. (Springer, 1995), vol. 1.
91. A. Heller, J. Brenizer, in *Neutron Imaging and Applications*. (Springer, 2009), pp. 67-80.
92. B. Allman, P. McMahon, K. Nugent, D. Paganin, D. Jacobson, M. Arif, S. Werner, Phase radiography with neutrons. *Nature (London)* **408**, 158-159 (2000).
93. F. Pfeiffer, C. Grünzweig, O. Bunk, G. Frei, E. Lehmann, C. David, Neutron phase imaging and tomography. *Physical review letters* **96**, 215505 (2006).
94. M. Strobl, C. Grünzweig, A. Hilger, I. Manke, N. Kardjilov, C. David, F. Pfeiffer, Neutron dark-field tomography. *Physical review letters* **101**, 123902 (2008).
95. N. Kardjilov, I. Manke, M. Strobl, A. Hilger, W. Treimer, M. Meissner, T. Krist, J. Banhart, Three-dimensional imaging of magnetic fields with polarized neutrons. *Nature Physics* **4**, 399-403 (2008).
96. J. R. Santisteban, L. Edwards, M. E. Fitzpatrick, A. Steuwer, P. J. Withers, M. R. Daymond, M. W. Johnson, N. Rhodes, E. M. Schooneveld, Strain imaging by Bragg edge neutron transmission. *Nuclear Instruments and Methods in Physics Research Section A: Accelerators, Spectrometers, Detectors and Associated Equipment* **481**, 765-768 (2002).
97. A. S. Tremsin, J. B. McPhate, J. V. Vallerga, O. H. W. Siegmund, W. Kockelmann, E. M. Schooneveld, N. J. Rhodes, W. B. Feller, High Resolution Neutron Resonance Absorption Imaging at a Pulsed Neutron Beamline. *Nuclear Science, IEEE Transactions on* **59**, 3272-3277 (2012).
98. N. Kardjilov, I. Manke, A. Hilger, M. Strobl, J. Banhart, Neutron imaging in materials science. *Materials Today* **14**, 248 (2011).
99. Webpage: http://www.psi.ch/niag/neutron-interaction-with-matter# (P. http://www.psi.ch/niag/neutron-interaction-with-matter), 2014
100. A. C. Kak, M. Slaney, *Principles of computerized tomographic imaging*. (Society for Industrial and Applied Mathematics, 2001).

101. T. M. Buzug, *Computed tomography: from photon statistics to modern cone-beam CT*. (Springer, 2008).
102. F. H. Kim, "DUAL-MODALITY (NEUTRON AND X-RAY) IMAGING FOR CHARACTERIZATION OF PARTIALLY SATURATED GRANULAR MATERIALS AND FLOW THROUGH POROUS MEDIA, University of Tennessee, (2013).
103. F. Gruenauer, "Design, optimization, and implementation of the new neutron radiography facility at FRM-II, Technische Univ. Muenchen (Germany), (2005).
104. N. Kardjilov, P. Böni, A. Hilger, M. Strobl, W. Treimer, Characterization of a focusing parabolic guide using neutron radiography method. *Nuclear Instruments and Methods in Physics Research Section A: Accelerators, Spectrometers, Detectors and Associated Equipment* **542**, 248-252 (2005); published online Epub4/21/.
105. A. S. Tremsin, W. Bruce Feller, R. Gregory Downing, Efficiency optimization of microchannel plate (MCP) neutron imaging detectors. I. Square channels with 10B doping. *Nuclear Instruments and Methods in Physics Research Section A: Accelerators, Spectrometers, Detectors and Associated Equipment* **539**, 278-311 (2005).
106. O. H. Siegmund, J. V. Vallerga, A. S. Tremsin, J. McPhate, B. Feller, High spatial resolution neutron sensing microchannel plate detectors. *Nuclear Instruments and Methods in Physics Research Section A: Accelerators, Spectrometers, Detectors and Associated Equipment* **576**, 178-182 (2007).
107. A. S. Tremsin, J. B. McPhate, W. Kockelmann, J. V. Vallerga, O. H. W. Siegmund, W. B. Feller, High resolution Bragg edge transmission spectroscopy at pulsed neutron sources: Proof of principle experiments with a neutron counting MCP detector. *Nuclear Instruments and Methods in Physics Research Section A: Accelerators, Spectrometers, Detectors and Associated Equipment* **633**, S235-S238 (2011).
108. P. Stewart, Cold neutron imaging for gas turbine inspection. *Real Time Radiologic Imaging*, 180-198 (1980).
109. R. Satija, D. L. Jacobson, M. Arif, S. A. Werner, In situ neutron imaging technique for evaluation of water management systems in operating PEM fuel cells. *Journal of Power Sources* **129**, 238-245 (2004).
110. I. Manke, C. Hartnig, M. Grunerbel, J. Kaczerowski, W. Lehnert, N. Kardjilov, A. Hilger, J. Banhart, W. Treimer, M. Strobl, Quasi-in situ neutron tomography on polymer electrolyte membrane fuel cell stacks. *Applied Physics Letters* **90**, (2007); published online EpubApr.
111. A. Bazylak, Liquid water visualization in PEM fuel cells: A review. *International Journal of Hydrogen Energy* **34**, 3845-3857 (2009); published online Epub5//.
112. R. Mukundan, R. L. Borup, Visualising Liquid Water in PEM Fuel Cells Using Neutron Imaging. *Fuel Cells* **9**, 499-505 (2009).
113. H. Sakaguchi, Y. Satake, K. Hatakeyama, S. Fujine, K. Yoneda, M. Matsubayashi, T. Esaka, Analysis of hydrogen distribution in hydrogen storage alloy using neutron radiography. *Journal of Alloys and Compounds* **354**, 208-215 (2003); published online Epub5/12/.

114. S. E. Oswald, M. Menon, A. Carminati, P. Vontobel, E. Lehmann, R. Schulin, Quantitative imaging of infiltration, root growth, and root water uptake via neutron radiography. *Vadose Zone Journal* **7**, 1035-1047 (2008).
115. U. Matsushima, W. Herppich, N. Kardjilov, W. Graf, A. Hilger, I. Manke, Estimation of water flow velocity in small plants using cold neutron imaging with D< sub> 2</sub> O tracer. *Nuclear Instruments and Methods in Physics Research Section A: Accelerators, Spectrometers, Detectors and Associated Equipment* **605**, 146-149 (2009).
116. J. M. Warren, H. Bilheux, M. Kang, S. Voisin, C.-L. Cheng, J. Horita, E. Perfect, Neutron imaging reveals internal plant water dynamics. *Plant and soil* **366**, 683-693 (2013).
117. M. Lanz, E. Lehmann, R. Imhof, I. Exnar, P. Novák, In situ neutron radiography of lithium-ion batteries during charge/discharge cycling. *Journal of power sources* **101**, 177-181 (2001).
118. D. Goers, M. Holzapfel, W. Scheifele, E. Lehmann, P. Vontobel, P. Novák, In situ neutron radiography of lithium-ion batteries: the gas evolution on graphite electrodes during the charging. *Journal of Power Sources* **130**, 221-226 (2004); published online Epub5/3/.
119. J. B. Siegel, X. Lin, A. G. Stefanopoulou, D. S. Hussey, D. L. Jacobson, D. Gorsich, Neutron imaging of lithium concentration in LFP Pouch cell battery. *Journal of the Electrochemical Society* **158**, A523-A529 (2011).
120. E. H. Lehmann, P. Vontobel, E. Deschler-Erb, M. Soares, Non-invasive studies of objects from cultural heritage. *Nuclear Instruments and Methods in Physics Research Section A: Accelerators, Spectrometers, Detectors and Associated Equipment* **542**, 68-75 (2005).
121. G. Festa, P. A. Caroppi, A. Filabozzi, C. Andreani, M. L. Arancio, R. Triolo, F. L. Celso, V. Benfante, S. Imberti, Composition and corrosion phases of Etruscan Bronzes from Villanovan Age. *Measurement Science and Technology* **19**, 034004 (2008).
122. E. Lehmann, S. Hartmann, M. Speidel, Investigation of the content of ancient Tibetan metallic Buddha statues by means of neutron imaging methods. *Archaeometry* **52**, 416-428 (2010).
123. S. Peetermans, R. van Langh, E. Lehmann, A. Pappot, Quantification of the material composition of historical copper alloys by means of neutron transmission measurements. *Journal of Analytical Atomic Spectrometry* **27**, 1674-1679 (2012).
124. N. Kardjilov, A. Hilger, I. Manke, M. Strobl, M. Dawson, J. Banhart, New trends in neutron imaging. *Nuclear Instruments and Methods in Physics Research Section A: Accelerators, Spectrometers, Detectors and Associated Equipment* **605**, 13-15 (2009).
125. W. Treimer, M. Strobl, N. Kardjilov, A. Hilger, I. Manke, Wavelength tunable device for neutron radiography and tomography. *Applied Physics Letters* **89**, 203504 (2006).
126. A. A. Van Well, Double-disk chopper for neutron time-of-flight experiments. *Physica B: Condensed Matter* **180-181, Part 2**, 959-961 (1992).
127. M. Strobl, R. Steitz, M. Kreuzer, A. Nawara, F. Mezei, M. Rose, P. Amitesh, M. Grunze, R. Dahint, BioRef – a time-of-flight neutron reflectometer combined with in-situ

infrared spectroscopy at the Helmholtz Centre Berlin. *Journal of Physics: Conference Series* **251**, 012059 (2010).
128. A. S. Tremsin, J. V. Vallerga, J. B. McPhate, O. H. W. Siegmund, W. B. Feller, L. Crow, R. G. Cooper, On the possibility to image thermal and cold neutron with sub-15 μm spatial resolution. *Nuclear Instruments and Methods in Physics Research Section A: Accelerators, Spectrometers, Detectors and Associated Equipment* **592**, 374-384 (2008).
129. A. S. Tremsin, J. B. McPhate, W. A. Kockelmann, J. V. Vallerga, O. H. W. Siegmund, W. B. Feller, Energy-Resolving Neutron Transmission Radiography at the ISIS Pulsed Spallation Source With a High-Resolution Neutron Counting Detector. *Nuclear Science, IEEE Transactions on* **56**, 2931-2937 (2009).
130. A. S. Tremsin, J. B. McPhate, J. V. Vallerga, O. H. W. Siegmund, W. B. Feller, H. Z. Bilheux, J. J. Molaison, C. A. Tulk, L. Crow, R. G. Cooper, D. Penumadu, Transmission Bragg edge spectroscopy measurements at ORNL Spallation Neutron Source. *Journal of Physics: Conference Series* **251**, 012069 (2010).
131. A. S. Tremsin, M. J. Muhlbauer, B. Schillinger, J. B. McPhate, J. V. Vallerga, O. H. W. Siegmund, W. B. Feller, High Resolution Stroboscopic Neutron Radiography at the FRM-II ANTARES Facility. *Nuclear Science, IEEE Transactions on* **57**, 2955-2962 (2010).
132. E. H. Lehmann, G. Frei, P. Vontobel, L. Josic, N. Kardjilov, A. Hilger, W. Kockelmann, A. Steuwer, The energy-selective option in neutron imaging. *Nuclear Instruments and Methods in Physics Research Section A: Accelerators, Spectrometers, Detectors and Associated Equipment* **603**, 429-438 (2009).
133. H. Postma, M. Blaauw, P. Schillebeeckx, G. Lobo, R. B. Halbertsma, A. J. Nijboer, Non-destructive elemental analysis of copper-alloy artefacts with epithermal neutron-resonance capture. *Czech J Phys* **53**, A233-A240 (2003); published online Epub2003/01/01.
134. H. Postma, P. Schillebeeckx, Neutron resonance capture and transmission analysis. *Encyclopedia of analytical chemistry*, (2009).
135. H. Sato, T. Kamiyama, Y. Kiyanagi, Pulsed neutron imaging using resonance transmission spectroscopy. *Nuclear Instruments and Methods in Physics Research Section A: Accelerators, Spectrometers, Detectors and Associated Equipment* **605**, 36-39 (2009).
136. E. P. Cippo, A. Borella, G. Gorini, W. Kockelmann, M. Moxon, H. Postma, N. J. Rhodes, P. Schillebeeckx, E. M. Schoonenveld, M. Tardocchi, Imaging of cultural heritage objects using neutron resonances. *Journal of analytical atomic spectrometry* **26**, 992-999 (2011).
137. A. S. Tremsin, S. C. Vogel, M. Mocko, M. A. M. Bourke, V. Yuan, R. O. Nelson, D. W. Brown, W. B. Feller, Non-destructive studies of fuel pellets by neutron resonance absorption radiography and thermal neutron radiography. *Journal of Nuclear Materials* **440**, 633-646 (2013); published online Epub9//.
138. N. Larson, Introduction to the theory and analysis of resolved (and unresolved) neutron resonances via SAMMY. (2001).

139. S. Vogel, A. Tremsin, A. Losko, in *NEUWAVE2014*. (Garching, Germany, 2014).
140. C. Grünzweig, F. Pfeiffer, O. Bunk, T. Donath, G. Kühne, G. Frei, M. Dierolf, C. David, Design, fabrication, and characterization of diffraction gratings for neutron phase contrast imaging. *Review of Scientific Instruments* **79**, - (2008).
141. L. Rigon, H.-J. Besch, F. Arfelli, R.-H. Menk, G. Heitner, H. Plothow-Besch, A new DEI algorithm capable of investigating sub-pixel structures. *Journal of Physics D: Applied Physics* **36**, A107 (2003).
142. M. Strobl, W. Treimer, A. Hilger, Small angle scattering signals for (neutron) computerized tomography. *Applied Physics Letters* **85**, 488-490 (2004).
143. M. Ando, E. Hashimoto, H. Hashizume, K. Hyodo, H. Inoue, T. Kunisada, A. Maksimenko, K. Mori, E. Rubenstein, J. Roberson, D. Shimao, H. Sugiyama, K. Takeda, F. Toyofuku, E. Ueno, K. Umetani, H. Wada, W. Pattanasiriwisawa, Clinical step onward with X-ray dark-field imaging and perspective view of medical applications of synchrotron radiation in Japan. *Nuclear Instruments and Methods in Physics Research Section A: Accelerators, Spectrometers, Detectors and Associated Equipment* **548**, 1-16 (2005); published online Epub8/11/.
144. F. Pfeiffer, M. Bech, O. Bunk, P. Kraft, E. F. Eikenberry, C. Bronnimann, C. Grunzweig, C. David, Hard-X-ray dark-field imaging using a grating interferometer. *Nat Mater* **7**, 134-137 (2008); published online Epub02//print.
145. H. Rauch, S. Werner, *Neutron Interferometry: Lessons in Experimental Quantum Mechanics*. (Oxford, 2000).
146. W. Treimer, M. Strobl, A. Hilger, C. Seifert, U. Feye-Treimer, Refraction as imaging signal for computerized (neutron) tomography. *Applied Physics Letters* **83**, 398-400 (2003).
147. N. Kardjilov, E. Lehmann, E. Steichele, P. Vontobel, Phase-contrast radiography with a polychromatic neutron beam. *Nuclear Instruments and Methods in Physics Research Section A: Accelerators, Spectrometers, Detectors and Associated Equipment* **527**, 519-530 (2004); published online Epub7/21/.
148. M. Dawson, I. Manke, N. Kardjilov, A. Hilger, M. Strobl, J. Banhart, Imaging with polarized neutrons. *New Journal of Physics* **11**, 043013 (2009).
149. M. Strobl, W. Treimer, P. Walter, S. Keil, I. Manke, Magnetic field induced differential neutron phase contrast imaging. *Applied Physics Letters* **91**, - (2007).
150. C. Grünzweig, C. David, O. Bunk, M. Dierolf, G. Frei, G. Kühne, R. Schäfer, S. Pofahl, H. M. R. Rønnow, F. Pfeiffer, Bulk magnetic domain structures visualized by neutron dark-field imaging. *Applied Physics Letters* **93**, - (2008).
151. S. W. Lee, K.-Y. Kim, O. Y. Kwon, N. Kardjilov, M. Dawson, A. Hilger, I. Manke, Observation of Magnetic Domains in Insulation-Coated Electrical Steels by Neutron Dark-Field Imaging. *Applied Physics Express* **3**, 106602 (2010).
152. Y. Zhu, *Modern techniques for characterizing magnetic materials*. (Springer, 2005).
153. E. Fermi, W. J. Sturm, R. G. Sachs, The Transmission of Slow Neutrons through Microcrystalline Materials. *Physical Review* **71**, 589-594 (1947); published online Epub05/01/.

154. L. Winsberg, D. Meneghetti, S. S. Sidhu, Total Neutron Cross Sections of Compounds with Different Crystalline Structures. *Physical Review* **75**, 975-979 (1949); published online Epub03/15/.
155. R. J. Weiss, J. R. Clark, L. Corliss, J. Hastings, Neutron Diffraction Studies of Cold-Worked Brass. *Journal of Applied Physics* **23**, 1379-1382 (1952).
156. J. Cassels, The scattering of neutrons by crystals. *Prog. Nucl. Phys., editor OR*, (1950).
157. P. Mikula, M. Vrána, P. Lukáš, J. Šaroun, P. Strunz, V. Wagner, B. Alefeld, Bragg optics for strain/stress measurement techniques. *Physica B: Condensed Matter* **213–214**, 845-847 (1995); published online Epub8/1/.
158. P. Strunz, P. Lukás, P. Mikula, V. Wagner, Z. Kouril, M. Vrána, in *Proc. of the 5th Int. Conference on Residual Stresses ICRS-5*. (1997), pp. 688-693.
159. V. Wagner, Z. Kouril, P. Lukas, P. Mikula, J. Saroun, P. Strunz, M. Vrana. (1997), vol. 2867, pp. 168-171.
160. J. M. Carpenter, Pulsed spallation neutron sources for slow neutron scattering. *Nuclear Instruments and Methods* **145**, 91-113 (1977); published online Epub8/15/.
161. R. Johnson, C. Bowman, High resolution powder diffraction by white source transmission measurements. *AIP Conf. Proc. 89* **89**, 53-56 (1982); published online Epub191.
162. J. D. Bowman, J. J. Szymanski, V. W. Yuan, C. D. Bowman, A. Silverman, X. Zhu, Current-mode detector for neutron time-of-flight studies. *Nuclear Instruments and Methods in Physics Research Section A: Accelerators, Spectrometers, Detectors and Associated Equipment* **297**, 183-189 (1990); published online Epub11/15/.
163. K. Meggers, H. G. Priesmeyer, W. J. Trela, C. D. Bowman, M. Dahms, Real time neutron transmission investigation of the austenite-bainite transformation in grey iron. *Nuclear Instruments and Methods in Physics Research Section B: Beam Interactions with Materials and Atoms* **88**, 423-429 (1994); published online Epub6/2/.
164. K. Meggers, H. G. Priesmeyer, W. J. Trela, M. Dahms, Investigation of the austenite-bainite transformation in gray iron using real time neutron transmission. *Materials Science and Engineering: A* **188**, 301-304 (1994); published online Epub11/30/.
165. D. Q. Wang, "Strain Measurement Using Neutron Diffraction, The Open University, (1996).
166. H. G. Priesmeyer, M. Stalder, S. Vogel, K. Meggers, R. Bless, W. Trela, Bragg-Edge Transmission as an Additional Tool for Strain Measurements. *Textures and Microstructures* **33**, 173-185 (1999).
167. J. R. Santisteban, L. Edwards, M. E. Fizpatrick, A. Steuwer, P. J. Withers, Engineering applications of Bragg-edge neutron transmission. *Applied Physics A: Materials Science & Processing* **74**, s1433-s1436 (2002).
168. A. Steuwer, P. J. Withers, J. R. Santisteban, L. Edwards, G. Bruno, M. E. Fitzpatrick, M. R. Daymond, M. W. Johnson, D. Wang, Bragg Edge Determination for Accurate Lattice Parameter and Elastic Strain Measurement. *physica status solidi (a)* **185**, 221-230 (2001).

169. J. R. Santisteban, L. Edwards, H. G. Priesmeyer, S. Vogel, Comparison of Bragg-Edge neutron-transmission spectroscopy at ISIS and LANSCE. *Applied Physics A: Materials Science & Processing* **74**, s1616-s1618 (2002).
170. C. Bowman, P. Egelstaff, H. Priesmeyer, Experiments using single neutron pulses. (1991).
171. P. Mikula, M. Vrána, V. Wagner, Bragg diffraction optics for energy-dispersive neutron transmission diffraction. *Physica B: Condensed Matter* **283**, 403-405 (2000); published online Epub6/3/.
172. M. A. M. Bourke, J. G. Maldonado, D. Masters, K. Meggers, H. G. Priesmeyer, Real time measurement by Bragg edge diffraction of the reverse ($\alpha' \rightarrow \gamma$) transformation in a deformed 304 stainless steel. *Materials Science and Engineering: A* **221**, 1-10 (1996).
173. A. Steuwer, J. R. Santisteban, P. J. Withers, L. Edwards, Pattern decomposition and quantitative-phase analysis in pulsed neutron transmission. *Physica B: Condensed Matter* **350**, 159-161 (2004).
174. A. Steuwer, P. J. Withers, J. R. Santisteban, L. Edwards, Using pulsed neutron transmission for crystalline phase imaging and analysis. *Journal of Applied Physics* **97**, 074903 (2005).
175. J. Huang, S. C. Vogel, W. J. Poole, M. Militzer, P. Jacques, The study of low-temperature austenite decomposition in a Fe–C–Mn–Si steel using the neutron Bragg edge transmission technique. *Acta Materialia* **55**, 2683-2693 (2007).
176. J. R. Santisteban, L. Edwards, V. Stelmukh, Characterization of textured materials by TOF transmission. *Physica B: Condensed Matter* **385-386, Part 1**, 636-638 (2006).
177. K. Iwase, T. Nagata, K. Sakuma, O. Takada, T. Kamiyama, Y. Kiyanagi, in *Nuclear Science Symposium Conference Record, 2007. NSS '07. IEEE*. (2007), vol. 2, pp. 1716-1719.
178. H. Sato, O. Takada, K. Iwase, T. Kamiyama, Y. Kiyanagi, Imaging of a spatial distribution of preferred orientation of crystallites by pulsed neutron Bragg edge transmission. *Journal of Physics: Conference Series* **251**, 012070 (2010).
179. J. R. Santisteban, L. Edwards, A. Steuwer, P. J. Withers, Time-of-flight neutron transmission diffraction. *Journal of Applied Crystallography* **34**, 289-297 (2001).
180. K. Iwase, H. Sato, S. Harjo, T. Kamiyama, T. Ito, S. Takata, K. Aizawa, Y. Kiyanagi, In situ lattice strain mapping during tensile loading using the neutron transmission and diffraction methods. *Journal of Applied Crystallography* **45**, 113-118 (2012).
181. W. Kockelmann, G. Frei, E. H. Lehmann, P. Vontobel, J. R. Santisteban, Energy-selective neutron transmission imaging at a pulsed source. *Nuclear Instruments and Methods in Physics Research Section A: Accelerators, Spectrometers, Detectors and Associated Equipment* **578**, 421-434 (2007).
182. M. Strobl, A. Hilger, M. Boin, N. Kardjilov, R. Wimpory, D. Clemens, M. Mühlbauer, B. Schillinger, T. Wilpert, C. Schulz, K. Rolfs, C. M. Davies, N. O'Dowd, P. Tiernan, I. Manke, Time-of-flight neutron imaging at a continuous source: Proof of principle using a scintillator CCD imaging detector. *Nuclear Instruments and Methods in Physics Research Section A: Accelerators, Spectrometers, Detectors and Associated Equipment* **651**, 149-155 (2011).

183. Y. Kiyanagi, T. Kamiyama, K. Kino, H. Sato, S. Sato, S. Uno, Pulsed neutron imaging using 2-dimensional position sensitive detectors. *Journal of Instrumentation* **9**, C07012 (2014).
184. J. R. Santisteban, M. A. Vicente-Alvarez, P. Vizcaino, A. D. Banchik, S. C. Vogel, A. S. Tremsin, J. V. Vallerga, J. B. McPhate, E. Lehmann, W. Kockelmann, Texture imaging of zirconium based components by total neutron cross-section experiments. *Journal of Nuclear Materials*, (2011).
185. M. Schulz, P. Böni, E. Calzada, M. Mühlbauer, B. Schillinger, Energy-dependent neutron imaging with a double crystal monochromator at the ANTARES facility at FRM II. *Nuclear Instruments and Methods in Physics Research Section A: Accelerators, Spectrometers, Detectors and Associated Equipment* **605**, 33-35 (2009); published online Epub6/21/.
186. L. Josic, A. Steuwer, E. Lehmann, Energy selective neutron radiography in material research. *Applied Physics A* **99**, 515-522 (2010); published online Epub2010/06/01.
187. L. Josic, E. Lehmann, A. Kaestner, Energy selective neutron imaging in solid state materials science. *Nuclear Instruments and Methods in Physics Research Section A: Accelerators, Spectrometers, Detectors and Associated Equipment* **651**, 166-170 (2011); published online Epub9/21/.
188. N. Kardjilov, I. Manke, A. Hilger, S. Williams, M. Strobl, R. Woracek, M. Boin, E. Lehmann, D. Penumadu, J. Banhart, Neutron Bragg-edge mapping of weld seams. *International Journal of Materials Research*, p. 151-154 (2012).
189. F. Salvemini, F. Grazzi, S. Peetermans, F. Civita, R. Franci, S. Hartmann, E. Lehmann, M. Zoppi, Quantitative characterization of Japanese ancient swords through energy-resolved neutron imaging. *Journal of Analytical Atomic Spectrometry* **27**, 1494-1501 (2012).
190. E. Lehmann, S. Peetermans, L. Josic, H. Leber, H. van Swygenhoven, Energy-selective neutron imaging with high spatial resolution and its impact on the study of crystalline-structured materials. *Nuclear Instruments and Methods in Physics Research Section A: Accelerators, Spectrometers, Detectors and Associated Equipment* **735**, 102-109 (2014).
191. M. Boin, nxs: a program library for neutron cross section calculations. *Journal of Applied Crystallography* **45**, 603-607 (2012).
192. B. Abbey, S. Y. Zhang, W. J. J. Vorster, A. M. Korsunsky, Feasibility study of neutron strain tomography. *Procedia Engineering* **1**, 185-188 (2009).
193. B. Abbey, S. Y. Zhang, W. Vorster, A. M. Korsunsky, Reconstruction of axisymmetric strain distributions via neutron strain tomography. *Nuclear Instruments and Methods in Physics Research Section B: Beam Interactions with Materials and Atoms* **270**, 28-35 (2012).
194. R. A. Winholtz, J. B. Cohen, GENERALIZED LEAST-SQUARES DETERMINATION OF TRIAXIAL STRESS STATES BY X-RAY-DIFFRACTION AND THE ASSOCIATED ERRORS. *Aust. J. Phys.* **41**, 189-199 (1988).

195. A. D. Krawitz, R. A. Winholtz, Use of position-dependent stress-free standards for diffraction stress measurements. *Materials Science and Engineering: A* **185**, 123-130 (1994).
196. R. Winholtz, A. Krawitz, The relaxation of residual stresses with postweld heat treatment in a high-performance weld measured with neutron diffraction. *Metallurgical and Materials Transactions A* **26**, 1287-1295 (1995).
197. D. Balzar, R. B. Von Dreele, K. Bennett, H. Ledbetter, Elastic-strain tensor by Rietveld refinement of diffraction measurements. *Journal of Applied Physics* **84**, 4822-4833 (1998).
198. B. Abbey, S. Y. Zhang, W. Vorster, A. M. Korsunsky, Reconstruction of axisymmetric strain distributions via neutron strain tomography. *Nuclear Instruments and Methods in Physics Research Section B: Beam Interactions with Materials and Atoms* **270**, 28-35 (2012).
199. J. A. James, J. R. Santisteban, L. Edwards, M. R. Daymond, A virtual laboratory for neutron and synchrotron strain scanning. *Physica B: Condensed Matter* **350**, E743-E746 (2004).
200. G. Burca, "Combined neutron imaging and diffraction: instrumentation and experimentation, Ph. D. Thesis, Milton Keynes, UK, (2012).
201. G. Burca, J. A. James, W. Kockelmann, M. E. Fitzpatrick, S. Y. Zhang, J. Hovind, R. van Langh, A new bridge technique for neutron tomography and diffraction measurements. *Nuclear Instruments and Methods in Physics Research Section A: Accelerators, Spectrometers, Detectors and Associated Equipment* **651**, 229-235 (2011); published online Epub9/21/.
202. R. van Langh, J. James, G. Burca, W. Kockelmann, S. Y. Zhang, E. Lehmann, M. Estermann, A. Pappot, New insights into alloy compositions: studying Renaissance bronze statuettes by combined neutron imaging and neutron diffraction techniques. *Journal of Analytical Atomic Spectrometry* **26**, 949-958 (2011).
203. W. Kockelmann, S. Y. Zhang, J. F. Kelleher, J. B. Nightingale, G. Burca, J. A. James, IMAT – A New Imaging and Diffraction Instrument at ISIS. *Physics Procedia* **43**, 100-110 (2013); published online Epub//.
204. A. King, P. Reischig, J. Adrien, W. Ludwig, First laboratory X-ray diffraction contrast tomography for grain mapping of polycrystals. *Journal of Applied Crystallography* **46**, 1734-1740 (2013).
205. G. Johnson, A. King, M. G. Honnicke, J. Marrow, W. Ludwig, X-ray diffraction contrast tomography: a novel technique for three-dimensional grain mapping of polycrystals. II. The combined case. *Journal of Applied Crystallography* **41**, 310-318 (2008).
206. S. Peetermans, A. King, W. Ludwig, P. Reischig, E. Lehmann, Cold neutron diffraction contrast tomography of polycrystalline material. *Analyst* **139**, 5766-5772 (2014).
207. R. Woracek, D. Penumadu, N. Kardjilov, A. Hilger, M. Strobl, R. C. Wimpory, I. Manke, J. Banhart, Neutron Bragg-edge-imaging for strain mapping under in situ tensile loading. *Journal of Applied Physics* **109**, 093506 (2011).

208. P. J. McMahon, B. E. Allman, D. L. Jacobson, M. Arif, S. A. Werner, K. A. Nugent, Quantitative Phase Radiography with Polychromatic Neutrons. *Physical Review Letters* **91**, 145502 (2003); published online Epub10/01/.
209. M. Strobl, W. Treimer, A. Hilger, First realisation of a three-dimensional refraction contrast computerised neutron tomography. *Nuclear Instruments and Methods in Physics Research Section B: Beam Interactions with Materials and Atoms* **222**, 653-658 (2004); published online Epub8//.
210. M. Strobl, N. Kardjilov, A. Hilger, E. Jericha, G. Badurek, I. Manke, Imaging with polarized neutrons. *Physica B: Condensed Matter* **404**, 2611-2614 (2009); published online Epub9/1/.
211. M. Schulz, A. Neubauer, M. Martin, C. Elbio, S. Burkhard, P. Christian, B. Peter, Polarized neutron radiography with a periscope. *Journal of Physics: Conference Series* **200**, 112009 (2010).
212. M. Strobl, C. Pappas, A. Hilger, S. Wellert, N. Kardjilov, S. O. Seidel, I. Manke, Polarized neutron imaging: A spin-echo approach. *Physica B: Condensed Matter* **406**, 2415-2418 (2011); published online Epub6//.
213. N. Kardjilov, S. Baechler, M. Bastürk, M. Dierick, J. Jolie, E. Lehmann, T. Materna, B. Schillinger, P. Vontobel, New features in cold neutron radiography and tomography Part II: applied energy-selective neutron radiography and tomography. *Nuclear Instruments and Methods in Physics Research Section A: Accelerators, Spectrometers, Detectors and Associated Equipment* **501**, 536-546 (2003); published online Epub4/1/.
214. E. H. Lehmann, G. Frei, G. Kühne, P. Boillat, The micro-setup for neutron imaging: A major step forward to improve the spatial resolution. *Nuclear Instruments and Methods in Physics Research Section A: Accelerators, Spectrometers, Detectors and Associated Equipment* **576**, 389-396 (2007).
215. P. Boillat, D. Kramer, B. C. Seyfang, G. Frei, E. Lehmann, G. G. Scherer, A. Wokaun, Y. Ichikawa, Y. Tasaki, K. Shinohara, In situ observation of the water distribution across a PEFC using high resolution neutron radiography. *Electrochemistry Communications* **10**, 546-550 (2008); published online Epub4//.
216. M. Tamaki, Conceptual monochromatic digital neutron radiography using continuous cold neutron beam. *Nuclear Instruments and Methods in Physics Research Section A: Accelerators, Spectrometers, Detectors and Associated Equipment* **542**, 32-37 (2005); published online Epub4/21/.
217. M. Strobl, Future prospects of imaging at spallation neutron sources. *Nuclear Instruments and Methods in Physics Research Section A: Accelerators, Spectrometers, Detectors and Associated Equipment* **604**, 646-652 (2009).
218. M. Strobl, R. Woracek, N. Kardjilov, A. Hilger, R. Wimpory, A. Tremsin, T. Wilpert, C. Schulz, I. Manke, D. Penumadu, Time-of-flight neutron imaging for spatially resolved strain investigations based on Bragg edge transmission at a reactor source. *Nuclear Instruments and Methods in Physics Research Section A: Accelerators, Spectrometers, Detectors and Associated Equipment* **680**, 27-34 (2012).

219. M. Strobl, N. Kardjilov, A. Hilger, D. Penumadu, I. Manke, Advanced neutron imaging methods with a potential to benefit from pulsed sources. *Nuclear Instruments and Methods in Physics Research Section A: Accelerators, Spectrometers, Detectors and Associated Equipment* **651**, 57-61 (2011).
220. M. Strobl, R. Steitz, M. Kreuzer, M. Rose, H. Herrlich, F. Mezei, M. Grunze, R. Dahint, BioRef: A versatile time-of-flight reflectometer for soft matter applications at Helmholtz--Zentrum Berlin. *Review of Scientific Instruments* **82**, 055101-055109 (2011).
221. A. S. Tremsin, J. B. McPhate, A. Steuwer, W. Kockelmann, A. M Paradowska, J. F. Kelleher, J. V. Vallerga, O. H. W. Siegmund, W. B. Feller, High-Resolution Strain Mapping Through Time-of-Flight Neutron Transmission Diffraction with a Microchannel Plate Neutron Counting Detector. *Strain* **48**, 296–305 (2012).
222. R. Woracek, S. Young, D. Penumadu, J. J. Frafjord, In-Situ Microstructure Evolution Under Stress Using a Large-Chamber SEM. *Microscopy and Microanalysis* **15**, 676-677 (2009).
223. C. Perry, Plane-shear measurement with strain gages. *Experimental Mechanics* **9**, 19N-22N (1969).
224. D. H. Chung, W. R. Buessem, The Elastic Anisotropy of Crystals. *Journal of Applied Physics* **38**, 2010-2012 (1967).
225. H. Dolle, The influence of multiaxial stress states, stress gradients and elastic anisotropy on the evaluation of (Residual) stresses by X-rays. *Journal of Applied Crystallography* **12**, 489-501 (1979).
226. M. A. Meyers, K. K. Chawla, *Mechanical Metallurgy: Principles and Applications*. (Prentice-Hall, Inc, Englewood Cliffs, N.J. 07632, U.S.A, 1984).
227. J. A. Wollmershauser, B. Clausen, S. R. Agnew, A slip system-based kinematic hardening model application to in situ neutron diffraction of cyclic deformation of austenitic stainless steel. *International Journal of Fatigue* **36**, 181-193 (2012).
228. M. Strobl, W. Treimer, C. Ritzoulis, A. G. Wagh, S. Abbas, I. Manke, The new V12 ultra-small-angle neutron scattering and tomography instrument at the Hahn-Meitner Institut. *Journal of Applied Crystallography* **40**, s463-s465 (2007).
229. A. Hilger, N. Kardjilov, M. Strobl, W. Treimer, J. Banhart, The new cold neutron radiography and tomography instrument CONRAD at HMI Berlin. *Physica B: Condensed Matter* **385-386, Part 2**, 1213-1215 (2006).
230. R. C. Wimpory, P. Mikula, J. Saroun, T. Poeste, J. Li, M. Hofmann, R. Schneider, Efficiency Boost of the Materials Science Diffractometer E3 at BENSC: One Order of Magnitude Due to a Horizontally and Vertically Focusing Monochromator. *Neutron News* **19**, 16-19 (2008).
231. R. Woracek, D. Penumadu, N. Kardjilov, A. Hilger, M. Boin, J. Banhart, I. Manke, 3D Mapping of Crystallographic Phase Distribution using Energy-Selective Neutron Tomography. *Advanced Materials*, n/a-n/a (2014).
232. M. Boin, R. C. Wimpory, A. Hilger, N. Kardjilov, S. Y. Zhang, M. Strobl, Monte Carlo simulations for the analysis of texture and strain measured with Bragg edge neutron transmission. *Journal of Physics: Conference Series* **340**, 012022 (2012).

233. F. Malamud, J. R. Santisteban, V. Alvarez, R. Bolmaro, J. Kelleher, S. Kabra, W. Kockelmann, Texture analysis with a time-of-flight neutron strain scanner. *Journal of Applied Crystallography* **47**, 1337-1354 (2014).
234. R. Woracek, D. Penumadu, N. Kardjilov, A. Hilger, M. Boin, J. Banhart, I. Manke, 3D Mapping of Crystallographic Phase Distribution using Energy-Selective Neutron Tomography. *Advanced Materials* **26**, 4069-4073 (2014).
235. B. Abbey, S. Y. Zhang, M. Xie, X. Song, A. M. Korsunsky, Neutron strain tomography using Bragg-edge transmission. *International Journal of Materials Research* **103**, 234-241 (2012); published online Epub2012/02/01.
236. H. J. Kirkwood, B. Abbey, H. M. Quiney, S. Y. Zhang, A. S. Tremsin, A. Korsunsky, BRAGG EDGE NEUTRON STRAIN TOMOGRAPHY. (2013).
237. R. A. Mayville, I. Finnie, Uniaxial stress-strain curves from a bending test. *Experimental Mechanics* **22**, 197-201 (1982); published online Epub1982/06/01.
238. W. C. Young, *Roark's Formulas for Stress and Strain*. (McGraw-Hill, New York, NY, ed. 7th Edition, 2002), pp. 832.
239. W. D. Pilkey, W. D. Pilkey, W. D. Pilkey, *Formulas for stress, strain, and structural matrices*. (John Wiley & Sons New Jersey, 2005).
240. W. D. Pilkey, D. F. Pilkey, *Peterson's stress concentration factors*. (John Wiley & Sons, 2008).
241. H. Neuber, Theory of stress concentration for shear-strained prismatical bodies with arbitrary nonlinear stress-strain law. *Journal of Applied Mechanics* **28**, 544-550 (1961).
242. Webpage: http://www.fracturemechanics.org/fm/index.html (B. McGinty), 2014
243. M. A. Sutton, J. H. Yan, V. Tiwari, H. W. Schreier, J. J. Orteu, The effect of out-of-plane motion on 2D and 3D digital image correlation measurements. *Optics and Lasers in Engineering* **46**, 746-757 (2008); published online Epub10//.
244. G. C. Kaschner, M. L. Lovato, M. G. Stout, G. Proust, C. Liu, I. J. Beyerlein, I. Usov, Y. Wang, C. N. Tomé, Mini-Tensile Experiments of Clock-Rolled Zirconium Plate. *Experimental Mechanics* **50**, 65-70 (2010); published online Epub2010/01/01.
245. V. Savic, L. G. Hector Jr, J. R. Fekete, Digital Image Correlation Study of Plastic Deformation and Fracture in Fully Martensitic Steels. *Experimental Mechanics* **50**, 99-110 (2010); published online Epub2010/01/01.
246. Webpage: http://www.isis.stfc.ac.uk/instruments/engin-x/engin-x2900.html (ISIS), 2015
247. A. S. Tremsin, J. V. Vallerga, J. B. McPhate, O. H. W. Siegmund, R. Raffanti, High Resolution Photon Counting With MCP-Timepix Quad Parallel Readout Operating at <formula formulatype="inline"> <img src="/images/tex/20632.gif" alt="> 1~{\rm KHz}"> </formula> Frame Rates. *Nuclear Science, IEEE Transactions on* **60**, 578-585 (2013).
248. F. Kropff, J. R. Granada, R. E. Mayer, The bragg lineshapes in time-of-flight neutron powder spectroscopy. *Nuclear Instruments and Methods in Physics Research* **198**, 515-521 (1982); published online Epub7/15/.

249. R. B. Von Dreele, J. D. Jorgensen, C. G. Windsor, Rietveld refinement with spallation neutron powder diffraction data. *Journal of Applied Crystallography* **15**, 581-589 (1982).
250. R. I. Todd, C. Borsa, B. Derby, M. A. M. Bourke, Analysis of neutron diffraction peak broadening caused by internal stresses in composite materials. *Nuclear Instruments and Methods in Physics Research Section A: Accelerators, Spectrometers, Detectors and Associated Equipment* **354**, 139-144 (1995); published online Epub1/15/.
251. P. J. Withers, H. K. D. H. Bhadeshia, Residual stress. Part 1 – Measurement techniques. *Materials Science and Technology* **17**, 355-365 (2001); published online Epub2001/04/01.
252. R. Woracek, J. R. Bunn, D. Penumadu, C. R. Hubbard, Method to determine hkl strains and shear moduli under torsion using neutron diffraction. *Applied Physics Letters* **100**, 191904 (2012).
253. T. Chu, W. Ranson, M. Sutton, Applications of digital-image-correlation techniques to experimental mechanics. *Experimental Mechanics* **25**, 232-244 (1985).
254. D. Post, Moiré interferometry: Advances and applications. *Experimental Mechanics* **31**, 276-280 (1991).
255. F. Zandman, paper presented at the Symposium on shear and torsion testing, 1961.
256. A. J. Wilkinson, G. Meaden, D. J. Dingley, High-resolution elastic strain measurement from electron backscatter diffraction patterns: New levels of sensitivity. *Ultramicroscopy* **106**, 307-313 (2006).
257. J. A. James, L. Edwards, Application of robot kinematics methods to the simulation and control of neutron beam line positioning systems. *Nuclear Instruments and Methods in Physics Research Section A: Accelerators, Spectrometers, Detectors and Associated Equipment* **571**, 709-718 (2007).
258. S. C. Vogel, C. Hartig, L. Lutterotti, R. B. V. Dreele, H.-R. Wenk, D. J. Williams, Texture measurements using the new neutron diffractometer HIPPO and their analysis using the Rietveld method. *Powder Diffraction* **19**, 65-68 (2004).
259. J. Ma, I. Karaman, Expanding the Repertoire of Shape Memory Alloys. *Science* **327**, 1468-1469 (2010); published online EpubMarch 19, 2010.
260. S. E. Offerman, N. H. van Dijk, J. Sietsma, S. Grigull, E. M. Lauridsen, L. Margulies, H. F. Poulsen, M. T. Rekveldt, S. van der Zwaag, Grain Nucleation and Growth During Phase Transformations. *Science* **298**, 1003-1005 (2002); published online EpubNovember 1, 2002.
261. M. Militzer, A Synchrotron Look at Steel. *Science* **298**, 975-976 (2002); published online EpubNovember 1, 2002.
262. M. Bayerlein, H. J. Christ, H. Mughrabi, Plasticity-induced martensitic transformation during cyclic deformation of AISI 304L stainless steel. *Materials Science and Engineering: A* **114**, L11-L16 (1989).
263. J. A. Venables, The martensite transformation in stainless steel. *Philosophical Magazine* **7**, 35-44 (1962); published online Epub1962/01/01.
264. G. B. Olson, M. Cohen, Kinetics of strain-induced martensitic nucleation. *MTA* **6**, 791-795 (1975); published online Epub1975/04/01.

265. S. H. Williams, A. Hilger, N. Kardjilov, I. Manke, M. Strobl, P. A. Douissard, T. Martin, H. Riesemeier, J. Banhart, Detection system for microimaging with neutrons. *Journal of Instrumentation* **7**, P02014 (2012).
266. K. Lefmann, K. Nielsen, McStas, a general software package for neutron ray-tracing simulations. *Neutron News* **10**, 20-23 (1999); published online Epub1999/01/01.
267. W. Kockelmann, L. C. Chapon, P. G. Radaelli, Neutron texture analysis on GEM at ISIS. *Physica B: Condensed Matter* **385–386, Part 1**, 639-643 (2006); published online Epub11/15/.
268. G. F. Vander Voort, W. Van Geertruyden, "Specimen Preparation for Electron Backscattered Diffraction (EBSD)," *Buehler technical advise* (2007).
269. N. Gey, B. Petit, M. Humbert, Electron backscattered diffraction study of ε/α′ martensitic variants induced by plastic deformation in 304 stainless steel. *Metallurgical and Materials Transactions A* **36**, 3291-3299 (2005).
270. B. Petit, N. Gey, M. Cherkaoui, B. Bolle, M. Humbert, Deformation behavior and microstructure/texture evolution of an annealed 304 AISI stainless steel sheet. Experimental and micromechanical modeling. *International journal of plasticity* **23**, 323-341 (2007).
271. J. A. Rodríguez-Martínez, R. Pesci, A. Rusinek, Experimental study on the martensitic transformation in AISI 304 steel sheets subjected to tension under wide ranges of strain rate at room temperature. *Materials Science and Engineering: A* **528**, 5974-5982 (2011).
272. Y. Shen, X. Li, X. Sun, Y. Wang, L. Zuo, Twinning and martensite in a 304 austenitic stainless steel. *Materials Science and Engineering: A* **552**, 514-522 (2012).
273. S. Peetermans, E. Lehmann, Simultaneous neutron transmission and diffraction contrast tomography as a non-destructive 3D method for bulk single crystal quality investigations. *Journal of Applied Physics* **114**, 124905 (2013).
274. S. Peetermans, E. H. Lehmann, A Double Detector Set-up for Simultaneous Transmission and Diffraction Neutron Imaging. *Physics Procedia* **43**, 179-185 (2013); published online Epub//.
275. A. King, P. Reischig, J. Adrien, S. Peetermans, W. Ludwig, Polychromatic diffraction contrast tomography. *Materials Characterization* **97**, 1-10 (2014); published online Epub11//.
276. J. R. Bunn, "Neutron Diffraction Study of Engineering Materials Subjected to Complex Loadings, "PhD diss., University of Tennessee, , (2014).
277. D. A. Witte, "Design of an automated mechanical loading device for applied stress measurements using neutron diffraction, University of Missouri, (1993).

Appendix

10.1 Portable Loading System

In order to accomplish the proposed in-situ studies under multi-axial loading, a portable loading system, capable of tension and torsional loading, has been developed within the dissertation frame work. The device was designed to be used at diffraction and imaging instruments available at neutron and x-ray synchrotron user facilities. The design of the loading system is largely based on a system that was given to our research group by Dr. Aaron Krawitz from the University of Missouri and that was designed by Dale A. Witte in 1993 as part of his bachelor thesis.(*Witte 1993,*[277]) This system is strictly capable of axial loading (up to 88 kN) and was already designed to be used for neutron diffraction instruments, for which is was mounted onto a Huber Eulerian Cradle which allowed free sample orientation with respect to the neutron beam. The original loading system is shown in Figure 10-1. It was modified as part of my research work to be used for in-situ investigations inside a Large Chamber SEM (*Woracek et al. 2009,*[222]) (Figure 10-1c), but that is not part of the dissertation.

The new loading system (depicted in Figure 10-2) was designed with the same concept of using a stepper motor, worm gears and a power screw to create the vertical axial force. The new requirement was that the system should also be able to apply torsion, and ideally even be capable of rotating the sample under load for tomography. Both of these two tasks have been realized by using two independently rotating grips, which are driven by separate stepper motors and a pinion wire – spur gear mechanism.

Within this chapter in the dissertation, the device and its integration with various instruments will be described. Figure 10-4 shows a diagram with schematic connections and Table 1 includes details of the control and data acquisition components which are used for the system. The system has been designed with the following specifications:

- Axial force capacity: up to 44 kN (range of load sensors can be used)
- Torque capacity: 12 Nm (Torque and axial force can be applied simultaneously)
- Specimen can freely rotate 360 degrees (with and without load; tomography mode)

- Axial deformation rate: 0-16000 micro-m/min
- Graphical user interface with PID control (stress, strain or deformation-control)
- Flexibility to test different specimens (materials, shapes) using custom grips
- Mobility of the system (Dimensions: 70 cm x 26 cm x 17 cm)
- Weight: 32 kg
- Motor and Drive System: Stepper Motor(s) and (Worm-) Gear System with power screw
- Up to 16 Strain Channels for strain gauges and/or extensometer

All the electronic control components and data acquisition have been newly configured within the framework of this dissertation. Furthermore, control software has been developed in LabView 8.5, providing a Graphical User Interface (GUI) as shown in Figure 10-6. The system has been implemented and used at several large scale user facilities in the USA, UK and Germany (examples given in Figure 10-8), where interfaces have been developed for commination between the loading system control and instrumentation controls of the beamline.

During the course between the initial development of the system and heavy usage for various projects, constant improvements have been undertaken. Significant changes that were made include the utilization of U-joints to improve the sample auto-alignment during loading. An alignment fixture was designed, built and installed by Mr. Ken Thomas. Dedicated software was written (Figure 10-7) and special alignment samples were made, according to ASTM specifications, to improve and characterize the sample alignment within the system.

Four versions of the loading system have been built as of now and are located and used at UTK, ORNL, HZB and the NOVA Center at Western Kentucky University (now hosting the Large Chamber SEM). One of the systems has been modified to be capable of 112 Nm torque, at the expense of the sample rotation capability.

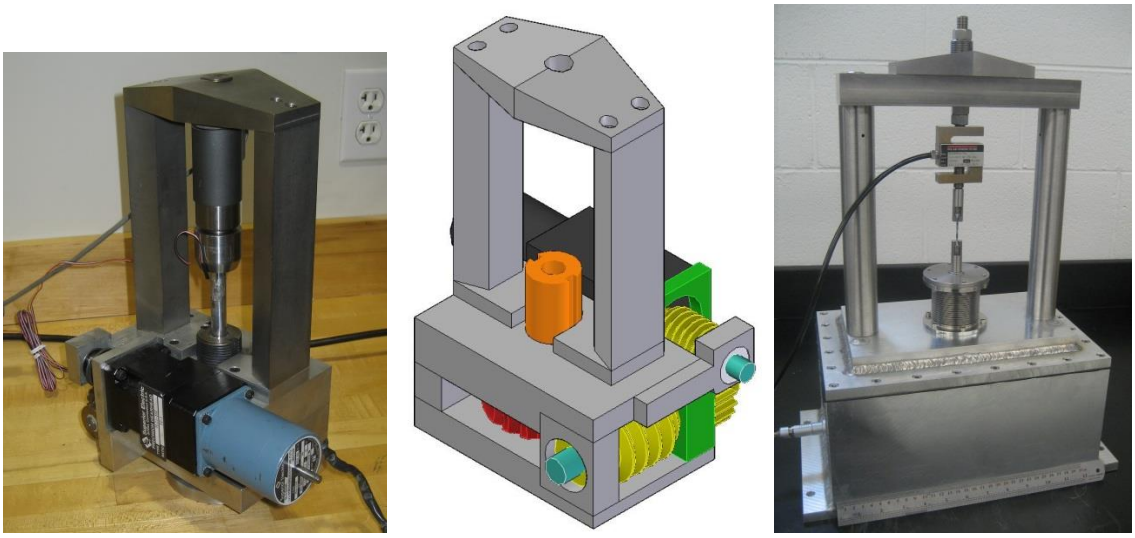

(a) (b) (c)

Figure 10-1. (a) Axial loading system (with 88 kN load cell) from the University of Missouri that was used as a basis for the new design. (b) 3D-CAD drawing based on the loading system. (c) The same loading system with a hermetically sealed casing so that it can be used inside of the evacuated Large Chamber SEM.

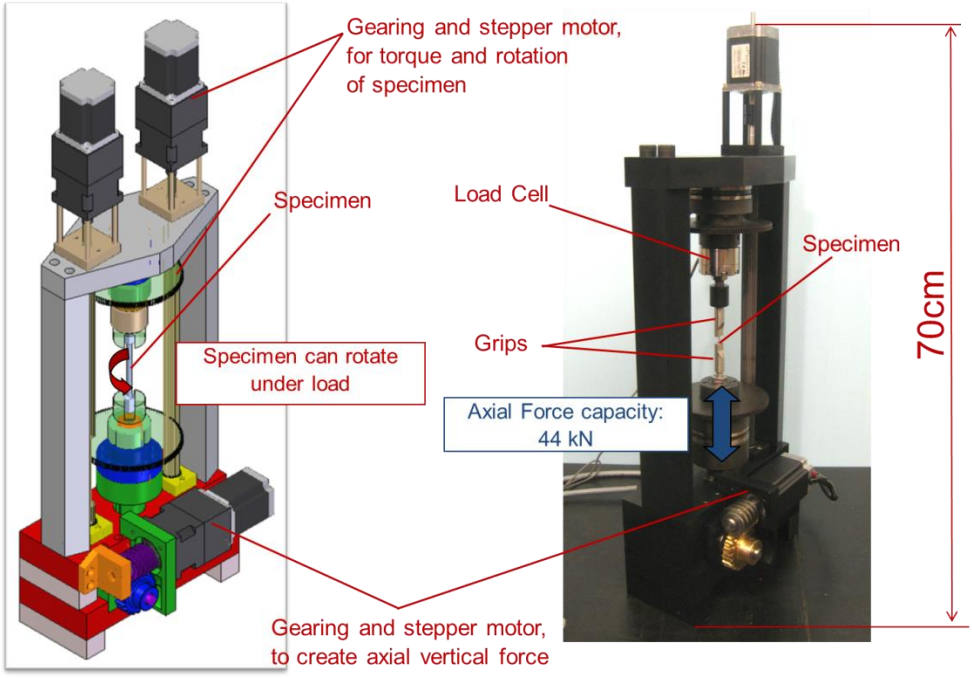

Figure 10-2. CAD model and photograph of the developed loading system, capable of tension, torsion, combination of both and sample rotation under load for tomography.

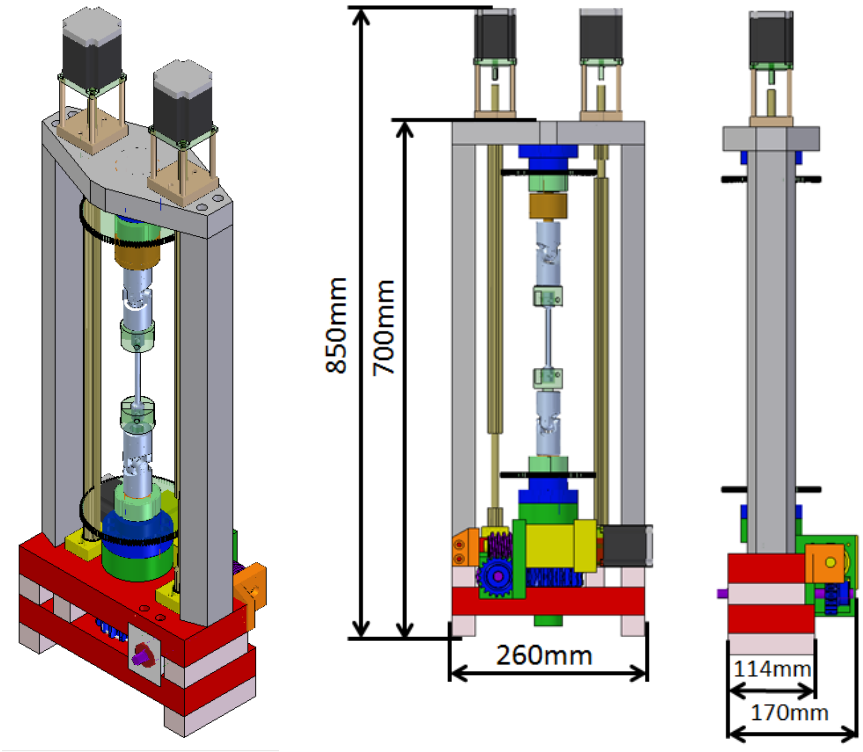

Figure 10-3. CAD drawing of the loading system, after upgrading the loading train for improved alignment using U-Joints.

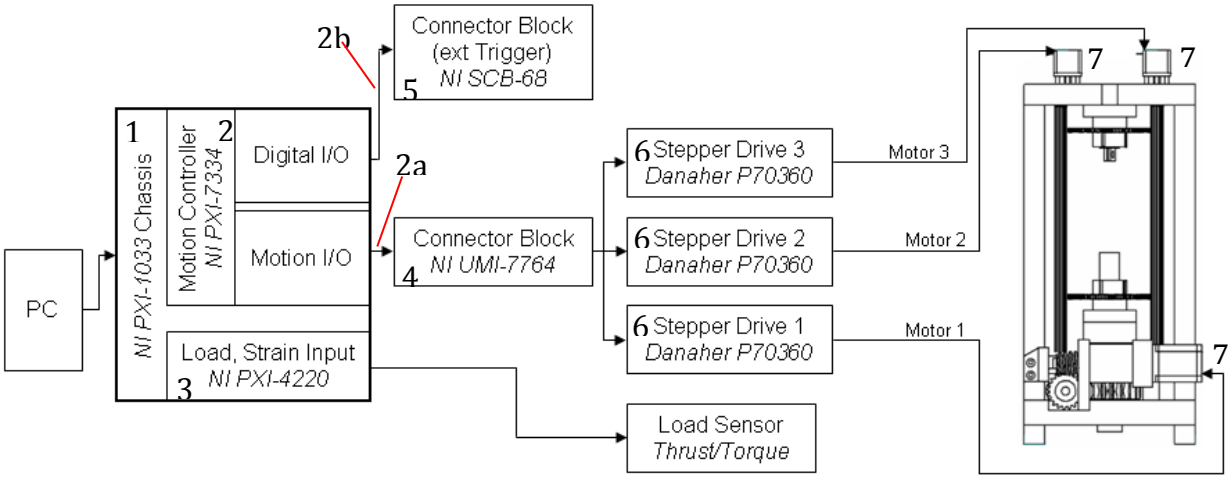

Figure 10-4. Schematic Setup of the Load Frame components.

Table 10-1. Electronic components of the Load Frame.

Item #	Description	Supplied by	Details
1	PXI DAQ Chassis	National Instruments	NI PXI-1033, 5-Slot PXI Chassis
2	Motion Controller	National Instruments	NI PCI-7334, Low Cost 4 Axis Stepper Only Controller
2a	Connection Cable (Motion Controller – UMI 7764)	National Instruments	SH68-C68-S, 68 pin VHDCI to 68 pin VHDCI, 0.5m
2b	Connection Cable (Motion Controller – SCB-68)	National Instruments	SH68-C68-S, 68 pin VHDCI to 68 pin VHDCI, 0.5m
3	Analog Input (Bridge Configuration)	National Instruments	NI PXI-4220, Strain, Pressure, Force, Load Sensor Input
4	Connector Block – User Motion Interface	National Instruments	NI UMI-7764, 4 Axis Motor Wiring Connectivity
5	Connector Block to send/receive trigger signals	National Instruments	NI SCB-68, Shielded I/O Connector Block for DAQ Devices with 68-Pin Connectors
6	Stepper Motor Drive	Danaher Motion/ National Instruments	P70360, 1-Axis, 525 W Stepper Drive, 3.5 A peak, 2.5 A continuous current output, 320 V bus voltage
7	Stepper Motor (NEMA 23 size)	Danaher Motion/ National Instruments	T23NRLC-LDN-NS-00 Step Mot, P70360, NEMA23, 380oz-in, dual shaft

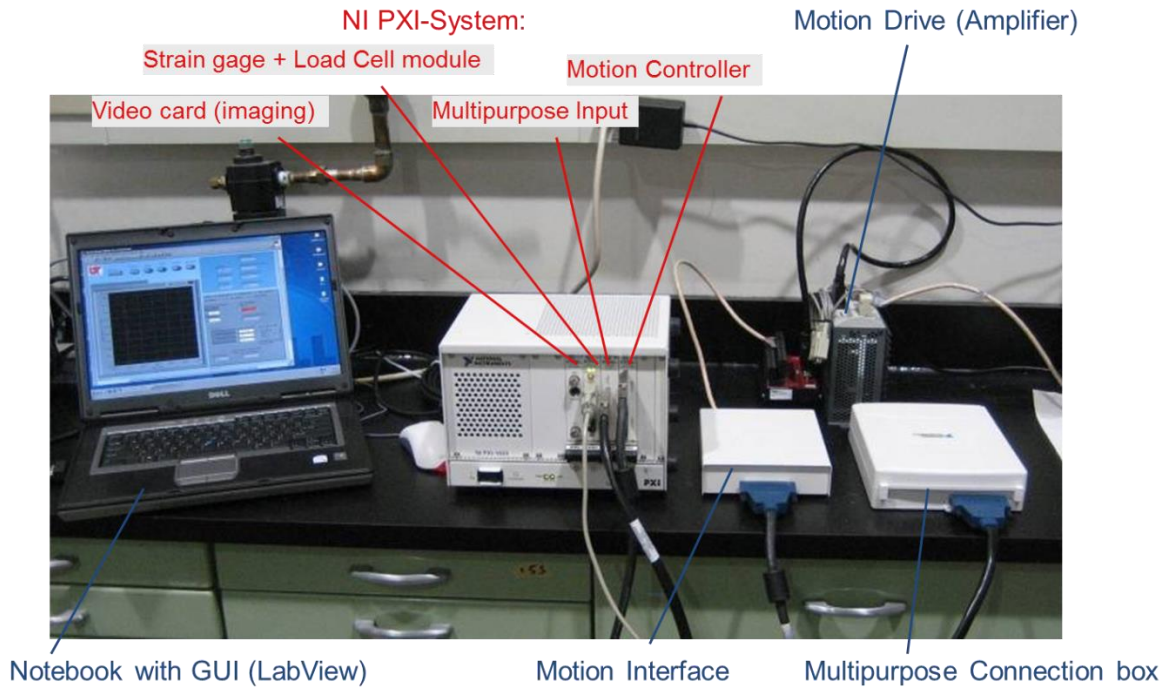

Figure 10-5. Picture of the electronic components of the loading system.

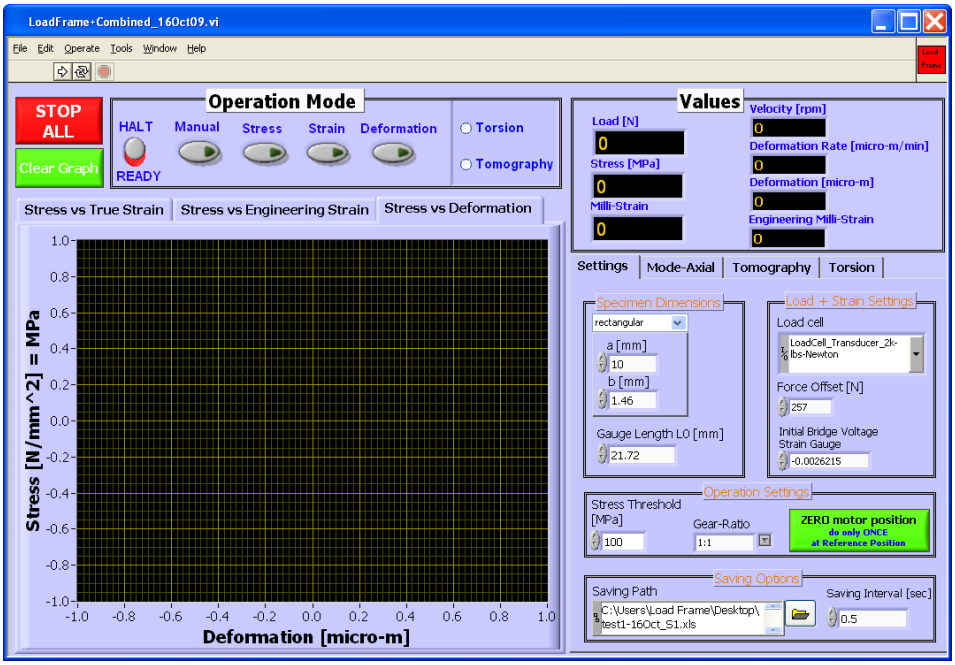

Figure 10-6. Graphical User Interface (GUI) for controlling the loading system.

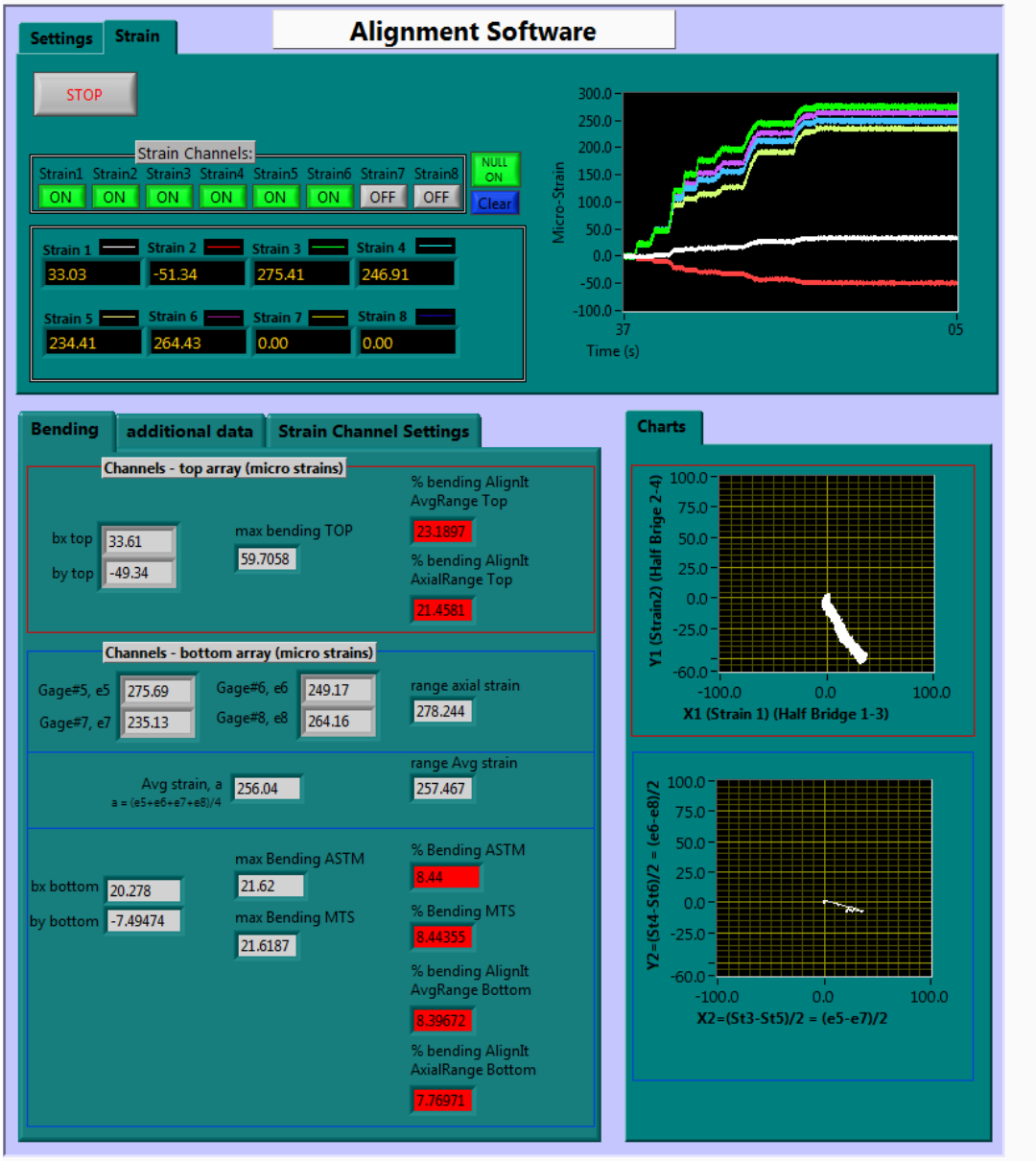

Figure 10-7. GUI of sample alignment software that was developed, based on ASTM specifications.

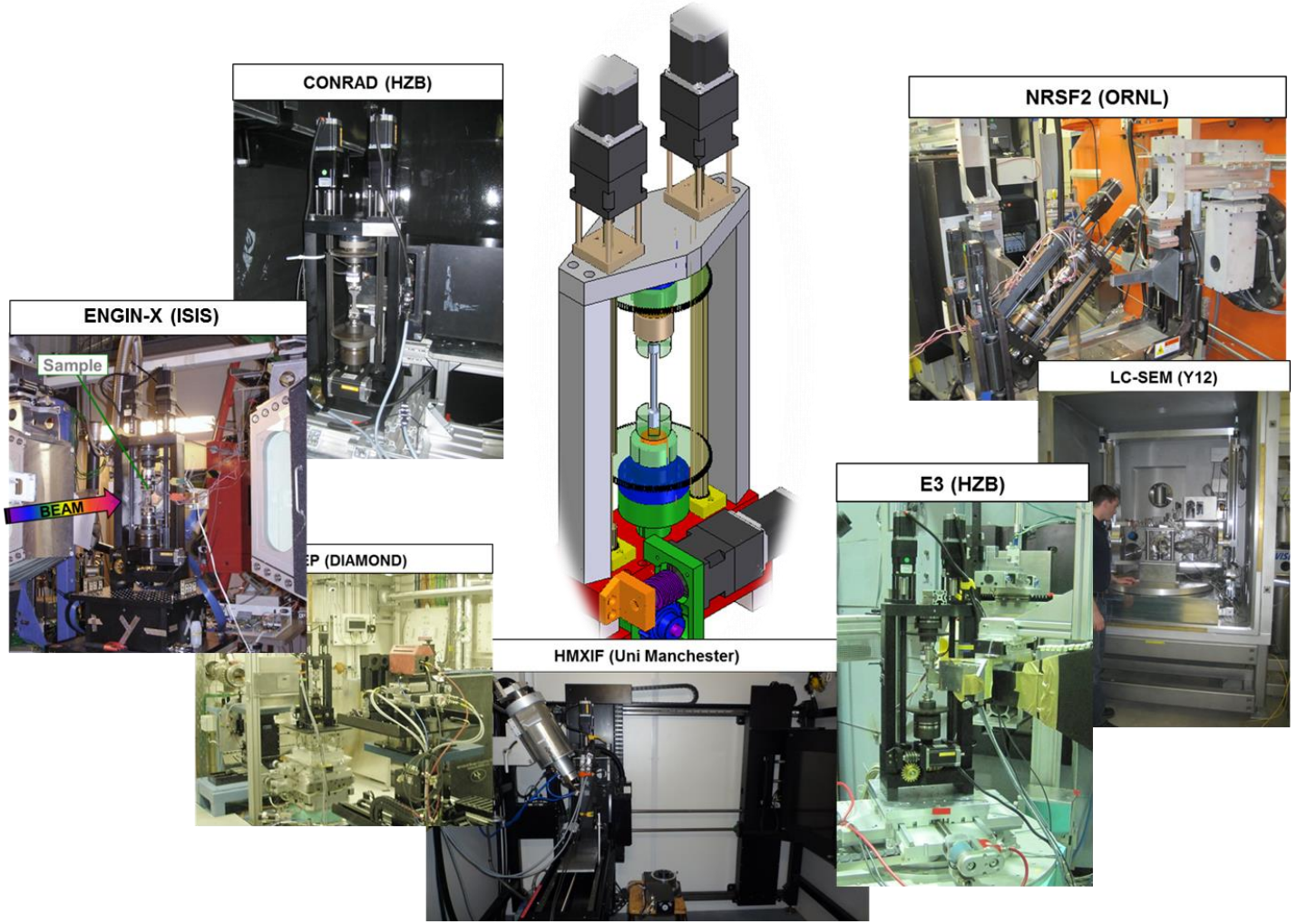

Figure 10-8. The loading system has been integrated and used at several user facilities for X-Ray and Neutron diffraction and imaging experiments, as shown in the individual photographs.

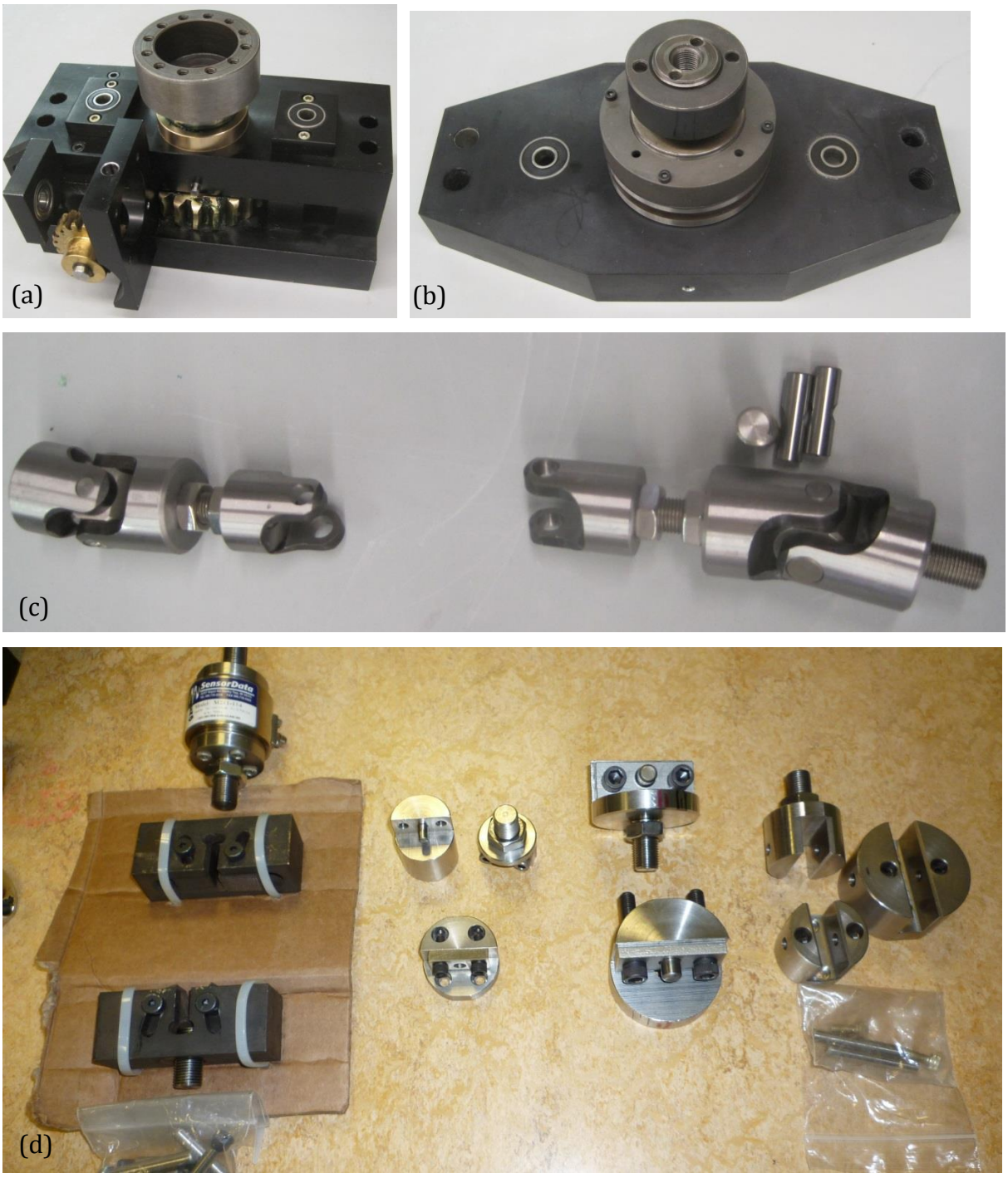

Figure 10-9. Components of the loading system: (a) Bottom unit that creates the axial force. (b) Top unit with ball bearing for sample rotation. (c) U-Joints. (d) Several types of grips that have been manufactured for different samples.

10.2 Properties of Radiation Relevant for Diffraction

Table 10-2. Comparison of various properties important for diffraction (and imaging) measurements, when using electrons, x-rays, photons and neutrons. *From* (*Hutchings et al. 2005,*[1])

Energy (E) (Target Used)	Laboratory X-rays			Hard X-rays			Electrons			Neutrons		
	6.40 keV (Fe)	8.04 keV (Cu)	17.4 keV (Mo)	35 keV	80 keV	250 keV	100 keV	200 keV	500 keV	1 meV	10 meV	100 meV
Relativistic mass (in m_e)	0.012	0.016	0.034	0.068	0.16	0.48	1.2	1.4	2.0	1839	1839	1839
Wavelength (Å)	1.94	1.54	0.71	0.35	0.15	0.05	0.037	0.025	0.014	9.0	2.9	0.9
Velocity (m/s)	3×10^8	3×10^8	3×10^8	3×10^8	3×10^8	3×10^8	1.65×10^8	2.1×10^8	2.6×10^8	437	1390	4370
Temperature (K)=E/k_b	0.74×10^8	0.93×10^8	2.0×10^8	4.1×10^8	9.2×10^8	29×10^8	11×10^8	23×10^8	57×10^8	12	116	1160
Attenuation length in Fe	18 μm	4 μm	34 μm	0.24 mm	2.18 mm	10.5 mm		~100 nm			~0.8cm	
Typical gauge volume	$1\times5\times0.01$(deep) mm³			$50\times50\times1000$ μm³			$5\times5\times100$(thick) nm³			$1\times1\times1$ mm³		

Note: Relativistic masses are in units of the rest mass of the electron. The neutron attenuation length cited is for a neutron wavelength of 1.8 Å (25 meV).

10.3 Neutron Classification

"The neutron can be described as a classical particle with mass m but it shows wave character too, which can be described with the deBroglie wave-length λ.. Let m=1.6749·10^{-27} kg be the neutron mass, v its velocity and h Planck's constant. Below are the relations for neutron energy E given in meV (i.e. 10^{-3}eV), wave-length λ in Ångstrom and velocity v in m/s." (*http://www.psi.ch/niag/neutron-interaction-with-matter 2014,*[99])

$$E = \frac{mv^2}{2} = \frac{h^2}{2m} \cdot \frac{1}{\lambda^2} \Rightarrow E[meV] = \frac{81.82}{(\lambda[\text{Å}])^2}$$

$$\lambda[\text{Å}] = \frac{9.045}{\sqrt{E[meV]}}$$

$$v[m/s] = \frac{3956}{\lambda[\text{Å}]} = 437 \cdot \sqrt{E[meV]}$$

From: http://www.psi.ch/niag/neutron-physics

When looking through various literature and resources, unambiguous classifications were found for neutron energy ranges, especially for classifying the epithermal, thermal and fast range (compare (*Larson 2001,*[138]*; Postma et al. 2009,*[134]*; Tremsin et al. 2012,*[97])). Below is the classification given by PSI:

Neutrons	Energy range	Wavelength [Å]	Velocity [m/s]
ultra cold	≤ 300 neV	≥ 500	≤ 8
very cold	300 neV - 0.12 meV	52.2 – 26.1	7.5 – 152
cold	0.12 meV - 12 meV	26.1 – 2.6	152 – 1515
thermal	12 meV - 100 meV	2.6 - 0.9	1515 - 4374
epithermal	100 meV - 1eV	0.9 - 0.28	4374 - 13.8 10^3
intermediate	1eV - 0.8MeV		
fast	> 0.8MeV		

From: http://www.psi.ch/niag/neutron-physics

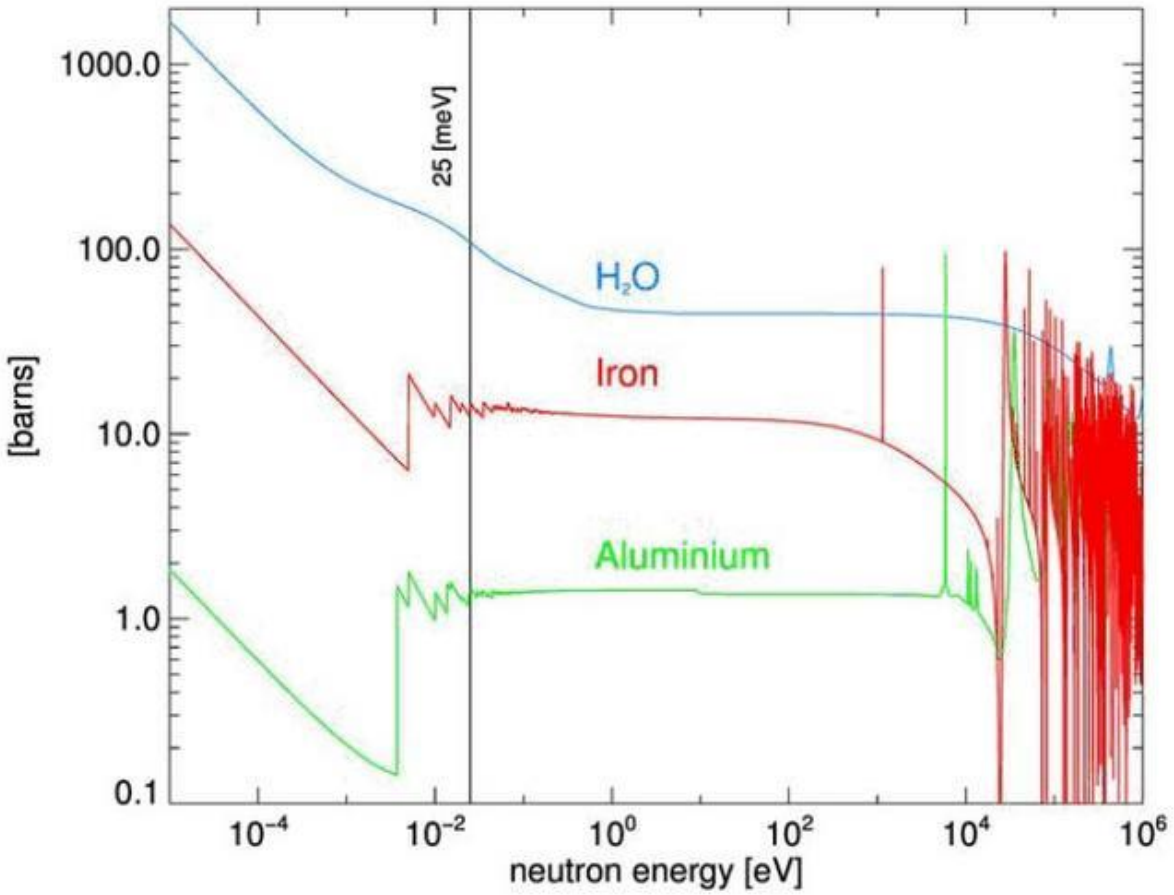

Thermal neutron cross section at 0.025 eV			
Material	ρ	σ [barns]	Σ [1/cm]
Water	1	112	3.74
Iron	7.9	14	1.18
Aluminium	2.7	1.7	0.1

Figure 10-10. Energy dependence of neutron cross sections shown for aluminum, iron and the water molecule. Bragg edges can be seen for iron and aluminum in the thermal and cold energy spectrum, wheras resonances are visible in the high energy range.
From (*http://www.psi.ch/niag/neutron-interaction-with-matter 2014,*[99])

10.4 Linear Attenuation Coefficients

Table 10-3. Linear attenuation coefficients for thermal neutrons.
From (*http://www.psi.ch/niag/neutron-interaction-with-matter 2014,*[99])

1a	2a	3b	4b	5b	6b	7b	8			1b	2b	3a	4a	5a	6a	7a	0
H																	He
3.44																	0.02
Li	Be											B	C	N	O	F	Ne
3.30	0.79											101.60	0.56	0.43	0.17	0.20	0.10
Na	Mg											Al	Si	P	S	Cl	Ar
0.09	0.15											0.10	0.11	0.12	0.06	1.33	0.03
K	Ca	Sc	Ti	V	Cr	Mn	Fe	Co	Ni	Cu	Zn	Ga	Ge	As	Se	Br	Kr
0.06	0.08	2.00	0.60	0.72	0.54	1.21	1.19	3.92	2.05	1.07	0.35	0.49	0.47	0.67	0.73	0.24	0.61
Rb	Sr	Y	Zr	Nb	Mo	Tc	Ru	Rh	Pd	Ag	Cd	In	Sn	Sb	Te	I	Xe
0.08	0.14	0.27	0.29	0.40	0.52	1.76	0.58	10.88	0.78	4.04	115.11	7.58	0.21	0.30	0.25	0.23	0.43
Cs	Ba	La	Hf	Ta	W	Re	Os	Ir	Pt	Au	Hg	Tl	Pb	Bi	Po	At	Rn
0.29	0.07	0.52	4.99	1.49	1.47	6.85	2.24	30.46	1.46	6.23	16.21	0.47	0.38	0.27			
Fr	Ra	Ac	Rf	Ha													
	0.34																

	Ce	Pr	Nd	Pm	Sm	Eu	Gd	Tb	Dy	Ho	Er	Tm	Yb	Lu
*Lanthanides	0.14	0.41	1.87	5.72	171.47	94.58	1479.04	0.93	32.42	2.25	5.48	3.53	1.40	2.75
	Th	Pa	U	Np	Pu	Am	Cm	Bk	Cf	Es	Fm	Md	No	Lr
**Actinides	0.59	8.46	0.82	9.80	50.20	2.86								

Table 10-4. Linear attenuation coeffitients for 150 keV X-ray.
From (*http://www.psi.ch/niag/neutron-interaction-with-matter 2014,*[99])

1a	2a	3b	4b	5b	6b	7b	8			1b	2b	3a	4a	5a	6a	7a	0
H																	He
0.02																	0.02
Li	Be											B	C	N	O	F	Ne
0.06	0.22											0.28	0.27	0.11	0.16	0.14	0.17
Na	Mg											Al	Si	P	S	Cl	Ar
0.13	0.24											0.38	0.33	0.25	0.30	0.23	0.20
K	Ca	Sc	Ti	V	Cr	Mn	Fe	Co	Ni	Cu	Zn	Ga	Ge	As	Se	Br	Kr
0.14	0.26	0.48	0.73	1.04	1.29	1.32	1.57	1.78	1.96	1.97	1.64	1.42	1.33	1.50	1.23	0.90	0.73
Rb	Sr	Y	Zr	Nb	Mo	Tc	Ru	Rh	Pd	Ag	Cd	In	Sn	Sb	Te	I	Xe
0.47	0.86	1.61	2.47	3.43	4.29	5.06	5.71	6.08	6.13	5.67	4.84	4.31	3.98	4.28	4.06	3.45	2.53
Cs	Ba	La	Hf	Ta	W	Re	Os	Ir	Pt	Au	Hg	Tl	Pb	Bi	Po	At	Rn
1.42	2.73	5.04	19.70	25.47	30.49	34.47	37.92	39.01	38.61	35.94	25.88	23.23	22.81	20.28	20.22		9.77
Fr	Ra	Ac	Rf	Ha													
	11.80	24.47															

	Ce	Pr	Nd	Pm	Sm	Eu	Gd	Tb	Dy	Ho	Er	Tm	Yb	Lu
*Lanthanides	5.79	6.23	6.46	7.33	7.68	5.66	8.69	9.46	10.17	10.91	11.70	12.49	9.32	14.07
	Th	Pa	U	Np	Pu	Am	Cm	Bk	Vf	Es	Fm	Md	No	Lr
**Actinides	28.95	39.65	49.08											

10.5 Double Crystal Monochromator at HZB

The following figures depict the most extreme settings between 2 Å and 6 Å, for the case of a monochromator crystal of PCG (002) and of a Silicon single crystal (111).

PCG Crystals

			Distance			
λ [Å]	Grazing angle [deg]	Shift [mm]	**74mm**	λ [Å]	Grazing angle [deg]	Shift [mm]
2	17.36	106.73		6	63.57	-56.07
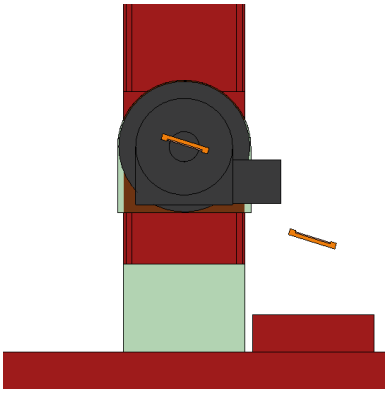				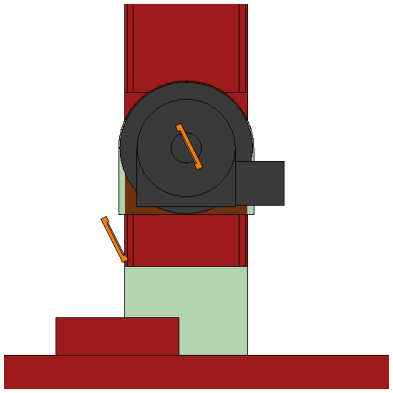		
λ [Å]	Grazing angle [deg]	Shift [mm]	**50mm**	λ [Å]	Grazing angle [deg]	Shift [mm]
2	17.36	72.11		6	63.57	-37.88
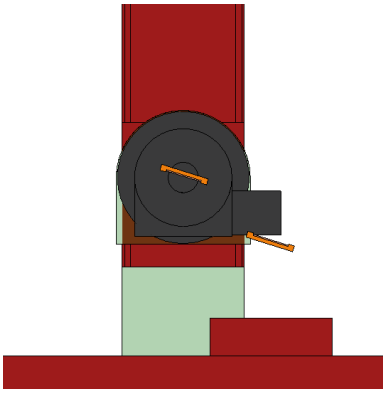				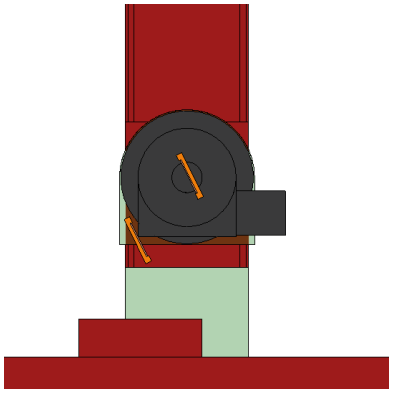		

λ [Å]	Grazing angle [deg]	Shift [mm]	**30mm**	λ [Å]	Grazing angle [deg]	Shift [mm]
2	17.36	43.27		6	63.57	-22.73
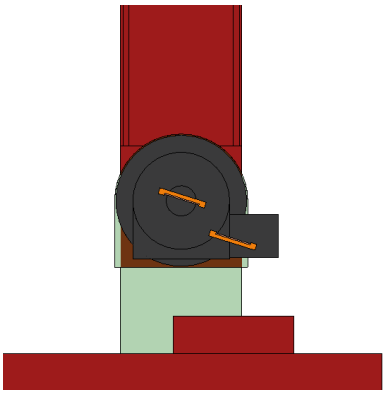				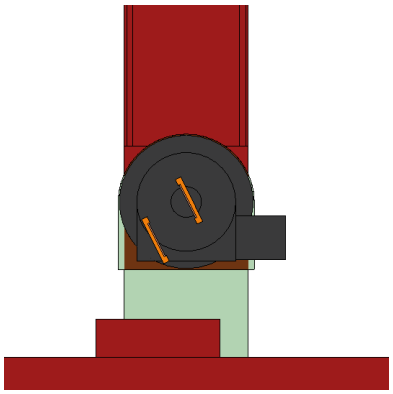		

Silicon Crystal (111)

			Distance			
λ [Å]	Grazing angle [deg]	Shift [mm]	**74mm**	λ [Å]	Grazing angle [deg]	Shift [mm]
2	18.60	97.51		6	73.09	-110.44
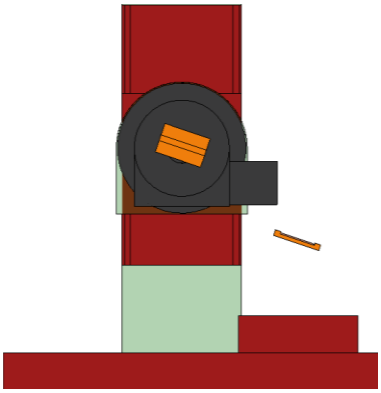				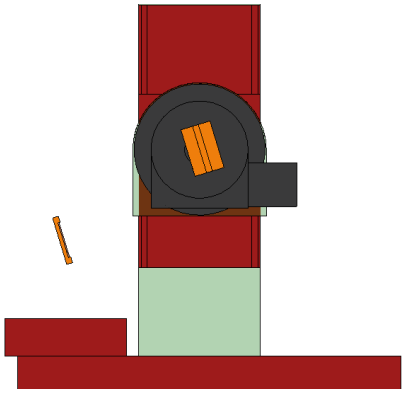		

λ [Å]	Grazing angle [deg]	Shift [mm]	**50mm**	λ [Å]	Grazing angle [deg]	Shift [mm]
2	18.60	65.88		6	73.09	-74.62
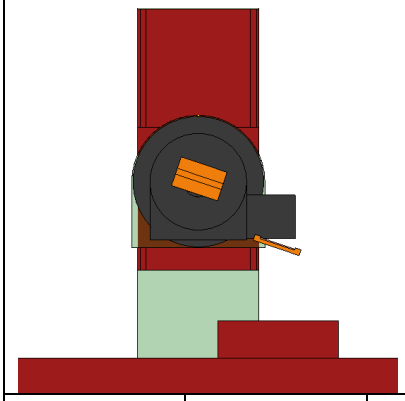				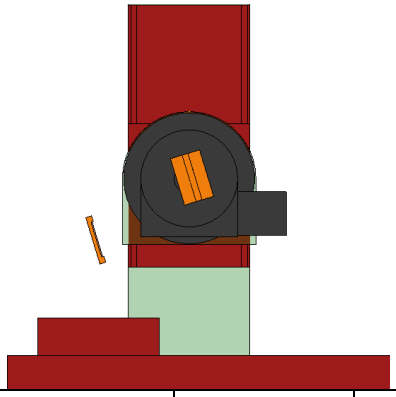		
λ [Å]	Grazing angle [deg]	Shift [mm]	**30mm**	λ [Å]	Grazing angle [deg]	Shift [mm]
2	18.60	39.53		6	73.09	-44.77
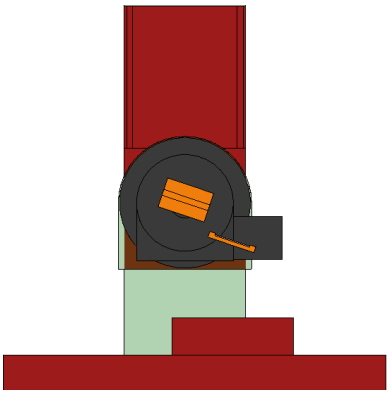				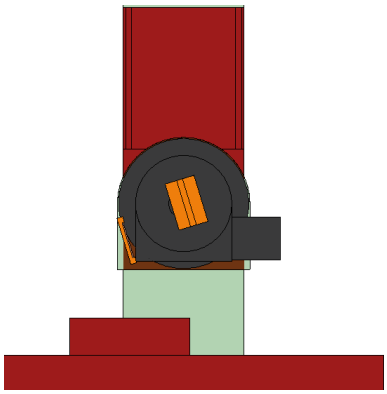		

10.6 HIPPO and GEM Instrument Layouts

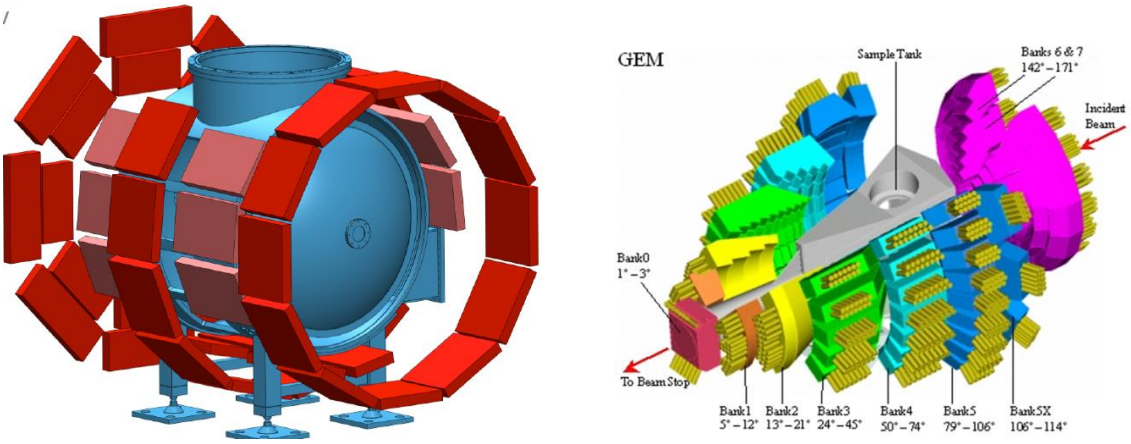

Figure 10-11. Diagram of time-of-flight diffractomters at LANSCE and ISI. left: HIPPO. *FROM* (*Vogel et al. 2004,*[258]). right: GEM. *FROM* (*Kockelmann et al. 2006,*[267])

10.7 Time of Flight Transmission Spectra from ENGIN-X

The following figures depict the quality of the tranmssion spectra of the partially transformed tensile sample (see section 7.7.4), that were obtained after diffrenet integration times for selected regions.

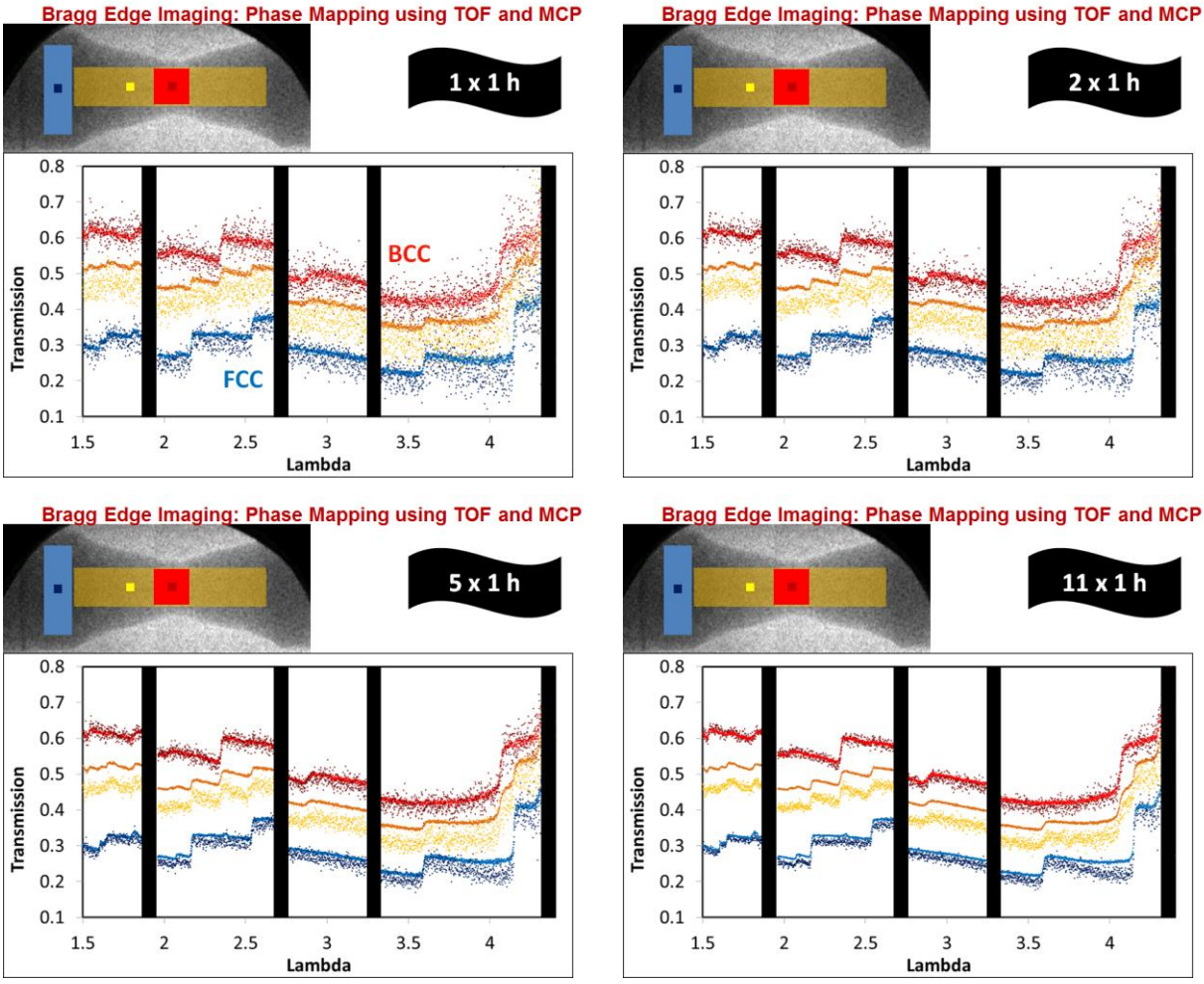

Figure 10-12. Transmission spectra recorded at ENGIN-X with increasing count times for different regions. The tensile sample is transformed from Austenite to Martensite in the center of the gauge section.

10.8 Refereed Publications

1. **R. Woracek**, D. Penumadu, N. Kardjilov, A. Hilger, M. Boin, J. Banhart, I. Manke
   3D Mapping of Crystallographic Phase Distribution using Energy-Selective Neutron Tomography
   Advanced Materials, DOI: 10.1002/adma.201400192 (2014)
   impact factor = 15.4

2. M. Boin, R. C. Wimpory, **R. Woracek**,
   Optimizing Experiment Performance by Realistic Sample Simulations
   Advanced Materials Research (Trans Tech Publ.), vol. 996, pp. 197-202 (2014)

3. **R. Woracek**, J. R. Bunn, D. Penumadu, A. Tremsin, A. Siriruk, N. Kardjilov, I. Manke, M. Boin, A. Hilger, C. R. Hubbard, B. Clausen, T. A. Sisneros
   Methodology for Combined Neutron Diffraction and Bragg Edge Imaging
   MRS Proceedings 1528 (2013)

4. J. R. Bunn, D. Penumadu, **R. Woracek**, N. Kardjilov, A. Hilger, I. Manke, S. Williams
   Detection of water with high sensitivity to study polymer electrolyte fuel cell membranes using cold neutrons at high spatial resolution
   Applied Physics Letters 102, p. 234102 (2013)
   impact factor = 3.8

5. M. Strobl, **R. Woracek**, N. Kardjilov, A. Hilger, R. Wimpory, A. Tremsin, T. Wilpert, C. Schulz, I. Manke, D. Penumadu
   Time-of-flight neutron imaging for spatially resolved strain investigations based on Bragg edge transmission at a reactor source
   Nuclear Instruments and Methods in Physics Research Section A, 680, 27-34 (2012)

6. **R. Woracek**, J. R. Bunn, D. Penumadu, C. R. Hubbard
   Method to determine hkl strains and shear moduli under torsion using neutron diffraction
   Applied Physics Letters 100, p. 191904 (2012)
   impact factor = 3.8

7. N. Kardjilov, I. Manke, A. Hilger, S. Williams, M. Strobl, **R. Woracek**, M. Boin, E. Lehmann, D. Penumadu, J. Banhart
   Neutron Bragg-edge mapping of weld seams
   International Journal of Materials Research, p. 151-154 (2012)

8. **R. Woracek**, D. Penumadu, N. Kardjilov, A. Hilger, M. Strobl, R. C. Wimpory, I. Manke, J. Banhart
   Neutron Bragg-edge-imaging for strain mapping under in situ tensile loading
   Journal of Applied Physics 109, p. 093506 (2011)

impact factor = 2.2

9. **R. Woracek**, S. Young, D. Penumadu, J. Frafjord
   In-Situ Microstructure Evolution Under Stress Using a Large-Chamber SEM
   Microscopy and Microanalysis 15, 676-677 (2009)

Publications in progress

10. A. Siriruk**, R. Woracek**, S. Puplampu, N. Kardjilov, A. Hilger, I. Manke, P. Withers, D. Penumadu
    Size effects in testing of carbon fiber vinyl ester laminate for marine application and damage evolution
    American Society for Composites, in preparation (2014)

11. **R. Woracek**, D. Penumadu, A. Tremsin, N. Kardjilov, J. Kelleher
    Spatial mapping of strain evolution around a stress concentration using time-of-flight neutron imaging
    Nuclear Instruments and Methods in Physics Research Section A, in preparation (2014)

12. J. R. Bunn, **R. Woracek**, D. Penumadu, C. R. Hubbard
    In Situ Strain Tensor Evolution for Steel Samples Subjected to Tension and Torsion
    Applied Physics Letters, in preparation (2014)

Conference and Meeting Presentations

<u>Oral</u>

1. R. Woracek, D. Penumadu, "Benefits and Challenges of using Energy Selective Neutron Imaging at Time of Flight and Reactor Sources", NEUWAVE 6, Workshop on Neutron Wavelength Dependent Imaging, Garching, Germany (2014)

2. R. Woracek, D. Penumadu, A. Tremsin, N. Kardjilov, A., M. Boin, A. Siriruk, I. Manke, M. Strobl, J. Kelleher, "In-Situ Bragg Edge Imaging for Strain and Phase Mapping under Multi-Axial Loading", TMS Annual Meeting, San Antonio, TX (2013)

3. R. Woracek, J. R. Bunn, D. Penumadu, A. Tremsin, A. Siriruk, N. Kardjilov, I. Manke, M. Boin, A. Hilger, C. R. Hubbard, B. Clausen, and T. A. Sisneros, "Measurement of hkl Strains under Complex Loading Paths and Methodology for Combined Neutron Diffraction and Imaging", MRS Fall Meeting, Boston, MA (2012)

4. R. Woracek, J. R. Bunn, D. Penumadu, C. Hubbard, "New Approach to Measure Lattice Strains under Torsional Shear Using In Situ Neutron Diffraction for Polycrystalline Materials" , TMS Annual Meeting, Orlando, FL (2012)

5. R. Woracek, I. Sen, D. Penumadu, " Wetting and Wicking Behavior of Refractory Coatings Used in Lost Foam Casting", TMS Annual Meeting, Orlando, FL (2012)

6. R. Woracek, D. Penumadu, N. Kardjilov, M. Strobl, A. Hilger, I. Manke, A. Tremsin, "In-situ Bragg-edge Imaging for strain mapping under multi-axial loading", NEUWAVE 4, Workshop on Neutron Wavelength Dependent Imaging, Gatlingburg, TN (2011)

7. R. Woracek, S. Young, D. Penumadu, J. Frafjord, "Integrating a mechanical Loading System into the Large-Chamber SEM", Western Kentucky University Nondestructive Analysis Center Conference, Bowling Green, KY (2011)

8. R. Woracek, D. Penumadu, N. Kardjilov, A. Hilger, M. Strobl, I. Manke, R. Wimpory, A.S. Tremsin, "Bragg-edge Imaging under in-situ mechanical loading at a reactor source and comparison to diffraction based results", 9th World Conference on Neutron Radiography, Kwa-Maritane, South Africa (2010)

9. R. Woracek, D. Penumadu, N. Kardjilov, A. Hilger, M. Strobl, R. Wimpory, I. Manke, "In-situ Bragg-edge Imaging under generalized loading conditions using a reactor source", NEUWAVE 3, Workshop on Neutron Wavelength Dependent Imaging, Sapporo, Japan (2010)

<u>Poster & Co-Author</u>

10. D. Penumadu, R. Woracek, F. Kim, "Accomplishments and future needs for engineering applications using energy selective neutron imaging", NEUWAVE 5, Workshop on Neutron Wavelength Dependent Imaging, Lund, Sweden (2013)

11. J. Leszczewicz, E. Kintzel, R. Woracek, D. Penumadu, S. Young, "Development of an In-Situ Load Frame in a Large Chamber Scanning Electron Microscope", Bulletin of the American Physical Society - 79th Annual Meeting of the APS Southeastern Section, Tallahassee, FL (2012)

12. R. Woracek, J. R. Bunn, D. Penumadu, A. Tremsin, N. Kardjilov, I. Manke, "Combined in-situ neutron diffraction and imaging for strain investigations", Science & Scientists @ ESS, Berlin, Germany (2012)

13. R. Woracek, J.R. Bunn, D. Penumadu, A. Tremsin, N. Kardjilov, I. Manke, "Combined in-situ neutron diffraction and imaging for strain investigations", NIUS2012 - ESS Neutron Imaging User Symposium, Bad Zurzach, Switzerland (2012)

14. R. Woracek, J.R. Bunn, D. Penumadu, C.R. Hubbard, " Measurement of hkl specific shear moduli based on lattice strain under torsional loading using in situ neutron diffraction", ORNL User Meeting, Oak Ridge, TN (2010)

15. R. Woracek, D. Penumadu, N. Kardjilov, A. Hilger, M. Dawson, I. Manke, "In-situ Bragg Edge Imaging Trials under Tensile and Torsional Loading at HZB", VULCAN at the SNS: Workshop, Oak Ridge, TN (2010)

Vita

Robin Woracek was born in Lippstadt, Germany in 1982. After attending Gymnasium Antonianum in Geseke, Germany until 10th grade, he pursued his 3 year Abitur (German form of High school diploma and required to attend a University) at the Boerde-Berufskolleg Soest, motivated by the fact that this particular program offered a focus in Mechanical Engineering.

In 2002, Robin enrolled at the "University of Applied Science Suedwestfalen" in Soest, Germany, where he studied Mechanical Engineering. During his studies between 2002 and 2006, Robin participated in a special scholarship program with the industrial "car headlamp/car electronics" manufacturer Hella KGaA Hueck & Co, where he had the opportunity to work as a trainee during the semester breaks. During the course of the four years, Robin was able to gain valuable insight in various departments, ranging from metal and electronic workshops, product design, pre-production planning, and assembly lines, to research departments. He especially enjoyed the work in the research departments. Robin received his Diploma Degree (FH) in Mechanical Engineering in 2006. The title of his Diploma thesis was "Investigation of Desiccants and Methods for the Prevention of Condensation in Automotive Headlights".

In fall 2006, Robin received a Fulbright scholarship and started to pursue a MS degree in Engineering Science at the University of Tennessee under the supervision of Dr. Dayakar Penumadu. He obtained his Master's degree in December 2009 and his thesis was titled "Wetting Behavior of Polymer Melts with Refractory Coatings at High Temperature". Upon completion of his M.S. degree, Robin continues his doctoral research at the University of Tennessee, in a joint research project with the Helmholtz Zentrum Berlin, Germany. The dissertation project is concerned with the development of advanced neutron imaging and diffraction methods for crystallographic investigations.